Ultra Luminous X-Ray Pulsars: Comparison with Galactic X-ray Pulsars

Manish Kumar

Supervisor: Professor Biswajit Paul



Raman Research Institute, Sadashivanagar, Bengaluru, Karnataka 560080, India

A doctoral thesis submitted in partial fulfilment of the requirements
for the degree of Doctor of Philosophy (Physics)
to



Jawaharlal Nehru University, New Delhi

2025

Certificate

This is to certify that the work submitted in the thesis titled '**Ultra Luminous X-Ray Pulsars: Comparison with Galactic X-ray Pulsars**,' submitted by **MANISH KUMAR** (Enrolment No. RRI/2020/002) to the Jawaharlal Nehru University for the award of the degree of **Doctor of Philosophy (Ph.D.) in Physical Sciences** is the bonafide record of the original research work carried out by Manish Kumar under my guidance and supervision at **Raman Research Institute (RRI)**, Bengaluru, India. The results embodied in the thesis have not been submitted to any other University or Institute for the award of any degree or diploma.

Prof. Tarun Souradeep
Director & Professor, RRI

Prof. Biswajit Paul
Supervisor

Astronomy & Astrophysics Group
Raman Research Institute (RRI)
Bengaluru 560080, Karnataka, India

Declaration

I, **MANISH KUMAR** (Enrolment No. RRI/2020/002), declare that the work reported in this thesis titled '**Ultra Luminous X-Ray Pulsars: Comparison with Galactic X-ray Pulsars**' is entirely original. This thesis has been composed by me at **Raman Research Institute (RRI)** under the supervision of **Professor Biswajit Paul** and is the result of my own work unless otherwise stated. I further declare that the subject matter presented in this thesis has not previously formed the basis for awarding any degree, diploma, membership, associateship, fellowship, or any other similar title of any university or institution. I also declare that this thesis has been checked using the plagiarism software DRILLBIT.

Biswajit Paul

Prof. BISWAJIT PAUL
(Supervisor)

MANISH KUMAR
(Candidate)

© Copyrights by **Manish Kumar**, 2025

All rights reserved.

Abstract

Ultra-luminous X-ray sources (ULXs) are extragalactic, off-nuclear X-ray sources with luminosities exceeding the Eddington limit for accretion onto stellar-mass compact objects. Their extreme luminosities, reaching several to over a hundred times the Eddington luminosity, initially motivated interpretations invoking intermediate-mass black holes accreting at sub-Eddington rates. However, subsequent observations and theoretical developments have favoured an alternative picture in which ULXs are powered by stellar-mass compact objects accreting at super-Eddington rates. A major breakthrough came with the discovery of coherent X-ray pulsations from several ULXs, unambiguously establishing neutron stars as the accretors in a subset of these sources and further supporting the super-Eddington accretion scenario onto stellar-mass compact objects. X-ray spectral studies reveal features such as high-energy curvature, soft excess emission, and ionized absorption or emission lines tracing powerful winds, while timing analyses, ranging from variability studies to pulsation detection, provide key constraints on the accretion geometry and emission mechanisms in these sources.

In this thesis, I presented our efforts to better understand the accretion processes and the environments of ULXs. The work started with a comparative study of the broadband spectra of ultra-luminous X-ray pulsars (ULXPs) and Galactic accretion-powered X-ray pulsars, including sources in the Magellanic Clouds, followed by an investigation of possible signatures of X-ray reprocessing in ULXs through iron line searches, hardness-ratio studies during the eclipse transitions, and eclipse flux to out-of-eclipse(OOE) flux ratio measurements in the eclipsing ULXs. Additionally, we investigated variability and pulse-profile properties in selected ULXs and ULXPs. Finally, I briefly presented my learning experience and contributions to the development and calibration of the POLIX, an X-ray polarimeter instrument.

Biswajit Paul

Prof. Biswajit Paul
(Supervisor)

Manish Kumar
(Candidate)

List of Publications

1. **Spectral analysis of ultraluminous X-ray pulsars with models of X-ray pulsars,**
   M. Kumar, R. Sharma, B. Paul, and V. Rana,
   Monthly Notices of the Royal Astronomical Society, **536**(1), 340–349 (2025).
   DOI: 10.1093/mnras/stae2558

2. **Reprocessing of X-ray emission in Ultra-Luminous X-ray sources,**
   M. Kumar, R. Sharma, and B. Paul,
   (Submitted to The Astrophysical Journal)
   e-Print: 2509.09133 [astro-ph.HE]

Biswajit Paul

Prof. Biswajit Paul
(Supervisor)

मनीष

Manish Kumar
(Candidate)

To my family

Acknowledgments

I would like to begin by expressing my deepest gratitude to my PhD supervisor, **Prof. Biswajit Paul**, for his constant guidance, patience, and encouragement throughout my PhD journey. His insights, support, and trust in my work have played a crucial role in shaping this thesis. Under his mentorship, I had the opportunity to work across a wide range of areas, from data analysis to instrumentation, which greatly enriched my understanding of research. I feel truly blessed and deeply grateful to have been guided by him throughout my doctoral journey. I sincerely thank the members of my advisory committee, **Prof. Vikram Rana** and **Prof. Sayantan Majumdar**, for their valuable suggestions, constructive feedback, and encouragement at different stages of my research. I am especially grateful to **Dr. Rahul Sharma** for his continuous help with data analysis and the writing process. His guidance and timely support were extremely helpful during the most challenging phases of my work. I would like to thank all the members of the X-ray Astronomy Laboratory and the POLIX team for their support and cooperation.

In particular, I would like to express my sincere gratitude to **Prof. Biswajit Paul** and **Prof. Vikram Rana** for their constant guidance and encouragement, especially during the initial stages of my involvement with the X-ray laboratory and the POLIX mission. I am especially thankful to **Rishin P. V.**, **Krishna Murthy S.**, **Gopala Krishna M. R.**, **Harikrishna Sahu**, and **Md. Irshad** for their support and guidance during the early phase of my laboratory activities. Their help was crucial in introducing me to the experimental setup, data handling, and the overall workflow of the lab. I am deeply grateful to **Hemanth M.** and **Ketan Rikame** for their invaluable assistance with the calibration of the POLIX data. Their patience, technical expertise, and willingness to help at every step played a very important role in my understanding of the instrument and data analysis. I sincerely thank **Sujay Mate** for his help with the POLIX simulations, which greatly contributed to my understanding of the instrument response and observational characteristics. I would also like to acknowledge **Nandini Srianand** and **Kinjal Roy** for their support in understanding the POLIX data analysis pipeline. Their timely help and discussions were extremely useful. I am thankful to **Puttaswamy M. A.** for his contribution to the ground test experiments of POLIX and for sharing his practical insights. I also thank **Sandhya**, **Mamatha T. S.**, **Pooja Verma**, **Rajgopala**, **Ashwin Devaraj**, **Rahul Sharma**, **Anirban Dutta**, and **Ajith Balu** for their support and help at various stages of the POLIX mission. Each interaction, whether technical or scientific, contributed in some way to the successful completion of this work. I would like to emphasize that the contributions mentioned above are only the aspects I recall most clearly, and there were many more stages during the development of the POLIX mission where I received help, guidance, and opportunities to learn. Throughout this journey, I benefited immensely from discussions, suggestions, and support from several members of the POLIX team, often beyond these specific roles. I am deeply grateful to each and every member of the POLIX team for the learning, encouragement, and support I received during the course of this work.

I would like to sincerely thank **Rahul Sharma**, **Sujay Mate**, **Ketan Rikame**, **Kinjal Roy**, **Ajith Balu**, **Mukesh**, **Aman**, and **Shovan** for reviewing my thesis and providing valuable comments and suggestions. I am also grateful to other members of the X-ray group, including **Abhisek**, **Akash**, **Shuvajit**, and **Barsha**, for their support and helpful inputs at various stages.

I would also like to sincerely thank the administration staff of RRI for their constant support throughout my PhD. I am grateful to all the members of the administration, including the secretaries of the Astronomy and Astrophysics Group, for their help with official procedures and timely assistance whenever required. I would like to especially acknowledge the library staff at RRI for their support during

the final stage of my thesis submission. Their help with plagiarism checking, printing, and preparing the bound copies of the thesis was extremely valuable and made the submission process smooth and stress-free. I also extend my heartfelt thanks to the non-academic staff of RRI for their support and co-operation during my time at the institute. Their help, often behind the scenes, contributed significantly to my PhD journey, and I am truly grateful to each and every one of them.

I would like to sincerely thank my batchmates **Mukesh, Rupak, Shashank, Vaibhav, Pooja, Anirban, Susovan, Sayari, Anson** for their companionship, encouragement, and shared experiences throughout this PhD journey. Walking this path together made the challenges easier and the successes more meaningful. I am grateful to the people on the RRI Astro Floor for creating a friendly, supportive, and intellectually stimulating environment. I would like to thank my sports friends for providing much-needed breaks from academic life. Playing and spending time together helped me stay motivated, refreshed, and balanced during the demanding phases of my PhD. **I would like to thank each and every member of the RRI family for the respect, support, and kindness I received, for which I am truly grateful.**

I bow with deep respect and gratitude to my grandparents, **Sh. Banwarilal (Dada Ji)** and **Sh. Thakarmal (Nana Ji)**, and to our entire family, including all elders and family members, whose blessings, love, and values have been a constant source of strength throughout my life. I am deeply grateful to my parents, **Smt. Lajwanti** and **Sh. Rajender Chhimpa**, for their unconditional love, sacrifices, and unwavering support. Their faith in me gave me the courage to pursue this long and challenging journey, and I owe everything I have achieved to them. I sincerely thank my elder brother, **Ashish**, and my Bhabhi Ji, **Priyanka Ji**, for standing by me and supporting every decision I made, even the random ones, with trust, patience, and unconditional support. I sincerely thank my siblings **Sarita**, **Minakshi**, **Nikhil**, **Nisha**, and **Jitu** for always being there for me, for picking up calls at any time, joining in moments of joy, and for their constant love and support throughout this journey. I am grateful to my entire family for standing by me at every stage of my life. Their blessings, patience, and trust have been my strongest support system throughout this journey.

In the end, I thank everyone from the bottom of my heart for the love and support that made this journey possible. I am deeply grateful to each and every one of you. And to the person who has reached this line, my sincere thanks for taking the time to walk through this work.

Contents

Abstract **vii**

List of Publications **ix**

Synopsis **1**

1 Introduction **5**
- 1.1 X-ray Binaries . . . 5
- 1.2 Accretion: Turning Gravity into Radiation . . . 6
  - Roche Lobe Overflow . . . 7
  - Stellar Wind Accretion . . . 9
  - Disc-Fed Accretion . . . 9
- 1.3 Accretion Disc . . . 9
- 1.4 X-ray Pulsars: Accretion Powered Pulsars . . . 10
- 1.5 Eddington Limit . . . 11
- 1.6 Ultra-Luminous X-ray Sources (ULXs) . . . 12
- 1.7 Understanding X-ray Emission from Compact Objects . . . 12
  - 1.7.1 Spectral Properties of X-ray Emission . . . 13
    - Thermal Emission . . . 13
      - Blackbody radiation. . . . 13
      - Thermal bremsstrahlung. . . . 14
    - Non-Thermal Emission . . . 14
      - Synchrotron radiation. . . . 14
      - Comptonization. . . . 14
    - Line Emission . . . 15
    - X-ray Absorption . . . 15
  - 1.7.2 Timing Properties . . . 16
- 1.8 Current Understanding of ULXs . . . 16
  - 1.8.1 Role of radiation pressure on the accretion flow in ULXs . . . 17
  - 1.8.2 Artistic sketches of the accretion onto the ULX having BH and NS . . . 19
  - 1.8.3 Observed spectral and timing properties . . . 20
  - 1.8.4 Motivation . . . 21

2 X-ray Astronomy and Techniques **23**
- 2.1 Introduction to X-ray Observations and Observatories . . . 23
- 2.2 X-ray Observatories . . . 25
  - 2.2.1 Chandra X-ray Observatory . . . 25
  - 2.2.2 X-ray Multi-Mirror Mission (*XMM-Newton*) . . . 28
  - 2.2.3 Nuclear Spectroscopic Telescope Array (*NuSTAR*) . . . 29
- 2.3 X-ray Data Analysis Techniques . . . 29
  - 2.3.1 Timing Analysis . . . 30
  - 2.3.2 Spectral Analysis . . . 31

3 Expressing ULXPs spectra with Local X-ray pulsar model * **35**
3.1 Introduction . . . 35
3.2 Observations & Source Selection . . . 37
3.2.1 NGC 7793 P13 . . . 38
3.2.2 NGC 5907 ULX1 . . . 38
3.2.3 M51 ULX7 . . . 38
3.2.4 NGC 300 ULX1 . . . 39
3.2.5 NGC 1313 X2 . . . 39
3.3 Data Reduction . . . 39
3.3.1 *XMM-Newton* . . . 39
3.3.2 NuSTAR . . . 39
3.4 Results . . . 42
3.5 Discussion . . . 43

4 Reprocessing of X-rays emission in Ultra-Luminous X-ray sources * **49**
4.1 Introduction . . . 49
4.2 Source Selection & Observations . . . 50
4.3 Data Reduction . . . 52
4.3.1 XMM-Newton . . . 52
4.3.2 Chandra . . . 53
4.4 Analysis and Results . . . 53
4.4.1 Search for iron emission line . . . 53
4.4.2 Hardness Ratio around the eclipse transitions . . . 54
4.4.3 Flux Ratio during Eclipse to Out-of-Eclipse Phase . . . 58
4.5 Discussion . . . 59

5 Flaring Study in the ULX sources NGC 4559 X7 and NGC 7456 ULX1 **67**
5.1 Introduction . . . 67
5.2 Observation & Source Selection . . . 68
5.3 Data Reduction . . . 71
5.4 Analysis and Results . . . 72
5.5 Discussion . . . 73

6 Energy dependence and luminosity dependence of pulse profiles in ULXPs **81**
6.1 Introduction . . . 81
6.2 Observation & Source Selection . . . 83
6.3 Data Reduction . . . 84
6.4 Analysis and Preliminary Results . . . 84
6.4.1 Reconstruction of Pulse Profiles . . . 85
6.4.2 Luminosity-Dependent Evolution of Pulse Profiles . . . 86
6.5 Discussion . . . 92

7 **POLIX** : **I**ndian **X**-ray **Pol**arimeter **97**
7.1 Introduction . . . 98
7.2 Standard formalism for polarization measurement . . . 99
7.3 POLIX . . . 101
7.3.1 Design . . . 101

7.3.2 Proportional Gas Counter and Detection Principle . . . 102
7.3.3 Gas mixture and gain Stability for Propotional Gas Counter . . . 105
7.4 Contributions to POLIX development activities . . . 106
7.4.1 Gas Filling and Leak Test During Detector Assembly . . . 107
7.4.2 Position and Energy Calibration . . . 110
7.4.3 Gain monitoring during the mission . . . 118
7.5 Summary . . . 120

8 Summary and Future Prospect **121**
8.1 Summary . . . 121
8.1.1 Expressing ULXP spectra with local X-ray pulsar models . . . 121
8.1.2 Reprocessing of X-rays in ULXs . . . 122
8.1.3 Flaring behaviour in NGC 4559 X7 and NGC 7456 ULX1 . . . 122
8.1.4 Energy dependence and luminosity dependence of pulse profiles in ULXPs . 123
8.1.5 POLIX: Indian X-ray Polarimeter . . . 124
8.2 Ongoing/Future Research Direction . . . 124

References **139**

Listing of figures

1.1 (a) Stellar-wind accretion in a high-mass X-ray binary (HMXB), where the compact object captures a fraction of the dense radiatively driven wind from an OB supergiant companion. (b) Roche-lobe overflow (RLOF) in a low-mass X-ray binary (LMXB), in which the donor star fills its Roche lobe and transfers material through the inner Lagrangian point L_1, forming an accretion disk. (c) Be/X-ray binary accretion, where the neutron star interacts with the decretion disc of a rapidly rotating Be-star companion during periastron passages, leading to periodic enhancements in the X-ray flux as shown in the bottom panel. (Fig. credit: Tauris & van den Heuvel (2006)) 7

1.2 Roche equipotential contours in the orbital plane of a binary with mass ratio $q = M_2/M_1 = 0.25$. The centre of mass (CM) and Lagrangian points L_1–L_5 are marked. The saddle point L_1 connects the two Roche lobes, shown by the figure-of-eight equipotential. L_4 and L_5 are local maxima of $\Phi_{\rm R}$, where Coriolis forces stabilize synchronous orbits of test particles. (Fig. credit: Frank et al. (2002)) 8

1.3 Left: Misalignment of the spin and magnetic axis of a neutron star produces X-ray pulsations. Right: Accretion disk around a magnetized neutron star, truncated at the magnetospheric radius, where matter follows magnetic field lines onto the magnetic poles. (Fig. credit: Frank et al. (2002), Srinivasan (2024)) 10

1.4 Schematic illustration of a super-Eddington slim accretion disk. The diagram shows the main structural regions of the accretion flow: (A) an outer sub-Eddington, geometrically thin disk; (B) an inner radiation-pressure-dominated region where the local energy release approaches the Eddington limit and the disk inflates vertically; (C) a porous, inhomogeneous layer forming above the convection zone; (D) a radiatively driven wind launched from regions where the porous structure becomes optically thin; and (E) the effective photosphere, which is located within the outflowing wind. (Fig. credit: Dotan & Shaviv (2011)) 20

1.5 Schematic of a ULX powered by accretion onto a strongly magnetized neutron star. The accretion disk is truncated at the magnetospheric radius ($R_{\rm m}$). When the spherization radius ($R_{\rm sph}$) exceeds $R_{\rm m}$, radiatively driven winds are launched, while the remaining matter is funneled along magnetic field lines to form accretion columns and an optically thick envelope characteristic of ULX pulsars (Fig. credit: Mushtukov et al. (2019)). . . 21

2.1 The electromagnetic spectrum. (Fig. Credits: (Culhane & Sanford 1981)) 24

2.2 Atmospheric transmission as a function of wavelength. As shown, the Earth's atmosphere is nearly opaque below ∼100 nm, necessitating space-based X-ray observatories. (Fig. credit: NASA; SVG by Mysid) 24

2.3 Schematic diagram of the *Chandra* X-ray Observatory. (Fig. credit: NASA/CXO) . . . 26

2.4 Schematic diagram of the *XMM-Newton* X-ray observatory. (Fig. credit: ESA/XMM–Newton) 26

2.5 Schematic diagram of the *NuSTAR* observatory in its mast-stowed configuration (bottom) and mast-deployed configuration (top). (Fig. credit: NASA/NuSTAR; (Harrison et al. 2013)) 27

2.6 Comparison of the effective area of the X-ray instruments used in this thesis. (Fig. credit: NASA/ESA) 29

3.1 Best-fit spectrum of ULXPs with simultaneous or quasi-simultaneous observations from *XMM-Newton* and NuSTAR. Green color data points correspond to the EPIC-pn spectra. Black and red data points represent the spectra from NuSTAR FPMA and FPMB, respectively. For NGC 5907 ULX1, the second NuSTAR observation is presented in cyan and magenta colors for FPMA and FPMB, respectively. For NGC 300 ULX1, the second *XMM-Newton* observation is presented in blue color. 41

3.2 Comparative studies of hydrogen column density (N_H: number of hydrogen atoms per squared cm projected along the line of sight) and equivalent width (EQW) of iron K-alpha line for SgHMXBs, SFXTs (Pradhan et al. 2018), LMXBs (Ng, C. et al. 2010), LMC X-4, SMC X-1 (Paul et al. 2002), Her X-1 (Naik & Paul 2003), 4U 1626-67 (Sharma et al. 2023a), M82 X-1 (Caballero-García 2011), NGC 7456 ULX1 (Mondal et al. 2021), XTE J1650-500 (Walton et al. 2012) and ULXPs. The SgHMXBs are indicated in orange, SXFTs in green, LMXBs in blue, LMC X-4 in cyan, SMC X-1 in red, Her X-1 in dark green, 4U 1626-67 in black, M82 X-1 in purple, XTE J1650-500 in red (different point type), and NGC 7456 ULX1 in midnight-blue color. The ULXPs measurements are indicated in magenta points. 44

4.1 Top panel presents the combined spectra from *XMM-Newton* observations of individual ULX (left) and ULXP (right) sources. The bottom panel (on the left) presents the combined spectra from all observations of 6 ULXs and 5 ULXPs analyzed in this work. On the right, residuals from the best-fit absorbed powerlaw model are shown for the combined spectra in the energy range of 5.5–7.5 keV, 5–8 keV, and 4–9 keV. 56

4.2 Residuals from the best-fit absorbed powerlaw model for the combined spectra of individual sources, shown over three energy ranges: 5.5–7.5 keV, 5–8 keV, and 4–9 keV. 57

4.3 Histogram for the EW recovered from fits to the combined simulated spectra of all sources. Different colors represent simulations in which artificial iron lines with EW values of 15 eV, 20 eV, and 30 eV were inserted into the individual source spectra before combining. 58

4.4 Light curves and hardness ratios around the eclipse transitions. The top row shows results for the well-known HMXBs (LMC X–4 and SMC X–1), while the subsequent rows present the eclipsing ULX sources. 60

4.5 Spectrum during eclipse and OOE phase for the CG X1 (Chandra), M51 S1 (*XMM-Newton*), M51 S2 (*XMM-Newton*), M51 ULX1 (Chandra) and M51 ULX2 (Chandra). Bottom panels shows the best-fit residuals. 61

4.6 Comparative studies of hydrogen column density (N_H: number of hydrogen atoms cm^{-2} along the line of sight) and equivalent width (EW) of iron Kα line for SgHMXBs, SFXTs (Pradhan et al. 2018), LMXBs (Ng, C. et al. 2010), LMC X-4, SMC X-1 (Paul et al. 2002), Her X-1 (Naik & Paul 2003), 4U 1626-67 (Sharma et al. 2023a), M82 X-1 (Caballero-García 2011), NGC 7456 ULX1 (Mondal et al. 2021), XTE J1650-500 (Walton et al. 2012) and ULXPs. The column density values are taken from previous studies mentioned in Table 4.2. The black dashed line corresponds to the expected EW value for a given column density ($\mathrm{EW} = 0.00329\,\mathrm{N_H^{22}\,keV}$) assuming the spherical reprocessing geometry around the X–ray source (Torrejón et al. 2010). 63

4.7 Expected column density calculations assuming the accretion through a spherically symmetric wind around the companion. The horizontal gray region denotes the range for measured column densities reported in previous studies (Table 4.2) for ULXPs/ULX sources. 64

5.1 Light curves for the observations listed in Table 5.1, shown in the 0.3–10.0 keV energy band. Observations of the same source are plotted using the same color. The fractional variability (%) is indicated in each panel. 69
5.2 The hardness ratio (H/S) as a function of the total count rate. The energy ranges used to define the hard and soft energy bands are indicated in each panel. 70
5.3 **NGC 4559 X7 (ObsID - 0842340201):** Panel (a) shows the X-ray light curves in different energy ranges, highlighting clear variability at higher energies. Panel (b) presents the hardness ratio as a function of total count rate, where the source becomes spectrally harder with increasing brightness. Panel (c) displays the energy spectra extracted in distinct count-rate states, illustrating that the hard power-law component strengthens during high-flux intervals while the soft disk component remains comparatively stable. 74
5.4 **NGC 4559 X7 (ObsID - 0883960201):** Panel (a) shows the X-ray light curves in different energy ranges, highlighting clear variability at higher energies. Panel (b) presents the hardness ratio as a function of total count rate, where the source becomes spectrally harder with increasing brightness. Panel (c) displays the energy spectra extracted in distinct count-rate states, illustrating that the hard power-law component strengthens during high-flux intervals while the soft disk component remains comparatively stable. 75
5.5 **NGC 7456 ULX1 (ObsID - 0901330101):** Panel (a) shows the X-ray light curves in various energy ranges, indicating that most of the variability originates in the soft band. Panel (b) displays the hardness ratio versus total count rate, showing that the source becomes spectrally softer at higher intensities. Panel (c) presents the spectra extracted in different count-rate states, illustrating that the soft thermal component strengthens during high-flux intervals while the hard component remains comparatively stable. . . 76
5.6 Evolution of the inner disk radius, column density, inner disk temperature, and power-law index as a function of luminosity. Blue symbols represent the two observations of NGC 4559 X7 (with different marke types), while red symbols correspond to NGC 7456 ULX1. The inner disk radius is plotted assuming a face-on disk geometry. But actually, the quantity shown on the y-axis of panel (a) is $R_{\rm in}\sqrt{\cos\theta}$. 77

6.1 Sample P–$\dot{P}$ diagrams for each ULXP, with the corresponding source name and observation ID indicated in the respective panel. 84
6.2 Pulse fraction as a function of energy for the two observations of NGC 300 ULX1 shown in panels (a) and (b). In each panel, the top plot shows the folded pulse profiles in different energy bands (indicated by different colours), and the bottom plot shows the corresponding pulse fraction as a function of energy. 87
6.3 Panels (a) and (b) show the folded pulse profiles of NGC 300 ULX1 for the observations listed at the top of each panel. Each panel contains two plots: the top plot shows the folded pulse profile in the 0.3–10 keV energy range (in blue), and the bottom plot shows the profiles in the soft (0.3–2.0 keV) and hard (2.0–10.0 keV) bands, plotted in red and green, respectively. 87

6.4 Folded pulse profiles of M51 ULX7 in the 0.3–$10.0\ \mathrm{keV}$ (blue), soft (0.3–$2.0\ \mathrm{keV}$; red), and hard (2.0–$10.0\ \mathrm{keV}$; green) bands. Panels (a)–(f) are arranged in order of increasing luminosity to highlight phase differences between the soft and hard profiles. The dashed curves represent the best-fitting sinusoidal model to the folded pulse profiles. 89

6.5 Folded pulse profiles of NGC 5907 ULX1 in the 0.3–$10.0\ \mathrm{keV}$ (blue), soft (0.3–$2.0\ \mathrm{keV}$; red), and hard (2.0–$10.0\ \mathrm{keV}$; green) bands. Panels (a)–(h) are arranged in order of increasing luminosity to highlight phase differences between the soft and hard profiles. The dashed curves represent the best-fitting sinusoidal model to the folded pulse profiles. 90

6.6 Folded pulse profiles of NGC 7793 P13, along with the best fitted sinusoidal modeled profile in dashed line, arranged in order of increasing luminosity (from top-left to bottom-center) to highlight soft–hard phase differences. 91

6.7 Folded pulse profiles of NGC 5907 ULX1 and NGC 1313 X2 in the 0.3–$10.0\ \mathrm{keV}$ (blue), soft (0.3–$2.0\ \mathrm{keV}$; red), and hard (2.0–$10.0\ \mathrm{keV}$; green) bands. No significant pulsed emission is observed. 92

6.8 Phase difference between the hard and soft pulse profiles (top panels) and pulse fraction (bottom panels) plotted as a function of luminosity for M51 ULX7, NGC 5907 ULX1, and NGC 7793 P13 in panels (a), (b), and (c), respectively. 93

7.1 Thomson scattering of linearly polarized X-rays. Polarized photons incident along the z-axis scatter anisotropically in the x–y plane, producing a $\cos^2\theta$ modulation of intensity with azimuth (Fig. credit: POLIX Team). 102

7.2 (a) Artistic illustration of the POLIX instrument with one detector removed to show the central Beryllium scatterer and internal structure. (b) Laboratory photograph of the fully assembled POLIX instrument, showing two of the four proportional counters and three attached back-end electronics modules (Fig. credit: POLIX Team). 103

7.3 (a) Exploded view of the POLIX proportional counter showing its main mechanical components: the detector housing (purple), the wireframe assembly (orange), the Mylar® window (grey), and the window support plate (green). (b) Illustration of the charge-division principle. The charge collected at the anode ends produces voltage pulses whose amplitudes are proportional to the distance travelled along the resistive wire. The ratio of the pulse amplitude at one end to the total pulse amplitude provides the position of photon interaction within the detector (Fig. credit: POLIX Team). 104

7.4 Side view of the wireframe. The red and blue segments represent detector channels 1 and 2, respectively, each formed by six main anode wires connected in series. The green segments correspond to the anti-anode wires connected to same HV source, which serve as an active veto layer for rejecting charged-particle background (Fig. credit: POLIX Team). 104

7.5 (a) Spectral response of the detector to the 5.9 keV line obtained from laboratory measurements. (b) Ratio distribution of the same data for the selected PHA range. Each pillar corresponds to one of the six anode wires, and the ratio distribution varies with the selected energy range. 107

7.6 Gain monitoring using the ^{55}Fe source to assess detector performance and confirm no gas leakage. The initial gain drop arises from water vapor diffusion through the Mylar® window, while vacuum storage restores the gain as the moisture outgasses. The final small decrease is due to a temporary rise in ambient temperature on that day. 108

7.7 Long-term gain evolution measured using the 5.9 keV line for Detectors FM01 and FM02 following assembly. The green region denotes intervals during which the detector was exposed to ambient atmospheric conditions, whereas the orange region indicates periods when the detector was maintained under vacuum. 109
7.8 (a) Experimental setup used for detector position calibration. The sources are placed sequentially at each calibration hole, and the corresponding ratio and PHA values are recorded. (b) A sample spectral response obtained from both sources when placed at calibration position x_1y_1. (c) Artistic schematic showing the 36 calibration positions distributed across the detector surface (Fig. credit: POLIX Team). 111
7.9 Panels (a) and (b) show the gain variation for Detector ID: FM01, corresponding to the ^{55}Fe (red) and ^{109}Cd (blue) sources across all 18 calibration positions in Channels 1 and 2, respectively, covering a total of 36 detector positions. 112
7.10 Panels (a) and (b) show the gain variation for Detector ID: FM02, corresponding to the ^{55}Fe (red) and ^{109}Cd (blue) sources across all 18 calibration positions in Channels 1 and 2, respectively, covering a total of 36 detector positions. 113
7.11 Panels (a) and (b) show the gain variation for Detector ID: FM03, corresponding to the ^{55}Fe (red) and ^{109}Cd (blue) sources across all 18 calibration positions in Channels 1 and 2, respectively, covering a total of 36 detector positions. 114
7.12 Panels (a) and (b) show the gain variation for Detector ID: FM04, corresponding to the ^{55}Fe (red) and ^{109}Cd (blue) sources across all 18 calibration positions in Channels 1 and 2, respectively, covering a total of 36 detector positions. In Detector FM04, seven anode wires (3 in CH1 and 4 in CH2) have a larger diameter, which leads to a higher gain relative to the other wires. 115
7.13 Panels (i), (ii), and (iii) show the position versus ratio distributions for both channels of detectors FM01, FM02, and FM03, respectively. As expected, the ratio spread across all six anode wires is narrower at higher energies. For Detector 2, Channel 1, the ratio trend appears reversed due to the interchange of the C1AN1 and C1AN2 ends during assembly. 116
7.14 Position versus ratio distributions for both channels of detectors FM04. As expected, the ratio spread across all six anode wires is narrower at higher energies. 117
7.15 Ratio value distribution for all 18 calibration positions of Detector FM01, Channel 1. Each peak corresponds to 18 positions of channel 1, and peaks with the same color represent different positions along the same anode wire. The top panel shows results for the ^{109}Cd source, while the bottom panel corresponds to the ^{55}Fe source. As expected, the ratio spread is narrower for the higher-energy photons. 117
7.16 (a) Ratio distribution for Detector 1, Channel 1, obtained from POLIX observations on 10-07-2024. (b) Energy spectrum for Wire 1 from the same dataset, showing a prominent background peak that is monitored daily. (c) Gain monitoring plots for the flight data over time up to 23-10-2025. 119

SYNOPSIS

Ultra Luminous X-Ray Pulsars: Comparison with Galactic X-ray Pulsars

Introduction

X-ray binaries are among the most luminous stellar systems, powered by the accretion of matter onto compact objects such as black holes (BHs) or neutron stars (NSs) (Shakura & Sunyaev 1973, Frank et al. 2002). The primary source of their energy output arises from the release of gravitational potential energy during accretion. However, radiation pressure imposes a fundamental limit on the accretion rate, giving rise to the so-called Eddington luminosity (Eddington 1920). Interestingly, observations have revealed a population of off-nuclear, point-like sources in nearby galaxies whose apparent luminosities exceed this classical Eddington limit. These objects are known as ultraluminous X-ray sources (ULXs), and understanding the underlying emission mechanism is one of the most intriguing challenges in high-energy astrophysics (Fabbiano 1989, Kaaret et al. 2017, King et al. 2023). In some systems, the accreting neutron stars reveal themselves as X-ray pulsars through their coherent pulsations, produced by magnetically channelled accretion onto the poles of the neutron star (Nagase 1989). Such pulsations are commonly observed in Galactic X-ray binaries as well as some of the ULXs.

Building on their discovery, extensive spectral and timing studies have been carried out to probe the physical nature of ULXs. X-ray spectroscopy has revealed characteristic features such as high-energy curvature and soft excesses, as well as broadened emission and absorption lines predominantly in the soft X-ray band ($\lesssim$ 2keV), that trace strong ionized winds originating from the inner accretion flow (Kosec et al. 2021). Collectively, these features indicate complex accretion processes that likely involve super-Eddington accretion flows, radiation-driven outflows, or geometrical beaming effects (King et al. 2023). Timing analyses, ranging from variability studies to the detection of coherent pulsations, provide further insights into the accretion geometry and the nature of the compact objects powering these systems. The discovery of pulsations in a growing number of ULXs has confirmed that at least a fraction of them host neutron stars, challenging our understanding of accretion physics at extreme luminosities (Bachetti et al. 2014, Fürst et al. 2016, 2017). Together, spectral and timing investigations are crucial for disentangling the physical mechanisms that enable these sources to radiate far above the classical Eddington limit, thereby shedding light on both the accretion physics and the demographics of compact objects in external galaxies.

Despite the significant progress, the geometry of accretion and the physical drivers of the observed spectral and timing properties in ULXs remain open questions. The objective of this work is to perform a detailed investigation of ULXs through combined spectral and timing analyses, with some emphasis on sources exhibiting pulsations. By comparing observational signatures with known galactic pulsars or the theoretical models of super-Eddington accretion and magnetically channeled flows, this study aims to advance our understanding of how compact objects can sustain such extreme luminosities and to provide new insights into the role of neutron stars and black holes in powering the ULXs.

This thesis is broadly divided into two parts. The first part focuses on the study of the environment and physical properties of Ultra-luminous X-ray Sources (ULXs), while the second part highlights my

learning experience and contributions towards the development of the **POLIX: Indian X-ray Polarimeter**. **Chapter 1** introduces the previous studies and the current understanding of X-ray binaries and ULXs, followed by **Chapter 2**, which outlines observational techniques, X-ray instrumentation, and data analysis methods for spectral and timing studies. **Chapter 3** discusses the spectral properties of ULX pulsars by applying models commonly used for local X-ray pulsars, while **Chapter 4** examines various aspects of X-ray reprocessing in ULXs. **Chapters 5 and 6** present study on the flaring behavior of ULXs and the evolution of pulse profiles of known ULXPs with time and intensity. **Chapter 7** describes my contributions to the development of POLIX, and finally, **Chapter 8** summarizes the results and outlines future research directions.

Expressing ULXPs spectra with Local X-ray pulsar model

A fraction of the Ultra Luminous X-ray (ULX) sources are known to be accreting neutron stars as they show coherent X-ray pulsations with pulse periods ranging from $\sim 1 - 30$ seconds. While initially thought to host intermediate-mass black holes, ULXs have since been recognized as a diverse class of objects, including ULX pulsars. The X-ray spectra of the ULX pulsars are often fitted with spectral model specifically tailored to account for their unique accretion physics, distinct from those used for Galactic black hole binaries. The X-ray spectra of all Galactic accreting X-ray pulsars (including sources in the Magellanic Clouds) are dominated by a high energy cut-off power-law and some of the sources show a soft excess, some emission lines, cyclotron absorption features, etc.

In this work, we undertake a comprehensive analysis of the broadband X-ray spectra of five ULX pulsars using simultaneous *XMM-Newton* and NuSTAR observations and show that their X-ray spectra can be effectively described by spectral models, similar to those used for the local accretion-powered X-ray pulsars. A soft excess is detected in all the sources which is also consistent with the local X-ray pulsars that have low absorption column density. We have marginal detection or low upper limit on the presence of the iron K-alpha emission line from these sources, which is a key difference of the ULX pulsars with the local accreting X-ray pulsars. We discuss the implication of this on the nature of the binary companion and the accretion mechanism in the ULX pulsars.

Reprocessing of X-rays in ULXs

After discovering the pulsation in some of the ultra-luminous X-ray sources (ULXs), it is quite clear that most of the ULXs harbor either a neutron star or a stellar mass black hole as a compact object accreting at super-Eddington rates. Having such a high accretion rate, signatures of the reprocessed emission in the ULX sources is quite meagre compared to that observed in galactic X-ray binaries, except for some absorption lines in the winds.

In this work, we investigate the nature of reprocessed emission in ULXs using three diagnostics: (i) searches for Fe $K\alpha$ lines in bright well-known ULXs and Ultra luminous X-ray Pulsars (ULXPs), (ii) evolution of hardness ratio with orbital phase, and (iii) the flux ratio between eclipse and out-of-eclipse (OOE) phase in eclipsing ULXs. We placed the most stringent constraints to date on the upper limits on EW of the iron line, $12 - 20$ eV. Furthermore, we have not observed any significant changes in the hardness ratio during the ingress or egress, while in galactic eclipsing X-ray binaries, an increase in the hardness ratio is observed during the transitions. Finally, the eclipse to OOE flux ratio is found to be larger in ULXs compared to galactic eclipsing X-ray binaries. Based on these results, we discuss the possibility of a metal-poor or highly ionized environment surrounding the ULXs, which suppresses reprocessed emission features.

Flaring Study in the ULX sources NGC 4559 X7 and NGC 7456 ULX1

Flaring or dipping activity is a common feature in X-ray binaries and has been studied both in Galactic systems and in some ULXs. In Galactic binaries, flares are often linked to changes in the accretion rate or instabilities in the accretion disk (Kolb 2010). Similar flaring has also been reported in a few ULXs, suggesting that such variability can provide important clues about their accretion processes and emission geometry.

In this work, we investigated spectral characteristics associated with the flaring activities of the ultraluminous X-ray sources (ULXs) NGC 4559 X7 and NGC 7456 ULX1. Our focus is on identifying the energy dependence of the variability and examining the spectral components responsible for it. These two sources display variability in opposite energy bands: NGC 4559 X7 shows stronger variability only in the hard energy band, while NGC 7456 ULX1 exhibits variability only in the lower energy band, suggesting that different emission components may be driving the observed variability. These results point towards the need for extensive similar studies on the whole class of variable ULXs to investigate whether there is a continuum of spectral dependence of the variability, of which these two sources are at the two extreme ends.

Energy dependence and luminosity dependence of pulse profiles in ULXPs

Most of the Galactic accreting pulsars show strong energy dependence of the pulse profiles, indicating different beaming patterns at different energies, or even an independent origin of multiple spectral components. In the sources with superorbital period, the phase between the soft and hard X-ray profiles also changes with the phase of the superorbital intensity variation. This conforms with a hypothesis that in these sources, the soft spectral component is reprocessed emission of the hard X-rays from the inner accretion disk, the visibility of which changes with the superorbital phase.

In this work, we reconstruct the folded pulse profiles for all available *XMM-Newton* observations of known ULX pulsars (ULXPs). Among these, NGC 7793 P13 provides data with sufficiently high statistical significance to allow a detailed comparison of pulse profiles across different energy bands. For this source, we investigate how the soft and hard X-ray energy band pulse profiles evolve with changes in flux or luminosity. In particular, we examine the relative phases between the soft and hard X-ray pulse profiles, along with the flux/luminosity of the sources, to explore the underlying emission geometry for the reprocessed emission.

POLIX: Indian X-ray Polarimeter

Till now, most studies of X-ray binaries (XRBs) have focused on the timing and spectral properties of their X-ray emission. However, polarization measurements can also provide crucial information about the emission mechanisms and offer deeper insight into the environment around compact objects. Currently, there are only two dedicated X-ray polarization missions in operation. The first is IXPE, launched by NASA, which operates in the 2–8 keV energy range. The second is POLIX (Indian X-ray Polarimeter), launched by ISRO on January 1, 2024, covering the 8–30 keV energy range.

POLIX is based on the principle of Thomson scattering. When linearly polarized X-ray photons incident along the z-direction interact with a scatterer, the scattered photons in the x–y plane exhibit a modulation in intensity as a function of azimuthal angle. The POLIX payload is essentially composed of four rectangular proportional counters arranged as the four walls of a room, with the scatterer placed on the base plate and a collimator mounted on the top. Each proportional counter contains 12 anode

wires, connected alternately to Channel-1 and Channel-2. Since POLIX rotates about the collimator axis, each of the 48 anode wires effectively acts as an independent polarimeter. The final polarization measurement is obtained by combining the results from all the wires after correcting for their relative phase offsets.

For proportional gas counters, it is essential to monitor the stability of the gas gain and to ensure that the detectors are leak-proof. To verify the leak-tightness, the PHA values corresponding to the 5.9 keV Fe calibration source are regularly monitored. In this chapter, we summarize these results along with the position and energy calibration measurements carried out for POLIX in the LAB and the energy calibration from the flight data.

Publications

1. **Spectral analysis of ultraluminous X-ray pulsars with models of X-ray pulsars**,
   M. Kumar, R. Sharma, B. Paul, and V. Rana,
   Monthly Notices of the Royal Astronomical Society, **536**(1), 340–349 (2025).
   DOI: 10.1093/mnras/stae2558

2. **Reprocessing of X-ray emission in Ultra-Luminous X-ray sources**,
   M. Kumar, R. Sharma, and B. Paul,
   (Submitted to The Astrophysical Journal)
   e-Print: 2509.09133 [astro-ph.HE]

Biswajit Paul

Prof. Biswajit Paul
(Supervisor)

Manish Kumar
(Candidate)

1 Introduction

X-ray astronomy opened a new observational window onto extreme astrophysical environments governed by strong gravity and high-energy radiation processes. Early observations revealed that some of the brightest point-like sources in the X-ray sky are X-ray binary (XRB) systems (Giacconi et al. 1962, Frank et al. 2002). These systems consist of a compact object such as a neutron star (NS), black hole (BH), or white dwarf (WD) accreting matter from a companion star in a binary orbit. The accreted material, drawn by the strong gravitational pull of the compact object, releases its gravitational potential energy as high-energy radiation, predominantly in the X-ray band.

However, accretion-powered luminosities cannot increase without bound. As inflowing matter radiates energy, the resulting outward radiation pressure counteracts the inward pull of gravity, establishing an upper theoretical limit on the luminosity of an accreting source, known as the Eddington luminosity (Frank et al. 2002). This limit is a natural consequence of the balance between gravity and radiation pressure, and for decades it was regarded as a firm boundary for the brightness of accreting compact objects. Surprisingly, with the advent of the Einstein Observatory (Fabbiano 1989), astronomers began to identify a population of off-nuclear, point-like X-ray sources in nearby galaxies whose inferred luminosities greatly exceeded this limit for a typical stellar-mass compact object. These enigmatic sources, termed Ultraluminous X-ray Sources (ULXs), immediately changed our current understanding of accretion physics for such compact object populations. Over the past four decades, ULXs have emerged as a central topic in high-energy astrophysics, with systematic surveys revealing more than 1800 candidates in the local Universe (Walton et al. 2021). Their extreme luminosities, diverse spectral and timing behaviors, and recent discoveries of pulsations have established them as a unique laboratory for probing accretion under extreme conditions. In this chapter, we begin with a discussion of X-ray binaries and their accretion processes, before introducing ultraluminous X-ray sources. We then summarize the current understanding of ULXs, focusing on their physical nature and the properties of their surrounding environments and then give the motivation for the research presented in this thesis.

1.1 X-ray Binaries

X-ray binaries (XRBs) represent a diverse class of systems where a compact object interacts with a normal stellar companion in a binary orbit, producing some of the brightest X-ray sources in the sky. Unlike isolated compact objects, which are faint in X-rays unless powered by residual cooling or magnetic activity, XRBs shine through/because of the accretion of matter from their companion stars. The infalling gas loses gravitational potential energy, which is converted into heat and radiation, making these systems powerful probes of high-energy astrophysical processes (Frank et al. 2002).

The compact object in an XRB may be a black hole (BH), a neutron star (NS), or a white dwarf (WD), and each case leads to distinct observational signatures. Black hole binaries often exhibit relativistic jets and characteristic spectral state transitions, neutron star binaries display thermonuclear (Type I)

bursts and X-ray pulsations, while accreting white dwarfs (cataclysmic variables) produce phenomena such as novae and dwarf novae.

The XRBs are further classified based on the mass of the companion star: high-mass X-ray binaries (HMXBs), low-mass X-ray binaries (LMXBs), and intermediate-mass X-ray binaries (IMXBs). High-mass X-ray binaries (HMXBs) contain companions with masses $M_{\rm comp} \gtrsim 10\,M_\odot$, generally belonging to the O- or B-type spectral class. Owing to the rapid evolution of such massive stars, HMXBs are associated with young stellar populations and are predominantly located in the Galactic disk and star-forming regions. In contrast, low-mass X-ray binaries (LMXBs) host donor stars with $M_{\rm comp} \lesssim 2\,M_\odot$, typically late-type stars (later than spectral class A). Mass transfer in LMXBs typically occurs through Roche-lobe overflow, which leads to the formation of an accretion disk around the compact object. Although the disk is dynamically stable in terms of angular momentum transport, its thermal–viscous structure can become unstable when the mass transfer rate falls below a critical threshold. These disk instabilities give rise to transient behavior and outburst cycles commonly observed in LMXBs. Because of their long-lived donor stars, LMXBs trace older stellar populations and are frequently found in the Galactic bulge and globular clusters. Intermediate-mass X-ray binaries (IMXBs) contain donor stars with masses in the range $2\,M_\odot \lesssim M_{\rm comp} \lesssim 10\,M_\odot$, exhibiting characteristics intermediate between HMXBs and LMXBs (Reig 2011, Frank et al. 2002).

The HMXBs are further classified based on the nature of the companion star. Systems with OBe stars of luminosity class III–V are referred to as Be/X-ray binaries (BeXBs), where mass transfer occurs through the decretion disk of the Be star, typically producing transient outbursts. In contrast, systems with companions of luminosity class I–II are known as supergiant X-ray binaries (SgXBs), in which the compact object accretes from the strong stellar winds of the supergiant, usually leading to more persistent X-ray emission (Reig 2011, Walter et al. 2015). Supergiant X-ray binaries (SgXBs) can be further divided into classical systems and supergiant fast X-ray transients (SFXTs). While both are powered by wind accretion from the supergiant companion, SFXTs display much stronger variability, producing sporadic short outbursts and flares on timescales of minutes to hours (Pradhan et al. 2018).

1.2 Accretion: Turning Gravity into Radiation

One may ask: what is the source of such enormous energy in these systems? One obvious mechanism could be nuclear burning, as occurs in normal stars. However, in X-ray binaries, the primary source of the energy is gravity. As matter falls onto a compact object, its gravitational potential energy is released and efficiently converted into radiation. This process is known as *accretion*. For a particle of mass m falling onto a compact star of mass M_* and radius R_*, the gravitational potential energy released is

$$\Delta E_{\rm acc} = \frac{GM_* m}{R_*}, \tag{1.1}$$

where G is the gravitational constant (Frank et al. 2002). For example, if 1 gram of matter falls onto a neutron star with $M_* \sim 1.4 M_\odot$ and $R_* \sim 10$ km, the released energy is about 10^{20} erg g^{-1}. For comparison, nuclear fusion of hydrogen into helium yields $\Delta E_{\rm nuc} \simeq 0.007 mc^2 \sim 6\times10^{18}$ erg g^{-1}, only 6% of the former. Thus, accretion onto compact objects is far more efficient in production of radiation than nuclear burning in stars (Frank et al. 2002).

The resulting *accretion luminosity* is expressed as

$$L_{\rm acc} = \frac{GM_* \dot{m}}{R_*}, \tag{1.2}$$

where $\dot{m}$ is the mass accretion rate. The manner in which mass is transferred from the donor star to the compact object depends on binary separation, stellar type, and orbital dynamics. The three principal mechanisms are: Roche lobe overflow, stellar wind accretion, and disc-fed accretion.

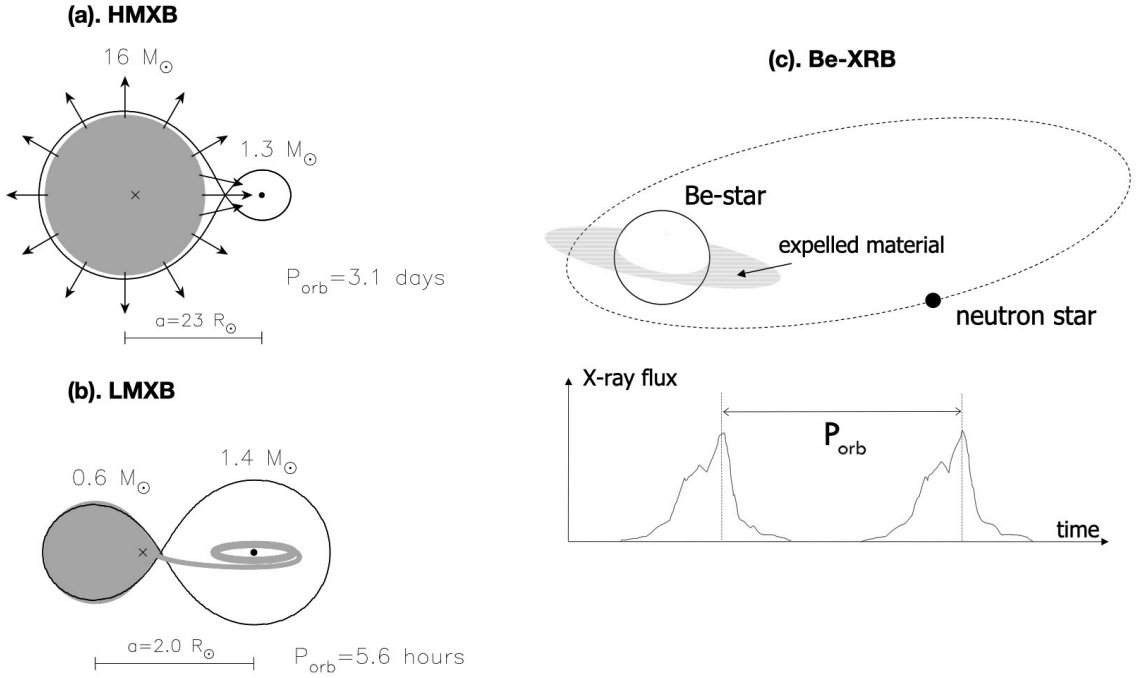


Figure 1.1: (a) Stellar-wind accretion in a high-mass X-ray binary (HMXB), where the compact object captures a fraction of the dense radiatively driven wind from an OB supergiant companion. (b) Roche-lobe overflow (RLOF) in a low-mass X-ray binary (LMXB), in which the donor star fills its Roche lobe and transfers material through the inner Lagrangian point L_1, forming an accretion disk. (c) Be/X-ray binary accretion, where the neutron star interacts with the decretion disc of a rapidly rotating Be-star companion during periastron passages, leading to periodic enhancements in the X-ray flux as shown in the bottom panel. (Fig. credit: Tauris & van den Heuvel (2006))

Roche Lobe Overflow

In an X-ray binary system, a compact object and its companion orbit around their common center of mass. Assuming a circular orbit and treating both stars as point masses M_1 and M_2, the effective potential (also called the Roche potential) experienced by a test particle in the co-rotating frame is given by (Frank et al. 2002):

$$\Phi_{\mathrm{R}}(\mathbf{r}) = -\frac{GM_1}{|\mathbf{r}-\mathbf{r}_1|} - \frac{GM_2}{|\mathbf{r}-\mathbf{r}_2|} - \frac{1}{2}(\boldsymbol{\omega}\times\mathbf{r})^2, \tag{1.3}$$

where $\mathbf{r}_1$ and $\mathbf{r}_2$ are the position vectors of the two stars, $\mathbf{r}$ is the position of the test particle, and $\boldsymbol{\omega}$ is the angular velocity of the binary system. The first two terms represent the gravitational potentials of the stars, while the third term accounts for the centrifugal potential in the rotating frame.

The equipotential surfaces of this potential are shown in Figure-1.2. One particular surface (highlighted in dark black) intersects at a saddle point known as the inner Lagrangian point (L_1) point, where the gravitational pull of both stars is balanced. The lobes defined by this equipotential surface are called Roche lobes. If a star expands beyond its Roche lobe, matter can flow toward the other star through the L_1 point, a process known as Roche lobe overflow (RLOF). The maximum radius a star can have while remaining gravitationally bound within its lobe is referred to as the Roche lobe radius. For a compact

star of mass M_1 in a binary with companion mass M_2, the Roche lobe radius can be approximated using Eggleton's formula (Eggleton 1983):

$$f(q) = \frac{R_{\mathrm{L},2}}{a} \simeq \frac{0.49q^{2/3}}{0.6q^{2/3} + \ln\left(1 + q^{1/3}\right)}, \tag{1.4}$$

where a is the separation between the stars and $q = M_2/M_1$ is the mass ratio of the companion star to the compact object. This radius provides an estimate of the critical size at which a star begins transferring mass via Roche lobe overflow.

In X-ray binaries, when a companion star fills or overflows its Roche lobe, the overflowing material can be captured by the compact object, forming an accretion flow. This process is one of the primary mechanisms powering the X-ray emission observed from these systems and is the dominant mass transfer mechanism in low-mass X-ray binaries (LMXBs).

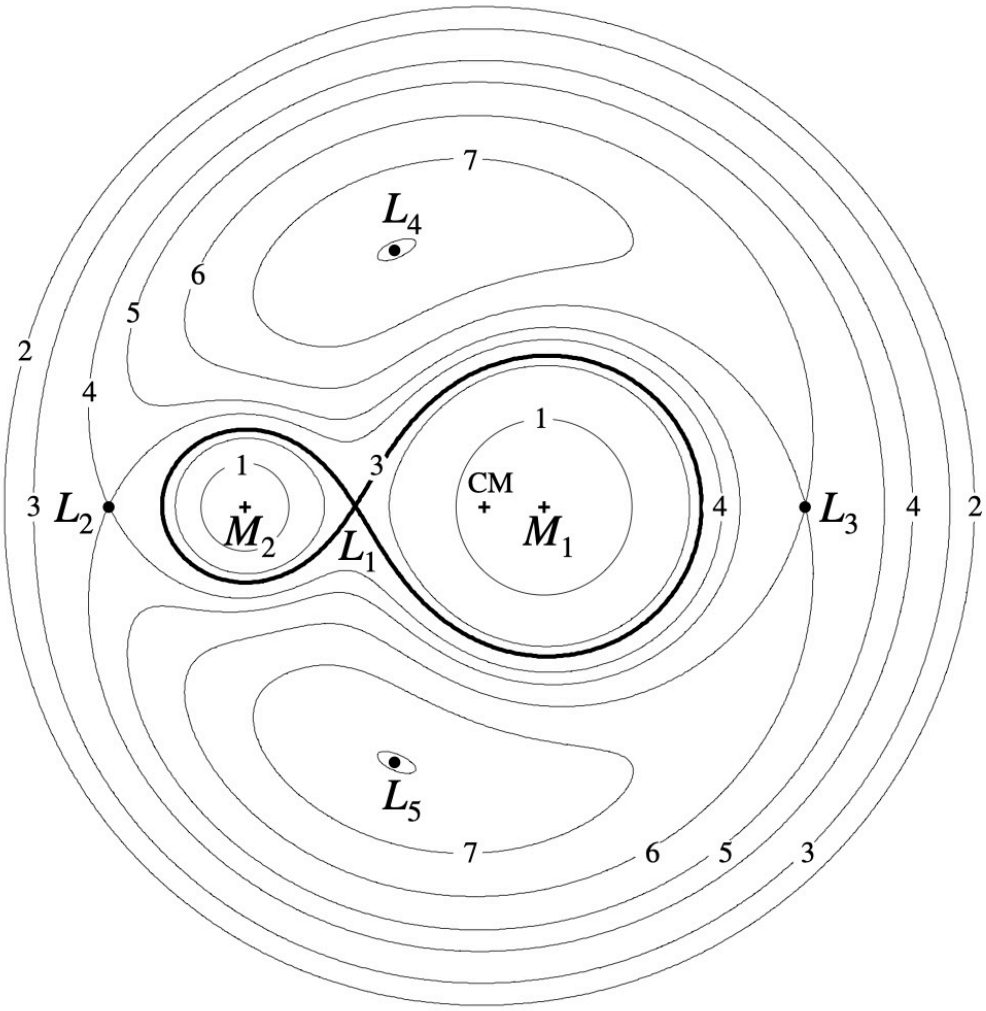


Figure 1.2: Roche equipotential contours in the orbital plane of a binary with mass ratio $q = M_2/M_1 = 0.25$. The centre of mass (CM) and Lagrangian points L_1–L_5 are marked. The saddle point L_1 connects the two Roche lobes, shown by the figure-of-eight equipotential. L_4 and L_5 are local maxima of Φ_{R}, where Coriolis forces stabilize synchronous orbits of test particles. (Fig. credit: Frank et al. (2002))

Stellar Wind Accretion

In HMXBs, unlike in low-mass systems, the donor star typically does not fill its Roche lobe, since the Roche lobe radius is relatively large compared to the stellar radius. As a result, Roche-lobe overflow is inefficient, and mass transfer instead occurs primarily through the powerful stellar wind continuously emitted by the massive companion. This hot, radiatively driven wind can be partially captured by the compact object, where the gravitational potential energy of the accreted matter is released in the form of X-rays. This process is known as stellar wind accretion (Frank et al. 2002).

These winds are accelerated outward from the companion's surface and asymptotically approach a terminal velocity v_∞. At a distance r from the star, the instantaneous velocity profile is well described by the β-law (Friend & Abbott 1986, Castor et al. 1975):

$$v_\omega(r) = v_\infty \left(1 - \frac{R_c}{r}\right)^\beta, \tag{1.5}$$

where R_c is the stellar radius and $\beta \sim 0.8$–1.2. For OB supergiants, these winds reach velocities up to a few thousand $\mathrm{km\,s^{-1}}$, much higher than the orbital velocity of the neutron star.

In this regime, accretion can be approximated by the Bondi-Hoyle-Littleton (BHL) model, in which the compact object gravitationally focuses the stellar wind flowing past it (Hoyle & Lyttleton 1939, Bondi 1952). The corresponding mass accretion rate is

$$\dot{M} = \frac{4\pi (G M_{\mathrm{NS}})^2 \, \rho_\omega(r)}{v_{\mathrm{rel}}^3}, \tag{1.6}$$

where M_{NS} is the neutron star mass, $\rho_\omega(r)$ is the local wind density, and v_{rel} is the relative velocity between the neutron star and the wind. The capture scale is set by the Bondi radius,

$$R_B = \frac{G M_{\mathrm{NS}}}{v_{\mathrm{rel}}^2}. \tag{1.7}$$

Since $v_{\mathrm{orb}} \ll v_\omega$ in most systems, one typically has $v_{\mathrm{rel}} \approx v_\omega$, giving

$$\dot{M} \propto \rho_\omega(r)\, v_\omega^{-3}. \tag{1.8}$$

This scaling shows that the accretion rate is extremely sensitive to the wind velocity. The resulting X-ray luminosities of wind-fed systems typically fall in the range $L_X \sim 10^{35}$–$10^{37}\,\mathrm{erg\,s^{-1}}$ (Frank et al. 2002).

Disc-Fed Accretion

Be X-ray binaries (Be XRBs) form a distinct subclass of HMXBs, where the companion is a rapidly rotating B-type star surrounded by a dense decretion disc in its equatorial plane. When the compact object, typically a neutron star, passes through this disc, episodic accretion occurs, producing bright outbursts (Type I and Type II) with X-ray luminosities reaching up to 10^{37} erg s^{-1} (Reig 2011).

1.3 Accretion Disc

While accreting matter from the companion star, the inflow does not follow a straight path, as it carries angular momentum. To conserve this angular momentum, the material settles into circular orbits around

the compact object, leading to the formation of an accretion disc. The characteristic radius where the incoming matter orbits with constant specific angular momentum is known as the circularization radius, defined as $R_{\rm circ} = \frac{GM}{J^2}$, where G is the gravitational constant, M is the mass of the compact object, and J is the specific angular momentum (Frank et al. 2002). A disc can only form when $R_{\rm circ}$ exceeds the effective size ($R_{\rm eff}$) of the accretor (Frank et al. 2002). For a magnetized neutron star, $R_{\rm eff}$ corresponds to the magnetospheric radius; for a non magnetized neutron star, it is the stellar radius itself; and in the case of a black hole, it is the radius of the innermost stable circular orbit (ISCO). Within the disc, viscosity arising from turbulence or magnetohydrodynamic (MHD) processes acts to redistribute angular momentum and dissipate energy (Shakura & Sunyaev 1973). Over sufficiently long timescales, this redistribution allows most of the material to spiral inward and accrete onto the central compact object, while only a small fraction is transported outward. The accretion disc also plays a crucial role in reprocessing the radiation emitted by the central source.

1.4 X-ray Pulsars: Accretion Powered Pulsars

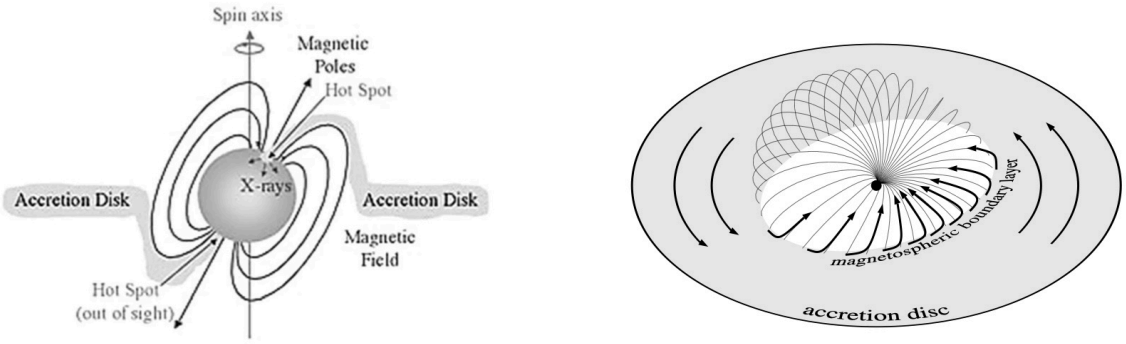


Figure 1.3: Left: Misalignment of the spin and magnetic axis of a neutron star produces X-ray pulsations. Right: Accretion disk around a magnetized neutron star, truncated at the magnetospheric radius, where matter follows magnetic field lines onto the magnetic poles. (Fig. credit: Frank et al. (2002), Srinivasan (2024))

In neutron star XRBs with strong magnetic fields ($B \sim 10^{12}$ G), the accreting plasma cannot flow directly onto the stellar surface. Instead, the magnetic pressure dominates the accretion flow at large radii and forces matter to couple to the field lines. The inflowing material is funneled toward the magnetic poles, forming narrow accretion columns. X-rays are then emitted from localized hot spots at the polar caps, where the kinetic and gravitational energy of the accreting plasma is released. If the magnetic axis of the neutron star is misaligned with its spin axis, these emission regions sweep across the observer's line of sight, producing periodic X-ray pulsations. Such systems are known as X-ray pulsars (XRPs) (Nagase 1989). The inner edge of the accretion disk around a magnetized neutron star is truncated at the Alfvén radius, where the ram pressure of the infalling gas balances the magnetic pressure. This radius can be approximated as (Frank et al. 2002):

$$r_{\rm A} \approx 5.1 \times 10^8 \, \dot{M}_{16}^{-2/7} \, M_1^{-1/7} \, \mu_{30}^{4/7} \text{ cm}, \tag{1.9}$$

where $\dot{M}_{16}$ is the mass accretion rate in units of 10^{16} g s^{-1}, M_1 is the neutron star mass in solar masses, and μ_{30} is the magnetic dipole moment in units of 10^{30} G cm^3.

Once inside r_A, the accretion disk cannot maintain Keplerian motion and the plasma is forced into corotation with the neutron star's magnetic field. If the neutron star's spin frequency exceeds the Keplerian frequency at the Alfvén radius (r_A), centrifugal forces inhibit accretion and expel the inflowing matter, leading to a state known as the *propeller regime* (Illarionov & Sunyaev 1975, Tsygankov et al. 2016). Conversely, if the neutron star rotates slower than the local Keplerian frequency, the matter is able to couple to the field lines and is funneled toward the magnetic poles, forming accretion columns. The resulting flow geometry produces anisotropic X-ray emission from the polar regions. When this beamed emission is combined with the misalignment between the neutron star's magnetic and rotational axes, it sweeps across the observer's line of sight, generating the coherent periodic modulation characteristic of X-ray pulsars. (see Fig. - 1.3)

1.5 Eddington Limit

However, mass accretion cannot produce an unlimited amount of energy, as the emitted radiation exerts a pressure that counteracts gravity. This balance imposes a fundamental limit on the luminosity of an accreting source, known as the *Eddington limit/Eddington luminosity*, which is set by the equilibrium between outward radiation pressure and inward gravitational attraction (Eddington 1920, Kolb 2010).

Assuming fully ionized hydrogen accreting spherically and isotropically onto the compact object, the Eddington luminosity is given by

$$L_{\rm Edd} = \frac{4\pi G M m_p c}{\sigma_{\rm T}}, \tag{1.10}$$

which can be expressed numerically as

$$L_{\rm Edd} \approx 1.3 \times 10^{38} \left(\frac{M}{M_\odot}\right), {\rm erg, s^{-1}}, \tag{1.11}$$

where M is the mass of the accretor. For a canonical neutron star of mass $1.4, M_\odot$, this corresponds to $\sim 2 \times 10^{38}, {\rm erg, s^{-1}}$.

The accretion luminosity is related to the mass accretion rate through $L = \eta \dot{M} c^2$, where η is the radiative efficiency. Equating this to the Eddington luminosity, we obtain the Eddington accretion rate,

$$\dot{M}_{\rm Edd} = \frac{L_{\rm Edd}}{\eta c^2}, \tag{1.12}$$

which corresponds numerically to

$$\dot{M}_{\rm Edd} \simeq 2.2 \times 10^{-8} \left(\frac{M}{M_\odot}\right) \left(\frac{0.1}{\eta}\right) M_\odot \ {\rm yr^{-1}}. \tag{1.13}$$

Accretion flows with $\dot{M} < \dot{M}_{\rm Edd}$ are commonly referred to as **sub-Eddington**, while those with $\dot{M} > \dot{M}_{\rm Edd}$ are described as **super-Eddington**. Most Galactic X-ray binaries are consistent with this limit, as their observed luminosities rarely exceed the Eddington value. Later on, however, observations of certain extragalactic X-ray sources revealed objects whose luminosities can surpass this limit, known as ultra-luminous X-ray sources (ULXs).

1.6 Ultra-Luminous X-ray Sources (ULXs)

In 1989, the Einstein Observatory detected highly luminous X-ray sources, located off-center in nearby galaxies and exceeding the Eddington luminosity for stellar-mass compact objects (Fabbiano 1989). Subsequent observations with *ROSAT*, *XMM-Newton*, and *Chandra* confirmed that these sources are distinct from the active galactic nuclei (AGN) typically associated with the supermassive black holes present at the centre of most galaxies. This discovery established a new class of X-ray sources, now known as Ultra-Luminous X-ray sources (ULXs) (Makishima et al. 2000, Fabrika et al. 2021, King et al. 2023). To date, approximately 1800 ULXs have been identified (Walton et al. 2021).

Persistent ULX sources, as well as transient ULXs during their bright states, exhibit apparent X-ray luminosities, estimated under the assumption of isotropic emission, in the range 10^{39}–10^{41} erg s^{-1} *, far exceeding the Eddington limit for typical stellar-mass compact objects. Such extreme luminosities can be explained either by intermediate-mass black holes (IMBHs) with masses of 10^3–$10^5 M_\odot$ accreting at sub-Eddington rates, or by stellar-mass black holes (5–80 $M_\odot$) accreting at super-Eddington rates (Fabrika et al. 2021, Pintore et al. 2017). In some ULXs, coherent X-ray pulsations have been detected, revealing neutron stars ($\sim 1.4 M_\odot$) as the compact objects. These sources are classified as Ultra-Luminous X-ray Pulsars (ULXPs), with the first detection in M82 X2 (Bachetti et al. 2014), and subsequent discoveries in NGC 7793 P13 (Israel et al. 2017a), NGC 5907 ULX1 (Israel et al. 2017b), M51 ULX7 (Castillo et al. 2020), NGC 300 ULX1 (Carpano et al. 2018), and NGC 1313 X2 (Sathyaprakash et al. 2019). In extreme cases where luminosities exceed 10^{41} erg s^{-1}, the sources are classified as Hyper-Luminous X-ray Sources (HLXs), thought to host IMBHs accreting at sub-Eddington rates (Kaaret et al. 2017). ULXs differ significantly from typical Galactic X-ray binaries due to their extreme luminosities, far exceeding the Eddington limit for stellar-mass compact objects. Studying these sources provides insight into how such high luminosities are generated and motivates detailed investigations of their spectral and timing properties.

1.7 Understanding X-ray Emission from Compact Objects

Accreting compact objects emit copious X-rays as material from the companion star falls into their deep gravitational potential well. The infalling matter is heated to high temperatures and interacts with the surrounding magnetic and plasma environment, giving rise to a rich variety of X-ray emission processes. Studying these emissions provides key diagnostics of accretion physics, the geometry of the system, and the properties of the compact object itself. Broadly, X-ray emission can be investigated through two complementary approaches:

- **Spectral analysis**
  The X-ray spectrum of such sources often contains several components originating from different regions of the accretion flow. Continuous emission, such as thermal blackbody radiation, multi-temperature disk emission, or power-law continua, typically arises from hot plasma, the inner disk, boundary layers, or a Comptonizing corona. In addition to the continuum, discrete atomic features, most notably emission and absorption lines, carry information about the chemical composition, ionization state, velocity distribution, and geometry of the emitting or absorbing material. The presence or strength of these spectral components therefore provides essential constraints on the physical conditions of the accretion environment and the radiation processes operating in X-ray binaries.

*All quoted and derived luminosities in this thesis assume isotropic emission from the source.

- **Timing analysis**
  Similarly, timing signatures carry complementary information about the dynamics of accretion. X-ray light curves may exhibit strictly periodic signals (e.g., pulsations from rotating neutron stars), quasi-periodic oscillations (QPOs) arising from disk instabilities or relativistic motion near the compact object, or aperiodic variability associated with turbulent mass transfer and stochastic accretion processes. In the Fourier domain, these behaviors manifest as narrow peaks, broad Lorentzian components, or red-noise–dominated continua in the power density spectrum (PDS). The timing properties therefore provide valuable insight into physical timescales, orbital and spin motions, and the structure of the accretion disk or magnetosphere, complementing the information obtained through spectral modeling.

1.7.1 Spectral Properties of X-ray Emission

The X-ray spectrum of an accreting compact object describes how the observed radiation is distributed as a function of photon energy. This emission is quantified through the spectral flux density, $S(E)$, which gives the energy received per unit area, per unit time, and per unit energy interval. In practice, X-ray spectra are often expressed in terms of the photon flux density, $N(E)$, defined as the number of photons detected per unit area, time, and energy. Since each photon carries energy E, the two quantities are related through $S(E) = E\,N(E)$. Integrating $S(E)$ over an energy range $[E_1, E_2]$ yields the total observed flux,

$$F = \int_{E_1}^{E_2} S(E)\, dE, \tag{1.14}$$

while the intrinsic luminosity of a source at distance D, assuming isotropic emission, is

$$L = 4\pi D^2 F. \tag{1.15}$$

While flux quantifies the brightness as measured by the observer, luminosity represents the intrinsic radiative power of the source. The shape of the spectrum encodes important information about the physical conditions of the emitting plasma. In X-ray binaries, the emission typically consists of both thermal and non-thermal components. Thermal processes include blackbody radiation from optically thick regions and thermal bremsstrahlung from hot, optically thin plasmas, while non-thermal mechanisms such as Comptonization and synchrotron radiation contribute to the higher-energy continuum. Disentangling these contributions is essential for understanding the geometry and dynamics of accretion flows.

Thermal Emission

Thermal radiation arises from the random motion of particles in the accretion flow and is directly linked to the system's temperature. The resulting emission depends on whether the plasma is optically thick or thin.

Blackbody radiation. Optically thick regions in or near the compact object (e.g., the neutron star surface, boundary layer, or the inner accretion disk) emit radiation that closely resembles a blackbody. The specific intensity is described by the Planck function:

$$I_\nu(T) = \frac{2h\nu^3}{c^2}\left[\frac{1}{e^{h\nu/k_B T} - 1}\right] \tag{1.16}$$

where T is the temperature, ν is the frequency, h is Planck's constant, k_B is the Boltzmann constant, and c is the speed of light. The spectrum peaks at a wavelength given by Wien's displacement law:

$$\lambda_{\max} T \simeq 2.9 \times 10^{-3}\,\mathrm{m\,K}. \tag{1.17}$$

The mean photon energy is $\langle E \rangle \simeq 2.7 k_B T$. The spectral shape follows the characteristic E^3 rise at low energies and exponential cutoff beyond $\sim k_B T$ for a single temperature. In accretion disks around compact objects, the temperature is not uniform but decreases with radius approximately as $T(r) \propto r^{-3/4}$. As a result, the disk radiates as a superposition of blackbody spectra with different temperatures. This produces a *multi-color blackbody spectrum*, which is broader than a single blackbody and peaks at higher energies, reflecting the hotter inner disk regions.

Thermal bremsstrahlung. In optically thin, hot plasmas, such as accretion columns in magnetized neutron stars, electrons are deflected by the Coulomb fields of ions and emit radiation in the process. This free–free emission, or thermal bremsstrahlung, produces a continuous spectrum. The emissivity per unit volume is given by:

$$j(E;\, T) = C\, g(E;\, T;\, Z)\, Z^2 n_e n_i T^{-1/2} e^{-E/k_B T}\,, \tag{1.18}$$

where n_e and n_i are the electron and ion number densities, Z is the ion charge, $g(E;\, T;\, Z)$ is the Gaunt factor, and C is a constant. The spectral shape is characterized by a flat distribution at low energies and an exponential decline above $\sim k_B T$, with the turnover energy providing a direct diagnostic of the plasma temperature. Bremsstrahlung dominates in low-density, hot environments and is particularly relevant for describing emission from shocked gas or accretion columns.

Non-Thermal Emission

Non-thermal processes, in which particle distributions deviate from Maxwellian equilibrium, are essential in explaining the high-energy tails of XRB and ULX spectra. These processes often yield power-law spectra that extend to hundreds of keV.

Synchrotron radiation. Relativistic electrons spiraling in magnetic fields radiate via synchrotron emission. For a single electron, the spectrum peaks at the critical frequency $\nu_c \propto \gamma^2 B$, where γ is the Lorentz factor and B the magnetic field. If the electron population follows a power-law distribution $N(E) \propto E^{-p}$, the resulting synchrotron spectrum also follows a power law:

$$I_\nu \propto \nu^{-\alpha}\,, \quad \alpha = \frac{p-1}{2}. \tag{1.19}$$

Synchrotron emission is often associated with collimated outflows or jets in black hole binaries, and with pulsar wind nebulae around neutron stars. Its broad-band, non-thermal character makes it distinguishable from thermal processes.

Comptonization. Inverse Compton scattering, where photons gain energy by scattering off energetic electrons, plays a central role in shaping the spectra of accreting compact objects. Soft seed photons from the disk (with energies $E_{\mathrm{seed}} \sim 0.1$–2 keV) can be up-scattered by hot electrons in a corona of temperature $kT_e \sim 10$–100 keV. The efficiency of this process is characterized by the Compton y-parameter:

$$y = \frac{4kT_e}{m_e c^2}\, \max(\tau, \tau^2)\,, \tag{1.20}$$

where τ is the Thomson optical depth. Repeated scatterings generate a power-law spectrum of the form

$$I(E) \propto E^{-\Gamma} \exp\left(-\frac{E}{E_c}\right) , \tag{1.21}$$

with photon index Γ depending on y, and cutoff energy $E_c \sim 2$–$3\ kT_e$. In XRBs and ULXs, this non-thermal component is a defining feature, tracing the presence of hot coronae and providing constraints on electron temperature and geometry.

Line Emission

In addition to the continuum, atomic transitions in the surrounding material imprint discrete features on the X-ray spectrum. These line emissions arise from fluorescence, produced when atoms re-emit photons after being excited or ionized by high-energy radiation. The centroid energy of the lines provides information about the ionization state of the plasma, while the line width reflects Doppler broadening due to thermal motion, orbital velocities, or turbulence. In regions close to the compact object, relativistic effects can further broaden and skew the line profiles. Modelling these spectral lines allows constraints on the physical conditions, composition, and dynamics of the emitting medium, and is an essential tool for understanding the environment around X-ray binaries.

X-ray Absorption

As X-ray photons travel towards the observer, they are attenuated by material along the line of sight, including the interstellar medium in our Galaxy, the host galaxy, intrinsic absorption near the source, and any circumsource matter. In the 0.1–10 keV range, photoelectric absorption dominates, where atoms absorb photons and eject electrons, reducing the observed intensity at low energies. The observed spectrum is related to the intrinsic source spectrum as:

$$I_{\text{obs}}(E) = I_{\text{source}}(E)\, e^{-\sigma(E) N_H} , \tag{1.22}$$

where $\sigma(E)$ is the energy-dependent photoelectric cross-section and N_H is the equivalent hydrogen column density along the line of sight. Accurately accounting for absorption is crucial for deriving the intrinsic spectral shape, determining plasma temperatures, photon indices, and fluxes, and for understanding the properties of the material surrounding the compact object.

In addition to continuum attenuation, absorbing material may imprint discrete spectral features. Atomic absorption lines arise when photons excite bound electrons in partially ionized gas; these transitions occur at characteristic energies and trace the composition, velocity field, and ionization state of the absorber. In X-ray binaries, highly ionized species such as OVII, OVIII, NeIX, and FeXXV/FeXXVI often produce narrow absorption lines or edges, which can originate from disk winds, outflows, or the accretion disk atmosphere.

A second important class of absorption features is produced in strongly magnetized neutron stars. In fields of order $B \sim 10^{12}$–10^{13} G, electrons occupy quantized Landau levels, and resonant scattering of photons between these levels produces Cyclotron Resonant Scattering Features (CRSFs). These appear as broad absorption lines with a centroid energy

$$E_{\text{cyc}} \simeq 11.6\, B_{12}\, (1+z)^{-1}\ \text{keV}, \tag{1.23}$$

where B_{12} is the magnetic field strength in units of 10^{12}G and z is the gravitational redshift near the neutron star surface. CRSFs provide a direct measurement of the magnetic field strength and are powerful

diagnostics of the accretion geometry and plasma conditions in X-ray pulsars.

1.7.2 Timing Properties

The timing properties of X-ray sources are obtained from the analysis of photon arrival times recorded by the instrument. This information encodes the spin frequency of the compact object (mainly, NS), often revealed by detecting coherent pulsations in the light curve. In binary systems, the orbital period can be measured from doppler shifts of the pulsed signal, or from the periodic eclipses, and it is closely related to the dynamics of the companion star (Charles & Coe 2006). A key diagnostic is the mass function, defined as

$$f(M) = \frac{(M_{\rm c} \sin i)^3}{(M_{\rm x} + M_{\rm c})^2} = \frac{P_{\rm orb} K^3}{2\pi G}, \tag{1.24}$$

where $M_{\rm x}$ is the compact object mass, $M_{\rm c}$ the companion mass, i the inclination, $P_{\rm orb}$ the orbital period, and K the semi-amplitude of the radial velocity curve (Rosswog & Bruggen 2003). Beyond the orbital timescale, superorbital periods are also observed in some X-ray binaries, typically attributed to the precession of a warped or tilted accretion disk (Ogilvie & Dubus 2001, Kotze & Charles 2012). On shorter timescales, quasi-periodic oscillations (QPOs) and aperiodic variability in the light curve trace different accretion regimes, such as instabilities in the disk, magnetospheric interactions, or relativistic effects close to the compact object (van der Klis 2006, Frank et al. 2002). Altogether, timing studies provide a powerful probe of binary dynamics, disk structure, and the coupling between accretion processes and compact object properties.

1.8 Current Understanding of ULXs

The discovery of ULXs fundamentally challenged the prevailing paradigm of accretion-powered X-ray binaries. Classical Galactic X-ray binaries, powered by accretion onto stellar-mass black holes or neutron stars, typically radiate below or around their respective Eddington luminosities. However, the apparent luminosities of ULXs often exceed the Eddington limit for a typical stellar-mass compact object by factors of a few up to nearly two orders of magnitude. Initially, these observations led to the interpretation that ULXs may host intermediate-mass black holes (IMBHs), with masses in the range of 10^2–$10^4\,M_\odot$ accreting at sub-Eddington rates (Colbert & Mushotzky 1999, King et al. 2023). However, sustaining such high accretion rates onto an IMBH would require the presence of a massive companion capable of transferring material at an exceptionally high rate for extended periods, which appears implausible in most observed ULX environments (King 2004). Moreover, population synthesis and spatial distribution studies indicate that ULXs are predominantly found in regions of active star formation, where high-mass X-ray binaries (HMXBs) containing stellar-mass compact objects are far more likely to form than IMBHs (King 2004). Theoretical studies also proposed that super-Eddington accretion onto stellar-mass compact objects could account for the extreme luminosities observed in ULXs (Begelman 2002, King 2004). A decisive breakthrough came with the discovery of coherent X-ray pulsations from M82 X-2 (Bachetti et al. 2014), unambiguously identifying the accretor as a neutron star. Subsequent detections of pulsations from NGC 7793 P13 (Israel et al. 2017a), NGC 5907 ULX1 (Israel et al. 2017b), NGC 300 ULX1 (Carpano et al. 2018), M51 ULX7 (Castillo et al. 2020), and NGC 1313 X-2 (Sathyaprakash et al. 2019) confirmed that at least a subset of ULXs are powered by accreting neutron stars, now classified as Ultra-Luminous X-ray Pulsars (ULXPs). In addition, the detection of a cyclotron resonance scattering feature (CRSF) in M51 ULX-8 (Brightman et al. 2018) provides independent, non-timing evidence for a neutron star accretor, further reinforcing the neutron-star–powered

ULX scenario. These discoveries demonstrated that super-Eddington accretion, aided by anisotropic emission (beaming) and magnetic channeling, can produce apparent luminosities exceeding the classical Eddington limit by factors of 10–100. However, a small number of sources exhibit luminosities reaching $\sim 10^{41}\,\mathrm{erg\,s^{-1}}$, placing them in the category of Hyper-Luminous X-ray Sources (HLXs). These systems, such as ESO 243-49 HLX-1 and M82 X-1, are believed to host IMBHs accreting at sub-Eddington rates (Kaaret et al. 2017).

1.8.1 Role of radiation pressure on the accretion flow in ULXs

Accretion flows around compact objects are commonly described by the standard thin-disc model of Shakura & Sunyaev (1973). In this framework, the disc is geometrically thin ($H/R \ll 1$), optically thick, and locally radiatively efficient. Energy released through viscous dissipation is immediately radiated away, so that the vertical energy balance is well approximated by $Q^+ \simeq Q^-$. Under these assumptions the disc cools efficiently, remains vertically stratified, and transports mass inward at a constant rate.

As the luminosity approaches the Eddington limit, radiation pressure becomes dynamically important and begins to inflate the disc. In vertical hydrostatic equilibrium the disc thickness increases approximately in proportion to the local luminosity (King et al. 2023),

$$\frac{H}{R} \propto \frac{L}{L_{\mathrm{Edd}}}, \tag{1.25}$$

When $L \gtrsim L_{\mathrm{Edd}}$, photon diffusion becomes inefficient, the vertical scale height grows to $H \sim R$, and the flow transitions from a thin, radiatively efficient configuration to a geometrically thick, quasi-spherical accretion structure.

At high mass accretion rates the disc structure naturally divides into regions governed by radiation pressure and photon trapping. The first important characteristic scale is the **spherization radius** R_{sph}, defined as the radius where the viscous energy flux produced in the disc equals the local Eddington flux. Outside R_{sph} the flow remains geometrically thin and follows the standard disc solution, while inside it radiation pressure inflates the disc vertically and the flow becomes geometrically thick. A commonly used approximation for this radius is

$$R_{\mathrm{sph}} \simeq 15\,\dot{m}\,R_{\mathrm{g}}, \tag{1.26}$$

where $R_{\mathrm{g}} = GM/c^2$ is the gravitational radius and $\dot{m} = \dot{M}/\dot{M}_{\mathrm{Edd}}$ is the mass inflow rate expressed in Eddington units (King et al. 2023). Thus the spherization radius marks the transition from a radiatively efficient, thin outer disc to an inner region that is dominated by radiation pressure and becomes geometrically thick.

A second important length scale in the supercritical regime is the **photon trapping radius** R_{trap}. At radii $R < R_{\mathrm{trap}}$ the radial inflow time becomes shorter than the photon diffusion time, so radiation is unable to escape vertically and is instead carried inward with the gas. In this region the local radiative balance changes from $Q^+ = Q^-$ to

$$Q^+ = Q^- + Q_{\mathrm{adv}}, \tag{1.27}$$

where Q_{adv} represents the advective transport of energy. A practical estimate for the trapping radius is (King et al. 2023)

$$R_{\mathrm{trap}} \simeq 20\left(\frac{H}{R}\right)\dot{m}\,R_{\mathrm{g}}. \tag{1.28}$$

Inside R_{trap} the disc becomes radiatively inefficient, most of the dissipated energy is advected inward rather than being radiated locally, and the accretion flow approaches a quasi-spherical configuration.

The standard thin-disc model assumes that all dissipated energy is radiated locally. Once the Eddington flux is reached this becomes unsustainable. Shakura & Sunyaev (1973) therefore proposed an alternative configuration, often called the "second" or "windy" solution. Inside $R_{\rm sph}$ the disc adjusts so that the emergent radiative flux remains close to the local Eddington value. To satisfy this condition the mass inflow rate must decrease with decreasing radius,

$$\dot{M}(R) \propto R, \tag{1.29}$$

so only a regulated fraction of the supplied material reaches small radii while the remainder is expelled as an outflow. Integrating over the thickened inner disc yields a luminosity that grows only logarithmically with $\dot{m}$,

$$L = L_{\rm thin} + L_{\rm thick} \simeq L_{\rm Edd}\,(1 + \ln \dot{m})\,. \tag{1.30}$$

Thus the inner accretion rate remains close to $\dot{M}_{\rm Edd}$ even when the external supply is strongly supercritical. In the Shakura & Sunyaev (1973) picture this is achieved by removing excess matter through a wind. However, for supercritical flows the spherization and trapping radii are comparable ($R_{\rm trap} \sim R_{\rm sph}$), so the excess energy can instead be retained by the flow and trapped in the inflowing gas rather than expelled. In this case the disc remains locally supercritical without launching a strong wind.

A different regime emerges from this behaviour: the **slim disc** model (Abramowicz et al. 1988, King et al. 2023). Here photon trapping dominates the energy transport, and the dissipated heat is advected inward instead of being radiated locally or carried away by an outflow. The local energy balance becomes $Q^+ = Q^- + Q_{\rm adv}$, and the surface density and radial velocity adjust such that the disc becomes geometrically thick with $H/R \sim 1$. The mass inflow rate remains approximately constant with radius. For black holes the advected energy is swallowed by the event horizon by increasing its mass, and advection acts as an additional cooling mechanism. For neutron stars the trapped energy must be radiated near the stellar surface, exceeding $L_{\rm Edd}$ and invalidating the steady solution. Slim discs reproduce the weak dependence of luminosity on inflow rate; the inner advective region yields

$$L_{\rm slim} \simeq L_{\rm Edd}\,\ln \dot{m}, \tag{1.31}$$

similar to the windy solution. However, slim discs do not create strong global outflows or low-density funnels, and their intrinsic luminosity remains close to $L_{\rm Edd}$. They therefore cannot explain the very high apparent luminosities of ULXs.

A another class of models are pressure-supported toroidal structures commonly termed **Polish doughnuts** (Kozlowski et al. 1978, Abramowicz et al. 1978, Paczyński & Wiita 1980, King et al. 2023). Here the disc thickness greatly exceeds the radius ($H/R \gg 1$), forming a thick torus with an evacuated polar funnel through which radiation escapes. Strong radial pressure gradients push the inner rim inward, even below the ISCO. Radiation from the photosphere is assumed to saturate at the local Eddington flux, and all structural properties follow from the prescribed angular momentum distribution. Although the geometry produces anisotropic emission, it does not lead to a large enhancement of the apparent luminosity. The radiative efficiency decreases as the inner edge approaches the innermost bound orbit, so the total luminosity remains comparable to the true accretion power. Polish doughnuts therefore provide a geometric configuration, not a physical accretion solution, and cannot account for ULX luminosities.

The limitations of both slim discs and Polish doughnuts point to the need for a mechanism that simultaneously regulates the inner inflow and collimates radiation. This is naturally achieved when

supercritical accretion drives an optically thick wind that leaves a pair of open funnels along the rotation axis. In the **SS73 windy solution** the inflated inner disc expels excess material into such a wind. Most photon escape paths through the disc body encounter high optical depth, whereas radiation traveling along the funnel is transmitted efficiently. The result is an anisotropic radiation field even if the intrinsic luminosity is only mildly super-Eddington.

This can be expressed using a beaming factor $0 < b < 1$, the fraction of solid angle into which radiation is emitted. If the intrinsic luminosity is L, the isotropic-equivalent luminosity inferred by an observer is

$$L_{\rm app} = \frac{L}{b}. \tag{1.32}$$

Numerical and analytic work suggests that the beaming strengthens with increasing mass supply. A widely used scaling is

$$b \propto \dot{m}^{-2}, \tag{1.33}$$

reflecting the narrowing of the funnel as the flow becomes more supercritical. Combining this with the intrinsic luminosity of a supercritical disc,

$$L \simeq L_{\rm Edd}(1 + \ln \dot{m}), \tag{1.34}$$

gives

$$L_{\rm app} \simeq \frac{L_{\rm Edd}(1 + \ln \dot{m})}{b}, \tag{1.35}$$

demonstrating that the observed luminosity can greatly exceed $L_{\rm Edd}$ even when the mass accreted near the compact object remains regulated at a modest level. In this picture, the extreme luminosities of ULXs arise naturally from geometric beaming by an optically thick disc wind, rather than from unusually massive compact objects or exotic accretion physics (King et al. 2023)

1.8.2 Artistic sketches of the accretion onto the ULX having BH and NS

In the super-Eddington regime, the accretion flow develops a stratified geometry consisting of a thin outer disk that transitions into a geometrically thick, radiation-pressure-dominated inner region inside the spherization radius (see Fig. 1.4). The inflated inner disk drives dense, radiatively accelerated winds that are optically thick to X-rays and surround the central emission region, placing the effective photosphere within the outflow itself. The density and optical depth of the wind are strongly angle-dependent, with the highest values near the disk plane and substantially lower values toward the rotation axis. As a result, photon escape is inhibited in equatorial directions but remains relatively unobstructed along the poles, naturally producing low-density polar funnels through which radiation preferentially escapes, resulting in geometrical collimation (beaming) of the emission. In neutron-star ULXs, this structure is further modified at the magnetospheric radius, where the thick disk is truncated and the accretion flow is redirected along magnetic field lines into accretion columns, while the surrounding optically thick envelope and wind continue to define the funnel geometry (see Fig. 1.5). This geometric configuration represents a widely used framework for interpreting super-Eddington accretion and successfully explains many observed properties of ULXs, although alternative models have also been proposed (King et al. 2023).

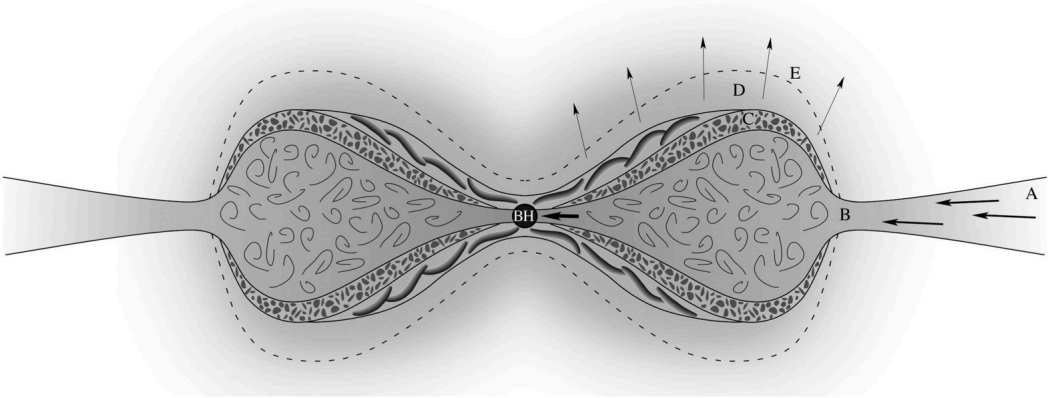


Figure 1.4: Schematic illustration of a super-Eddington slim accretion disk. The diagram shows the main structural regions of the accretion flow: (A) an outer sub-Eddington, geometrically thin disk; (B) an inner radiation-pressure-dominated region where the local energy release approaches the Eddington limit and the disk inflates vertically; (C) a porous, inhomogeneous layer forming above the convection zone; (D) a radiatively driven wind launched from regions where the porous structure becomes optically thin; and (E) the effective photosphere, which is located within the outflowing wind. (Fig. credit: Dotan & Shaviv (2011))

1.8.3 Observed spectral and timing properties

Spectroscopically, ULXs exhibit a distinctive two-component continuum: a soft excess ($kT \sim 0.1$–0.3 keV) and a curved high-energy component ($kT \sim 2$–5 keV). These are often interpreted as emission from an optically thick, geometrically inflated inner disk, and Comptonization in an overlying corona or wind. In addition to the continuum, several ULXs show a broad emission or absorption feature near ~ 1 keV, whose physical origin has been widely debated. Kosec et al. (2018) used deep *XMM-Newton* observations to detect blue-shifted absorption lines in several ULXs, consistent with winds launched at velocities up to $0.2c$. These winds are a natural outcome of super-Eddington accretion, driven by intense radiation pressure. Chakraborty et al. (2024) further demonstrated, using the spectral synthesis code `Cloudy`, that the $\sim$1 keV feature is not a single atomic transition but a blend of multiple emission and absorption lines arising from highly ionized plasma in the outflow. The observed strength and shape of this feature depend on the density, ionization parameter, and viewing angle, making it a valuable probe of the wind–disk geometry and physical conditions in the accretion environment.

Timing studies have been essential for understanding ULX accretion physics. The detection of coherent pulsations provided direct evidence of magnetically channeled accretion onto neutron stars. Beyond pulsations, power density spectra (PDS) of ULXs often exhibit broadband variability and quasi-periodic oscillations (QPOs). Atapin et al. (2019) identified flat-topped noise components and low-frequency QPOs ($\sim$20–200 mHz) in several ULXs, suggesting variability analogous to that observed in the high-accretion states of Galactic X-ray binaries. These QPOs are interpreted as signatures of oscillations in the inner accretion disk or transitions between different accretion regimes. In super-Eddington flows, the thickened inner disk and massive radiative winds may produce characteristic variability through instabilities in the inner funnel or precession of the disk structure (Middleton et al. 2015). The presence of such variability across multiple ULXs suggests that their inner accretion geometry is highly dynamic, with feedback between the inflow and outflow regions.

Longer-term modulations, including orbital and superorbital periods, have also been observed. Orbital periods provide constraints on the mass function and binary separation, while superorbital period-

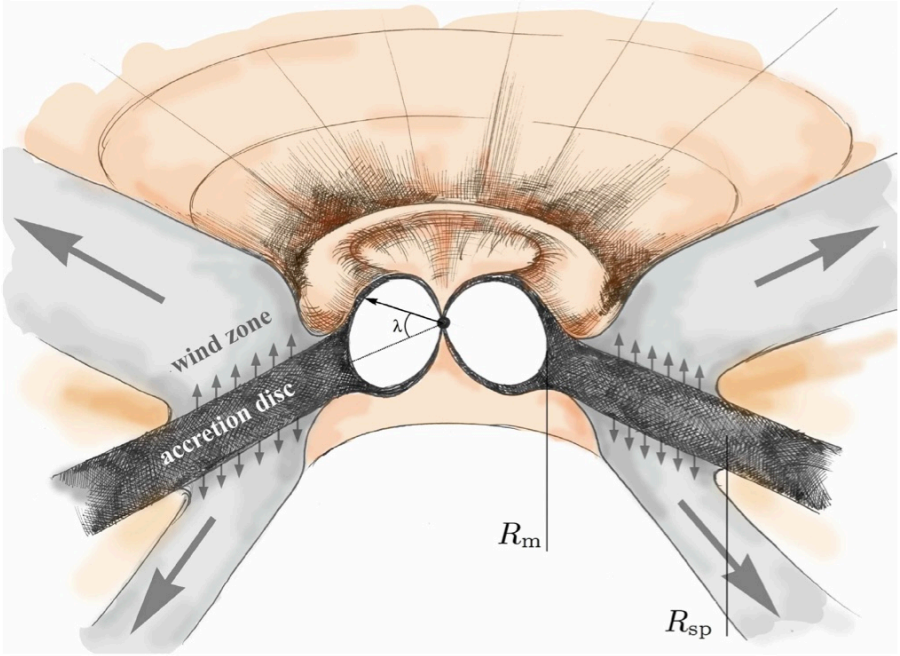


Figure 1.5: Schematic of a ULX powered by accretion onto a strongly magnetized neutron star. The accretion disk is truncated at the magnetospheric radius ($R_{\rm m}$). When the spherization radius ($R_{\rm sph}$) exceeds $R_{\rm m}$, radiatively driven winds are launched, while the remaining matter is funneled along magnetic field lines to form accretion columns and an optically thick envelope characteristic of ULX pulsars (Fig. credit: Mushtukov et al. (2019)).

icities are often linked to precession of the accretion disk or changes in the beaming angle (Walton et al. 2016, Wang et al. 2018, Qiu et al. 2019). These multi-timescale variations together reveal the complex interplay between magnetic fields, radiation pressure, and disk geometry in shaping the observed ULX behavior.

1.8.4 Motivation

Despite remarkable progress, several key questions remain unresolved about the ULXs. It is still unclear whether all ULXs can be explained by super-Eddington accretion onto stellar remnants, or whether a subset truly hosts IMBHs. The role of magnetic field strength in regulating mass accretion rates and radiative beaming remains an active area of research. Additionally, the coupling between the accretion disk, the wind, and the neutron star magnetosphere introduces a complex set of feedback mechanisms not yet fully captured in numerical simulations.

Over the past decade, the study of ULXs has significantly reshaped our understanding of accretion physics. Once considered strong IMBH candidates, ULXs are now recognized as exceptional laboratories for studying super-Eddington accretion onto stellar mass compact objects. Their rich spectral and timing phenomenology from broad-band variability and quasi-periodic oscillations to emission line diagnostics provides unique insights into the structure and dynamics of radiation dominated accretion flows. In this context, ULXs serve as crucial testbeds for exploring accretion, outflow, and radiative processes far beyond the regimes accessible in typical Galactic X-ray binaries. Motivated by these developments, we have undertaken detailed spectral and timing analyses of ULXs and compared their properties with those of Galactic systems to better understand their physical nature.

This thesis is broadly divided into two parts. The first part focuses on the study of the environment and physical properties of Ultra-luminous X-ray Sources (ULXs), while the second part highlights my learning experience and contributions towards the development of the **POLIX: Indian X-ray Polarimeter**. **Chapter 1** introduces the previous studies and the current understanding of X-ray binaries and ULXs, followed by **Chapter 2**, which outlines observational techniques, X-ray instrumentation, and data analysis methods for spectral and timing studies. **Chapter 3** discusses the spectral properties of ULX pulsars by applying models commonly used for local X-ray pulsars, while **Chapter 4** examines various aspects of X-ray reprocessing in ULXs. **Chapters 5 and 6** present study on the flaring behavior of ULXs and the evolution of pulse profiles of known ULXPs with time and intensity. **Chapter 7** describes my contributions to the development of POLIX, and finally, **Chapter 8** summarizes the results and outlines future research directions.

2

X-ray Astronomy and Techniques

2.1 Introduction to X-ray Observations and Observatories

Accreting compact objects such as neutron stars (NSs) and black holes (BHs) in X-ray binaries (XRBs) are among the most energetic stellar sources in the Universe. They emit radiation over a broad range of the electromagnetic (EM) spectrum, extending from radio to γ-rays. However, the emission processes occurring in the immediate vicinity of the compact object where matter is accreted under the influence of intense gravitational and magnetic fields are predominantly manifested in the X-ray band (see Fig. 2.1). This high-energy radiation arises from hot plasma in the accretion disk, the boundary layer, and the accretion column near the NS surface, as well as from inverse compton scattering in the corona. Consequently, X-ray observations provide direct probes of the physical conditions close to the compact object, such as temperature, density, and magnetic field strength. Despite their astrophysical importance, X-rays from cosmic sources cannot be observed from the ground, as the Earth's atmosphere is effectively opaque to photons above $\sim$10eV (or below 100nm) (see Fig. 2.2). Therefore, X-ray astronomy required the development of space borne or high altitude instruments capable of operating above the absorbing layers of the atmosphere.

The first detection of cosmic X-rays was achieved in 1962 using a rocket-borne Geiger counter experiment, which led to the discovery of the bright source Sco X-1 and marked the beginning of X-ray astronomy (Giacconi et al. 1962). Subsequently, balloon and sounding rocket experiments provided valuable insights into solar and cosmic X-ray emission during the 1960s. The launch of the first dedicated X-ray satellite, *Uhuru* (1970), represented a major milestone, as it performed the first all-sky survey and catalogued hundreds of sources including X-ray binaries, supernova remnants, and clusters of galaxies (Giacconi et al. 1972). Following *Uhuru*, several missions progressively advanced the field through improved detector sensitivity and spectral resolution. The *HEAO* series (1977–1979) carried proportional counters and imaging detectors, pioneering studies of diffuse X-ray backgrounds. The *Einstein Observatory* (HEAO-2; 1978–1981) introduced focusing X-ray optics for the first time (Giacconi et al. 1979), enabling arcminute-scale imaging and spectral analysis of extended sources. Later missions such as *EXOSAT* (1983–1986), *Ginga* (1987–1991), and *ROSAT* (1990–1999) further refined timing and spectral capabilities, laying the foundation for modern observatories.

The development of various detector technologies has been central to the evolution of X-ray astronomy. Early instruments used gas filled proportional counters, in which incident X-rays ionize gas atoms and produce electron avalanches proportional to the photon energy. These were later succeeded by solid state detectors such as silicon PIN diodes and CdZnTe (CZT) pixel detectors that convert X-ray photons directly into charge carriers, offering improved spectral resolution and timing accuracy. Charge Coupled Devices (CCDs), widely used in missions such as *XMM–Newton*, *Chandra*, and *Suzaku*, provide both moderate spectral resolution and two dimensional imaging capability by storing and transferring photo generated charge across an array of pixels. Each of these detector types offers distinct advan-

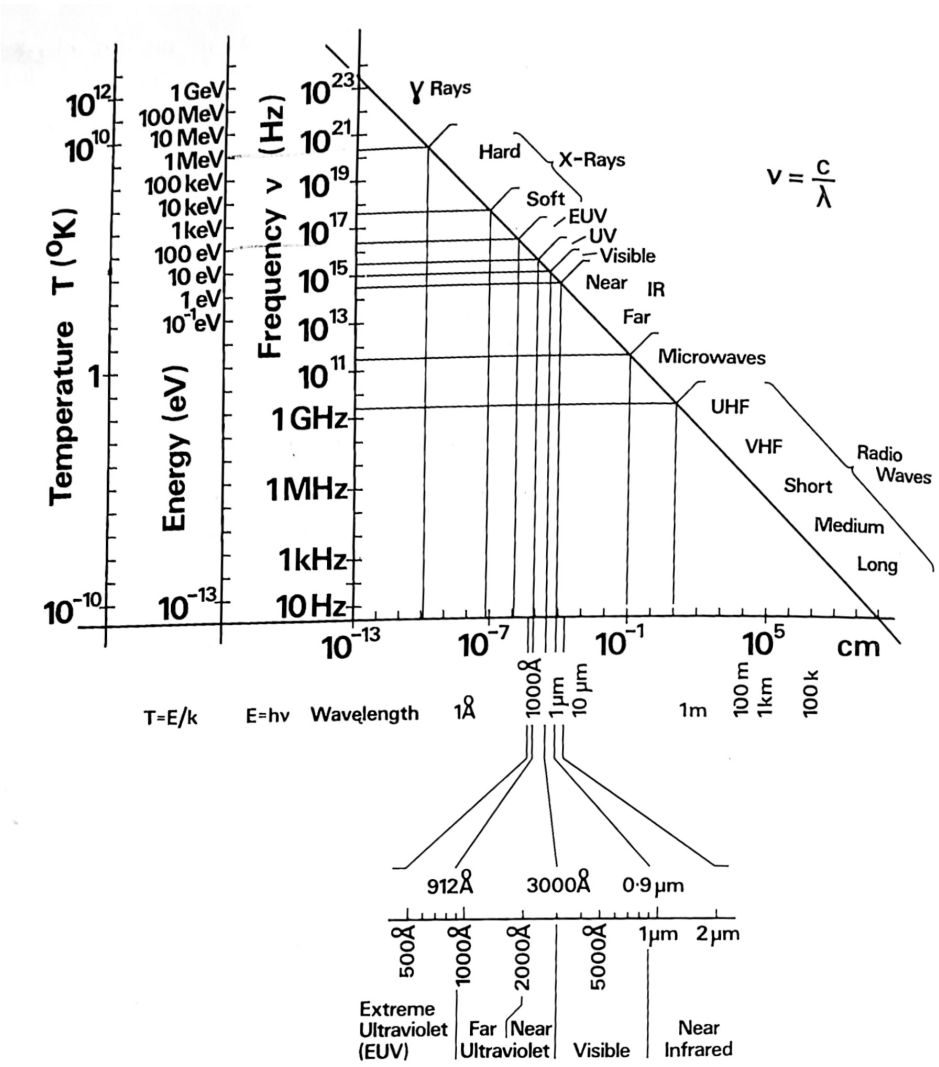


Figure 2.1: The electromagnetic spectrum. (Fig. Credits: (Culhane & Sanford 1981))

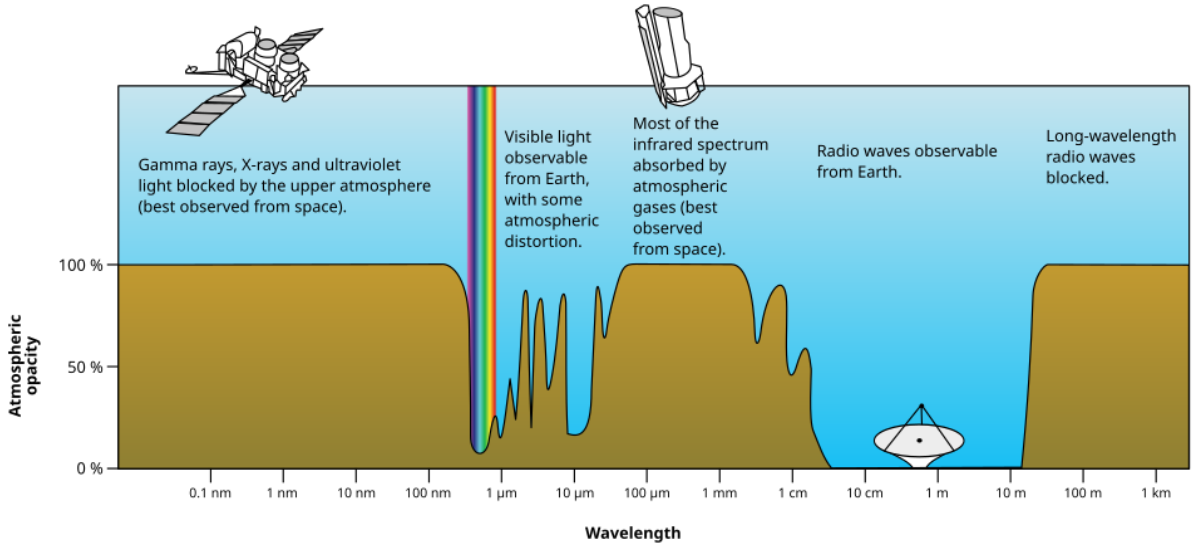


Figure 2.2: Atmospheric transmission as a function of wavelength. As shown, the Earth's atmosphere is nearly opaque below ∼100 nm, necessitating space-based X-ray observatories. (Fig. credit: NASA; SVG by Mysid)

tages in energy resolution, spatial resolution, and count rate capability, making the choice of detector closely tied to the scientific goals of a mission.

In parallel, the introduction of focusing optics based on grazing-incidence Wolter type-I mirror assemblies revolutionized X-ray astronomy by concentrating photons collected over a large mirror surface onto a compact detector region. This design reduces the effective detector area exposed to particle-induced and instrumental backgrounds, thereby increasing sensitivity. For point-like sources, the focused beam allows photons to be extracted from a restricted sky region, suppressing diffuse background and further enhancing the signal-to-noise ratio. High-precision imaging is additionally enabled by the narrow point-spread functions produced by grazing-incidence optics and the spatial sampling of modern pixelated detectors. Together, these advances allow accurate source localization, spatially resolved spectroscopy, and the detection of faint extended emission around compact objects. The first successful implementation of this approach on the *Einstein Observatory* (HEAO-2) established the foundation for all modern imaging X-ray telescopes.

Building upon these technological developments, a new generation of observatories emerged. Missions such as *ASCA* (1993–2000), *BeppoSAX* (1996–2002), and *ROSAT* (1990–1999) introduced improved detector technologies, broadened spectral coverage, and advanced calibration schemes, enabling detailed spectroscopy of both Galactic and extragalactic sources. In contrast, instruments such as *RXTE* (1995–2012) and *AstroSat*/LAXPC were designed primarily for fast timing studies. In these missions, sensitivity was achieved through large effective collecting areas rather than focusing optics, enabling precise measurements of rapid variability, coherent pulsations, and burst phenomena in accreting compact objects. Contemporary imaging observatories such as *Chandra* (1999–present), *XMM–Newton* (1999–present), and *NuSTAR* (2012–present) combine high collecting areas with fine spectral resolution and sub-arcsecond imaging, with *Chandra* still providing the best angular resolution achieved in X-ray astronomy. These missions are complemented by all-sky monitors such as *MAXI* and *Swift/BAT*, which provide long-term observational baselines and enable the discovery of transient and explosive events in the X-ray sky.

In this chapter, we briefly mention the observatories and instruments utilized in this thesis (Sec. 2.2), and the analysis techniques employed (Sec. 2.3), including the methodologies for timing (Sec. 2.3.1) and spectral (Sec. 2.3.2) studies.

2.2 X-ray Observatories

This section provides an overview of the major X-ray observatories used in this thesis, with emphasis on their instrumental design, observational capabilities, and scientific strengths. The three missions discussed here *Chandra*, *XMM-Newton*, and *NuSTAR* represent the current generation of space based X-ray telescopes. Their complementary energy coverage and effective areas (Fig. 2.6) make them idealiled imaging, timing, and spectroscopic studies of compact objects.

2.2.1 Chandra X-ray Observatory

The *Chandra* X-ray Observatory, launched in 1999 as part of NASA's flagship mission, remains the premier facility for high resolution X-ray imaging (Weisskopf et al. 2002, Garmire et al. 2003). It operates in a highly elliptical orbit (apogee $\sim$140,000 km, perigee $\sim$16,000 km), allowing uninterrupted observations of up to $\sim$55 hours. *Chandra*'s principal strength lies in its sub-arcsecond angular resolution, achieved through a high-precision Wolter type-I mirror assembly. The observatory hosts two primary focal-plane detectors and two sets of transmission gratings for high-resolution spectroscopy.

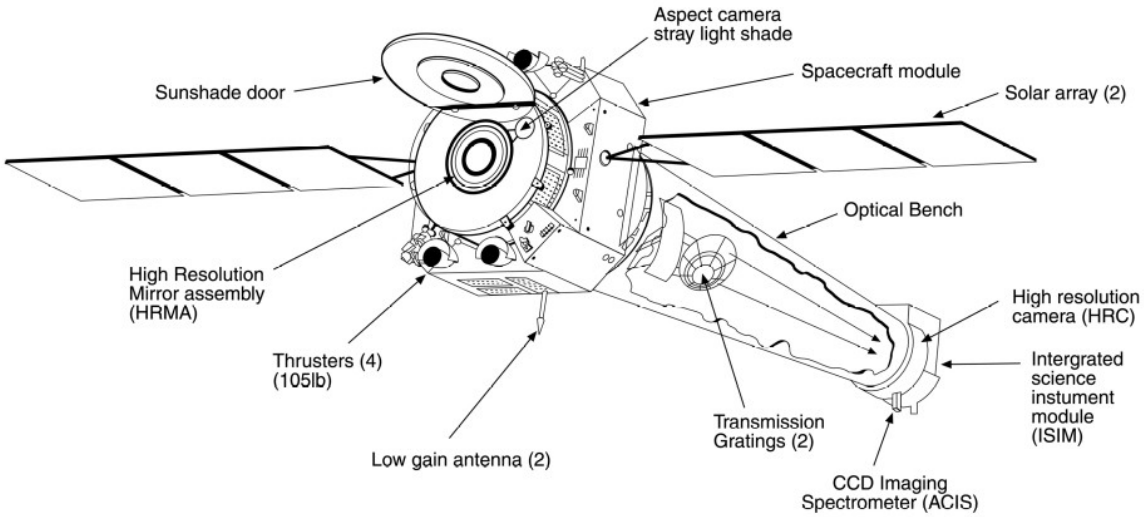


Figure 2.3: Schematic diagram of the *Chandra* X-ray Observatory. (Fig. credit: NASA/CXO)

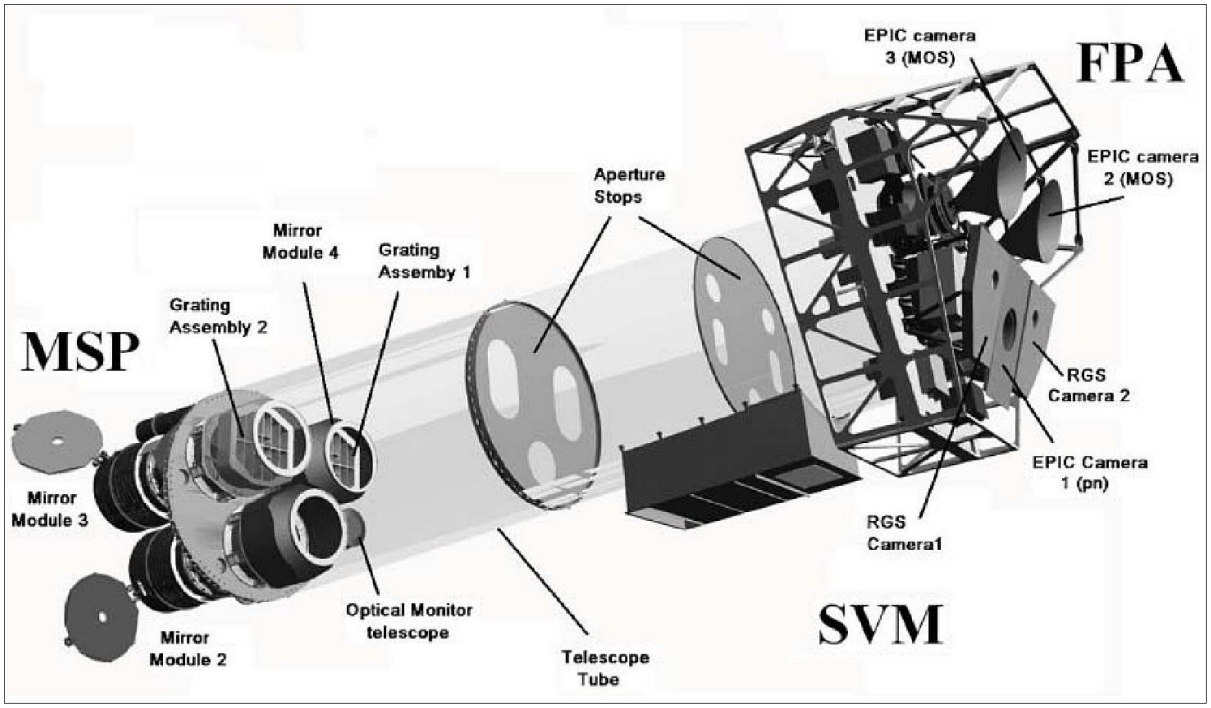


Figure 2.4: Schematic diagram of the *XMM-Newton* X-ray observatory. (Fig. credit: ESA/XMM–Newton)

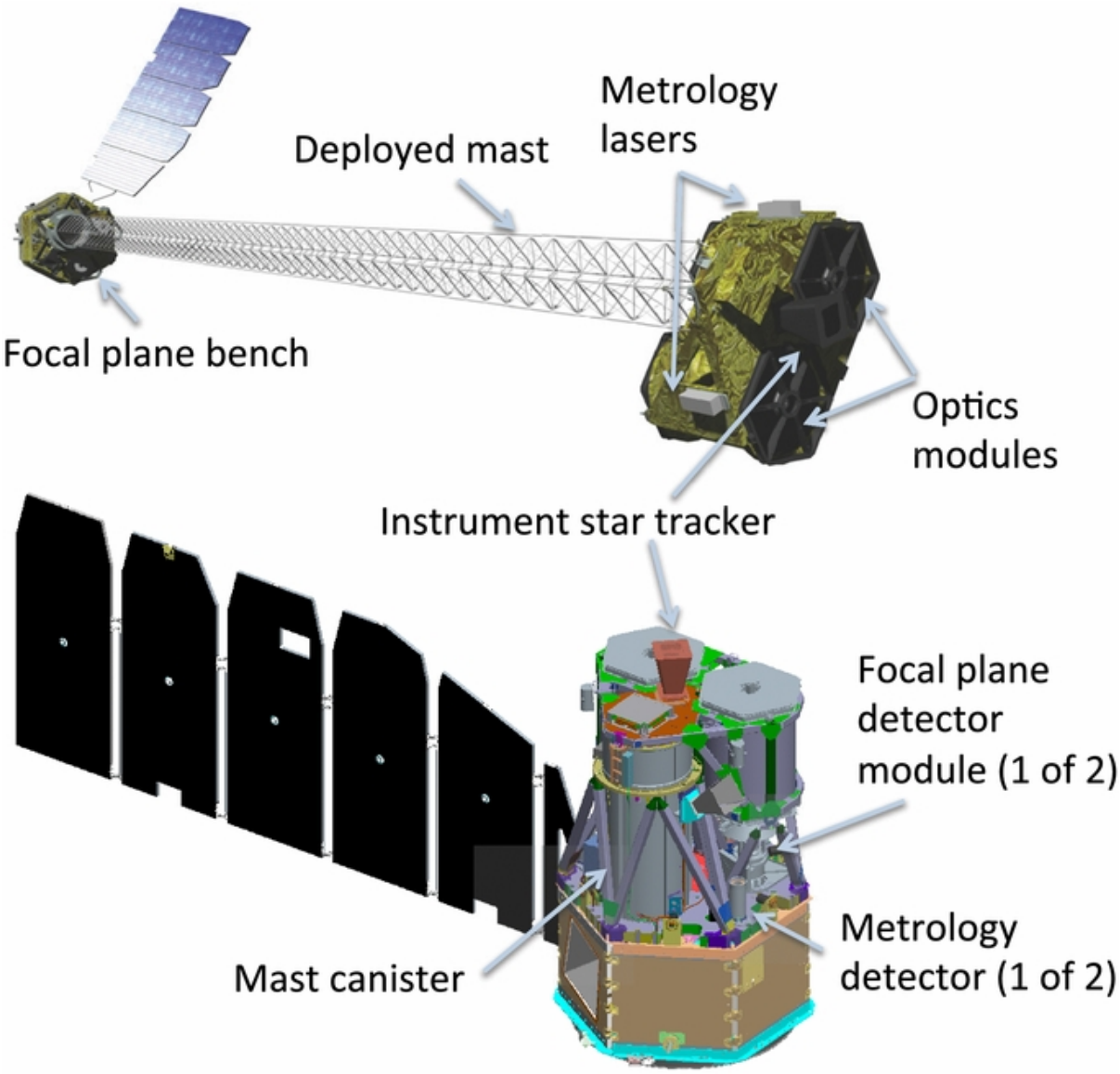


Figure 2.5: Schematic diagram of the *NuSTAR* observatory in its mast-stowed configuration (bottom) and mast-deployed configuration (top). (Fig. credit: NASA/NuSTAR; (Harrison et al. 2013))

- **Advanced CCD Imaging Spectrometer (ACIS):**
  ACIS consists of ten CCDs arranged into two arrays: ACIS-I for wide field imaging and ACIS-S optimized for spectroscopy. It provides imaging and moderate resolution spectroscopy in the 0.2–10 keV range, with an energy resolution of $\sim$100–150 eV at 1 keV. The timing resolution is 3.2s in full frame mode and 2.85ms in continuous clocking mode.

- **High Resolution Camera (HRC):**
  The HRC employs microchannel plate detectors, with HRC-I dedicated to imaging and HRC-S designed for use with the transmission gratings. It offers excellent time resolution of 16μs and a broad energy response from 0.08–10keV, though with limited intrinsic spectral resolution.

- **High Energy Transmission Grating (HETG):**
  Installed in front of ACIS-S, HETG disperses X-rays into high-resolution spectra, achieving a resolving power of $E/\Delta E \sim 1000$ at 1keV. It operates effectively across the 0.4–10keV band.

- **Low Energy Transmission Grating (LETG):**
  Used with HRC-S or ACIS-S, LETG enables high-resolution soft X-ray spectroscopy in the 0.08–2keV range and is particularly suited for studies of diffuse plasmas and stellar coronae.

2.2.2 X-ray Multi-Mirror Mission (*XMM-Newton*)

The *XMM-Newton* observatory, launched by ESA in 1999, is one of the most productive X-ray missions to date (Jansen et al. 2001). It features three co-aligned Wolter type-I telescopes, each comprising 58 nested mirror shells with a focal length of 7.5m. At the focal plane, *XMM-Newton* hosts the European Photon Imaging Camera (EPIC), the Reflection Grating Spectrometer (RGS), and the Optical Monitor (OM):

- **EPIC-MOS:**
  The two MOS cameras consist of front illuminated CCD arrays that provide imaging and moderate-resolution spectroscopy in the 0.3–10 keV energy range. Their energy resolution is $\sim$70 eV at 1 keV, and they support several windowed and timing readout modes.

- **EPIC-PN:**
  The PN camera comprises twelve large area back illuminated silicon CCDs arranged in two rows. It offers the largest effective area among the EPIC instruments and supports modes optimized for bright sources, including TIMING and BURST modes. The PN detector covers 0.3–10 keV with a timing resolution of 200 ms (Extended Full Frame) to 7 μs (BURST mode), and an energy resolution of $\sim$150 eV at 6 keV.

- **Reflection Grating Spectrometer (RGS):**
  The RGS provides high-resolution soft X-ray spectroscopy (0.35–2.5 keV), with resolving powers up to $E/\Delta E \sim 300$. It is optimized for studies of narrow emission and absorption features in extended or line rich sources.

- **Optical Monitor (OM):**
  The OM is a 30 cm optical/UV telescope operating simultaneously with the X-ray instruments, enabling multiwavelength monitoring in the 170–650 nm band.

XMM-Newton operates in a highly elliptical orbit (apogee $\sim$115,000 km, perigee $\sim$6,000 km), providing uninterrupted exposures of up to $\sim$48 hours.

2.2.3 Nuclear Spectroscopic Telescope Array (*NuSTAR*)

The *NuSTAR* mission (Harrison et al. 2013), launched in 2012 under NASA's SMEX program, is the first space telescope to focus hard X-rays (3–79 keV). It operates in a low-Earth orbit at an altitude of ∼600 km. *NuSTAR* employs depth graded multilayer coated Wolter type-I optics to achieve focusing at high energies. The telescope consists of two identical co-aligned optics modules (FPMA/FPMB), each paired with a focal-plane detector assembly. Each focal-plane assembly contains four CdZnTe (CZT) pixel detectors arranged in a 2×2 configuration. Each detector module is 20 mm $\times$ 20 mm $\times$ 2 mm, subdivided into 32×32 pixels with independent readout. The detectors provide ∼400 eV energy resolution below 50 keV and ∼2 μs timing resolution, while avoiding pile-up for count rates up to ∼400 cts s^{-1}. Each mirror assembly contains 133 nested shells with a focal length of ∼10 m, achieving an angular resolution of ∼18" (FWHM). The deployable mast connecting the optics and focal plane enables the long focal length required for hard X-ray focusing. By combining focusing optics with pixelated CZT detectors, *NuSTAR* achieves a significant improvement in sensitivity over previous hard X-ray missions, allowing detailed broadband spectroscopy of faint and bright sources.

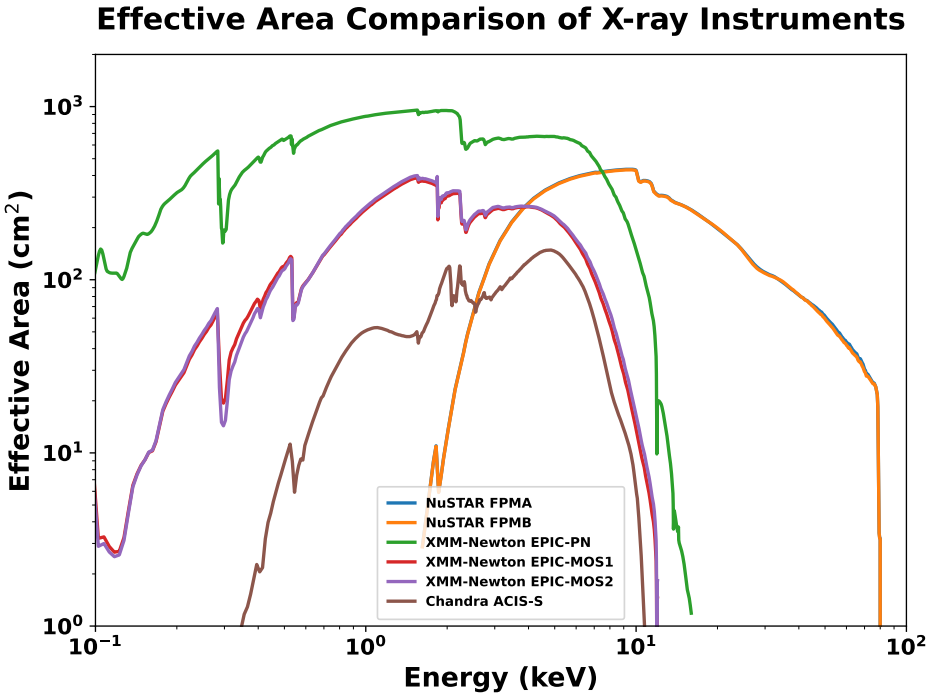


Figure 2.6: Comparison of the effective area of the X-ray instruments used in this thesis. (Fig. credit: NASA/ESA)

2.3 X-ray Data Analysis Techniques

Before analysing the timing and spectral properties of the ULXs, the raw observation files were first processed to obtain calibrated and cleaned event lists. The detailed data reduction procedures for each source and observatory are described in the corresponding analysis chapters of the thesis. Here, we outline the general techniques used for timing and spectral analysis. All scientific analysis was carried out using the HEASoft software package provided by NASA's HEASARC, together with mission specific tools where appropriate.

2.3.1 Timing Analysis

The photon arrival time series from an X-ray observation constitutes a light curve, denoted as $c(t_n)$, where $n \in [0, 1, 2, \ldots, N-1]$. Wherever necessary, arrival times were corrected to the solar system barycentre using the `barycorr`* tool. Light curves of XRPs typically exhibit periodic modulations associated with the neutron star (NS) spin, its orbital motion around the companion, or, in some cases, longer-timescale super-orbital variations. Light curves were extracted and visualised using the XRONOS† tool `lcurve`‡.

Power Spectral Density

The Fourier power spectral density (PSD) represents a light curve as a superposition of sinusoidal components with different temporal frequencies. Concentration of power at a particular frequency or within a narrow frequency range indicates variability on the corresponding timescales. In X-ray pulsars (XRPs), the PSD typically shows three characteristic features: (i) coherent pulsations, which appear as narrow peaks at the spin frequency of the neutron star and its harmonics; (ii) quasi-periodic oscillations (QPOs), observed as broader peaks; and (iii) broadband low-frequency noise associated with stochastic accretion variability.

For a uniformly sampled light curve $c(t_n)$ with $n = 0, 1, 2, \ldots, N-1$, the discrete Fourier transform yields

$$C^2(f_k) = \frac{1}{N}\left|\sum_{n=0}^{N-1} c_n\, e^{-i\frac{2\pi nk}{N}}\right|^2, \qquad k = 0, 1, 2, \ldots, N-1, \tag{2.1}$$

where $C^2(f_k)$ is the power at frequency $f_k = k/(N\Delta t)$, c_n is the light-curve value in the n^{th} time bin, N is the total number of samples, and Δt is the time bin size. The exponential term represents the complex Fourier basis functions, and the modulus squared ensures that the power is real and non-negative.

For evenly sampled data, the maximum measurable frequency is set by the Nyquist limit,

$$f_{\text{Nyq}} = \frac{1}{2\Delta t},$$

while the minimum frequency spacing (frequency resolution) is determined by the total duration of the light curve,

$$\delta f = \frac{1}{N\Delta t}.$$

PSDs were generated using the XRONOS task `powspec`§.

To improve signal-to-noise, PSDs are often computed from multiple shorter segments of the light curve. The power spectrum is calculated for each segment independently, and the resulting spectra are averaged, which reduces statistical fluctuations in individual periodograms. However, this approach also decreases the frequency resolution because shorter segments correspond to smaller total time durations. PSDs are commonly reported in Leahy normalization, in which the integrated power equals the total number of detected photons, and a purely Poissonian light curve produces a flat, white-noise level of 2. In this convention, the PSD values are dimensionless, which makes coherent pulsations appear as sharp peaks above the noise level and quasi-periodic oscillations (QPOs) as broadened excesses around characteristic frequencies. Despite their utility, Fourier-based PSDs have limitations: non-sinusoidal

*https://heasarc.gsfc.nasa.gov/lheasoft/help/barycorr.html
†https://heasarc.gsfc.nasa.gov/docs/xanadu/xronos/xronos.html
‡https://heasarc.gsfc.nasa.gov/xanadu/xronos/help/lcurve.html
§https://heasarc.gsfc.nasa.gov/lheasoft/ftools/fhelp/powspec.txt

pulse shapes distribute power into harmonics, causing spectral leakage, and observational gaps, frequent in X-ray astronomy, introduce windowing effects that distort the periodogram. Consequently, complementary techniques such as epoch folding are often employed when necessary.

Epoch Folding Method

Pulsations in X-ray time series are most effectively detected with the epoch-folding method (Leahy 1987). The light curve is folded over a set of trial periods (P_j), producing folded profiles C_i ($i \in [1, 2, \ldots, N]$, where N is the number of phase bins). For each profile, the statistic

$$S_j = \sum_{i=1}^{N} \frac{(C_i - C)^2}{\sigma_i^2} \tag{2.2}$$

is computed, where

$$C = \frac{1}{N} \sum_{i=1}^{N} C_i \tag{2.3}$$

is the mean count rate and σ_i is the uncertainty in bin i. In the absence of periodic modulation, S_j follows a χ^2 distribution with $N - 1$ degrees of freedom. A significant excess above this distribution indicates a periodic signal. The XRONOS tool `efsearch`[¶] was employed to measure spin periods, while final folded pulse profiles were generated with the `efold`[‖] task. For long observations of pulsars with intrinsic period change, a non-zero period derivative ($\dot{P}$) can be incorporated during period search or folding to avoid phase smearing and preserve pulse coherence.

2.3.2 Spectral Analysis

The spectrum describes the distribution of flux across photon energies and encodes the underlying emission processes (Chapter 1). In X-ray astronomy, spectra are typically expressed in units of counts s^{-1} cm^{-2} keV^{-1}, with energies measured in keV. Instruments measure photon energies through pulse height amplitudes (PHA), which depend on detector gain. These values are corrected and converted into Pulse-height Invariant (PI) channels.

The relationship between photon energy (E) and measured PI channels is characterised by the Redistribution Matrix File (RMF), while the effective area of the instrument as a function of energy is described by the Ancillary Response File (ARF). The RMF depends on both E and PI, whereas the ARF depends only on E. Because of the finite energy resolution of detectors, it is generally not possible to invert observed PI spectra directly into physical energy spectra. Instead, forward modelling is applied: a model spectrum $S(E)$ is convolved with the instrument responses and compared with the observed counts.

Formally, the observed spectrum $O(\mathrm{PI})$ is given by

$$O(\mathrm{PI}) = \int RMF(\mathrm{PI}, E) \times ARF(E) \times S(E)\, dE, \tag{2.4}$$

where the integral extends over all incident photon energies. Model fitting was carried out using the XSPEC package (Arnaud 1996)[**], which provides a comprehensive library of physical and phenomeno-

[¶] https://heasarc.gsfc.nasa.gov/xanadu/xronos/help/efsearch.html
[‖] https://heasarc.gsfc.nasa.gov/docs/xanadu/xronos/help/efold.html
[**] https://heasarc.gsfc.nasa.gov/xanadu/xspec/

logical models[††]. User defined models can also be implemented when required. Where appropriate, spectra were binned following the tool `ftgrouppha`[‡‡], ensuring that essential spectral features were preserved while improving parameter constraints. Errors on model parameters were estimated using standard χ^2 minimisation techniques. In what follows, we briefly summarize the XSPEC models that were employed to describe the spectral components relevant to X-ray pulsars and accreting compact objects.

TBABS

This model describes photoelectric absorption by the interstellar medium (ISM) using the Tübingen–Boulder formalism (Wilms et al. 2000). The total absorption cross section is computed as the sum of contributions from gas-phase atoms, ISM dust grains, and molecular hydrogen. Gas-phase absorption includes the photoionization cross sections of individual elements, weighted by their abundances and accounting for depletion onto grains. The model uses the ISM abundance pattern of Wilms et al. (2000) (set via abund `wilm`) and the photoionization cross sections of Verner et al. (1996) (via `xsect vern`). Although the relative abundances of all elements are included, only the neutral hydrogen column density $N_{\rm H}$ is a free parameter in `tbabs`. This parameter (in cm^{-2}) represents the total line–of–sight absorption, with all other elemental contributions scaled according to the adopted abundance table.

BBODYRAD

This model represents thermal emission from a uniform spherical blackbody surface. The photon flux is given by

$$A(E) = \frac{K \times 1.0344 \times 10^{-3}\, E^2}{\exp(E/kT) - 1},$$

where E is the photon energy (in keV) and kT is the blackbody temperature. The normalization is proportional to the emitting surface area and is defined as

$$K = \frac{R_{\rm km}^2}{D_{10}^2},$$

where $R_{\rm km}$ is the effective radius of the emission region (in kilometers) and D_{10} is the source distance in units of 10kpc. Thus, `bbodyrad` provides a direct estimate of the physical scale of the emitting region.

POWERLAW

This model describes a non-thermal photon spectrum commonly produced by inverse Compton scattering or magnetospheric processes. It assumes a simple power-law dependence on energy,

$$A(E) = K E^{-\alpha},$$

where E is the photon energy (in keV), α is the photon index, and K is the normalization. The parameter α controls the spectral slope, with larger values producing softer spectra. The normalization K corresponds to the photon flux at 1 keV in units of photons cm^{-2} s^{-1} keV^{-1}.

HIGHECUT

This model applies an exponential rollover to a continuum spectrum, typically a power-law, to describe

[††] https://heasarc.gsfc.nasa.gov/xanadu/xspec/manual/Models.html
[‡‡] https://heasarc.gsfc.nasa.gov/docs/software/lheasoft/help/ftgrouppha.html

the spectral steepening observed in accreting neutron stars. The multiplicative form is

$$M(E) = \begin{cases} 1, & E \leq E_c, \\ \exp\left[-\dfrac{(E - E_c)}{E_f}\right], & E > E_c, \end{cases}$$

where E_c is the cutoff energy and E_f is the e-folding energy, both in keV. The cutoff energy E_c defines the onset of spectral attenuation, while the e-folding energy E_f sets the exponential scale of the rollover; small E_f values produce a sharp break, whereas larger E_f values yield a slow and gradual decay.

DISKBB

This model describes thermal emission from a geometrically thin, optically thick accretion disk, where the disk is assumed to radiate as a series of concentric blackbody annuli with a radial temperature profile $T(r) \propto r^{-3/4}$, as derived in the standard Shakura–Sunyaev disk framework. The resulting spectrum is a superposition of blackbody components rather than a single Planck function, producing a characteristically broadened continuum (see e.g.; Mitsuda et al. (1984), Makishima et al. (1986)). The primary parameter is the temperature at the inner disk radius, $kT_{\rm in}$ (in keV). The normalization is defined as

$$K = \left(\frac{R_{\rm in}}{D_{10}}\right)^2 \cos\theta,$$

where $R_{\rm in}$ is the apparent inner disk radius (in km), D_{10} is the source distance in units of 10kpc, and θ is the disk inclination ($\theta = 0^\circ$ for a face-on disk). Because the model assumes Newtonian geometry and does not include radiative transfer corrections, $R_{\rm in}$ typically underestimates the true physical radius. A correction factor accounting for spectral hardening and boundary conditions (see, e.g., Kubota et al. (1998)) is required to infer realistic disk radii.

DISPKBB

This model extends the standard multicolor accretion disk spectrum by allowing the radial temperature profile to follow a power law $T(r) \propto r^{-p}$, where p is a free parameter. In the geometrically thin, optically thick Shakura–Sunyaev disk, viscous dissipation yields $p = 0.75$, and the model reduces to `diskbb`. Values of $p < 0.75$ indicate a flatter temperature structure, typically associated with radial advection of energy or super-Eddington accretion flows (see e.g; Mineshige et al. (1994), Hirano et al. (1995), Watarai et al. (2000), Kubota & Makishima (2004), Kubota et al. (2005)). Consequently, `diskpbb` provides a phenomenological means to probe deviations from standard thin-disk behavior in luminous accreting systems. The free parameters are:

- $T_{\rm in}$: temperature at the apparent inner disk radius (keV),
- p: exponent describing the radial dependence of the disk temperature,
- $K = (R_{\rm in}/D_{10})^2 \cos\theta$: model normalization, where $R_{\rm in}$ is the apparent inner disk radius (km), D_{10} is the source distance in units of 10 kpc, and θ is the inclination angle of the disk ($\theta = 0^\circ$ corresponds to a face-on geometry).

As in the `diskbb` model, the inferred radius is an *apparent* inner disk radius, since spectral hardening effects and boundary conditions are not included. A correction factor must therefore be applied to obtain a physically meaningful inner radius; see Kubota et al. (1998) for further discussion.

3

Expressing ULXPs spectra with Local X-ray pulsar model *

3.1 Introduction

The luminosity of ULXs is often in the range of $10^{39} - 10^{41}$ erg s^{-1} in the X-ray energy band, which is much greater than Eddington luminosity for stellar mass compact objects. Such extraordinary luminosities are explained by assuming that the compact objects in ULXs are either intermediate-mass black holes (IMBHs) with masses ranging from $10^3 - 10^5\ M_\odot$, accreting at sub-Eddington rates, or stellar-mass black holes (with masses between 5–80 $M_\odot$), accreting at super-Eddington rates (Fabrika et al. 2021, Pintore et al. 2017).

However, subsequent timing analyses of these ULX sources have unveiled pulsations in some of them, suggesting that the compact object is a neutron star ($\sim 1.4\,M_\odot$) in those sources. These pulsating ULX sources are referred to as Ultra-Luminous X-ray Pulsars (ULXPs). The first ULX source in which pulsations were discovered was M82 X-2 (Bachetti et al. 2014). Subsequently, coherent pulsations were identified in several other sources, including NGC 7793 P13 (Israel et al. 2017a), NGC 5907 ULX1 (Israel et al. 2017b), M51 ULX7 (Castillo et al. 2020), NGC 300 ULX1 (Carpano et al. 2018) and NGC 1313 X2 (Sathyaprakash et al. 2019). Apart from these extra-galactic sources, three ultra-luminous X-ray pulsars were also identified in Small Magellanic Cloud (SMC) and in our own Galaxy, namely SMC X-3 (Tsygankov et al. 2017a, Koliopanos & Vasilopoulos 2018), RX J0209.6-7427 (Vasilopoulos et al. 2020, Chandra et al. 2020), and Swift J0243.6+6124 (Wilson-Hodge et al. 2018, Beri et al. 2021, Bykov et al. 2022).

Phenomenological modelling of the X-ray spectra of ULXs shows them to have two spectral components: a power-law with a photon index of 1.5 that has an exponential cutoff below 10 keV, and a soft excess that dominates below 1 keV (Kaaret et al. 2017). Similar to the galactic black hole binaries, the relative strength of the soft and the hard components vary from source to source and in different spectral states of the same source. ULXPs tend to exhibit continuum-dominated spectra with a few line features. Blue shifted absorption lines have been detected in a few sources indicating outflow (Pinto et al. 2016, Kosec et al. 2017). Rest frame emission lines have been detected in rare cases (Pinto et al. 2017), with the exception of the galactic ULXs (Tsygankov et al. 2017a, Vasilopoulos et al. 2020). Absence of strong iron K-alpha emission line is a notable difference between the extragalactic ULXs and the known Galactic accreting compact stars. Most Galactic High Mass X-ray Binaries show a large absorption column density of hydrogen, in excess of 10^{22} cm^{-2}, which is not seen in the ULXs. With a few exceptions, owing to the limited photon statistics, multiple phenomenological spectral models can often be fitted to the same spectrum of ULXs.

*The work presented in this chapter, aimed at improving our understanding of the ULXPs environment, has been published in Kumar et al. (2025).

Table 3.1: Observed spectral properties of ULXPs in previous literature

SOURCE	NGC 7793 P13 [1]	NGC 5907 ULX1 [2]	M51 ULX7 [3]	NGC 300 ULX1 [4]	NGC 1313 X2 [5]
$N_{\rm H}\vert_{\rm GAL}$ (10^{20} cm^{-2})	1.2^{a}	1.38^{a}	-	11 ± 1	-
$N_{\rm H}\vert_{\rm ISM}$ (10^{20} cm^{-2})	8 ± 1	85^{+14}_{-12}	$3.9^{+1.3}_{-0.6}$	75 ± 7	32^{+3}_{-2}
$\rm CV_{frac}$	-	-	-	0.85 ± 0.03	-
$kT_{\rm diskbb}$ (keV)	$0.45^{+0.03}_{-0.04}$	$0.30^{+0.09}_{-0.06}$	$0.33^{+0.03}_{-0.03}$	$0.178^{+0.008}_{-0.007}$	0.21 ± 0.02
$kT_{\rm diskpbb}$ (keV)	2.0 ± 0.3	-	$2.26^{+0.54}_{-0.17}$	-	$1.57^{+0.07}_{-0.05}$
p	> 1.3	-	$0.99^{u}_{-0.25}$	-	0.57 ± 0.02
Γ	$3.7^{+0.9}_{-1.1}$	$0.83^{+0.13}_{-0.15}$	0.8^{a}	1.52 ± 0.03	-
$E_{\rm fold}$ (keV)	-	$5.3^{+0.7}_{-0.6}$	-	7.0 ± 0.3	-
$E_{\rm cut}$ (keV)	-	-	8.1^{a}	5.6 ± 0.2	-
References	Walton et al. (2018a)	Fürst et al. (2017)	Brightman et al. (2022)	Carpano et al. (2018)	Robba et al. (2021)

[1] Model Used : tbnew * tbnew * (diskbb + diskpbb * SIMPL)

[2] Model Used : tbabs * tbabs * (diskbb + cutoffpl)

[3] Model Used : tbabs * (diskbb + diskpbb + cutoffpl)

[4] Model Used : tbabs * pcfabs * (diskbb + highecut*powerlaw)

[5] Model Used : tbabs * (diskbb + diskpbb)

[a] These parameters are fixed to corresponding values

[u] This parameter reached to its upper bound in fit

In previous studies, ULXPs spectra have typically been explored using models designed for various types of accreting mechanisms onto the compact object. Among these, certain models have become widely used as phenomenological approaches to explain the spectra of ULXPs (Fürst et al. 2017, Walton et al. 2018a, Brightman et al. 2022). We tabulated the detailed properties of ULXPs spectra studied previously in Table 3.1.

The softer part of the spectrum is usually considered a thermal emission, modelled using either an accretion disk blackbody (`diskbb`) or sometimes a combination of disk blackbody (`diskbb`) and accretion disk blackbody with a power-law radial temperature profile (`diskpbb`). For `diskpbb`, the inner disk temperature usually falls within $kT_{\rm in} \sim 1.5 - 3.0$ keV with a power-law index $p \sim 0.55 - 1.3$ of the radial temperature profile, referred to as the hotter component. This hotter component dominates above the energy 1.0 keV and is usually associated with the emission from the innermost region of the supercritical accretion disk (Robba et al. 2021). For the low temperature disk blackbody model (`diskbb`), the inner disk temperature is typically lower, around $kT_{\rm in} \sim 0.17 - 0.45$ keV, and referred to as a cooler component. This cooler component dominates below 1.0 keV and is often associated with the emission from a larger part of the accretion disk outside the spherization radius. In these spectral models, the cooler component likely represents the emission from the outflowing winds from the disc due to the mass loss caused by radiation pressure (Robba et al. 2021, Brightman et al. 2022). The harder part of the spectrum is often fitted with either a simple power-law model or a power-law with an exponential cutoff, which accounts for the emission from the accretion columns onto the neutron star. The cutoff energy typically lies around $E_{\rm cutoff} \sim 5 - 8$ keV. In ULXPs spectra, the column density is usually found to be $N_{\rm H} \sim 3 - 85 \times 10^{20}$ cm^{-2}, which is generally associated with the absorption from the local surrounding medium or the galactic medium (Carpano et al. 2018, Robba et al. 2021, Brightman et al. 2022).

In the accretion-powered pulsars, the strong magnetic field of the neutron star interrupts the disk at the magnetospheric radius (Pringle & Rees 1972, Davidson & Ostriker 1973). Even at the Eddington accretion rate, the magnetospheric radius is quite large and the disk temperature due to viscous dissipation is not high enough to emit in the X-rays. The spectral model, a multi-color disk blackbody

Table 3.2: Observed Properties of ULXPs

Sources	Distance(Mpc)	P_{spin}	P_{orb}	$P_{sup-orb}$	L_{peak} (erg s^{-1})	References
M82 X-2	3.6	1.37 s	2.5 d	-	4.9×10^{39}	Bachetti et al. (2014)
NGC 7793 P13	3.9	0.42 s	64 d	-	$\sim 10^{40}$	Karachentsev et al. (2004),Israel et al. (2017a),Fürst et al. (2016)
NGC 5907 ULX1	17.06	1.13 s	5 d	78 d	$\sim 10^{41}$	Tully et al. (2016), Israel et al. (2017b), Fürst et al. (2017)
M51 ULX7	8.6	2.8 s	2 d	38 d	$\sim 10^{39-40}$	McQuinn et al. (2016), Castillo et al. (2020), Brightman et al. (2022)
NGC 300 ULX1	1.88	31.6 s	-	-	4.7×10^{39}	Gieren et al. (2005), Carpano et al. (2018)
NGC 1313 X2	4.2	1.5 s	-	-	9×10^{39}	Tully et al. (2016) , Sathyaprakash et al. (2019), Robba et al. (2021)

used to fit the soft excess of these ULXPs, is not applicable for accretion onto a high magnetic field neutron star. In a few galactic X-ray pulsars (e.g., Her X-1, 4U 1626-67; Hickox et al. 2004), and some pulsars in the Magellanic Clouds (SMC X–1, LMC X–4; Paul et al. 2002, Naik & Paul 2004, Sharma et al. 2023b) which have relatively low absorption column density, the soft excess is explained as re-processed emission from the inner accretion disk, that is heated by the X-rays from the neutron star. A single-temperature blackbody component fits the soft excess in these sources quite well.

In contrast to previous studies that primarily employed models mentioned in the above paragraphs when analyzing the X-ray spectra of ULXPs (e.g., Fürst et al. 2017, Walton et al. 2018a, Brightman et al. 2022), we aim to examine the broadband spectra of the ULXPs with models that are most commonly used to describe the spectra of the Galactic accretion-powered X-ray pulsars (including sources in the Magellanic Clouds). To achieve this, we employ a single spectral model comprising of a power-law with a high energy exponential cut-off and a blackbody component for the soft excess that describes the spectra of most local accreting pulsars (e.g. White et al. 1983, Paul et al. 2002). The emission model is modified by an absorption component characterizing the absorption of X-rays due to the material enveloping the compact object and along our line of sight. The key focus is on the blackbody temperature ($\mathrm{kT_{BB}}$), which as observed in most local X-ray pulsars, tends to exhibit low values indicative of a soft excess in the X-ray spectrum (Paul et al. 2002, Hickox et al. 2004, Naik & Paul 2004, Sharma et al. 2023b).

By applying this unified spectral model to analyze the observed spectra of ULXPs, we aim to draw direct comparisons with local X-ray pulsars. Additionally, we seek to detect the iron emission lines or determine the upper limits of equivalent widths for iron K-alpha line in the ULXPs and examine their potential correlations with absorption column density and compare them with local pulsars. This comparison allows us to shed light on the unique characteristics of ULXPs while exploring their similarities with the local pulsars and trying to probe the nature of their companion stars.

3.2 Observations & Source Selection

For this work, we have selected the brightest (quasi-)simultaneous observations from *XMM-Newton* (Jansen et al. 2001) and Nuclear Spectroscopic Telescope Array (NuSTAR: Harrison et al. 2013) of ULXPs. Our analysis focuses on ULXP sources, namely NGC 7793 P13, NGC 5907 ULX1, M51 ULX7, NGC 300 ULX1, and NGC 1313 X2, utilizing the available simultaneous X-ray data from both observatories. We did not include M82 X-2 in this spectral study because of contamination from M82 X-1 source within close proximity. The ULXPs do not show significant variation in spectra over time (e.g. Fürst et al. 2017). Therefore, we considered only observations which are simultaneously or quasi-simultaneously observed by both instruments with sufficiently good statistics. Details of observation are given in Table 3.3.

Table 3.3: The X-ray observation log of ULXPs used in this work.

Sources	Co-ordinates	Instrument	Date	Obs. ID	Good Time Exposure (ks)	Source Region	Flaring Correction	References
NGC 7793 P13	RA = $23^h57^m50.9^s$	NuSTAR	20-05-2016	80201010002	106	$50''$	-	Walton et al. (2018a),
	Dec = $-32°37'26.6''$	*XMM-Newton*	20-05-2016	0781800101	22	$30''$	Yes	Israel et al. (2017a)
NGC 5907 ULX1	RA = $15^h15^m58.62^s$	NuSTAR	09-07-2014	80001042002	57	$40''$	-	Fürst et al. (2017),
	Dec = $56°18'10.3''$	NuSTAR	12-07-2014	80001042004	56	$35''$	-	Israel et al. (2017b)
		XMM-Newton	09-07-2014	0729561301	38	$35''$	No Need	
M51 ULX7	RA = $13^h30^m1.02^s$	NuSTAR	10-07-2019	60501023002	169	$30''$	-	Brightman et al. (2022),
	Dec = $47°13'43.8''$	*XMM-Newton*	11-07-2019	0852030101	59	$20''$	Yes	Castillo et al. (2020)
NGC 300 ULX1	RA = $00^h55^m4.85^s$	NuSTAR	16-12-2016	30202035002	163	$50''$	-	Carpano et al. (2018)
	Dec = $-37°41'43.5''$	*XMM-Newton*	17-12-2016	0791010101	84	$30''$	Yes	
		XMM-Newton	19-12-2016	0791010301	40	$30''$	Yes	
NGC 1313 X2	RA = $3^h18^m22.00^s$	NuSTAR	16-12-2012	30002035002	100	$40''$	-	Robba et al. (2021)
	Dec = $-66°36'4.3''$	*XMM-Newton*	16-12-2012	0693850501	91	$30''$	Yes	

3.2.1 NGC 7793 P13

NGC 7793 P13 is an X-ray binary object situated in a nearby galaxy NGC 7793 ($D = 3.9$ Mpc; Karachentsev et al. 2004). The pulsations in NGC 7793 P13 were discovered by Israel et al. (2017a) in the X-ray emission using the *XMM-Newton* data with a spin period of 0.42 s and spin-up was also observed with a period derivative of $\dot{P} \sim -4.0 \times 10^{-11}$ s s^{-1} using two one-year apart observations. The maximum observed luminosity of this source is L $\sim 1.6 \times 10^{40}$ erg s^{-1} in the energy range of 0.3–10 keV (Israel et al. 2017a). This source is also observed in the Optical and UV bands. By studying the optical counterparts of this source, Motch et al. (2014) concluded that the companion is B9Ia spectral type star having a mass of 18–23 $M_\odot$ and orbital period is about 64 d, observed with radial velocity of He-II emission (Motch et al. 2014).

3.2.2 NGC 5907 ULX1

NGC 5907 ULX1 is located in edge-on spiral galaxy NGC 5907 at a distance ($D = 17.06$ Mpc; Tully et al. 2016). The pulsations in NGC 5907 ULX1 were discovered by Israel et al. (2017b) in observations of epoch 2003 (*XMM-Newton*) and 2014 (*XMM-Newton* and NuSTAR) with spin period of 1.427 s and 1.137 s, respectively. A spin-up trend was also observed with a period derivative of $\dot{P} \sim -9.6 \times 10^{-9}$ s s^{-1} and $\dot{P} \sim -5.0 \times 10^{-9}$ s s^{-1} in years 2003 and 2014, respectively. The observed peak luminosity of this source is L $\sim (2.2 \pm 0.3) \times 10^{41}$ erg s^{-1}. The neutron star orbits around its companion star in a nearly circular orbit with an orbital period of 5.3 days and a projected semi-major axis of 2.5 light-seconds (Israel et al. 2017b). A super-orbital period of 78.1 days was also observed in this source (Walton et al. 2016).

3.2.3 M51 ULX7

M51 ULX7, located in spiral galaxy M51 ($D = 8.6$ Mpc; McQuinn et al. 2016), is another ULX source in which pulsations are observed with a spin period of 2.8 s and spinning-up with a period derivative of $\dot{P} \sim -1.5 \times 10^{-10}$ s s^{-1}. The observed luminosity of this source is L $\sim (6 - 8) \times 10^{39}$ erg s^{-1} in the energy ranges of 0.3–10 keV. In this X-ray binary, the neutron star is orbiting around its companion star (an OB-type giant/supergiant star having mass greater than 8 $M_\odot$) with an orbital period of about 2 days (Castillo et al. 2020). A super-orbital period of ∼38 days was also observed in this source (Brightman et al. 2022).

3.2.4 NGC 300 ULX1

NGC 300 ULX1 (earlier known as SN 2010da) is located in the spiral galaxy NGC 300 at a distance of 1.88 Mpc (Gieren et al. 2005). Pulsations are observed in NGC 300 ULX1 using data of *XMM-Newton* and NuSTAR during epoch 2016 with a spin period of 31.6 s and spinning-up with an unusually high period derivative of $\dot{P} \sim -5.56 \times 10^{-7}$ s s^{-1}. The observed luminosity of this source is L $\sim 4.7 \times 10^{39}$ erg s^{-1} in the energy ranges of 0.3–30 keV (Carpano et al. 2018).

3.2.5 NGC 1313 X2

NGC 1313 X2 is located in the barred spiral galaxy NGC 1313 at a distance 4.2 Mpc (Tully et al. 2016). The pulsations in this source were observed at a period of ∼1.5 s with the *XMM-Newton* observation during the epoch of 2017 (Sathyaprakash et al. 2019). These observed pulsations were weak compared to other ULXP sources (Sathyaprakash et al. 2019). The observed maximum luminosity of this source is L $\sim 9 \times 10^{39}$ erg s^{-1} in the energy ranges of 0.3–10 keV (Robba et al. 2021).

3.3 Data Reduction

3.3.1 *XMM-Newton*

In this work, we used only EPIC-pn data for our spectral analysis. For the reduction of *XMM-Newton* data, we used *XMM-Newton* Science Analysis System (SAS) version 20.0.0 and followed SAS Data analysis threads. First, the raw events files were extracted using `epproc` for the listed observations. Then we performed the background flaring correction depending on the observations, if required. For removing background flare, we extracted PN lightcurve in the energy ranges of 10–12 keV and removed the time intervals in which count rate is greater than 0.45 for NGC 7793 P13, 0.6 for M51 ULX7, 0.4 for NGC 1313 X2, and 0.35 for both observations of NGC 300 ULX1. The source events were extracted from the circular region of radius, centred at the source coordinates, mentioned in table 3.3. The background events were extracted from a region twice the size of the source area, positioned away from the source location. Then we grouped the spectrum by selecting minimum counts of 20 and oversample equal to 3 using task `specgroup`. Instrument response file (rmf) and ancillary response file (arf) are generated using the tasks `rmfgen` and `arfgen`, respectively.

3.3.2 NuSTAR

We used both FPMA and FPMB data for our spectral analysis. For the reduction of NuSTAR data, we used standard NuSTARDAS software and latest calibration files (version: 20220118). The clean event files were generated using nupipeline (v: 0.4.9) and then nuproducts was used for extracting the barycentre-corrected light curves and spectrum files for both instruments FPMA and FPMB. The source events were extracted from a circular region of radius mentioned in table 3.3 centered at the source position and background events were selected from the area doubled by source area region away from the source. Then spectral files were grouped to a minimum S/N ratio including background using ftgrouppha with groupscale between 3.0 to 5.0 depending upon the statistics of data.

Table 3.4: Best-fit spectral parameters for the ULXPs sources using model `cons*tbabs*(bbodyrad+highecut*powerlaw+gaussian)`.

Component	Parameter	Units	NGC 7793 P13	NGC 5907 ULX1	M51 ULX7	NGC 300 ULX1	NGC 1313 X2
TBabs	N_H	10^{20} cm^{-2}	$9.1^{+4.1}_{-5.1}$	$72.5^{+4.5}_{-3.3}$	$9.9^{+2.9}_{-2.6}$	$6.6^{+0.9}_{-1.0}$	$21.8^{+5.1}_{-6.1}$
BBodyrad	$kT_{\rm BB}$	keV	$0.17^{+0.12}_{-0.04}$	0.27^{*}	$0.217^{+0.025}_{-0.026}$	$0.211^{+0.013}_{-0.012}$	$0.36^{+0.05}_{-0.03}$
BBodyrad	norm$_{\rm BB}$ [a]		$16.8^{+81.4}_{-13.4}$	< 2.2	$6.1^{+4.7}_{-2.2}$	$26.1^{+6.9}_{-5.0}$	$2.1^{+1.5}_{-1.4}$
BBodyrad	$R_{\rm BB}$	10^8 cm	$1.6^{+2.3}_{-0.9}$	< 2.5	$2.1^{+0.7}_{-0.4}$	$1.0^{+0.1}_{-0.1}$	$0.6^{+0.8}_{-0.4}$
highecut	$E_{\rm cutoff}$	keV	$5.0^{+0.3}_{-0.8}$	$5.1^{+0.5}_{-0.8}$	$6.0^{+0.8}_{-0.7}$	$4.7^{+0.3}_{-0.3}$	$3.2^{+0.2}_{-0.2}$
highecut	$E_{\rm Fold}$	keV	$5.6^{+0.2}_{-1.4}$	$8.1^{+0.9}_{-0.9}$	$6.7^{+1.6}_{-1.3}$	$6.3^{+0.3}_{-0.3}$	$3.0^{+0.5}_{-0.5}$
powerlaw	Γ		$0.99^{+0.06}_{-0.32}$	$1.46^{+0.04}_{-0.15}$	$1.39^{+0.12}_{-0.13}$	$1.29^{+0.05}_{-0.07}$	$1.34^{+0.25}_{-0.40}$
powerlaw	norm	10^{-4}	$4.53^{+0.41}_{-2.33}$	$3.56^{+0.39}_{-0.62}$	$0.90^{+0.19}_{-0.16}$	$6.27^{+0.40}_{-0.47}$	$3.78^{+1.32}_{-1.35}$
gaussian	norm[b]	10^{-7}	23^{+18}_{-16}	7^{+9}_{-7}	$0.6^{+5.1}_{-0.6}$	16^{+9}_{-9}	3^{+5}_{-3}
EQW(upper limit)	-	eV	74.9	80.4	88.5	60.7	78.6
BB Lum.[c]	$L_{\rm BB}$	10^{39} erg s^{-1}	$0.28^{+0.16}_{-0.12}$	< 3.11	$1.18^{+0.11}_{-0.19}$	$0.22^{+0.02}_{-0.02}$	$0.78^{+0.14}_{-0.14}$
Total Lum.[c]	L_X	10^{39} erg s^{-1}	$13.6^{+0.3}_{-0.3}$	118^{+6}_{-6}	$9.5^{+0.7}_{-0.6}$	$3.07^{+0.06}_{-0.07}$	$6.1^{+0.5}_{-0.4}$
Constant	$C_{\rm FPMA1}$		1.00	1.00	1.00	1.00	1.00
	$C_{\rm FPMB1}$		$1.05^{+0.03}_{-0.03}$	$1.04^{+0.07}_{-0.06}$	$0.96^{+0.08}_{-0.08}$	$1.01^{+0.02}_{-0.02}$	$1.15^{+0.09}_{-0.08}$
	$C_{\rm FPMA2}$		-	$0.97^{+0.07}_{-0.06}$	-	-	-
	$C_{\rm FPMB2}$		-	$1.01^{+0.07}_{-0.06}$	-	-	-
	$C_{\rm PN1}$		$0.87^{+0.03}_{-0.02}$	$0.93^{+0.05}_{-0.05}$	$0.89^{+0.07}_{-0.06}$	$0.81^{+0.02}_{-0.02}$	$0.99^{+0.07}_{-0.06}$
	$C_{\rm PN2}$		-	-	-	$0.98^{+0.02}_{-0.02}$	-
χ^2/dof			549.7/549	517/573	198/206	796.6/656	229.3/233

[*] Blackbody temperature is fixed to values at 0.27 keV

[a] norm$_{\rm BB} = (R_{\rm km}/D_{10\ \rm kpc})^2$.

[b] Line center and width were fixed to values of 6.4 keV and 0.10 keV, respectively.

[c] Unabsorbed X-ray Luminosity in the energy range of 0.3–20 keV.

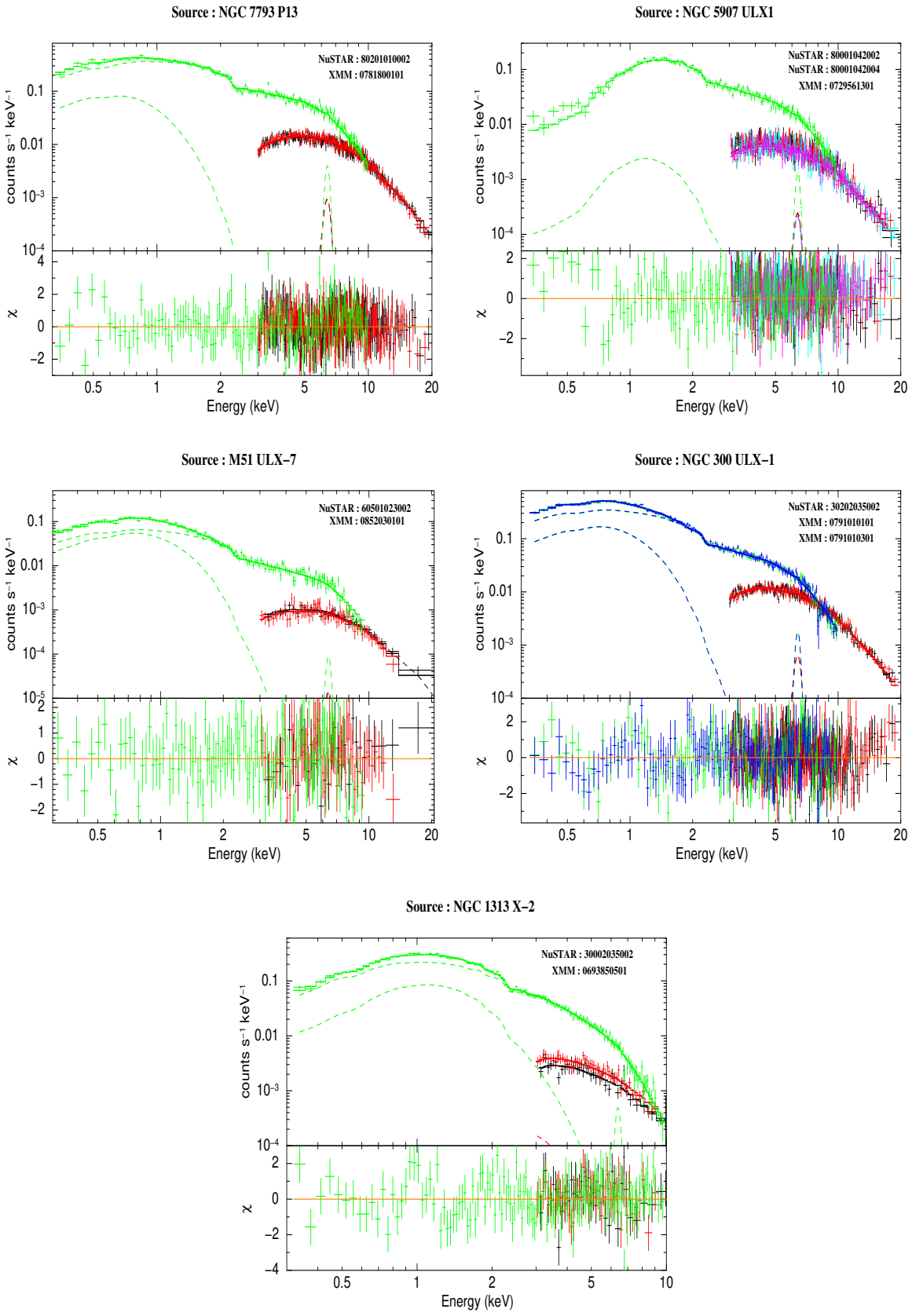


Figure 3.1: Best-fit spectrum of ULXPs with simultaneous or quasi-simultaneous observations from *XMM-Newton* and NuSTAR. Green color data points correspond to the EPIC-pn spectra. Black and red data points represent the spectra from NuSTAR FPMA and FPMB, respectively. For NGC 5907 ULX1, the second NuSTAR observation is presented in cyan and magenta colors for FPMA and FPMB, respectively. For NGC 300 ULX1, the second *XMM-Newton* observation is presented in blue color.

3.4 Results

To perform a comprehensive spectral analysis, we have considered an energy range spanning from 0.3 keV to 20.0 keV, employing xspec software for spectral fitting (Arnaud 1996). We simultaneously fitted the EPIC-pn, NuSTAR-FPMA and NuSTAR-FPMB spectra. A `constant` was included to account for the cross-calibration between these three instruments and fixed it to 1 for FPMA, and allowed it to vary for others. Our spectral model consists of an absorbed power-law with an exponential high-energy cutoff (`highecut`) with a blackbody component added to investigate the soft excess in the spectrum. A similar model is used to study Galactic X-ray binary pulsars (e.g., White et al. 1983, Paul et al. 2002, Doroshenko et al. 2017, Sharma et al. 2023b). For the blackbody component, we use `bbodyrad` model which gives information about the radius of the emission region from where soft excess X-ray emission originates. To model interstellar absorption, `tbabs` was used, with the abundances set to *wilm* (Wilms et al. 2000) and cross-sections set to *vern* (Verner et al. 1996). Additionally, a Gaussian component was included to examine the equivalent width of the iron line. The final model used in xspec is `cons*tbabs*(bbodyrad+highecut*powerlaw+gaussian)`. In Figure 3.1, we present the energy spectra fitted with the model combination presented above for all the five selected sources. The source name and observation ID are marked in each figure. The best-fit spectral parameters are given in Table 3.4.

For NGC 7793 P13, the spectral analysis includes one NuSTAR and one *XMM-Newton* simultaneous observation from 2016. The 0.3–20 keV spectra can be well fitted with absorbed power-law with an exponential cutoff (χ^2/dof $\sim 562.9/551$). Addition of a soft component (`bbodyrad`) further improved fit statistics (χ^2/dof $\sim 549.7/549$) and gave a blackbody temperature of $kT_{\rm BB} = 0.17^{+0.12}_{-0.04}$ keV with normalization of norm$_{\rm BB}$ = 16.8^{+81}_{-13}, cutoff at energy $E_C = 5.0^{+0.3}_{-0.8}$ keV and folding energy at $E_F = 5.6^{+0.2}_{-1.4}$ keV with power-law index $\Gamma = 0.99^{+0.06}_{-0.32}$.

NGC 5907 ULX1 has been observed at two distinct epochs, occurring in 2013 and 2014, during which it was observed simultaneously or nearly simultaneously by both *XMM-Newton* and NuSTAR instruments. The results obtained from examining the spectra in 2013 and 2014 are in agreement with the absence of spectral variability (Fürst et al. 2017). Therefore in this report, we only present the analysis of observations in epoch 2014 which have higher statistics. In 2014, we had nearly simultaneous NuSTAR observations separated by ∼3 d. We carefully checked both observations and found no significant variation between them. Hence, we simultaneously fitted both NuSTAR observations with the *XMM-Newton* observation. The spectra can be well fitted with an absorbed power-law with an exponential cutoff without a blackbody component. Amongst the five sources, NGC 5907 ULX1 has the largest absorption column density and perhaps a low temperature blackbody component is, therefore, not directly detectable. If a blackbody component is added to the model, it is not possible to constrain both its temperature and normalisation. Therefore, we fitted the spectrum with the blackbody temperature fixed at 0.27 keV, which is the best-fit value of the initial unfrozen fit and found the upper limit on blackbody normalization to be 2.2. Also, we obtained cutoff at energy $E_C = 5.1^{+0.5}_{-0.8}$ keV and folding energy $E_F = 8.1 \pm 0.9$ keV with power-law index of $\Gamma = 1.46^{+0.04}_{-0.15}$.

For M51 ULX7, simultaneous observations from NuSTAR and *XMM-Newton* during 2019 were utilized. The NuSTAR-FPMA spectrum was used in the energy ranges of 3–20 keV. However, NuSTAR-FPMB spectrum was found to be dominated by background above 15 keV, so we restricted FPMB spectrum in the 3–15 keV energy range. The spectral fit with the absorbed blackbody and power-law with an exponential cutoff model yielded cutoff at energy $E_C = 6.0^{+0.8}_{-0.7}$ keV and folding energy at $E_F = 6.7^{+1.6}_{-1.3}$ keV with power-law index of $\Gamma = 1.39^{+0.12}_{-0.13}$. The soft excess blackbody component is found to be at temperature $kT_{\rm BB} = 0.217^{+0.025}_{-0.026}$ keV with norm$_{\rm BB}$ = $6.1^{+4.7}_{-2.2}$.

For NGC 300 ULX1, we analyzed one NuSTAR and two *XMM-Newton* simultaneous observations during epoch 2016. We obtained cutoff at energy $E_C = 4.7 \pm 0.3$ keV and folding energy $E_F = 6.3 \pm 0.3$ keV with power-law index $\Gamma = 1.29^{+0.05}_{-0.07}$. A soft excess blackbody component was found at temperature $kT_{\rm BB} = 0.211 \pm 0.012$ keV with normalization of norm$_{\rm BB}$ = $26.1^{+6.9}_{-5.0}$.

Lastly, for NGC 1313 X2, the spectral analysis focuses on one NuSTAR and one *XMM-Newton* simultaneous observation from 2012 in the energy range of 0.3–10 keV. Above 10 keV, both NuSTAR-FPMA and FPMB spectra were dominated by the background. The best-fit model gave cutoff at energy $E_C = 3.2 \pm 0.2$ keV and folding energy $E_F = 3.0 \pm 0.5$ keV with power-law index $\Gamma = 1.34^{+0.25}_{-0.40}$. The soft excess component was found at temperature $kT_{\rm BB} = 0.36^{+0.05}_{-0.03}$ keV with normalization of norm$_{\rm BB}$ = $2.1^{+1.5}_{-1.4}$.

In this work, we also tried to study any correlation between the equivalent width of iron K-alpha line and column density following a similar study for galactic X-ray binaries done by Pradhan et al. (2018). Although there is no clear detection of the iron line but to find the 90% upper limit on equivalent width, we used a Gaussian component with a fixed line center at 6.4 keV and line width at 0.1 keV. After fitting, the value of the upper limit (90%) on equivalent width was found to be 74.9, 80.4, 88.5, 60.7 and 78.6 eV for sources NGC 7793 P13, NGC 5907 ULX1, M51 ULX7, NGC 300 ULX1 and NGC 1313 X2, respectively. The column density for these sources was found to be $9.1^{+4.1}_{-5.1}$, $72.5^{+4.5}_{-3.3}$, $9.9^{+2.9}_{-2.6}$, $6.6^{+0.9}_{-1.0}$ and $21.8^{+5.1}_{-6.1}$ in units of 10^{20} atoms $\rm cm^{-2}$, respectively (see, Table 3.4). Similar low absorption column density is also observed in previous studies as mentioned in Table 3.1.

3.5 Discussion

Since the discovery, the ULXs have been believed to be accreting intermediate-mass black holes or stellar mass black holes with super Eddington accretion. But now a fraction of them are known to host neutron stars accreting at super-Eddington rates. Even larger number of ULXs may have neutron stars as the compact star, pulsation from which may not have been detected for various reasons (faintness, decoherence of a fast pulsar due to orbital motion, etc.) (King & Lasota 2016, King et al. 2023). In this work, we carried out a broad-band spectral analysis of five ULXPs using (near)simultaneous observations from *XMM-Newton* and NuSTAR from the observations with the highest statistical quality of data for each source. The resulting broad-band spectra help us evaluate the suitability of the pulsar spectral model for fitting the spectra of ULXPs. We fitted all the spectra with an absorbed power-law with a high-energy exponential cutoff to account for emission from the accretion column and a blackbody component for the soft excess. This model has been used extensively to fit the X-ray spectra of local accreting pulsars.

The spectra of all 5 sources were well-fitted with this model. The spectral analysis revealed common characteristics among them. They exhibited a photon index in the range of $\sim 1 - 1.5$ with an exponential cutoff at $\sim 3 - 6$ keV. A similar cutoff was also observed in previous studies for sources NGC 5907 ULX1, NGC 300 ULX1 and M51 ULX7 as mentioned in Table 3.1 (Fürst et al. 2017, Carpano et al. 2018, Brightman et al. 2022). Most local X-ray pulsars show a cutoff at about 10 keV, however, a similar spectral cutoff at ~ 5 keV was observed from SMC X-1 (Paul et al. 2002). ULXP sources showed low absorption column density (in the range of $0.6 - 7 \times 10^{21}$ cm^{-2}) and a soft excess at $\sim 0.2 - 0.3$ keV except for NGC 5907 ULX1. Similar soft excess at $\sim 0.1 - 0.3$ keV has been observed in local X-ray pulsars like SMC X-1 (Paul et al. 2002), LMC X-4 (Paul et al. 2002, Naik & Paul 2004, Sharma et al. 2023b), Her X-1 (dal Fiume et al. 1998) and 4U 1626-67 (Beri et al. 2015), with low absorption column density.

In previous studies, the soft excess observed in ULXPs has often been modelled as emission from

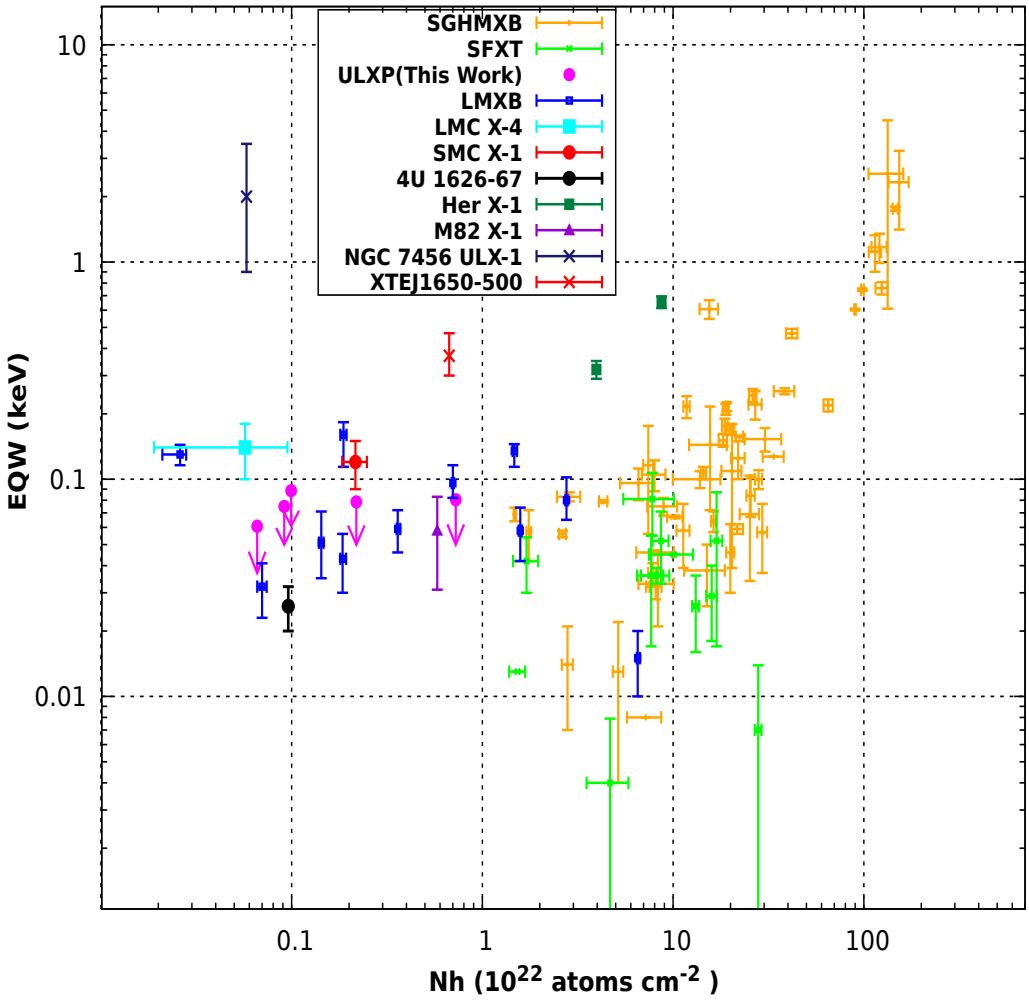


Figure 3.2: Comparative studies of hydrogen column density (N_H: number of hydrogen atoms per squared cm projected along the line of sight) and equivalent width (EQW) of iron K-alpha line for SgHMXBs, SFXTs (Pradhan et al. 2018), LMXBs (Ng, C. et al. 2010), LMC X-4, SMC X-1 (Paul et al. 2002), Her X-1 (Naik & Paul 2003), 4U 1626-67 (Sharma et al. 2023a), M82 X-1 (Caballero-García 2011), NGC 7456 ULX1 (Mondal et al. 2021), XTE J1650-500 (Walton et al. 2012) and ULXPs. The SgHMXBs are indicated in orange, SXFTs in green, LMXBs in blue, LMC X-4 in cyan, SMC X-1 in red, Her X-1 in dark green, 4U 1626-67 in black, M82 X-1 in purple, XTE J1650-500 in red (different point type), and NGC 7456 ULX1 in midnight-blue color. The ULXPs measurements are indicated in magenta points.

the outer regions of the accretion disk, beyond the spherization radius, using xspec model `diskbb` (Robba et al. 2021, Brightman et al. 2022). In our analysis, however, we used a blackbody component (`bbodyrad`) to model the observed soft excess, assuming it as the reprocessed emission of hard X-rays originating near the neutron star surface by an optically thick material, most likely located near the inner edge of the accretion disk. We have measured the blackbody radius, which can be approximated as the radius of the reprocessing shell from which the soft energy photons are re-emitted, to be about $R_{\rm BB} \sim 10^8\,{\rm cm}$ for all five sources. We also calculated the co-rotation radius (R_Ω) for all five sources as mentioned in Table 3.5 using equation (3.1),

$$R_\Omega = \left(\frac{GMP_{\rm spin}^2}{4\pi^2}\right)^{1/3} = 1.5\times10^8\,P_{\rm spin}^{2/3}\,M_{\rm NS}^{1/3}\ {\rm cm} \tag{3.1}$$

where $P_{\rm spin}$ is the spin period of ULXP. For all five sources, the inner disk radius ($R_{\rm BB}$) is smaller than or comparable to the co-rotation radius (R_Ω).

Assuming that the radius of the blackbody component is same as the magnetospheric radius ($R_{\rm m}$) such that $R_{\rm BB} \sim R_{\rm m}$, we can estimate the magnetic field strength of the neutron star, using the relation from Frank et al. (2002),

$$R_{\rm m} \sim 0.5\,R_{\rm A} \sim 1.5\times10^8\times M_{\rm NS}^{1/7}R_6^{10/7}L_{37}^{-2/7}B_{12}^{4/7}\ {\rm cm} \tag{3.2}$$

where $R_{\rm A}$ is a standard Alfven radius, $M_{\rm NS}$ is neutron star mass in units of solar mass $M_\odot$, R_6 is NS radius in units of 10^6 cm, L_{37} is the X-ray Luminosity in units of 10^{37} erg s^{-1}, B_{12} is the surface magnetic field of neutron star in units of 10^{12} G. Assuming neutron star mass $M_{\rm NS} \sim 1.4\,M_\odot$ and radius $R_{\rm NS} \sim 10$ km, we found that the surface magnetic field of the ULXPs should be in the range of $B \sim 10^{13} - 10^{14}$ G for the inner disk radius not to be larger than the co-rotation radius.

A local X-ray pulsar, SMC X-1, exhibits a peak luminosity of $1.2\times10^{39}{\rm erg\,s^{-1}}$ during its peak superorbital intensity phase (Pradhan et al. 2020), which is significantly above the Eddington limit for a neutron star accretor. Remarkably, the observed luminosities of four out of five ULXPs (with the exception of NGC 5907 ULX1) fall within a factor of 2.5 to 11 of SMC X-1's peak luminosity. Other local X-ray pulsars, such as SMC X-3 (Tsygankov et al. 2017a) and Swift J0243.6+6124 (Beri et al. 2021), have also shown super-Eddington luminosities during outbursts, indicating similar super-Eddington accretion onto neutron stars. Moreover, the surface magnetic field of SMC X-1 has been estimated to be $\rm B \sim 4.2\times10^{12}\,G$ (Pradhan et al. 2020), which is comparable to the magnetic field estimated for ULXPs like NGC 1313 X2, and lies within a factor of 2 to 12 for three other ULXPs as given in Table 3.5. These findings suggest that the accretion processes in ULXPs may be similar to that observed in local X-ray pulsars. However, the precise magnetic field strengths of ULXPs still remain uncertain. For instance, Chen et al. (2021) studied the magnetic field of ULXPs using various accretion torque models. They calculated magnetic fields of ULXPs of the order $\rm B \sim 10^{13} - 10^{14}$ G, using accretion torques models from Ghosh & Lamb (1979), Wang (1995), Kluźniak & Rappaport (2007) and Campbell (2012), and $\rm B \sim 10^{12}$ G using accretion torques model from Lovelace et al. (1995). Additionally, Meng et al. (2022) estimated magnetic fields of $\rm B \sim 10^{13} - 10^{14}$ G for ULXPs (excluding NGC 7793 P13) using the Ghosh & Lamb (1979) accretion torque model, with NGC 7793 P13 exhibiting a magnetic field of $\rm B \sim 10^{12}$ G. Similarly, for M51 ULX7, Hu et al. (2021) estimated a magnetic field of $\rm B \sim 10^{13}$ G. Indeed, there are studies where the estimated magnetic field strengths for ULXPs are lower than what we estimated. For instance, Middleton et al. (2019) studied the spectrum of M51 ULX-8, where a Cyclotron Resonant Scattering Feature (CRSF) was observed, and they derived an upper limit on the dipole magnetic field of

10^{12} G. Additionally, King & Lasota (2019) concluded that magnetar field strengths are not required to describe ULXPs. These studies suggest that there may be variability in magnetic field strengths among ULXPs, and the observed phenomena may not always require extremely strong magnetic fields.

Using the value of L_X and R_{BB} mentioned in Table 3.4, we estimated the temperature of the blackbody emission as mentioned in Table 3.5 using the following equation (3.3),

$$\frac{L_X}{4\pi R_{BB}^2} = \sigma T^4 \tag{3.3}$$

where σ is the Stefan-Boltzmann constant. For all five sources, the blackbody temperature is calculated to be 0.36–0.62 keV, which is close to measured values as mentioned in Table 3.4. And the luminosity of the blackbody component, as indicated in the Table 3.4, varies from $(0.2-3.1)\times10^{39}$ erg s^{-1}, which is notably higher than the Eddington luminosity for a neutron star accretor. This implies an intrinsically high luminosity from the accretion column and a high accretion rate, implying a large thickness of the accretion disc on its inner edge. This results in the reprocessing of a significant part of pulsar radiation in the disc observed as the soft excess. To account for this, either a very strong magnetic field or reprocessing by an optically thick curtain is required (Mushtukov et al. 2015a, 2017). However, such extreme luminosities would inevitably result in significant radiation pressure, leading to enormous mass loss. This lost mass would form an optically thick photosphere at a certain distance from the centre, which then reprocesses the emission and contributes to the observed soft excess in the spectrum (Qiu & Feng 2021). The current work can not very firmly establish the origin of the soft excess, but it shows that, empirically, the spectral characteristics of the ULXPs are quite similar to the local X-ray pulsars. The soft component, which is considered to be emitted from the accretion disk, is super Eddington in our model, just as it is in the models employed in several previous works. The spectral model employed in this work is however, simpler with only two components instead of three, one of which is a disk blackbody with an ad-hoc power-law radial dependence of temperature. In these models (Robba et al. 2021, Brightman et al. 2022), the cooler component likely represents the emission from the outflowing winds from the disc due to the mass loss caused by radiation pressure. Same can be true for the blackbody components measured in our model. However, an additional hot blackbody component is not required here.

Iron emission lines observed in X-ray binary spectra typically arise from the interaction between X-rays emitted by the binary system and surrounding material. This surrounding material can be at various locations, including accretion disks (LMXB systems), the high-mass companion star's stellar wind, circumstellar shells situated at a distance from the star, material along the observer's line of sight, and the accretion column (Naik & Paul 2003, Cackett et al. 2010, Fabian & Ross 2010, Paul 2017, Pradhan et al. 2018). For ULXPs, we did not detect a significant iron emission line in the 6–7 keV energy range and have determined the upper limits on the equivalent width for the 6.4 keV line of $\sim 60-90$ eV. Till now there are only two ULX sources (M82 X-1 and NGC 7456 ULX1) in which tentative detection of iron emission line has been reported. In M82 X-1, a weak broadened iron emission line is observed with EW of 59^{+25}_{-27} eV (Caballero-García 2011) and in NGC 7456 ULX1, iron emission line is observed with EW of 2000^{+1500}_{-1100} eV (Mondal et al. 2021), which is much higher than the M82 X-1. The ULX pulsar like SMC X–3 which stands at the threshold between sub-Eddington X-ray pulsars and ULXPs, has shown a clear detection of iron line features with an equivalent width of ~ 70 eV along with low absorption column density of $1-2\times10^{21}$ cm^{-2} (Tsygankov et al. 2017a, Koliopanos & Vasilopoulos 2018). Galactic ULXP candidate, RX J0209.6-7427 also show a presence of Fe K-alpha emission line (Vasilopoulos et al. 2020). Swift J0243.6+6124, another Galactic ULXP candidate, shows evolution in the iron emission line from a narrow 6.4 keV line at the sub-Eddington regime to a broad line in the

Table 3.5: Corotation Radius (R_Ω), magnetic field (B) and Blackbody temperature ($kT_{\rm BB}$), estimation for ULXPs using equation 3.1, 3.2 and 3.3, respectively. We utilize the luminosity ($L_{\rm X}$), blackbody radius ($R_{\rm BB}$) and spin period ($P_{\rm spin}$) values mentioned in Table 3.4 and Table 3.2, respectively.

Source	$R_{\rm BB}(10^8{\rm cm})$	$B(10^{13}{\rm G})$	$kT_{\rm BB}$ (keV)	$R_\Omega(10^8{\rm cm})$
NGC 7793 P13	1.6	3.80	0.45	0.94
NGC 5907 ULX1	< 2.5	24.41	0.62	1.82
M51 ULX7	2.1	5.11	0.36	3.33
NGC 300 ULX1	1.0	0.79	0.39	16.77
NGC 1313 X2	0.6	0.46	0.60	2.20

super-Eddington regime (Jaisawal et al. 2019, Bykov et al. 2022).

In Fig. 4.6, we show the absorption column density and the equivalent width of iron line observed in ULXPs to those of Super-giant high-mass X-ray Binaries (SgHMXBs), Supergiant Fast X-ray Transients (SFXTs; Pradhan et al. 2018), Low Mass X-ray Binaries (LMXBs; Ng, C. et al. 2010), Galactic stellar mass black hole binary XTE J1650-500 (Walton et al. 2012) and two ULX sources M82 X-1 (Caballero-García 2011) and NGC 7456 ULX1 (Mondal et al. 2021). Despite the ULXPs accreting at super-Eddington rates, they exhibit low absorption column density. At least two of the ULXPs M82 X2 and M51 ULX7 have high mass companion of mass $M_{\rm c} > 5.2\,M_\odot$ (Bachetti et al. 2014) and $M_{\rm c} > 8\,M_\odot$ (Castillo et al. 2020) respectively and long duration eclipses indicate high mass companion for many, if not all ULXs (Urquhart & Soria 2016). In comparison with Galactic X-ray binaries, the absorption column density in ULXPs is found to be on the lower side of that for the SgHMXBs. Be-X-ray pulsars, however, can have very low column density. On the other hand, upper limits of equivalent width for the iron K-alpha line determined for ULXPs are not in conflict with the low equivalent width generally observed in galactic LMXBs and disk-fed pulsars. In some galactic high-mass X-ray binaries, the iron line has an equivalent width ranging from several hundred eV up to 1.5 keV (Pradhan et al. 2018). Despite having high mass companion and small binary orbit, the reason for very low absorption column density and the absence of iron emission lines in ULXP is still to be understood.

Three ULXPs, M51 ULX7, M82 X-2 and NGC 5907 ULX1 have short orbital periods between 2–5 d, suggesting compact orbits. Given that ULXPs have about 2–4 orders of magnitude higher X-ray luminosity than the persistent SgHMXBs, if the accretion were driven by stellar wind, it would require very dense stellar winds, resulting in higher absorption column densities and strong emission lines. However, the lack of strong iron line and low column density indicates the accretion process in ULXPs is likely due to Roche lobe overflow. X-ray pulsars like LMC X-4, SMC X-1 and 4U 1626-67 are believed to have accretion driven by Roche Lobe overflow and show relatively low column density and iron line strength (e.g. Paul et al. 2002, Sharma et al. 2023a).

In the ULX regime, the entire magnetosphere becomes dominated by optically thick material, which reprocesses all the primary photons of the accretion column (Mushtukov et al. 2017). This essentially erases the pulsation information and the spectral characteristics of the accretion column emission. Therefore, it is possible that other ULX sources with no detection of pulsed emission may also harbour neutron star at their central core (King et al. 2017, Pintore et al. 2017, Koliopanos & Vasilopoulos 2018, Walton et al. 2018b). This study puts forward a comprehensive comparison between ULXPs and local X-ray pulsars which may be further helpful in understanding other ULX sources.

4

Reprocessing of X-rays emission in Ultra-Luminous X-ray sources *

4.1 Introduction

Ultra-luminous X-ray sources (ULXs) are extragalactic, off-nuclear X-ray sources with luminosities of 10^{39}–10^{41} erg s^{-1}, well above the Eddington limit for stellar-mass compact objects. Although their basic observational properties have been known for decades, the recent detection of coherent pulsations in sources such as M82 X-2, NGC 5907 ULX1, NGC 7793 P13, NGC 300 ULX1, M51 ULX-7, and NGC 1313 X-2 has confirmed that at least a subset of ULXs host neutron-star accretors, or more generally, stellar-mass compact objects accreting at super-Eddington rates. In several ULXPs, orbital parameters have been measured, enabling estimates of the mass function and hence the minimum companion mass. For example, in M82 X-2, Bachetti et al. (2014) derived a mass function of $f = 2.1\,M_{\odot}$, implying a companion mass of $\mathrm{M_c} > 5.2\,\mathrm{M_{\odot}}$, consistent with a high-mass X-ray binary (HMXB). Likewise, M51 ULX-7 requires a donor with $\mathrm{M_c} > 8\,\mathrm{M_{\odot}}$ (Castillo et al. 2020), and NGC 5907 ULX1 has been suggested to be an HMXB viewed nearly face-on, with an orbital inclination of $i < 5^{\circ}$ (Belfiore et al. 2024). Additionally, the presence of long-duration eclipses in some ULXs further supports the idea that high-mass companions are common in most of ULXs if not all (Urquhart & Soria 2016). The combination of high luminosity and massive donor stars implies substantial surrounding material, and thus ULXs are expected to show strong signatures of X-ray reprocessing from the environment of the compact object.

One common approach to study the environment surrounding a compact object is to examine the Fe $K\alpha$ line, which arises from the fluorescence of iron atoms in the reprocessing environment when illuminated by X-rays. Previously, this iron line feature has been studied for many Galactic X-ray binaries, and the equivalent width (EW) of the iron line varies from a few eV to keV (Torrejón et al. 2010, Ng, C. et al. 2010, Giménez-García et al. 2015, Pradhan et al. 2018). The surrounding material that produces the iron emission line can also cause absorption. Galactic classical supergiant high-mass X-ray binaries (Sg HMXBs) exhibit a correlation between the column density and the equivalent width of the iron line. This is expected, as the primary accretion mechanism in these systems is the stellar wind from the companion star. At larger column density, more material is exposed to X-ray illumination, leading to a stronger iron line and a higher EW (Torrejón et al. 2010, Giménez-García et al. 2015, Pradhan et al. 2018). However, the average EW of the iron line in supergiant fast X-ray transients (SFXTs) is generally lower than that observed in classical Sg HMXBs (Pradhan et al. 2018). Ng, C. et al. (2010) found the EW of the iron line for low-mass X-ray binaries (LMXBs) ranges from 17 eV to 189 eV, which is, on average, smaller than that observed in HMXBs.

Another way to study the reprocessing of X-rays from a compact object is to study them during the

*The work carried out in this chapter, focused on reprocessing signatures in ULXs, has been submitted to the Astrophysical Journal. (e-Print: 2509.09133 [astro-ph.HE])

eclipses and eclipse transitions, as the emission of X-rays that come directly from the compact object is mostly suppressed by the companion star. Galactic eclipsing HMXBs show an increase in hardness ratio during ingress/egress (Balu et al. 2024, Tamang et al. 2025), which indicates a larger absorption column density, hence more absorption of soft photons near the compact object, during ingress/egress. In addition, the X-ray flux in Galactic HMXBs significantly drops during the eclipse phase. Aftab et al. (2019) and Aftab & Paul (2024) found that the ratio of flux for out-of-eclipse (OOE) to eclipse varies between ∼8–237 in HMXBs and ∼6–54 in LMXBs, varying from source to source. In this work, we aim to study the above three aspects of X-ray reprocessing in the ULX systems: the Fe $K\alpha$ emission line, the hardness ratio around the eclipse transitions, and the flux ratio during the eclipse to OOE phase.

4.2 Source Selection & Observations

To study the iron line properties, we selected five known ULXPs and six well-known bright ULXs, as listed in Table 4.2. For the hardness–ratio and flux–ratio analysis, we focused on five eclipsing ULXs: CG X-1, CXOM51 J132943.3+471135 (M51 S1), CXOM51 J132946.1+471042 (M51 S2), CXOM51 J132940.0+471237 (M51 ULX1), and CXOM51 J132939.5+471244 (M51 ULX2).

For the iron line investigation, we utilized all available *XMM-Newton* observations for the six ULXs and five ULXPs, chosen for their long exposures and high-quality spectra. A similar study carried out for Ho IX X-1 and NGC 1313 X-1 by Walton et al. (2012) reported upper limits on the iron line EW of ∼30 eV and ∼50 eV, respectively. The total exposure times of the XMM Newton observations of the 11 selected ULXs are summarized in Table 4.2, and the full observation log is provided in Table 4.1. Although NGC 300 ULX1 showed a prominent iron line near 6.4 keV in its 2010 observation (Carpano et al. 2018), the spectral properties differed significantly from those of other ULXs, and no pulsations were detected; therefore, this dataset was excluded from the present analysis.

For the eclipsing ULX sample, our goal was to examine the hardness ratio as a function of orbital phase, particularly during eclipse ingress and egress, and to measure the flux ratio between eclipse and out-of-eclipse (OOE) phases. Since M51 S1 and M51 S2 are well resolved with *XMM-Newton*, we used *XMM-Newton* observations for these two systems. For CG X-1, M51 ULX1, and M51 ULX2, we relied on *Chandra* observations, as detailed in Table 4.3.

Table 4.1: Detailed list of XMM-Newton observations used in this work for the selected bright well-known ULX Sources and ULXPs in the search for iron emission line.

Source	ObsID	MJD	Src Rgn	GTE (ks)
M51 ULX7	0112840201	52654.57	20″	17.12
	0212480801	53552.29	20″	20.86
	0303420101	53875.29	20″	28.85
	0303420201	53879.48	20″	20.66
	0677980701	55719.22	20″	3.84
	0824450901	58251.92	20″	64.73
	0830191501	58282.10	20″	51.59
	0830191601	58284.09	20″	51.66
	0852030101	58675.49	20″	58.78
	0883550201	59542.39	20″	70.49
	0883550301	59586.26	20″	104.95
NGC 300 ULX1	0791010101	57739.40	30″	96.29
	0791010301	57741.39	30″	44.78
NGC 1313 X2	0150280301	52994.10	30″	7.23
	0150280601	53012.16	30″	5.86
	0205230301	53161.27	30″	8.69
	0205230501	53332.31	30″	12.49
	0205230601	53408.50	30″	8.48
	0301860101	53800.71	30″	17.18
	0405090101	54024.01	30″	71.01
	0693850501	56277.68	30″	67.83
	0693851201	56283.67	30″	54.29
	0722650101	56451.24	30″	9.09
	0742490101	57111.19	30″	66.46
	0742590301	56843.97	30″	53.52
	0764770101	57361.20	30″	32.88
	0764770401	57470.95	30″	13.25
	0782310101	57669.90	30″	73.97
	0794580601	57841.25	30″	13.97
	0803990101	57918.89	30″	106.32
	0803990201	57924.91	30″	109.23
	0803990301	57996.68	30″	28.89
	0803990401	57998.75	30″	24.19
	0803990501	58094.47	30″	53.65
	0803990601	58096.46	30″	44.65
NGC 5907 ULX1	0145190101	52698.59	30″	7.07
	0145190201	52690.67	30″	10.14
	0673920301	55966.59	30″	12.82
	0729561301	56847.95	30″	37.57
	0804090401	57939.02	30″	31.30
	0804090501	57942.79	30″	32.27
	0804090601	57949.26	30″	32.47
	0804090801	58656.78	30″	15.40
	0804090901	58658.79	30″	14.87
	0804091001	58663.83	30″	35.53
	0804091101	58669.41	30″	29.99
	0804091201	58670.76	30″	9.62
	0824320201	58646.82	30″	42.85
	0824320301	58653.21	30″	40.64
	0824320401	58660.79	30″	41.60
	0824320601	59053.74	30″	26.45
	0824320701	59159.90	30″	24.89
	0851180701	58705.51	30″	48.35
	0851180801	58707.45	30″	41.14
	0884220201	59265.10	30″	19.87
	0884220301	59271.09	30″	44.50
	0891801501	59453.39	30″	49.44
	0893810301	59585.18	30″	27.02
	0913080201	59889.87	30″	55.30
	0931410101	60152.77	30″	22.58
	0953011001	60521.89	30″	25.56
NGC 7793 P13	0693760401	56621.21	30″	41.1
	0748390901	57002.00	30″	41.97
	0781800101	57528.58	30″	15.61
	0804670301	57893.66	30″	39.89
	0804670401	57904.90	30″	24.99
	0804670601	57924.11	30″	21.05
	0804670701	58083.00	30″	41.81
	0823410301	58449.79	30″	19.35
	0823410401	58479.60	30″	18.78
	0840990101	58619.99	30″	10.24
	0853981001	58809.36	30″	30.43
	0861600101	59027.79	30″	42.42
	0883780101	59363.72	30″	33.33
	0883780201	59538.40	30″	13.12
	0922840101	60100.91	30″	13.17
	0922840201	60284.30	30″	5.58

Source	ObsID	MJD	Src Rgn	GTE (ks)
Circ ULX5	0111240101	52127.40	30″	63.96
	0656580601	56717.44	30″	20.95
	0701981001	56326.32	30″	28.29
	0792382701	57623.73	30″	13.34
	0824450301	58377.73	30″	86.30
	0932990101	60342.30	30″	88.83
Holmberg II X-1	0112520601	52374.60	30″	4.64
	0112520901	52535.11	30″	3.69
	0200470101	53110.86	30″	32.73
	0561580401	55281.41	30″	21.63
	0724810101	56544.29	30″	4.65
	0724810301	56552.27	30″	5.81
	0864550201	59281.06	30″	18.97
	0864550301	59285.05	30″	19.58
	0864550401	59289.07	30″	17.60
	0864550501	59293.02	30″	11.30
	0864550601	59297.01	30″	17.77
	0864550701	59301.00	30″	14.05
	0864550801	59308.98	30″	19.55
	0864550901	59313.00	30″	17.66
	0864551101	59304.99	30″	10.02
	0864551201	59316.96	30″	12.99
Holmberg IX X-1	0112521001	52374.74	30″	7.05
	0112521101	52380.73	30″	7.64
	0200980101	53274.31	30″	48.21
	0657802201	55888.05	30″	12.17
	0693850801	56223.20	30″	5.69
	0693851001	56227.19	30″	3.73
	0693851101	56247.14	30″	2.67
	0693851701	56243.15	30″	7.14
	0693851801	56245.14	30″	6.59
	0870900201	59169.40	30″	17.87
	0870930101	59139.51	30″	15.50
	0870930301	59151.44	30″	7.70
	0870930501	59171.38	30″	14.50
NGC 1313 X1	0150280301	52994.10	30″	7.22
	0150280601	53012.16	30″	5.85
	0205230301	53161.27	30″	8.69
	0205230501	53332.31	30″	12.48
	0205230601	53408.50	30″	8.33
	0301860101	53800.71	30″	17.12
	0405090101	54024.01	30″	71.63
	0693850501	56277.68	30″	67.84
	0693851201	56283.67	30″	54.31
	0722650101	56451.24	30″	9.09
	0742490101	57111.19	30″	66.40
	0742590301	56843.97	30″	53.68
	0764770101	57361.20	30″	32.74
	0764770401	57470.95	30″	13.15
	0782310101	57669.90	30″	73.99
	0794580601	57841.25	30″	14.01
	0803990101	57918.89	30″	106.81
	0803990201	57924.91	30″	109.70
	0803990301	57996.68	30″	29.13
	0803990401	57998.75	30″	24.41
	0803990501	58094.47	30″	53.58
	0803990601	58096.46	30″	44.66
M33 X8	0102640601	52095.66	40″	2.31
	0102642001	52136.35	40″	8.02
	0102642101	52299.50	40″	8.97
	0141980301	52845.33	40″	5.68
	0141980601	52662.84	40″	10.61
	0141980801	52682.65	40″	5.57
	0650510101	55386.31	40″	68.08
	0650510201	55388.31	40″	65.46
	0800350101	57955.35	40″	17.40
	0800350201	57957.79	40″	18.34
	0800350301	57967.32	40″	18.98
	0831590201	58681.68	40″	10.78
	0831590401	58677.73	40″	15.35
	0102642301	52301.43	40″	8.98
NGC 4559 ULX7	0152170501	52786.13	30″	32.33
	0842340201	58650.8	30″	56.42
	0883960201	59743.86	30″	75.85

Table 4.2: Total good-time exposure (GTE) for each ULX and ULXP included in the search for iron emission line, based on all available XMM-Newton observations used in the analysis.

Source Name	RA	Dec	GTE(ks)	$N_{\rm H}$ (10^{22} cm^{-2})
M51 ULX7[a1]	$13^{\rm h}30^{\rm m}1.02^{\rm s}$	$47^{\circ}13^{'}43.80^{''}$	493.53	0.099^{b1}
NGC 300 ULX1[a2]	$00^{\rm h}55^{\rm m}4.85^{\rm s}$	$-37^{\circ}41^{'}43.50^{''}$	141.07	0.066^{b1}
NGC 1313 X2[a3]	$3^{\rm h}18^{\rm m}22.00^{\rm s}$	$-66^{\circ}36^{'}4.30^{''}$	883.13	0.218^{b1}
NGC 5907 ULX1[a4]	$15^{\rm h}15^{\rm m}58.62^{\rm s}$	$56^{\circ}18^{'}10.30^{''}$	779.24	0.725^{b1}
NGC 7793 P13[a5]	$23^{\rm h}57^{\rm m}50.90^{\rm s}$	$-32^{\circ}37^{'}26.60^{''}$	412.84	0.091^{b1}
Circ ULX5[a6]	$14^{\rm h}12^{\rm m}39.00^{\rm s}$	$-65^{\circ}23^{'}34.00^{''}$	301.67	0.610^{b2}
Holmberg II X-1[a7]	$08^{\rm h}19^{\rm m}28.99^{\rm s}$	$70^{\circ}42^{'}19.37^{''}$	232.64	0.059^{b3}
Holmberg IX X-1[a8]	$09^{\rm h}57^{\rm m}53.20^{\rm s}$	$69^{\circ}03^{'}48.30^{''}$	156.46	0.119^{b3}
NGC 1313 X1[a9]	$03^{\rm h}18^{\rm m}20.00^{\rm s}$	$-66^{\circ}29^{'}11.00^{''}$	884.82	0.253^{b4}
M33 X8[a10]	$01^{\rm h}33^{\rm m}50.60^{\rm s}$	$30^{\circ}39^{'}31.00^{''}$	264.53	0.187^{b5}
NGC 4559 ULX7[a11]	$12^{\rm h}35^{\rm m}51.71^{\rm s}$	$27^{\circ}56^{'}4.10^{''}$	164.60	0.150^{b6}

1. References for the source co-ordinates and previous detailed studies: [a1](Castillo et al. 2020, Brightman et al. 2022), [a2](Carpano et al. 2018), [a3](Robba et al. 2021), [a4](Fürst et al. 2017, Israel et al. 2017b), [a5](Fürst et al. 2016, Israel et al. 2017a), [a6](Mondal et al. 2021), [a7](Barra et al. 2024), [a8](Walton et al. 2012, Walton et al. 2017), [a9](Walton et al. 2012), [a10](West et al. 2018), [a11](Pintore et al. 2021)

2. Column density ($N_{\rm H}$) values for the curve of growth are adopted from the previous literature as follows: [b1]Kumar et al. (2025), [b2]Mondal et al. (2021), [b3]Pintore et al. (2014), [b4]Walton et al. (2020), [b5]West et al. (2018), [b6]Pintore et al. (2021)

4.3 Data Reduction

4.3.1 XMM-Newton

In this work, we used only EPIC-pn data for our spectral analysis. For the reduction of *XMM-Newton* data, we used *XMM-Newton* Science Analysis System (SAS) version 20.0.0 and followed SAS Data analysis threads. First, the raw event files were extracted using `epproc` for the listed observations. Then we performed the background flaring correction depending on the observations, if required. The clean event files are barycenter corrected using the SAS task `barycen`. The source events were extracted from the circular region of radius, centered at the source coordinates, mentioned in Table 4.1 and 4.3. The background events were extracted from a circular region of radius 1.5 times the radius of the source region, except for M51 S1 and S2, where a region twice the radius of the source region was used, positioned away from the source location. Instrument response files (rmf) are generated using the tasks `rmfgen`*, which also include the pile-up corrections (if any), and ancillary response files (arf) are generated using the tasks `arfgen`. We use the tool `epiccombine` and `addspec` for combining the spectra and `ftgrouppha` for grouping of the combined spectra. We extracted the source and background light curves for all good single and double events ($\rm PATTERN <= 4$) using `evselect` and obtained final

*https://www.cosmos.esa.int/web/xmm-newton/sas-thread-epatplot

Table 4.3: Observation log for the eclipsing ULX sources analyzed in this work, including the datasets used for studying hardness ratio evolution and flux variations between eclipse and OOE phases.

Source Name	Co-ordinates	Instrument	Obs Id	MJD	Source Region	Total GTE (ks)
CG X-1[1]	RA = $14^{h}13^{m}12.21^{s}$	Chandra (ACIS-S)	12823	55547.75	$4''$	142.87
	Dec = $-65°20'13.7''$					
M51 S1[2]	RA = $13^{h}29^{m}43.32^{s}$	XMM-Newton	0824450901	58251.92	$20''$	64.73
	Dec = $+47°11'34.9''$	XMM-Newton	0852030101	58675.49	$20''$	58.78
M51 S2[2]	RA = $13^{h}29^{m}46.13^{s}$	XMM-Newton	0830191501	58282.10	$15''$	51.59
	Dec = $+47°10'42.3''$	XMM-Newton	0830191601	58284.09	$15''$	51.66
		XMM-Newton	0852030101	58675.49	$20''$	58.78
M51 ULX1[3]	RA = $13^{h}29^{m}39.94^{s}$	Chandra (ACIS-S)	13813	56179.74	$4''$	166.07
	Dec = $+47°12'36.6''$					
M51 ULX2[3]	RA = $13^{h}29^{m}39.44^{s}$	Chandra (ACIS-S)	13813	56179.74	$4''$	166.07
	Dec = $+47°12'43.3''$					

[1]Qiu et al. (2019), [2]Wang et al. (2018), [3]Urquhart & Soria (2016).

background-subtracted light curves using `epiclccorr`. Although, in some of the observations, the source is on-chip gap, but that does not affect the spectra around 6.4 keV much, except some flux loss that is taken care by the task `arfgen`, hence for studying the iron $K\alpha$ line, those observations are also included (XMM-Newton Science Operations Centre 2025).

4.3.2 Chandra

For event file extraction, we used the Chandra Interactive Analysis of Observations (`CIAO`) software package version 4.15 together with the corresponding `CALDB` calibration database version 4.10.7 (Fruscione et al. 2006). We reprocessed the data using the `CIAO` task `chandra_repro`. We performed the flaring and barycenter correction using task `deflare` and `axbary`, respectively. Source light curves were extracted with `dmextract` from circular regions of radius $4''$ centered on the source coordinates listed in Table 4.3. Background regions were selected as circles of radius $15''$ for CG X-1 and $10''$ for M51 ULX1/ULX2, positioned away from the source location. Energy spectra were extracted from the reprocessed event files using the `specextract` task.

4.4 Analysis and Results

4.4.1 Search for iron emission line

To examine the possible presence of an iron line feature in the combined spectra of individual sources, we utilized only EPIC-pn data, owing to its large effective area in the relevant energy band and restricted the analysis to the energy range from 5.0 keV to 8.0 keV, which encompasses the Fe Kα band (6.4–7 keV) while minimizing contamination from softer spectral components. Spectral fitting was performed using the xspec software package (Arnaud 1996). Previous studies suggest that the spectra of most ULX sources are likely dominated by a power-law in the energy range considered above (Walton et al. 2021, King et al. 2023). Accordingly, we considered an absorbed power-law model to describe the

continuum. Although the absorption from the interstellar medium is mostly dominated in the lower energy range, `tbabs` was used for a fixed value of the column density ($N_{\rm H} = 0.15 \times 10^{22}$ cm^{-2}, which is the median of the previously reported values as mentioned in table 4.2), with the abundances set to `wilm` (Wilms et al. 2000) and cross-sections set to `vern` (Verner et al. 1996).

To investigate the presence of an iron emission line, we added a Gaussian component to the continuum model, resulting in the final xspec model `tbabs*(powerlaw+gauss)`. The top panels of Fig. 4.1 show the combined spectra from *XMM-Newton* observations of individual ULX (left) and ULXP (right) sources. In all cases, the spectra in the 5–8 keV range are well-fitted with this simple model and the best-fit spectral parameters with χ^2/dof values for each source are summarized in Table 4.4. The powerlaw photon index is found to lie between 1.68 and 3.14 for these 11 sources. Since no significant detection of the line was found, we estimated the 90% confidence upper limits on the EW by fixing the Gaussian centroid at 6.4 keV and the line width at 0.1 keV. The resulting upper limits on the EW range from 16.1 eV to 60.4 eV across the individual ULX and ULXP spectra (Table 4.4).

We also attempted to fit the spectra by slightly adjusting the energy range, both narrowing and widening it, to observe the effect on the EW based on the selected energy range. The narrower range used was 5.5–7.5 keV, while the wider range extended from 4.0–9.0 keV. The results, summarized in Table 4.5, demonstrate that for most sources, the chosen energy range does not significantly influence the upper limit for the EW of the iron line. For all cases, continuum is fitted using a powerlaw model except for M51 ULX-7 in the energy range 4.0–9.0 keV, in which a powerlaw with high-energy cutoff is used for the continuum fitting. $\rm E_{cut}$ and $\rm E_{fold}$ are frozen to values 7.2 keV and 3.5 keV, respectively, which are obtained from fitting the full spectrum in the energy range 0.3–10 keV. Fig. 4.2 shows the residuals from the best-fit absorbed powerlaw model in the energy range of 5.5–7.5 keV, 5–8 keV, and 4–9 keV for individual ULX sources.

Additionally, we fit the combined spectra of all sources, with the best-fit parameters given in Table 4.4. The bottom panel of Fig. 4.1 shows the combined spectra (left) obtained from all observations of the selected sources, along with the residuals (right) from the best-fit absorbed powerlaw model in the energy range of 5.5–7.5 keV, 5–8 keV, and 4–9 keV. Based on these analyses, we constrain the upper limit on EW of the iron line for the ULX sources to be in the range 11.1–20 eV (Table 4.5), marking a significant improvement over previous studies.

To validate the upper limit on the EW of the iron line obtained from the combined spectrum of all sources, we simulated the spectrum for each source by adding an iron line with an EW of 30 eV. Then combined the simulated spectra of all sources and determined the EW of the iron line by fitting the combined spectrum in the energy range 5.0–8.0 keV. This process is repeated for 10,000 sets of simulated spectra, and the histogram of the obtained EW values is shown in Fig. 4.3. A similar process is also repeated by adding the iron line of EW of 15 eV and 20 eV. As illustrated in Fig. 4.3, the recovered EWs for the combined spectra are very well Gaussian distributed around the simulated value of the EW, which validates our results on the upper limit on EW obtained using the combined spectrum for all sources.

4.4.2 Hardness Ratio around the eclipse transitions

We investigated the hardness ratio during the eclipse and the eclipse transitions for five eclipsing ULX sources. For calculating the hardness ratio[†], we selected the soft and hard X-ray energy bands such that the total counts in both bands are approximately similar. The selected energy bands were: 0.3–0.57 keV and 0.57–2.0 keV for M51 S1, 0.3–0.7 keV and 0.7–2.0 keV for M51 S2, 0.3–2.25 keV and 2.25–

[†]HR $= \frac{H-S}{H+S}$, where H and S are the count rates in the hard and soft X-ray bands, respectively.

Table 4.4: Values of spectral parameters from fit in the energy range of 5.0–8.0 keV with `tbabs*(powerlaw+gauss)` model. $N_{\rm H}$ was fixed at $0.15 \times 10^{22}\,{\rm cm}^{-2}$. The Gaussian line center and line width (σ) were fixed at 6.4 keV and 0.1 keV, respectively.

Source	Γ	norm (10^{-3})	Gauss norm* (10^{-7})	EW (eV)	χ^2/dof
M51 ULX7	1.68 ± 0.20	$0.11^{+0.05}_{-0.03}$	< 1.70	< 34.1	178.8/164
NGC 300 ULX1	2.08 ± 0.15	$1.76^{+0.55}_{-0.41}$	< 14.74	< 40.1	330.9/345
NGC 1313 X2	2.80 ± 0.13	$1.91^{+0.51}_{-0.40}$	< 5.24	< 49.2	196.8/215
NGC 5907 ULX1	1.85 ± 0.13	$0.22^{+0.06}_{-0.05}$	< 3.23	< 44.5	534.6/495
NGC 7793 P13	1.79 ± 0.10	$0.61^{+0.12}_{-0.10}$	< 6.51	< 30.0	573.8/555
Circ ULX5	2.57 ± 0.12	$4.47^{+1.04}_{-0.84}$	< 12.36	< 32.8	485.5/480
Ho II X1	3.08 ± 0.21	$2.92^{+1.34}_{-0.90}$	< 3.94	< 41.3	224.9/254
Ho IX X1	2.40 ± 0.09	$6.05^{+1.12}_{-0.94}$	< 15.34	< 21.8	483.1/551
NGC 1313 X1	2.24 ± 0.07	$1.49^{+0.20}_{-0.17}$	< 4.35	< 18.5	629.9/596
M33 X8	3.14 ± 0.10	$20.84^{+4.12}_{-3.32}$	< 9.88	< 16.1	406.7/459
NGC 4559 X7	2.80 ± 0.20	$2.45^{+1.05}_{-0.73}$	< 8.26	< 60.4	286.6/258
Combined	2.37 ± 0.03	$1.59^{+0.10}_{-0.09}$	< 2.77	< 14.2	584.2/596

Table 4.5: Comparison of the upper limits on the equivalent width (EW) of the iron line derived from spectral fits across different energy ranges: Range 1 (5.5–7.5 keV), Range 2 (5.0–8.0 keV), and Range 3 (4.0–9.0 keV).

Source	Range 1 (eV)	Range 2 (eV)	Range 3 (eV)
M51 ULX7	< 19.8	< 34.1	< 25.9
NGC 300 ULX1	< 30.4	< 40.1	< 59.1
NGC 1313 X2	< 47.3	< 49.2	< 44.7
NGC 5907 ULX1	< 47.7	< 44.5	< 52.7
NGC 7793 P13	< 20.5	< 30.0	< 42.3
Circ ULX5	< 27.9	< 32.8	< 38.9
Ho II X1	< 42.0	< 41.3	< 40.2
Ho IX X1	< 24.1	< 21.8	< 26.2
NGC 1313 X1	< 15.4	< 18.5	< 26.2
M33 X8	< 15.4	< 16.1	< 16.4
NGC 4559 X7	< 60.0	< 60.4	< 61.6
Combined	< 11.1	< 14.2	< 20.0

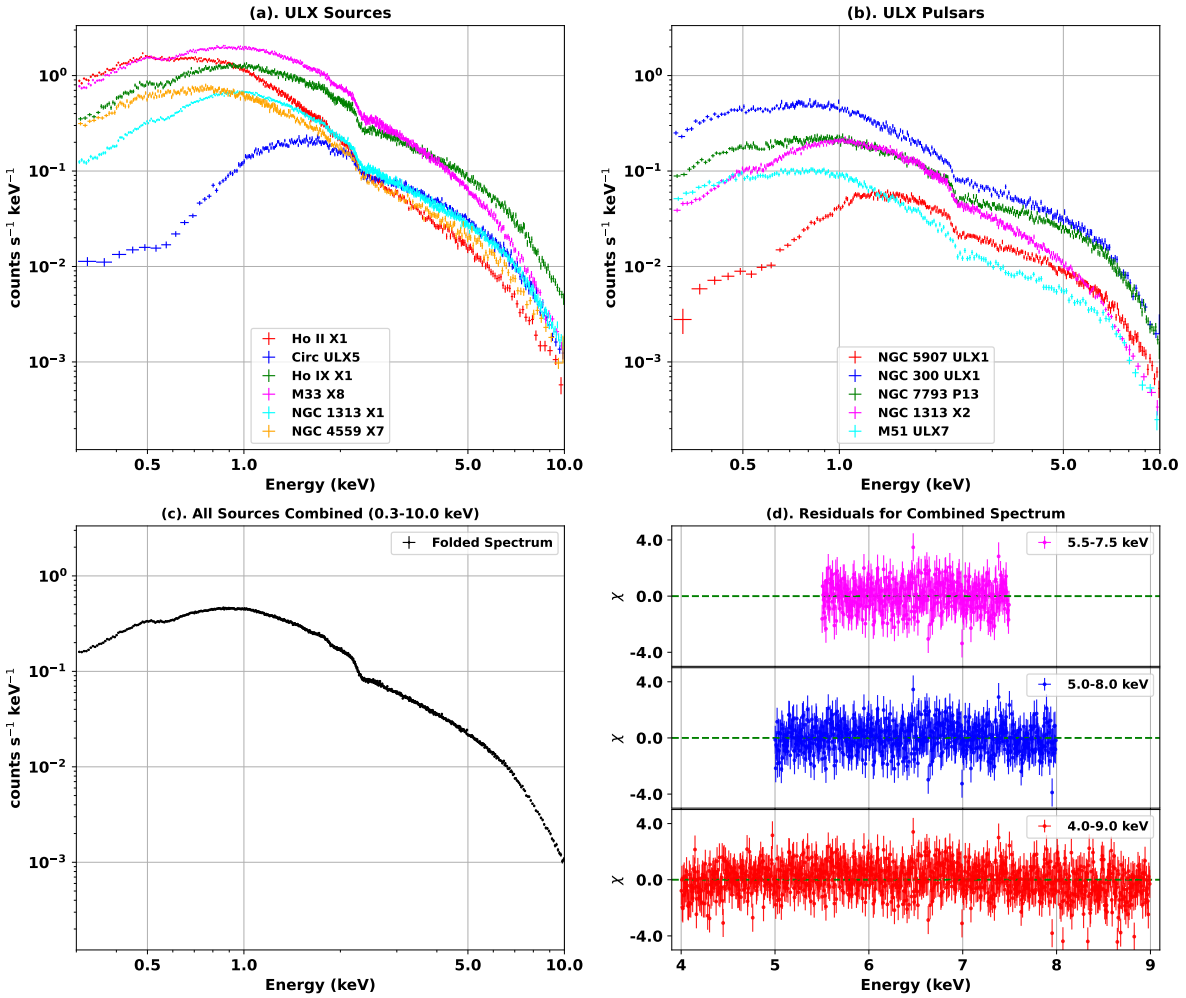


Figure 4.1: Top panel presents the combined spectra from *XMM-Newton* observations of individual ULX (left) and ULXP (right) sources. The bottom panel (on the left) presents the combined spectra from all observations of 6 ULXs and 5 ULXPs analyzed in this work. On the right, residuals from the best-fit absorbed powerlaw model are shown for the combined spectra in the energy range of 5.5–7.5 keV, 5–8 keV, and 4–9 keV.

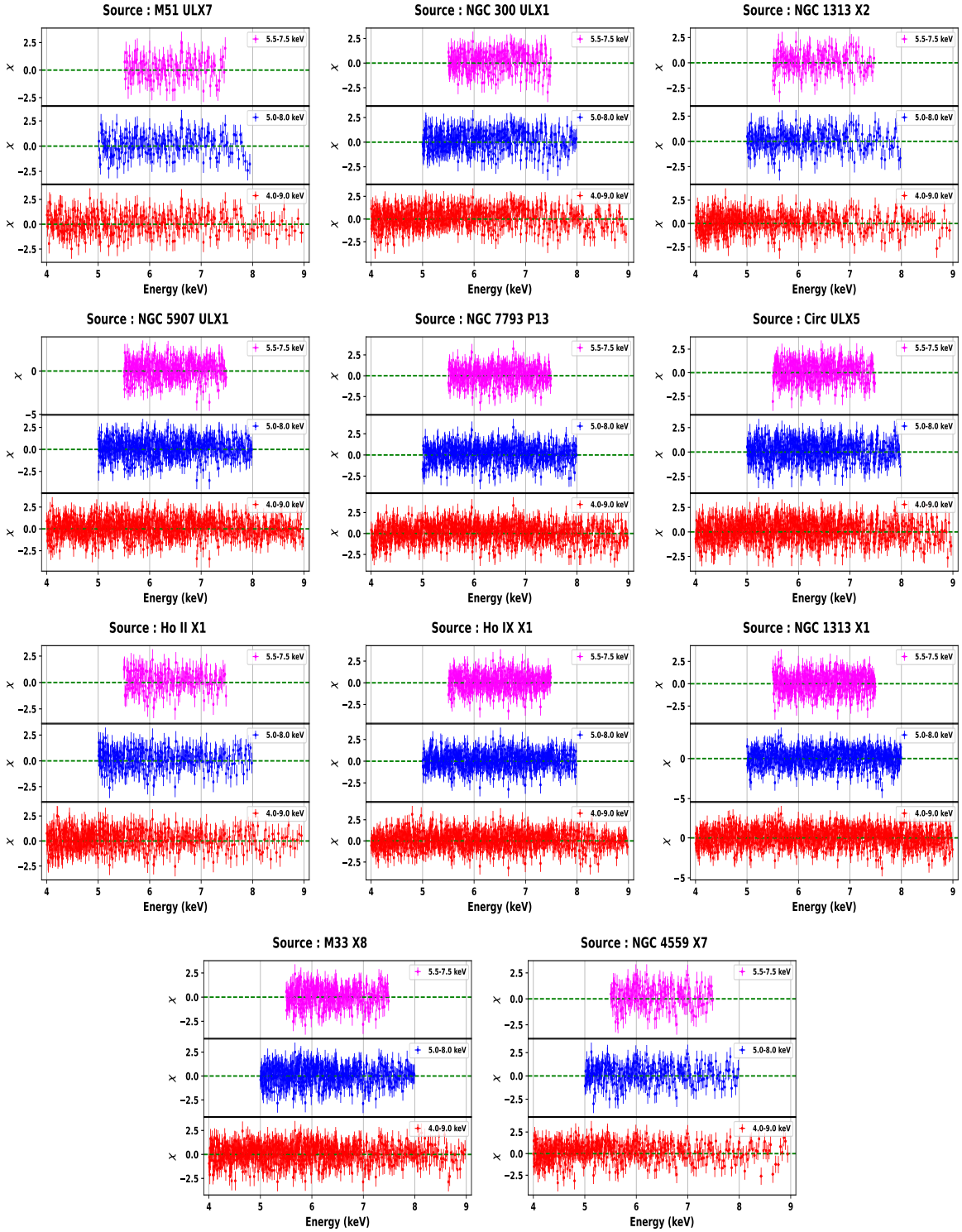


Figure 4.2: Residuals from the best-fit absorbed powerlaw model for the combined spectra of individual sources, shown over three energy ranges: 5.5–7.5 keV, 5–8 keV, and 4–9 keV.

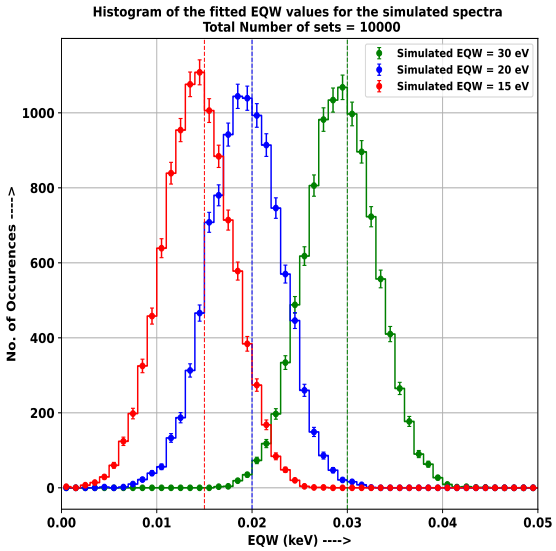


Figure 4.3: Histogram for the EW recovered from fits to the combined simulated spectra of all sources. Different colors represent simulations in which artificial iron lines with EW values of 15 eV, 20 eV, and 30 eV were inserted into the individual source spectra before combining.

7.0 keV for CG X-1, 0.3–1.0 keV and 1.0–4.0 keV for M51 ULX1, and 0.3–1.4 keV and 1.4–4.0 keV for M51 ULX2. The eclipse profiles and respective hardness ratios are shown in Fig. 4.4. For M51 S1, M51 S2, M51 ULX1, and M51 ULX2, only a single eclipse/partial eclipse cycle is covered in the observation, so the hardness ratio is plotted as a function of time. In contrast, for CG X-1, the observation spans approximately six orbital cycles (Qiu et al. 2019). To examine the hardness ratio around the eclipse transitions, the light curve was folded using the HEASARC tool `efold` with the best orbital period $\mathrm{P} = 26175\,\mathrm{sec}$, determined using the epoch-folding method with `efsearch`. The resulting folded light curve and hardness ratio with orbital phase is also shown in Fig. 4.4.

To compare the hardness ratio pattern with known Galactic eclipsing HMXBs, we also plotted the hardness ratio for LMC X–4 and SMC X–1 using the *XMM-Newton* observations, with Obs-Ids 0142800101 and 011450101, respectively (see Fig. 4.4). For LMC X–4, the energy ranges 0.3–1.5 keV and 1.5–10.0 keV were selected as soft and hard energy bands, respectively, while for SMC X–1, 0.3–2.0 keV and 2.0–10.0 keV were selected as soft and hard energy bands, respectively.

As shown in Fig. 4.4, both LMC X–4 and SMC X–1 exhibit a pronounced increase in hardness ratio during eclipse ingress and egress, consistent with the expected additional absorption as the compact object moves behind the stellar companion. In contrast, no significant changes in hardness ratio are observed for the ULX sources during eclipse transitions.

4.4.3 Flux Ratio during Eclipse to Out-of-Eclipse Phase

During X-ray eclipses, most X-ray binaries exhibit residual X-ray emission, which is generally attributed to reprocessed emission from the stellar wind (Aftab et al. 2019, Aftab & Paul 2024, Rikame et al. 2024). The ratio of OOE to eclipse flux shows a wide range in Galactic binaries, typically between $\sim 8 - 237$ for HMXBs, and $\sim 6 - 54$ for LMXBs. It is therefore of particular interest to examine this flux ratio for the ULXs, where mass accretion rates are expected to be much higher and the accretion geometry potentially more complex.

For calculating the flux, the spectra are fitted using the `xspec` model `tbabs*(diskbb)` for M51 S1 and S2, and `tbabs*(powerlaw)` for CG X-1, M51 ULX1, and M51 ULX2. The results are summarized

Table 4.6: Best-fit spectral parameters for selected eclipsing ULX sources, comparing Eclipse and OOE spectra. For CG X1, M51 ULX1 and M51 ULX2, the spectra were fitted with the `tbabs*(powerlaw)` model, whereas for M51 S1 and M51 S2, the `tbabs*(diskbb)` model was used.

			tbabs	powerlaw		diskbb			Flux *	Flux Ratio
Source	Obs Id	Phase	$N_{\rm H}$ (10^{22} cm^{-2})	Γ	norm$_{\rm po}$ (10^{-5})	kT (keV)	norm$_{\rm diskbb}$	χ^2/dof	(10^{-14} erg cm^{-2} s^{-1})	(OOE/Eclipse)
CG X1	12823	OOE	1.54 ± 0.10	$1.68^{+0.08}_{-0.07}$	51 ± 5	-	-	228.6/197	182.8 ± 5.1	$23.4^{+3.4}_{-3.7}$
		Eclipse	$0.97^{+0.29}_{-0.25}$	$2.06^{+0.58}_{-0.34}$	3^{+2}_{-1}	-	-	30.4/33	$7.8^{+1.2}_{-1.1}$	
M51 S1	0824450901	OOE	$0.19^{+0.06}_{-0.05}$	-	-	0.13 ± 0.01	191^{+270}_{-103}	32.2/20	9.0 ± 0.5	4.5 ± 0.5
		Eclipse	< 0.17	-	-	0.19 ± 0.04	< 8.5	35.9/23	2.0 ± 0.2	
	0852030101	OOE	0.09 ± 0.03	-	-	0.16 ± 0.01	36^{+28}_{-15}	65.5/36	10.4 ± 0.5	5.2 ± 0.8
		Eclipse	< 0.20	-	-	0.19 ± 0.05	< 15.4	16.1/23	2.0 ± 0.3	
M51 S2	0830191501	OOE	< 0.06	-	-	0.32 ± 0.05	$0.38^{+0.53}_{-0.16}$	27.2/19	6.1 ± 0.6	4.4 ± 0.8
		Eclipse	$0.25^{+0.21}_{-0.14}$	-	-	0.14 ± 0.04	< 409	18.1/21	1.4 ± 0.2	
	0830191601	OOE	< 0.03	-	-	0.37 ± 0.04	$0.18^{+0.14}_{-0.06}$	31.6/31	5.4 ± 0.4	$3.9^{+0.6}_{-0.9}$
		Eclipse	< 0.28	-	-	0.18 ± 0.06	< 36.5	20.8/13	$1.4^{+0.3}_{-0.2}$	
	0852030101	OOE	< 0.04	-	-	0.33 ± 0.04	$0.36^{+0.35}_{-0.13}$	32.8/34	$6.4^{+0.4}_{-0.5}$	$3.0^{+0.3}_{-0.4}$
		Eclipse	$0.11^{+0.11}_{-0.08}$	-	-	$0.17^{+0.04}_{-0.03}$	< 32.6	30.4/23	2.1 ± 0.2	
M51 ULX1	13813	OOE	0.36 ± 0.05	$3.81^{+0.21}_{-0.19}$	$6.5^{+0.9}_{-0.7}$	-	-	105.4/106	5.6 ± 0.2	32.9 ± 19.4
		Eclipse	0.36 [a]	3.81 [a]	0.20 ± 0.11	-	-	2.65/5	0.17 ± 0.10	
M51 ULX2	13813	OOE	$0.33^{+0.08}_{-0.07}$	$2.22^{+0.19}_{-0.18}$	$3.1^{+0.5}_{-0.4}$	-	-	81.7/76	2.3 ± 0.1	17.7 ± 9.6
		Eclipse	0.33 [a]	2.22 [a]	0.18 ± 0.10	-	-	2.29/5	0.13 ± 0.07	

* : Flux is calculated for the energy range 0.3-8.0 keV for CG X1, 0.3-2.0 keV for M51 S1/S2 and 0.3-1.4 keV for M51 ULX1/ULX2 .
[a] : parameters are frozen to corresponding values during the fit.

in Table 4.6, and the corresponding spectrum with residuals is shown in Fig. 4.5. The flux is calculated in the energy range 0.3–2.0 keV for M51 S1/S2 and 0.3–8.0 keV for CG X-1. For M51 ULX1 and ULX2, insufficient statistics during eclipse prevented a reliable spectral fit. In these cases, we estimated the eclipse flux by first fitting the OOE spectrum and then refitting the eclipse spectrum with all spectral parameters fixed except for the normalization of the powerlaw component. Since no significant counts were detected above 1.4 keV during eclipse, fluxes were computed in the 0.3–1.4 keV energy range.

As indicated in Table 4.6, the flux drops approximately 3–5 times while transitioning from OOE to eclipse phase for M51 S1/S2 and ∼23 times for CG X-1. For M51 ULX1 and M51 ULX2, the OOE-to-eclipse flux ratios are estimated to be in the ranges ∼13.5–52.3 and ∼8.1–27.3, respectively, although these values are limited by the available statistics. When compared to most Galactic HMXBs, where flux ratios typically span ∼8–237 (Aftab et al. 2019), the ULXs generally exhibit equal or lower OOE-to-eclipse flux ratios. This suggests that the reprocessing efficiency (eclipse to OOE flux ratio) is larger for the ULX sources as compared to the Galactic HMXBs.

4.5 Discussion

X-ray absorption/reprocessing is a well-known and well-studied phenomenon in X-ray binaries. There are many characteristics of the X-ray emission from which we can know about the reprocessed emission of X-ray binary: emission/absorption lines in X-ray spectra, the spectral and timing properties during the eclipse or ingress/egress phases for eclipsing X-ray binaries, etc. One important outcome of X-ray reprocessing is studying the Fe $K\alpha$ line, which is fluorescent emission from the material in the environment of the compact object when illuminated with the X-rays from the compact star. Both HMXBs and LMXBs clearly show the iron line emission having EW varying from a few eV to keV (Torrejón et al. 2010, Ng, C. et al. 2010, Pradhan et al. 2018, Giménez-García et al. 2015). Another manifestation of the reprocessing is an increase in the hardness ratio for eclipsing X-ray binaries during the ingress and egress in Galactic eclipsing X-ray binaries (Ioannou et al. 2002, Raman et al. 2018, Balu et al. 2024, Tamang et al. 2025), attributed to the absorption of softer photons by the dense stellar wind near the surface of the companion star. Furthermore, during the eclipse phase, most of the observed X-ray

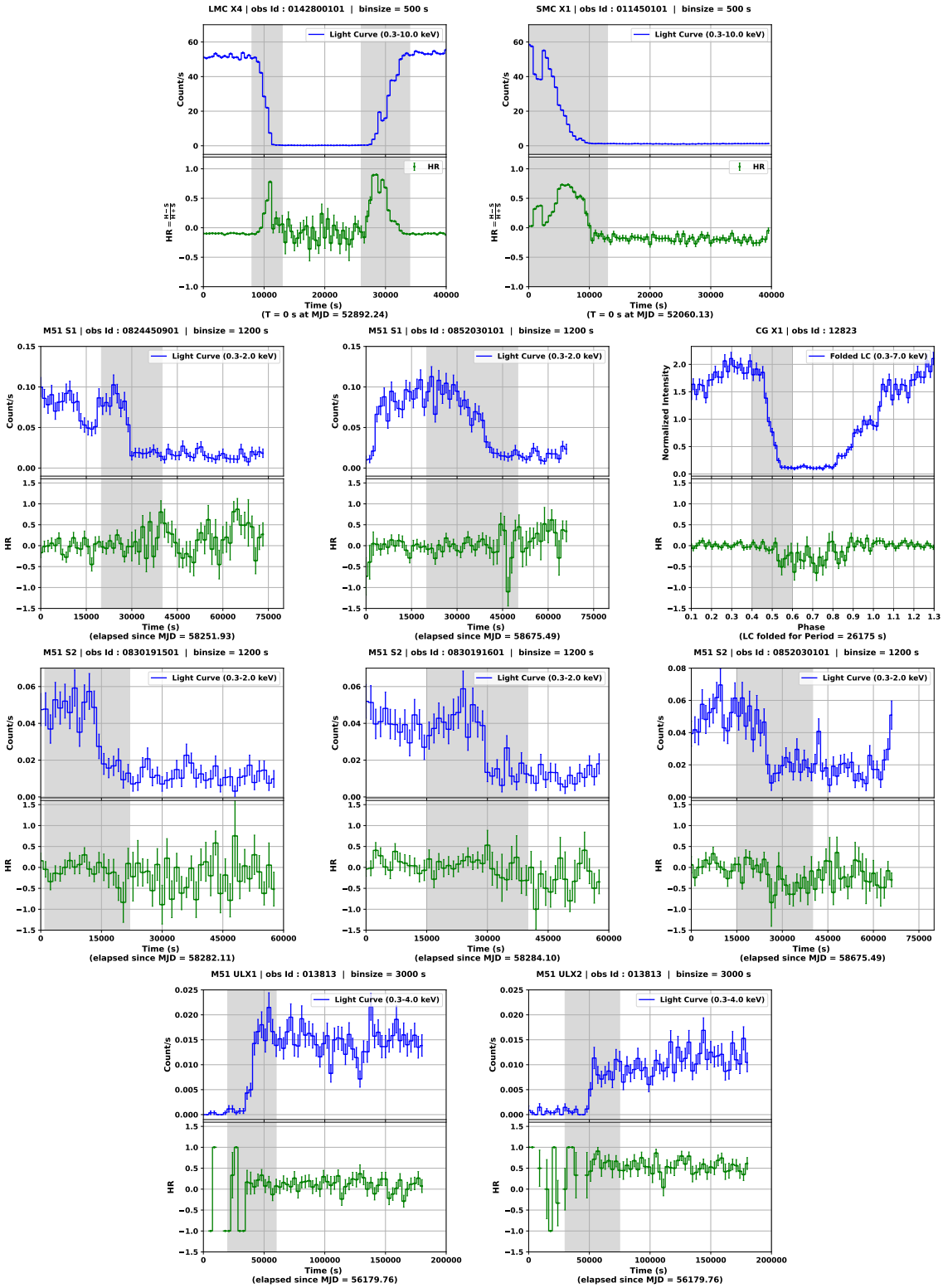


Figure 4.4: Light curves and hardness ratios around the eclipse transitions. The top row shows results for the well-known HMXBs (LMC X–4 and SMC X–1), while the subsequent rows present the eclipsing ULX sources.

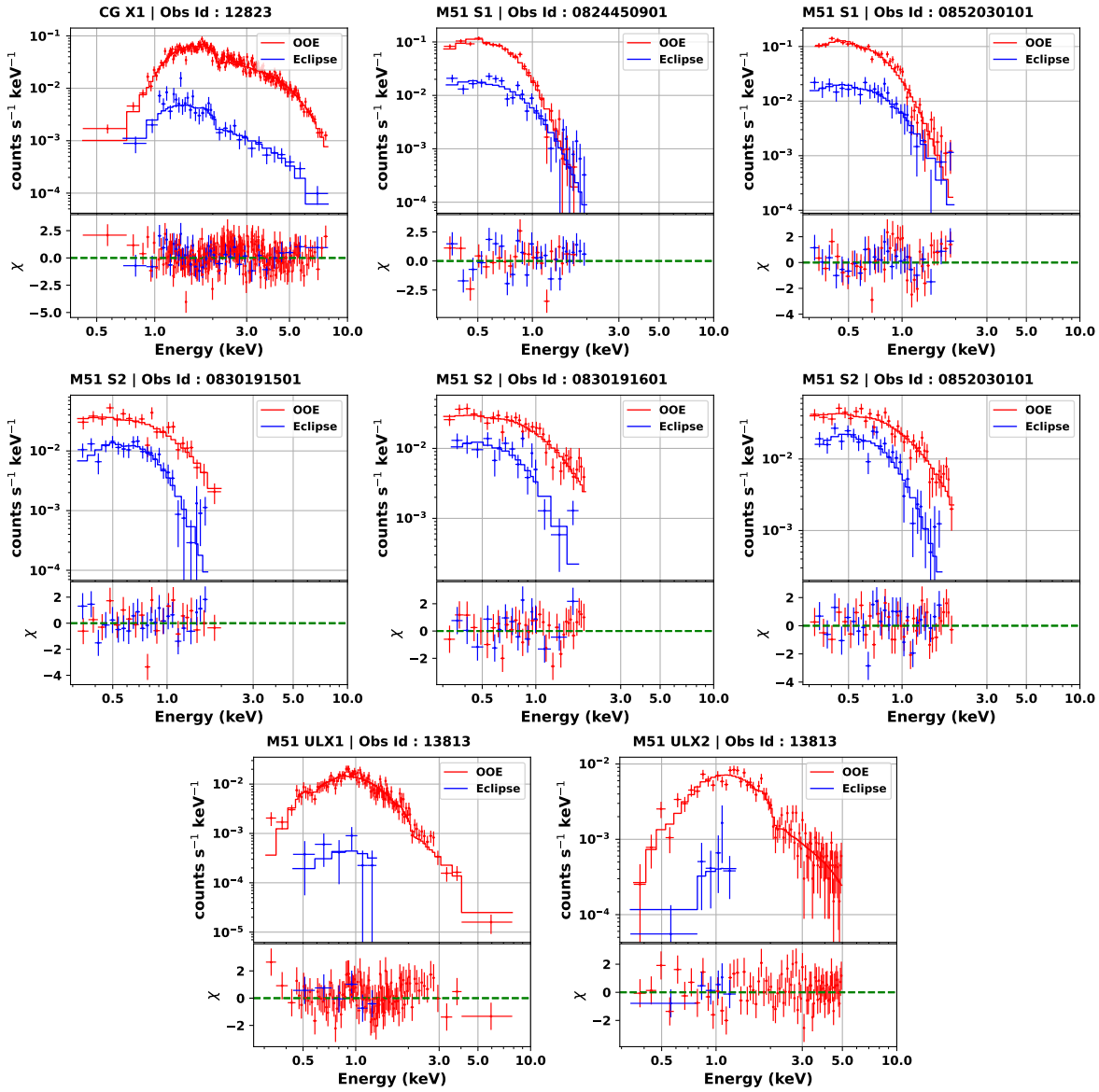


Figure 4.5: Spectrum during eclipse and OOE phase for the CG X1 (Chandra), M51 S1 (*XMM-Newton*), M51 S2 (*XMM-Newton*), M51 ULX1 (Chandra) and M51 ULX2 (Chandra). Bottom panels shows the best-fit residuals.

emission is secondary emission reprocessed by a larger region compared to the size of the compact object.

Nominally, one would expect similar reprocessing phenomena in the ULXs because they are also compact objects powered by accretion from a binary companion star (Castillo et al. 2020, Belfiore et al. 2024, Qiu & Feng 2021). However, signatures of X-ray reprocessing in ULXs have been meagre, except for the cases of absorption lines in the winds (Kosec et al. 2017, Pinto et al. 2016, Walton et al. 2016). So far, only two ULX sources, M82 X1 and NGC 7456 ULX1, have shown tentative detections of iron emission lines. In M82 X-1, a weak and broadened iron line with an EW of 59^{+25}_{-27} eV has been reported (Caballero-García 2011). A possible detection of an iron emission line has also been reported in NGC 7456 ULX1, with an EW of 2000^{+1500}_{-1100} eV (Mondal et al. 2021), which is significantly higher than that observed in M82 X-1. Additionally, only during the 2010 epoch, an iron emission line with an EW of 343 ± 93 eV was reported from the ULXP NGC 300 ULX1 (Carpano et al. 2018); however, no pulsations were detected during that observation. Overall, iron emission lines remain largely absent in most ULX sources.

To look more into the reprocessed emission from ULXs, we have carried out the following three types of investigations: (i) search for Iron $K\alpha$ emission line feature, (ii) hardness ratio evolution during ingress and egress, and (iii) flux ratio between OOE and eclipse phases. We have investigated a large volume of data carefully selected from all existing XMM-Newton and Chandra databases. For studying the iron $K\alpha$ emission line, we selected all *XMM-Newton* observations of six bright, well-known ULXs and five ULXPs. For studying the hardness ratio during ingress/egress of eclipse and flux ratio during OOE to eclipse phase, we have selected all known eclipsing ULXs: CG X-1, M51 S1, M51 S2, M51 ULX1, and M51 ULX2. Since M51 S1 and M51 S2 are well resolved with *XMM-Newton* instrument, we used *XMM-Newton* observations for these two sources, while Chandra data were utilized for the sources CG X-1, M51 ULX1, and M51 ULX2.

In our analysis, we did not detect any significant iron Kα line feature. For the individual sources, the 90% confidence upper limit on the EW lies in the range of 15–60 eV, whereas for the combined spectra we obtained a much tighter constraint of 11–20 eV, which is a significant improvement from the previous studies, by a factor of a few. For instance, Walton et al. (2012) obtained the upper limit on the iron $K\alpha$ line of $\sim$30 eV for Ho IX X1 and $\sim$50 eV for NGC 1313 X1. In comparison, Galactic X-ray binaries almost ubiquitously show the iron Kα emission in a majority of the sources, with EW varying between a few eV to keV depending on the system type. In classical SG HMXBs, the EW can vary from a few eV to keV, while in SFXTs, it is typically observed up to the order of 100 eV (Giménez-García et al. 2015, Pradhan et al. 2018). In LMXBs, the EW typically ranges between 17–189 eV (Ng, C. et al. 2010).

Next, we constructed a curve of growth for the ULX sources by utilizing the EW values from the Table 4.4 and column density values from the previous literature as mentioned in Table 4.2 (Mondal et al. 2021, Pintore et al. 2014, Walton et al. 2020, West et al. 2018, Pintore et al. 2021, Kumar et al. 2025). For comparison, we also included measurements from classical SG HMXBs, SFXTs (Pradhan et al. 2018), LMXBs (Ng, C. et al. 2010), accreting disk-fed X-ray pulsars (Paul et al. 2002, Naik & Paul 2003, Sharma et al. 2023a), the Galactic stellar-mass black hole binary XTE J1650–500 (Walton et al. 2012), and the two ULXs with previously reported iron lines, M82 X-1 (Caballero-García 2011) and NGC 7456 ULX1 (Mondal et al. 2021). The resulting plot (Fig. 4.6) clearly demonstrates that ULXs occupy the low $N_{\rm H}$ regime compared to Galactic binaries. This is somewhat counterintuitive that despite their extreme luminosities and expected presence of dense reprocessing material, ULXs consistently exhibit relatively low absorbing column densities.

We also estimated the expected absorption in the ULX binary environment assuming a spherical symmetric radiation-driven wind from the companion star, following the model given by Castor et al.

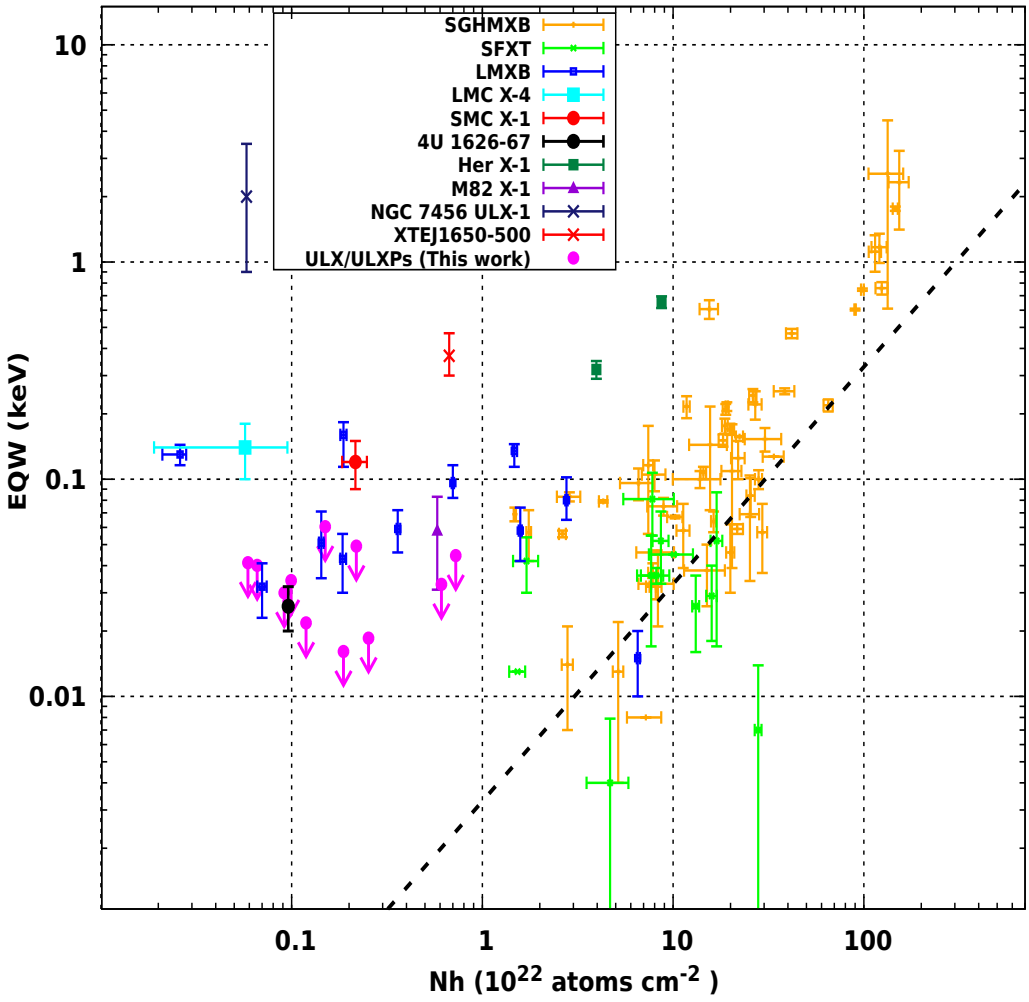


Figure 4.6: Comparative studies of hydrogen column density (N_H: number of hydrogen atoms cm^{-2} along the line of sight) and equivalent width (EW) of iron Kα line for SgHMXBs, SFXTs (Pradhan et al. 2018), LMXBs (Ng, C. et al. 2010), LMC X-4, SMC X-1 (Paul et al. 2002), Her X-1 (Naik & Paul 2003), 4U 1626-67 (Sharma et al. 2023a), M82 X-1 (Caballero-García 2011), NGC 7456 ULX1 (Mondal et al. 2021), XTE J1650-500 (Walton et al. 2012) and ULXPs. The column density values are taken from previous studies mentioned in Table 4.2. The black dashed line corresponds to the expected EW value for a given column density ($\mathrm{EW} = 0.00329\,\mathrm{N_H^{22}\,keV}$) assuming the spherical reprocessing geometry around the X–ray source (Torrejón et al. 2010).

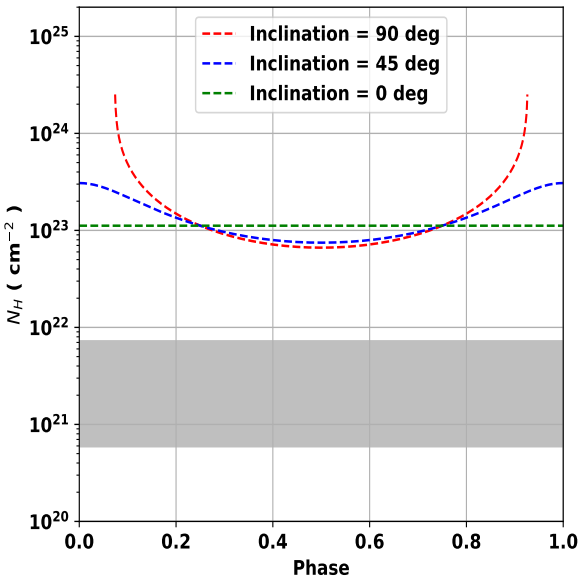


Figure 4.7: Expected column density calculations assuming the accretion through a spherically symmetric wind around the companion. The horizontal gray region denotes the range for measured column densities reported in previous studies (Table 4.2) for ULXPs/ULX sources.

(1975). For this, we adopted binary parameters from previous studies, in a manner similar to Balu et al. (2024) and Tamang et al. (2025) for Galactic HMXBs. The wind velocity profile is given by:

$$v(r) = v_\infty \left(1 - \frac{R_*}{r}\right)^\beta \tag{4.1}$$

where v_∞ is the terminal wind velocity, R_* is the companion star radius, β velocity gradient parameter fixed to a value 0.8 (Friend & Abbott 1986). Assuming the donor star is losing the mass isotropically with a mass loss rate $\dot{M}$, the radial mass density profile of the wind is given by:

$$\rho(r) = \frac{\dot{M}}{4\pi r^2 v(r)} = \frac{\dot{M}}{4\pi r^2 v_\infty} \frac{1}{\left(1 - \frac{R_*}{r}\right)^\beta} \tag{4.2}$$

The hydrogen mass density is $\rho_H(r) = x_H\, \rho(r)$, x_H is the hydrogen mass fraction (adopted as $x_H \approx 0.7$ from (Wilms et al. 2000)). The equivalent hydrogen column density is calculated by integrating the above equation along the line of sight.

$$N_H(\phi') = \kappa \int_{x_{\phi'}}^{\infty} \rho_H(r(x', y_{\phi'}, z_{\phi'}))\, dx' \tag{4.3}$$

where ϕ' is the orbital phase, κ is the conversion factor for mass density to particle density, r is the radial distance from the donor star center, and x' is the line-of-sight coordinate. We adopted the binary parameter values for the ULXP M82 X-2 reported by Bachetti et al. (2022). Assuming a circular binary orbit of radius $R_{\rm orbit} = 18.0 R_\odot$ with the terminal velocity $v_\infty = 1500$ km/s, the companion star radius $R_* = 8.0 R_\odot$, and the mass loos rate from the companion star is $\dot{M} = 4.7\,\mathrm{x}\,10^{-6}\,\mathrm{M_\odot yr^{-1}}$, we calculated the expected column density for viewing the binary at three different angles: edge-on (inclination angle; i = 90^o), face-on (i = 0^o), and an intermediate angle i = 45^o. These results are shown in the Fig. 4.7, where the observed column density ($\mathrm{N_H}$) values for the ULX sources are shaded in gray color. The measured column densities for ULX sources are systematically lower than the values

predicted from wind accretion onto the compact object.

Also, we do not observe any significant change in the hardness ratio during eclipse ingress or egress in ULXs (Fig. 4.4), whereas eclipsing Galactic X-ray binaries exhibit a clear increase in hardness ratio near these phases. Additionally, the flux drops by approximately 3–5 times while transitioning from OOE to eclipse phase for M51 S1/S2 and ∼23 times for CG X-1. The flux ratio (OOE to eclipse phase) is obtained in ranges ∼13.5–52.3 and ∼8.1–27.3 for M51 ULX1 and M51 ULX2, respectively, given the limited statistics. In contrast, the eclipse to OOE flux ratio is larger for the ULX sources as compared to Galactic X-ray binaries (Aftab et al. 2019, Aftab & Paul 2024). Also, it is intriguing that for M51 S1, the OOE and eclipse spectra almost overlap above 1.3 keV (Fig 4.5).

Unlike HMXBs, which show a wide range of $N_{\rm H}$ values and prominent iron emission lines with varying equivalent widths, ULXs typically exhibit lower $N_{\rm H}$ and a lack of detectable iron emission lines. Furthermore, ULXs do not display any significant increase in hardness ratio during eclipses that is commonly observed in HMXBs, which commonly exhibit absorption effects due to the dense stellar winds of the companion during egress and ingress phases. The higher eclipse to OOE flux ratio in ULXs suggests the presence of strong scattering. Considering this, the absence of detectable iron emission lines and the lack of increased hardness during eclipse could be indicative of lower metallicity in the winds of ULX companion stars or a very high level of ionisation of the metallic composition of the stellar wind.

Population studies show that metal-poor galaxies with $\rm Z < 0.2Z_{\odot}$ host a significantly larger number of ULXs compared to metal-rich systems of similar star-formation rate (Mapelli et al. 2010), suggesting that the environments surrounding most ULXs are metal-poor (Pakull & Mirioni 2002, Mapelli et al. 2009, Lara-López et al. 2021). For example, Lara-López et al. (2021) found that ULX-1 in NGC 925 lies in a region of very low gas metallicity, while Soria et al. (2005) suggested that the ultra luminous source NGC 4559 X7 also resides in a metal-poor environment. These results reinforce the general trend that ULXs are preferentially associated with low-metallicity surroundings. However, in the same galaxy NGC 925, ULX-3 is located in a region of comparatively higher metallicity (Lara-López et al. 2021). In addition to metallicity, there is strong evidence for a highly ionized medium around many ULXs, inferred from characteristic emission and absorption lines detected both in X-rays (Kosec et al. 2021) and in the optical (Pakull & Mirioni 2002, Zampieri et al. 2004, Lara-López et al. 2021). Taken together, these findings suggest that the surroundings of most ULXs are either metal-poor or dominated by highly ionized gas.

5

Flaring Study in the ULX sources NGC 4559 X7 and NGC 7456 ULX1

5.1 Introduction

Ultra-luminous X-ray sources (ULXs) are a distinct class of extragalactic, off-nuclear X-ray sources whose luminosities exceed the Eddington limit expected for accretion onto stellar-mass compact objects such as black holes or neutron stars. Their extreme brightness, often reaching a few times to over a hundred times the Eddington luminosity, immediately challenged our understanding of accretion-powered systems. Early interpretations suggested that such emission could arise from intermediate-mass black holes (IMBHs) accreting steadily at sub-Eddington rates. However, ULXs are most often found in young, star-forming regions, where stellar-mass compact objects are common and naturally form high mass X-ray binaries (HMXBs) (King 2004). Over the past decade, the discovery of coherent pulsations from several ULXs (Bachetti et al. 2014, Israel et al. 2017b,a, Carpano et al. 2018, Castillo et al. 2020, Sathyaprakash et al. 2019) has demonstrated that some of these sources are powered by neutron stars, supporting the view that super-Eddington accretion, aided by geometric collimation and strong outflows (King et al. 2023), can account for their extraordinary luminosities. Thus, ULXs represent a diverse class of accreting systems, with most understood as stellar-mass compact objects accreting in the super-Eddington regime.

Flaring type and rapid variability are well-known characteristics of Galactic X-ray binaries, where changes in the accretion rate, thermal–viscous instabilities in the disk, or magnetospheric interactions can produce large flux variations over a wide range of timescales. In such systems, the relative strengths of the thermal disk emission and the non-thermal Comptonized component often trace changes in the inner accretion flow and geometry (e.g. van der Klis 1994, 1997, Done et al. 2007). Examples of this behaviour are seen across several well-studied Galactic sources: LMC X-4 and SMC X-1 show super-orbital modulation and episodes of rapid flaring linked to disk precession or variable accretion flow (Moon et al. 2003, Neilsen et al. 2004, Beri & Paul 2017), while supergiant fast X-ray transients (SFXTs) exhibit extreme, short-timescale flares arising from clumpy stellar winds (Sidoli et al. 2008, Bozzo et al. 2015). Together, these systems illustrate the diverse variability patterns that can emerge from fluctuations in accretion rate and the complex structure of the inflowing material.

In contrast, strong variability in ULXs is considerably less common. Most ULXs remain relatively stable over long timescales, and only a minority exhibit pronounced temporal variability or recurrent flaring episodes (Heil et al. 2009, Sutton et al. 2013, Middleton et al. 2015, Atapin et al. 2019). The ULXs studied in detail so far, including NGC 4559 X7 (Pintore et al. 2021, Pintore et al. 2025), NGC 7456 ULX-1 (Pintore et al. 2020), NGC 253 ULX-1 (Barnard 2010), NGC 6946 ULX-3 (Earnshaw et al. 2019), NGC 247 ULX-1 (Pinto et al. 2021), and NGC 4395 ULX-1 (Ghosh et al. 2022), demonstrate that when variability does occur, it can be substantial and energetically significant. Even more complex behaviour,

including heartbeat-like variability that resembles limit-cycle patterns, has also been reported in a few ULXs, such as 4XMM J111816.0–324910 in NGC 3621 and M51 ULX7 (Motta et al. 2020, Imbrogno et al. 2024). These diverse behaviours indicate that ULX variability is neither uniform nor governed by a single mechanism. Investigating how their thermal (disk-like) and non-thermal (power-law) components evolve during flux changes therefore provides crucial insight into how super-Eddington accretion responds to fluctuations in mass inflow, whether disks undergo structural instabilities, and how winds or funnel geometries shape the emergent emission. Current evidence suggests that ULXs do not follow a universal variability pattern but instead occupy a range of accretion regimes, motivating detailed, source-specific studies of the systems that exhibit strong variability.

In this work, we focus on two such sources: NGC 4559 X7 and NGC 7456 ULX1, both of which exhibit marked X-ray variability. Our goal is to examine how the variability in different sources depends on photon energy and to determine which spectral components dominate at different flux levels. Using time-resolved analysis together with state-resolved spectroscopy, we identify the variability patterns exhibited by both sources and investigate their spectral characteristics across different luminosity states.

5.2 Observation & Source Selection

Table 5.1: List of ULX sources initially examined before selecting NGC 4559 X7 and NGC 7456 ULX1 for detailed analysis. References correspond to previous studies of each source, from which the source coordinates were adopted.

Source Name	Obs Id	MJD	Total GTE (ks)	$F_{\rm var}$ (%)	References
Circ ULX5	0932990101	60342.30	88.83	7.94 ± 0.83	Mondal et al. (2021)
NGC 4395 ULX1	0824610401	58485.24	73.36	26.88 ± 0.59	Ghosh et al. (2022)
Holmberg II X1	0561580401	55281.41	21.63	20.23 ± 0.66	Heil et al. (2009)
Holmberg II X1	0864551101	59304.99	10.02	22.11 ± 0.83	
NGC 1313 X1	0782310101	57669.90	73.99	10.42 ± 0.38	Heil et al. (2009)
NGC 1313 X1	0803990101	57918.89	106.81	27.65 ± 0.26	Kara et al. (2019)
NGC 1313 X2	0782310101	57669.90	73.97	27.41 ± 0.52	Heil et al. (2009)
NGC 1313 X2	0803990201	57924.91	109.23	28.41 ± 0.55	Heil et al. (2009)
NGC 55 ULX	028740101	52228.05	19.85	19.11 ± 0.93	Stobbart et al. (2004)
NGC 55 ULX	0864810101	58993.92	97.35	16.22 ± 0.38	
NGC 4559 X7	**0842340201**	**58650.80**	**56.42**	**23.27 ± 0.41**	Pintore et al. (2021)
NGC 4559 X7	**0883960201**	**59743.86**	**75.85**	**23.23 ± 0.34**	Pintore et al. (2025)
NGC 7456 ULX1	**0901330101**	**60063.00**	**84.67**	**30.82 ± 0.88**	Pintore et al. (2020)
NGC 6946 ULX3	0940870101	60393.11	18.45	43.01 ± 1.04	Earnshaw et al. (2019)

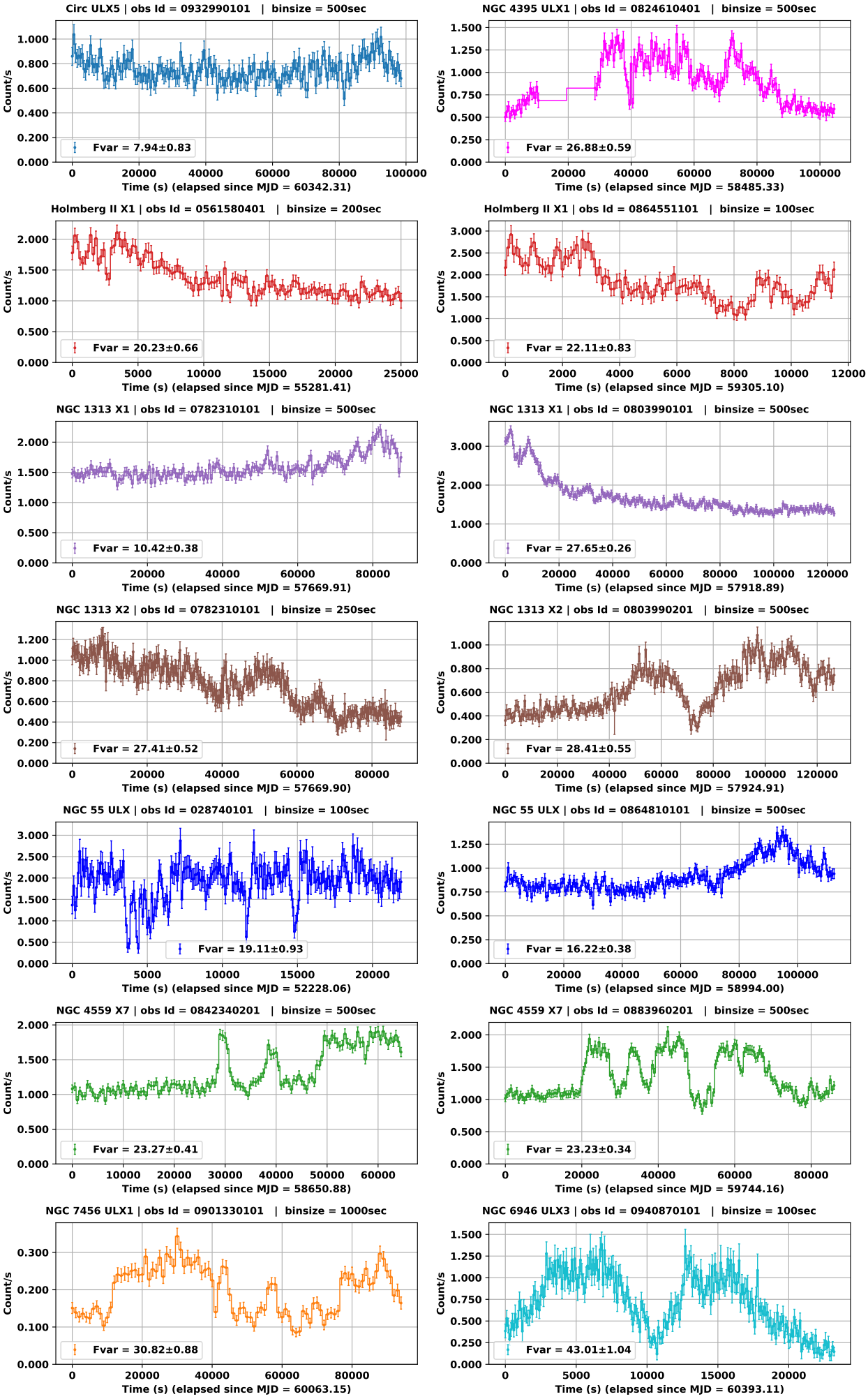


Figure 5.1: Light curves for the observations listed in Table 5.1, shown in the 0.3–10.0 keV energy band. Observations of the same source are plotted using the same color. The fractional variability (%) is indicated in each panel.

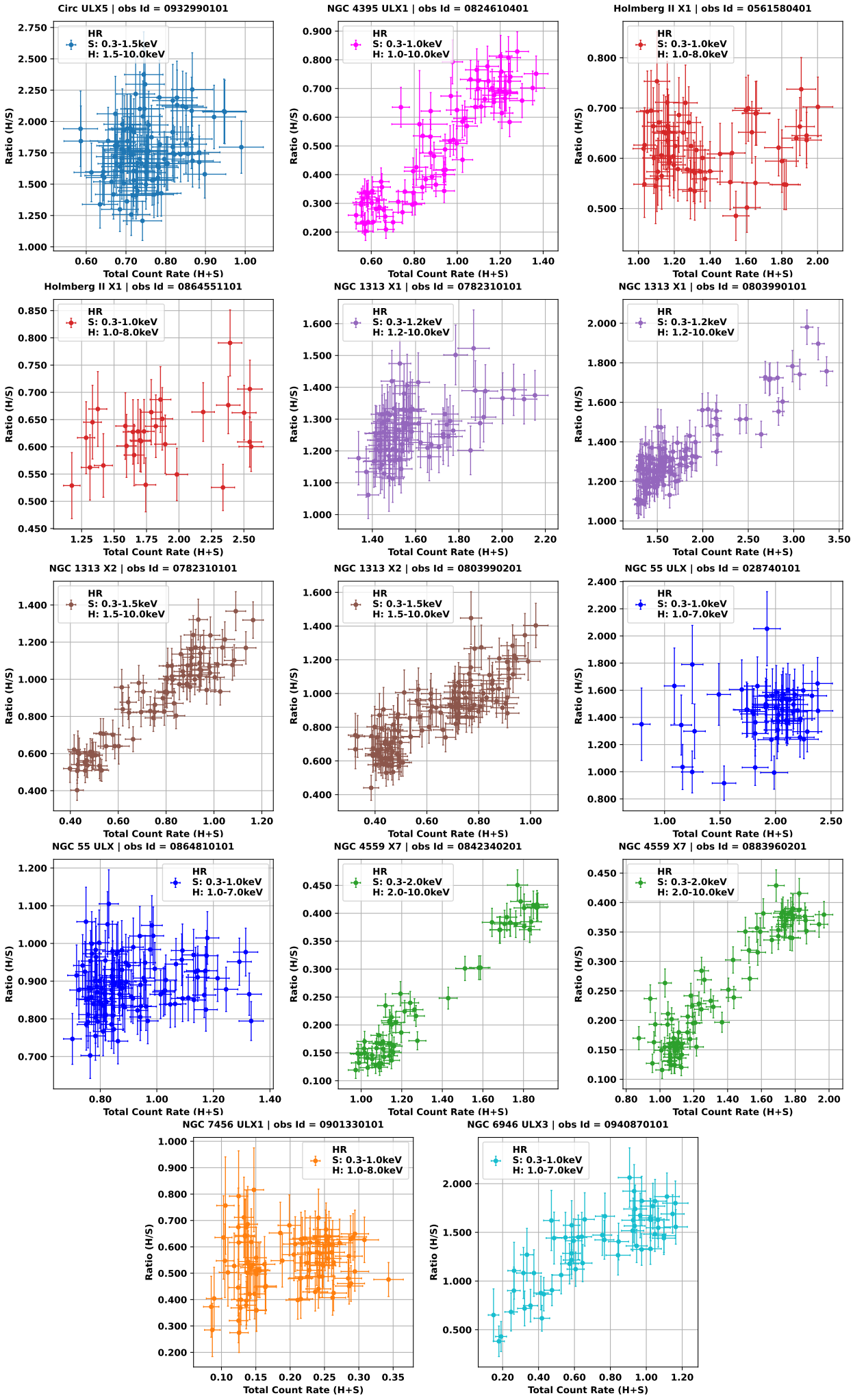


Figure 5.2: The hardness ratio (H/S) as a function of the total count rate. The energy ranges used to define the hard and soft energy bands are indicated in each panel.

We began our study by examining the flaring behaviour present in the *XMM-Newton* observations listed in Table 5.1. Since our goal was to identify ULXs exhibiting significant intrinsic variability, we focused on the known variable ULX candidates in the sample and extracted their background-subtracted light curves (see Fig. 5.1). To quantify the strength of variability, we computed the fractional variability amplitude ($F_{\rm var}$) for each source, with the resulting values summarized in Table 5.1. Fractional variability is derived from the excess variance, which measures intrinsic source variability after removing the contribution from statistical (Poisson) noise (Nandra et al. 1997, Naik et al. 2010, Lobban et al. 2018). The normalized excess variance is given by

$$\sigma^2_{\rm NXS} = \frac{S^2 - \overline{\sigma^2_{\rm err}}}{\bar{x}^2}, \tag{5.1}$$

where S^2 is the total variance of the light curve, $\overline{\sigma^2_{\rm err}}$ is the mean squared measurement error, and $\bar{x}$ is the mean count rate. The fractional variability is then given by

$$F_{\rm var} = \sqrt{\sigma^2_{\rm NXS}}. \tag{5.2}$$

A positive excess variance indicates detectable intrinsic variability, while values consistent with zero imply that the observed fluctuations are dominated by statistical noise. After quantifying the variability strengths, we next examined the spectral behaviour of the sample by studying the hardness ratio evolution of each source as a function of total count rate (see Fig. 5.2). This analysis revealed two broad variability tendencies often noted in accreting systems. In some cases, the hardness ratio increases with increasing intensity, indicating that the contribution of the high-energy emission becomes relatively stronger at higher flux levels. In other cases, the hardness ratio remains approximately constant with intensity, even though significant flux variations are present. These spectral–timing behaviours provide useful constraints on the origin of variability, helping to distinguish whether changes arise from the inner Comptonizing region, the accretion disk, or reprocessing in an outflow.

From this initial sample, we selected two sources NGC 4559 X7 and NGC 7456 ULX1 that are representative of two different spectral–variability behaviours observed among variable ULXs, with the aim of examining how variability manifests under different conditions. NGC 4559 X7 exhibits pronounced flaring predominantly in the hard X-ray band and follows a clear harder-when-brighter trend, with the hardness ratio increasing with intensity. In contrast, NGC 7456 ULX1 shows most of its variability in the soft X-ray band, while its hardness ratio remains approximately constant with intensity. This complementary behaviour makes the pair particularly suitable for investigating how variability mechanisms differ across ULXs. Although NGC 4559 X7 has been extensively studied in previous works (Pintore et al. 2021, Pintore et al. 2025), we reanalysed its archival *XMM-Newton* data to ensure that both sources were treated with a consistent methodology. The following sections present a detailed spectral and timing analysis of NGC 4559 X7 and NGC 7456 ULX1, aimed at identifying the physical components driving their variability.

5.3 Data Reduction

Data reduction was carried out using the *XMM-Newton* Science Analysis System (SAS) version 20.0.0, following the standard SAS processing threads. For each observation, raw event files were produced using the task `epproc`, after which intervals of high background were screened and removed. The cleaned event files were then corrected to the solar system barycenter using `barycen`. Source events were extracted from circular regions centered on the respective source coordinates (see Table 5.2).

Table 5.2: Observation log of the ULX sources used for detailed spectral and timing analysis in this work.

Source Name	Distance	Co-ordinates	Instrument	Obs Id	MJD	Source Region	Total GTE (ks)
NGC 4559 X7[1]	10 Mpc	RA = $12^{h}35^{m}51.71^{s}$	XMM-Newton	0842340201	58650.80	$35''$	56.42
		Dec = $+27°56'4.10''$	XMM-Newton	0883960201	59743.86	$35''$	75.85
NGC 7456 ULX1[2]	15.7 Mpc	RA = $23^{h}02^{m}3.80^{s}$	XMM-Newton	0901330101	60063.00	$35''$	84.66
		Dec = $-39°36'17.0''$					

[1](Pintore et al. (2021), Pintore et al. (2025)), [2](Pintore et al. (2020), Mondal et al. (2021)).

Table 5.3: Best-fit spectral parameters for the ULXs.

			tbabs	diskbb		power-law			R_{in}	L_X [c]
Source	Obs Id	State	N_H (10^{22} cm^{-2})	kT (keV)	norm$_{diskbb}$	Γ	norm$_{po}$ (10^{-4})	χ^2/dof	(10^3 km)	(10^{39} ergs s^{-1})
NGC 4559 X7	0842340201	Low	$0.24^{+0.03}_{-0.02}$	$0.14^{+0.04}_{-0.02}$	$161.2^{+602.8}_{-140.6}$	$2.54^{+0.04}_{-0.04}$	$8.71^{+0.41}_{-0.39}$	148.96/119	$12.7^{+14.9}_{-8.2}$	56.8 ± 0.5
		Middle	0.26[a]	$0.11^{+0.02}_{-0.02}$	$1090.9^{+3045.9}_{-696.3}$	$2.14^{+0.06}_{-0.06}$	$10.82^{+0.53}_{-0.58}$	82.84/89	$33.0^{+31.3}_{-13.2}$	82.0 ± 1.7
		High	$0.29^{+0.06}_{-0.06}$	$0.11^{+0.01}_{-0.01}$	$1738.6^{+2761.3}_{-1245.4}$	$1.89^{+0.04}_{-0.04}$	$12.34^{+0.70}_{-0.65}$	176.76/134	$41.7^{+25.4}_{-19.5}$	113.0 ± 1.2
NGC 4559 X7	0883960201 [b]	Low	$0.20^{+0.02}_{-0.02}$	$0.18^{+0.05}_{-0.04}$	$23.67^{+73.25}_{-18.03}$	$2.43^{+0.05}_{-0.05}$	$7.99^{+0.38}_{-0.47}$	134.35/124	$4.8^{+5.0}_{-2.5}$	49.5 ± 0.4
		Middle	$0.19^{+0.07}_{-0.06}$	$0.14^{+0.13}_{-0.03}$	$153.42^{+1267.04}_{-152.18}$	$1.98^{+0.08}_{-0.08}$	$9.13^{+0.84}_{-0.88}$	128.88/102	$12.4^{+25.3}_{-11.3}$	66.5 ± 1.1
		High	$0.17^{+0.04}_{-0.03}$	$0.20^{+0.16}_{-0.06}$	$17.40^{+227.15}_{-16.39}$	$1.73^{+0.07}_{-0.10}$	$10.3^{+0.78}_{-1.28}$	194.22/149	$4.2^{+11.5}_{-3.2}$	81.4 ± 0.7
NGC 7456 ULX1	0901330101	Low	$0.066^{+0.035}_{-0.031}$	$0.27^{+0.04}_{-0.04}$	$1.4^{+1.4}_{-0.7}$	$2.27^{+0.34}_{-0.36}$	$0.40^{+0.18}_{-0.15}$	104.68/67	$1.8^{+0.8}_{-0.5}$	9.0 ± 0.2
		High	$0.076^{+0.032}_{-0.030}$	$0.32^{+0.03}_{-0.03}$	$1.1^{+0.6}_{-0.5}$	$2.44^{+0.24}_{-0.27}$	$0.85^{+0.31}_{-0.27}$	86.91/83	$1.6^{+0.4}_{-0.4}$	17.4 ± 0.3

[a] : parameters are frozen to corresponding values during the fit.

[b]: An additional **HIGHECUT** component is required to fit the high-state spectrum, with best-fit values $E_{cut} = 5.3^{+0.9}_{-0.5}$ keV and $E_{fold} = 6.2^{+1.9}_{-2.0}$ keV. For the low and middle state spectra, E_{cut} and E_{fold} are frozen at these values for consistency.

[c] : Unabsorbed luminosity is calculated for the energy range 0.3-10.0 keV.

Background events were obtained from nearby circular regions with radii of $70''$ for NGC 4559 X7 and $55''$ for NGC 7456 ULX1. Instrumental response matrices (RMFs) were generated with `rmfgen`, while ancillary response files (ARFs) were produced using `arfgen`. The resulting spectra were grouped using `specgroup`. For timing analysis, source and background light curves were extracted from single and double events (PATTERN $\leq$ 4) using `evselect`, and the final background subtracted light curves were obtained with `epiclccorr`.

5.4 Analysis and Results

To investigate the temporal variability of the sources, we first examined their light curves in multiple energy bands (see Fig. 5.3 – 5.5). From these plots, it is evident that NGC 4559 X7 exhibits stronger variability in the higher energy bands, whereas NGC 7456 ULX1 shows more pronounced variability in the lower energy bands. To explore how this variability is accompanied by changes in the spectral properties, we divided the data into distinct count-rate intervals. ULXs often display spectral evolution with luminosity, suggesting changes in the accretion flow or emission geometry. Therefore, comparing different intensity states allows us to examine how the relative contributions of thermal disk emission and hard X-ray components vary with source brightness.

Based on the hardness ratio and total count rate(see Fig. 5.3 – 5.5), we selected three intervals for NGC 4559 X7: (i) Set–1: 0.8–1.3 counts s^{-1}, (ii) Set–2: 1.3–1.6 counts s^{-1}, and (iii) Set–3: 1.6–2.1 counts s^{-1}. For NGC 7456 ULX1, only two clear intervals could be defined: (i) Set–1: 0.07–0.18 counts s^{-1} and (ii) Set–2: 0.21–0.35 counts s^{-1}. Accordingly, we refer to these sets as Low, Middle, and High states for NGC 4559 X7, and Low and High states for NGC 7456 ULX1. After extracting the spectra for

each state, spectral fitting was performed using the XSPEC software package (Arnaud 1996). We employed a model commonly used for ULX sources, `tbabs*(diskbb+pow)`. The absorption component `tbabs` accounts for absorption from the surroundings of the ULXs or interstellar material along the line of sight, with abundances set to `wilm` (Wilms et al. 2000) and photoionisation cross-sections set to `vern` (Verner et al. 1996). The `diskbb` component represents the multicolour thermal emission from the accretion disk, while the `pow` component models the non-thermal hard X-ray emission associated with the inner accretion flow onto a compact object. All spectra were well described by this model, with the exception of the high-state spectrum of NGC 4559 X7 for observation ID: 0883960201. In this case, an additional `highecut` component was required to account for the spectral cutoff at higher energies. The best-fit cutoff and folding energies were found to be $E_{\rm cut} = 5.3^{+0.9}_{-0.5}$ keV and $E_{\rm fold} = 6.2^{+1.9}_{-2.0}$ keV, respectively. For consistency in comparing the different states of this observation, we refitted the low and middle state spectra using the same additional component, while keeping $E_{\rm cut}$ and $E_{\rm fold}$ fixed to the values obtained from the high-state fit. The fitted spectral parameters are summarized in Table-5.3

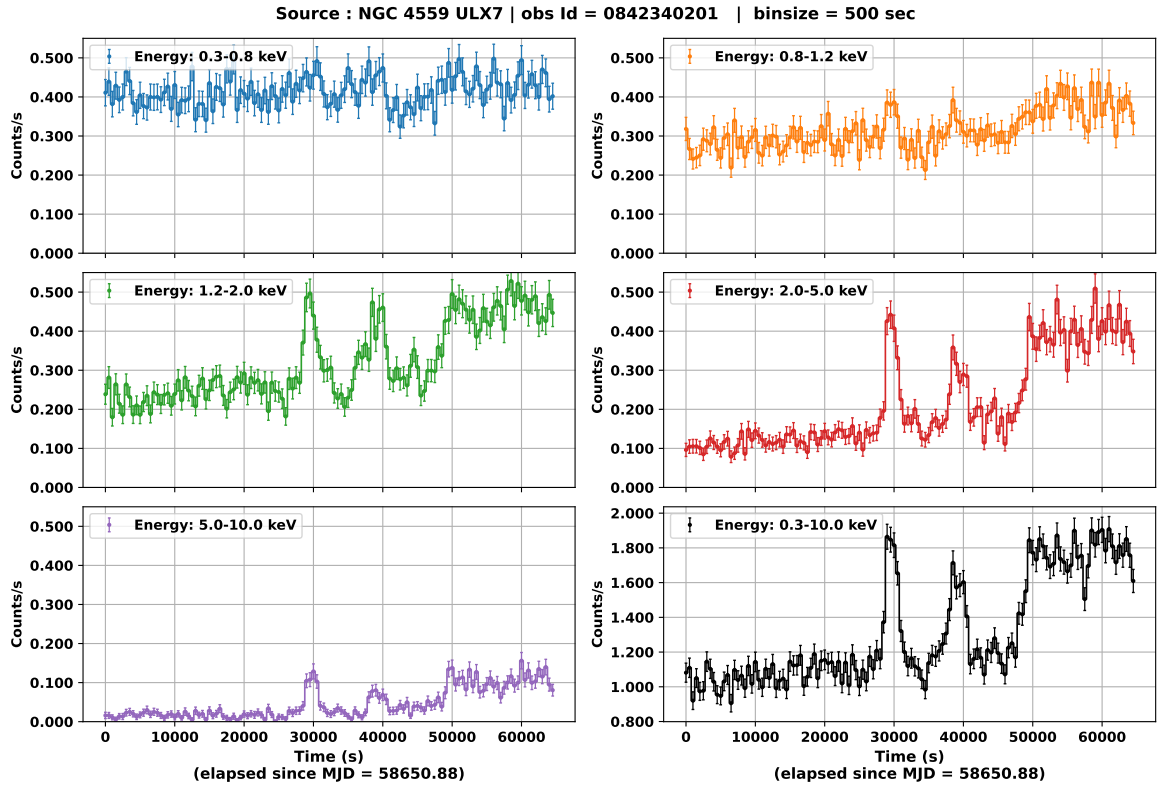
For NGC 4559 X7, the best-fit column density varies between 0.24–0.29×10^{22} $\rm cm^{-2}$ in the first observation and between 0.17–0.20×10^{22} $\rm cm^{-2}$ in the second, showing no significant change from the low to high state. The disk temperature remains low in all states, ranging from 0.11–0.14 keV in the first observation and 0.14–0.20 keV in the second. In contrast, the power-law index decreases systematically with brightness, from 2.54 to 1.89 in the first observation and from 2.43 to 1.73 in the second. For NGC 7456 ULX1, the column density increases slightly from 0.66 to 0.76×10^{21} $\rm cm^{-2}$ from the low to high state. The disk temperature increases from 0.27 to 0.32 keV, and the power-law index varies from 2.27 to 2.44 between the two states.

To visualize the trends associated with the intrinsic brightness of the sources, we plotted the column density, inner disk temperature, inner disk radius (estimated under the assumption of a face-on disk geometry), and power-law index against the luminosity in Figure 5.6. Considering the uncertainties associated with each parameter, the components responsible for the soft emission, namely $N_{\rm H}$, $kT_{\rm disk}$, and $R_{\rm in}$, remain broadly similar across all three states of NGC 4559 X7, while the power-law index decreases systematically with luminosity in both observations. For NGC 7456 ULX1, although only two states are available, the disk temperature shows an increase with luminosity, accompanied by a slight increase in the column density and a small decrease in the inner disk radius.

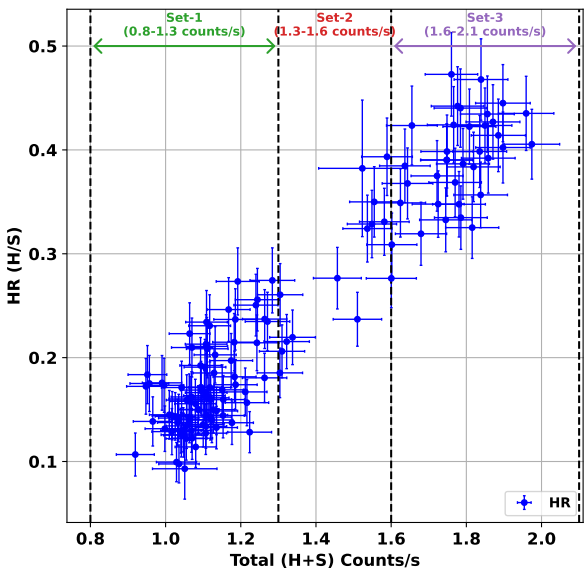
5.5 Discussion

Variability in X-ray binaries has long been recognized as a powerful diagnostic of accretion physics. In Galactic systems, a wide range of variability behaviours, ranging from aperiodic fluctuations to quasi-periodic oscillations and flaring episodes, arise from changes in the mass–accretion rate, thermal–viscous instabilities in the accretion disk, and magnetospheric interactions between the plasma and the compact object (e.g. van der Klis 1997, Done et al. 2007). These variability patterns are usually associated with changes in spectral state: transitions between soft, disk-dominated regimes and hard, Comptonized regimes often reflect variations in disk truncation, coronal geometry, or cooling efficiency of the inner flow. As a result, Galactic binaries provide a well-established framework where spectral and temporal behaviours can be linked to the structure of the accretion flow and the mass-transfer history of the system.

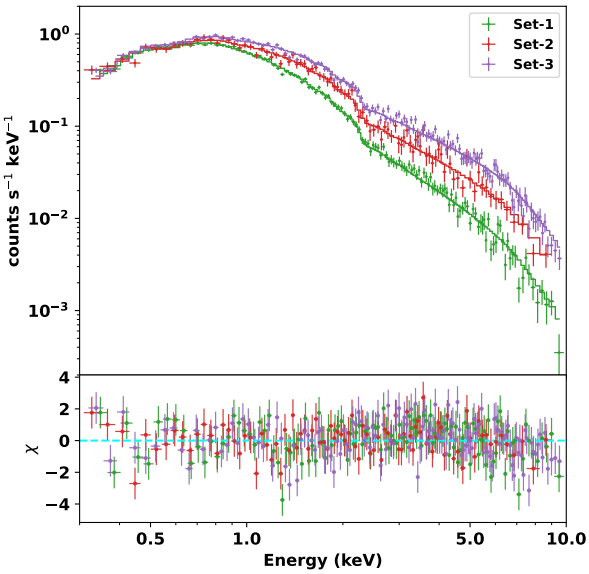
In contrast, strong variability is less prevalent in the ULXs and its physical origin remains less understood. While many ULXs exhibit relatively stable luminosities over long periods, a small subset shows significant flux changes, rapid flaring events, or even quasi-periodic behaviours such as heartbeat-like



(a) Light curves in multiple energy bands.

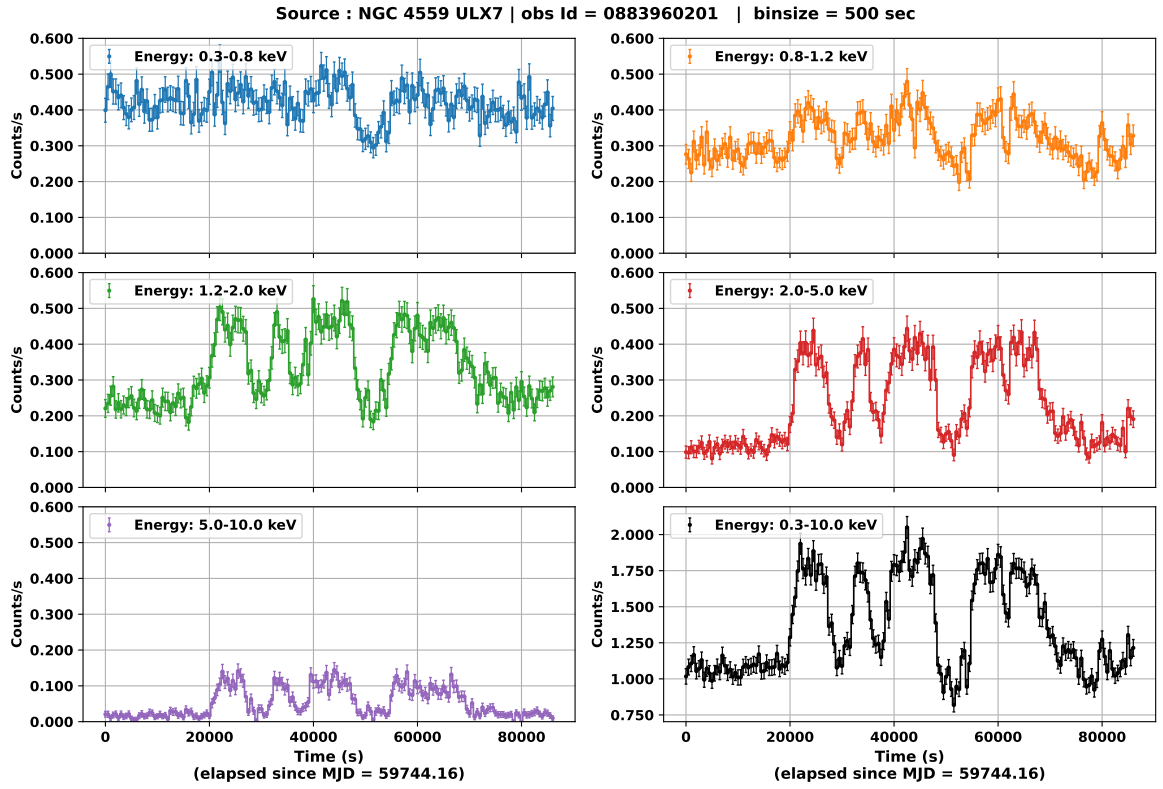


(b) Hardness ratio as a function of total count rate.

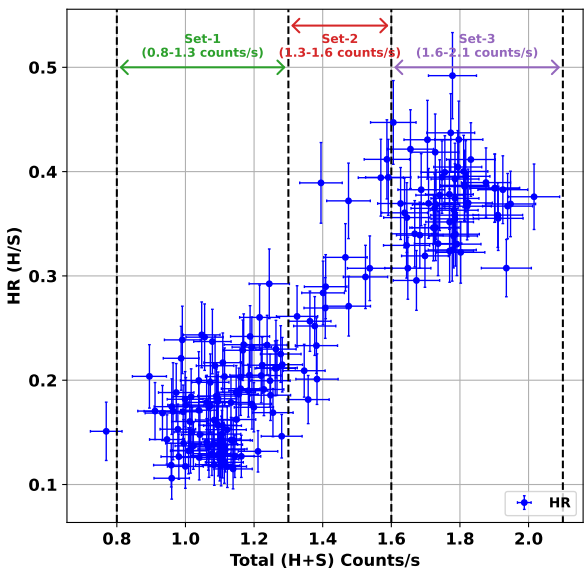


(c) Spectra corresponding to different flux states.

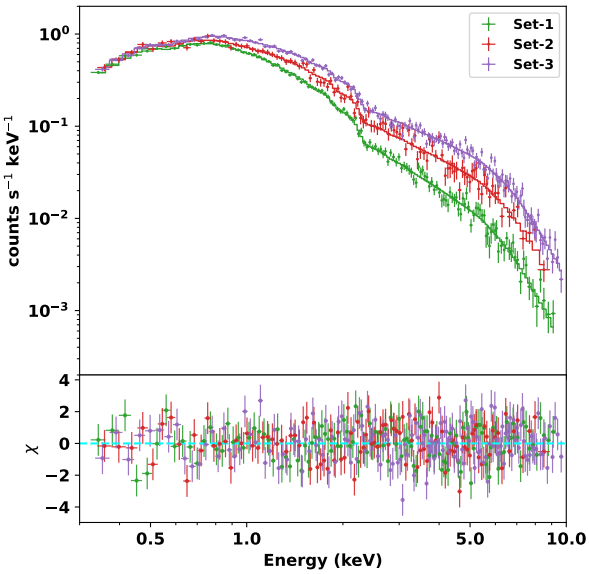
Figure 5.3: NGC 4559 X7 (ObsID - 0842340201): Panel (a) shows the X-ray light curves in different energy ranges, highlighting clear variability at higher energies. Panel (b) presents the hardness ratio as a function of total count rate, where the source becomes spectrally harder with increasing brightness. Panel (c) displays the energy spectra extracted in distinct count-rate states, illustrating that the hard power-law component strengthens during high-flux intervals while the soft disk component remains comparatively stable.



(a) Light curves in multiple energy bands.

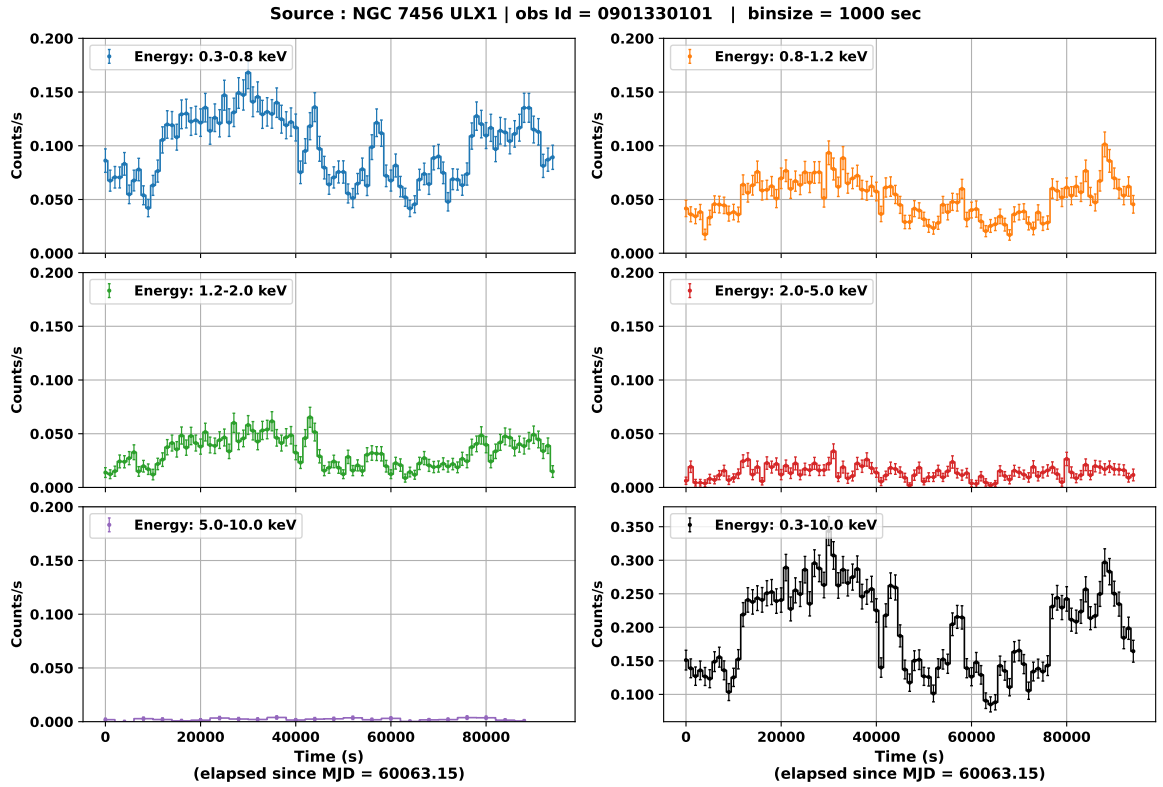


(b) Hardness ratio as a function of total count rate.

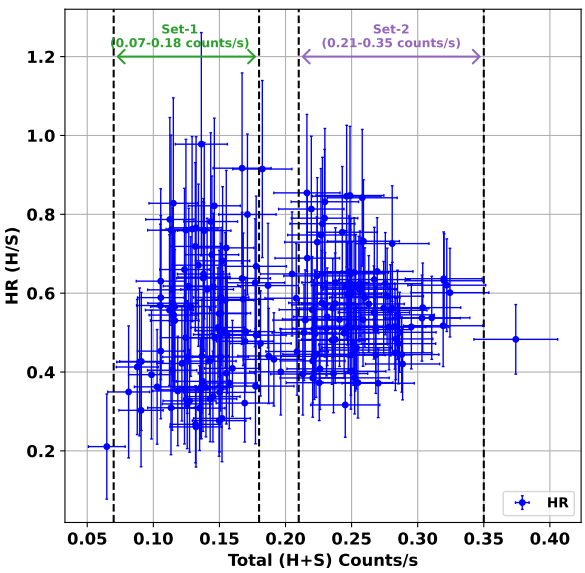


(c) Spectra corresponding to different flux states.

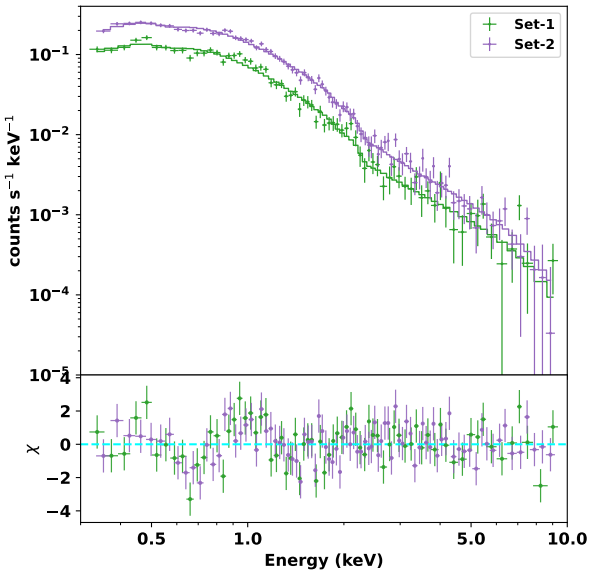
Figure 5.4: NGC 4559 X7 (ObsID - 0883960201): Panel (a) shows the X-ray light curves in different energy ranges, highlighting clear variability at higher energies. Panel (b) presents the hardness ratio as a function of total count rate, where the source becomes spectrally harder with increasing brightness. Panel (c) displays the energy spectra extracted in distinct count-rate states, illustrating that the hard power-law component strengthens during high-flux intervals while the soft disk component remains comparatively stable.



(a) Light curves in multiple energy bands.



(b) Hardness ratio as a function of total count rate.



(c) Spectra corresponding to different flux states.

Figure 5.5: NGC 7456 ULX1 (ObsID - 0901330101): Panel (a) shows the X-ray light curves in various energy ranges, indicating that most of the variability originates in the soft band. Panel (b) displays the hardness ratio versus total count rate, showing that the source becomes spectrally softer at higher intensities. Panel (c) presents the spectra extracted in different count-rate states, illustrating that the soft thermal component strengthens during high-flux intervals while the hard component remains comparatively stable.

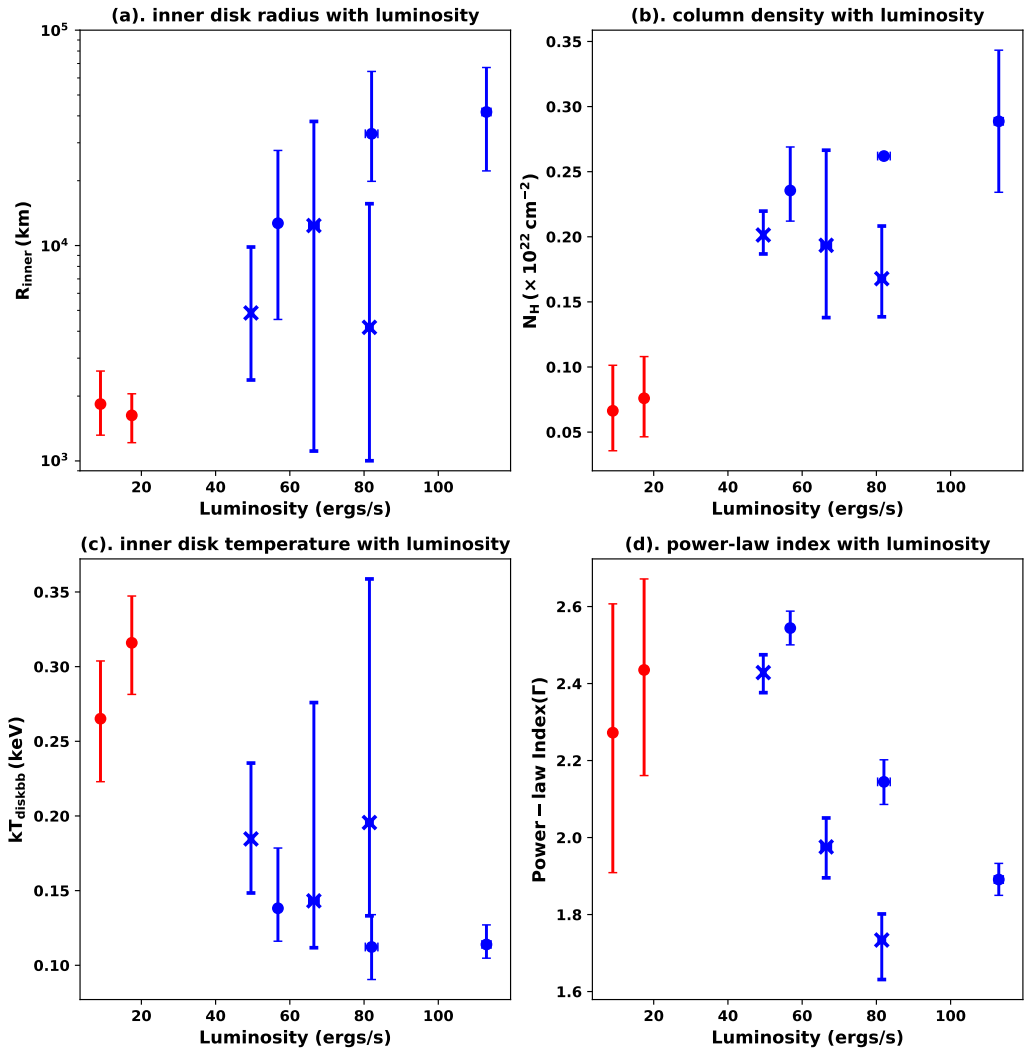


Figure 5.6: Evolution of the inner disk radius, column density, inner disk temperature, and power-law index as a function of luminosity. Blue symbols represent the two observations of NGC 4559 X7 (with different marke types), while red symbols correspond to NGC 7456 ULX1. The inner disk radius is plotted assuming a face-on disk geometry. But actually, the quantity shown on the y-axis of panel (a) is $R_{\rm in}\sqrt{\cos\theta}$.

variability (Heil et al. 2009, Motta et al. 2020). These rare cases suggest that super-Eddington accretion flows, despite strong radiation pressure, massive disk winds, and potential geometrical beaming, may undergo dynamical changes similar to those in Galactic accretors, though possibly modified by optically thick outflows, collimation, or strong central magnetic fields (e.g. Middleton et al. 2015). The infrequent detection of such behaviours may indicate that they arise under specific accretion conditions, or that they are transient phenomena associated with particular disk states or evolutionary phases of the binary.

In this work, we investigated two ULXs NGC 4559 X7 and NGC 7456 ULX1 that display temporal variability in opposite energy bands. NGC 4559 X7 shows prominent variability in the hard X-ray regime. Our state-resolved spectral analysis indicates that the soft thermal component remains nearly constant across different luminosity intervals, while the power-law index decreases with increasing count rate. This behaviour is consistent in both XMM-Newton observations and may reflect changes in the emission from the inner accretion flow, such as variations in the Comptonizing region or changes in the geometry of the high-energy emitting zone.

NGC 7456 ULX1, by contrast, displays variability almost entirely in the soft X-ray band. The spectral evolution is characterized by an increase in disk temperature and a slight decrease in apparent disk radius, while the power-law component shows little variation between states. These trends are indicative of variability in the optically thick component, possibly connected to fluctuations in the outer disk or in reprocessing layers associated with super-Eddington winds (e.g. Middleton et al. 2015, Pinto et al. 2016). Unlike X7, this behaviour does not require substantial changes in the high-energy emission region.

The differences between the two sources likely reflect differences in the regions of the accretion flow that dominate the observed variability, rather than a single, universal variability mechanism. In NGC 4559 X7, the pronounced harder-when-brighter behaviour indicates that variability is primarily associated with the high-energy emission, similar to what is observed in some ULX pulsars and other ULXs where the hard component becomes increasingly dominant at higher flux levels (Walton et al. 2020). Such behaviour may arise from changes in the inner accretion flow or Comptonizing region, for example through variations in plasma temperature, optical depth, or geometry close to the central accretor. In contrast, NGC 7456 ULX1 exhibits variability that is strongest in the soft X-ray band, while its hardness ratio remains approximately constant within uncertainties. This behaviour indicates that the flux changes are not accompanied by strong spectral evolution and are therefore consistent with variability being dominated by the soft-emitting component. Such behaviour may arise from changes in the outer accretion disk or from reprocessed emission in an optically thick wind. Similar soft-dominated variability has been reported in wind-dominated ULXs, such as NGC 247 ULX-1 (Pinto et al. 2021), where variations have been discussed in the context of changes in the wind photosphere or the disk–wind interface.

These observational trends do not uniquely determine the underlying physical drivers, but they are broadly consistent with theoretical models of super-Eddington accretion, which predict a stratified accretion structure consisting of a dense inner region, a funnel-like geometry producing collimated high-energy emission, and powerful radiation-driven winds (Shakura & Sunyaev 1973, King et al. 2023). Within this framework, variability can arise in different regions of the flow depending on the accretion rate, magnetic field configuration, and system geometry. In the present study, the spectral evolution of NGC 4559 X7 is more consistent with changes occurring in the high-energy emitting region, while NGC 7456 ULX1 appears to be dominated by variability in the soft X-ray emission, potentially associated with the disk–wind interface. These interpretations should be regarded as qualitative, given the limited number of flux states sampled and the use of simplified spectral models.

In addition to intrinsic changes in the accretion flow, the role of the line of sight remains an important and unknown factor in shaping the observed variability of ULXs. In super-Eddington systems, geometrical beaming, optically thick winds, and reprocessing effects can strongly modulate the observed X-ray emission as a function of inclination. Consequently, the same intrinsic source may exhibit different spectral hardness and variability properties when viewed from different angles, even in the absence of substantial changes in the mass accretion rate. A similar orientation-dependent effect is well established in active galactic nuclei, where the AGN unification framework demonstrates that a single intrinsic source can appear as a Seyfert 1 or Seyfert 2 galaxy primarily due to differences in viewing angle relative to the obscuring structure, leading to distinct spectral hardness, absorption, and variability properties (Antonucci 1993, Urry & Padovani 1995, Netzer 2015). By analogy, orientation effects in ULXs may influence whether the observed variability is dominated by the hard inner emission or by softer, reprocessed components associated with the wind.

The contrasting behaviours observed in this work suggest that variability in ULXs may not be governed by a single physical mechanism, but instead may span a continuum of accretion regimes. Test-

ing this scenario requires systematic, population-level studies of variable ULXs. Such studies should compare the spectral and temporal properties of different subclasses, including pulsating ULXs, wind-dominated systems, and relatively stable high-luminosity sources, to assess whether ULXs follow a continuous variability–spectral sequence, or whether they represent physically distinct accretion states. Placing sources such as NGC 4559 X7 and NGC 7456 ULX1 within this broader framework will help determine whether they represent different regions of this continuum or reflect source-specific effects related to geometry, inclination, or local accretion conditions.

6

Energy dependence and luminosity dependence of pulse profiles in ULXPs

6.1 Introduction

Ultra-luminous X-ray sources (ULXs) are extragalactic, non-nuclear X-ray emitters with luminosities of $10^{39} - 10^{41}$, far exceeding the Eddington limit for typical stellar-mass compact objects. Although initially interpreted as sub-Eddington accreting intermediate-mass black holes, subsequent observations, including studies of their environments, suggest that most ULXs host stellar-mass compact objects (neutron stars or black holes) accreting at super-Eddington rates (King 2004). A major breakthrough in this field came with the discovery of coherent pulsations, first in M82 X-2 (Bachetti et al. 2014), and later in several other ULXs such as NGC 7793 P13 (Israel et al. 2017a), NGC 5907 ULX1 (Israel et al. 2017b), M51 ULX7 (Castillo et al. 2020), NGC 300 ULX1 (Carpano et al. 2018), and NGC 1313 X-2 (Sathyaprakash et al. 2019). These ultra-luminous X-ray pulsars (ULXPs) provide compelling evidence that highly magnetized neutron stars can sustain accretion at rates well above the classical Eddington limit. In addition to extragalactic ULXPs, a few Galactic and SMC systems have also exhibited super-Eddington luminosities during outbursts, including SMC X-3 (Tsygankov et al. 2017a, Koliopanos & Vasilopoulos 2018), RX J0209.6−7427 (Vasilopoulos et al. 2020, Chandra et al. 2020), and Swift J0243.6+6124 (Wilson-Hodge et al. 2018, Beri et al. 2021, Bykov et al. 2022). These discoveries have renewed interest in understanding the geometry and physics of super-Eddington accretion onto magnetized neutron stars.

Pulse profiles in accreting X-ray pulsars have been extensively studied in several Galactic high-mass X-ray binaries (HMXBs) as well as in systems within the Magellanic Clouds, such as LMC X-4, SMC X-1, and SMC X-3. These sources consistently exhibit a strong energy dependence in both the shape of their pulse profiles and their modulation strength. In many systems, the pulse fraction increases with energy, a behaviour commonly interpreted as the result of soft X-ray emission being diluted by reprocessing, while hard X-rays more directly trace the intrinsic emission from the accretion columns near the magnetic poles (Paul et al. 2002, Naik & Paul 2004, Hickox et al. 2004, Lutovinov & Tsygankov 2009a, Tsygankov et al. 2017b). Correspondingly, soft X-ray pulse profiles are often smooth and nearly sinusoidal, whereas hard X-ray profiles are more structured and asymmetric. This behaviour is observed in sources such as SMC X-1 and LMC X-4, where reprocessed soft emission is thought to smear the intrinsic pulsations, while hard emission preserves the underlying beam geometry (Paul et al. 2002, Hickox et al. 2004). However, some systems exhibit the opposite trend, showing complex pulse profiles at soft X-ray energies and comparatively simpler profiles at higher energies. In sources such as Vela X-1 (Sato et al. 1986, Nagase 1989), this behaviour is often attributed to phase-dependent absorption or scattering that preferentially modulates the soft X-ray emission, while the hard X-rays are less affected and retain a simpler pulse morphology.

Apart from the regular intensity variability associated with the neutron-star spin and the binary orbital phase, some X-ray binaries (XRBs) exhibit an additional long-term modulation of intensity on timescales much longer than the orbital period, referred to as super-orbital variability (Katz 1973). LMC X-4 and SMC X-1 are well-known examples, with LMC X-4 showing a stable super-orbital period of $\sim$ 30 days and SMC X-1 exhibiting a variable period of $\sim$ 40 60 days (Heemskerk & van Paradijs 1989, Wojdowski et al. 1998, Paul & Kitamoto 2002). These long-term variations are generally interpreted as arising from a precessing, warped accretion disk, which periodically alters the visibility of the central X-ray source. Observational studies have shown that the pulse profiles in both systems vary systematically over the super-orbital cycle, consistent with the changing line of sight caused by the precessing disk (Neilsen et al. 2004, Hickox & Vrtilek 2005, Hung et al. 2010, Brumback et al. 2020). Beyond changes in pulse amplitude, it has also been firmly established that the *relative phase* between the soft and hard X-ray pulses evolves with the super-orbital phase (Paul 2017). This behaviour arises because the changing orientation of the warped disk modulates the visibility of both the accretion column and the reprocessing region. Two distinct geometric scenarios have been proposed to explain this phenomenon. When the soft and hard pulses appear nearly in phase, the observer has an essentially unobscured view of both the accretion column and the inner-disk reprocessing region, allowing the direct and reprocessed emission components to vary coherently (Hickox et al. 2004). Conversely, when the pulses exhibit an approximate 180° phase offset, the warped disk is thought to partially obscure the direct line of sight to the accretion column; the observer then predominantly detects reprocessed soft photons from the far side of the disk, leading to a strong anti-correlation between the soft and hard pulses (Hickox & Vrtilek 2005, Brumback et al. 2020). Consequently, the systematic evolution of soft–hard phase offsets with super-orbital phase provides one of the clearest observational signatures of a precessing, warped accretion disk in systems such as LMC X-4 and SMC X-1, offering valuable insights into disk structure, beam geometry, and the physical processes operating in the accretion column of luminous X-ray pulsars. An alternative explanation that has also been proposed for super-orbital intensity modulation is the free precession of the neutron star, which can lead to a periodic change in the viewing angle of the X-ray beam and hence modulate the observed flux (Truemper et al. 1986, Postnov et al. 2013). For example, Heyl et al. (2023) showed that the $\sim$ 35 days super-orbital period observed in Her X-1 is plausibly driven by free precession of the neutron star.

The similarities between Galactic X-ray pulsars and ULXPs naturally raise the question of whether the same physical mechanisms, such as energy-dependent modulation, soft–hard phase offsets, and geometric effects driven by disk structure, operate in the super-Eddington regime of ULXs. Given the presence of thick accretion disks, strong outflows, and extreme luminosities in ULXPs, these behaviours may be amplified or may manifest in fundamentally different ways. To investigate this, we examined the pulse profiles of ULXPs across energy and luminosity bands to determine whether they exhibit trends analogous to those observed in Galactic systems, or whether they reveal new signatures unique to super-Eddington accretion.

Table 6.1: Observed Properties of ULXPs

Sources	Distance(Mpc)	$P_{\rm spin}$	$P_{\rm orb}$	$P_{\rm sup-orb}$	$L_{\rm peak}$ (erg s^{-1})	References
M82 X-2	3.6	1.37 s	2.5 d	-	4.9×10^{39}	Bachetti et al. (2014)
NGC 7793 P13	3.9	0.42 s	64 d	-	$\sim 10^{40}$	Karachentsev et al. (2004),Israel et al. (2017a),Fürst et al. (2016)
NGC 5907 ULX1	17.06	1.13 s	5 d	78 d	$\sim 10^{41}$	Tully et al. (2016), Israel et al. (2017b), Fürst et al. (2017)
M51 ULX-7	8.6	2.8 s	2 d	38 d	$\sim 10^{39-40}$	McQuinn et al. (2016), Castillo et al. (2020), Brightman et al. (2022)
NGC 300 ULX1	1.88	31.6 s	-	-	4.7×10^{39}	Gieren et al. (2005), Carpano et al. (2018)
NGC 1313 X-2	4.2	1.5 s	-	-	9×10^{39}	Tully et al. (2016) , Sathyaprakash et al. (2019), Robba et al. (2021)

6.2 Observation & Source Selection

To date, coherent pulsations have been detected in only six extragalactic ULX sources, and their key properties are summarised in Table 6.1. Among these, the ULX pulsar M82 X-2 cannot be spatially resolved from the nearby ULX source M82 X-1 with *XMM-Newton* due to their close separation, leading to contamination in the extracted light curves. Consequently, we do not use *XMM-Newton* data for the ULXP M82 X-2 in this work. For the remaining ULX pulsars, we analysed all available *XMM-Newton*/EPIC-PN observations. Our initial goal was to generate folded pulse profiles for each of these sources across all observations. During this process, we found that NGC 7793 P13 provides sufficiently high-quality statistics to enable a detailed comparison of its soft and hard X-ray pulse profiles as a function of luminosity, allowing us to investigate potential phase shifts between energy bands and how these evolve with luminosity. The complete set of *XMM-Newton* observations used in this study is listed in Table 6.2.

Table 6.2: Observation log of the ULX pulsars analysed in this work, listing the *XMM-Newton* ObsID, observation date (MJD), source extraction region, and total good-time exposure (GTE).

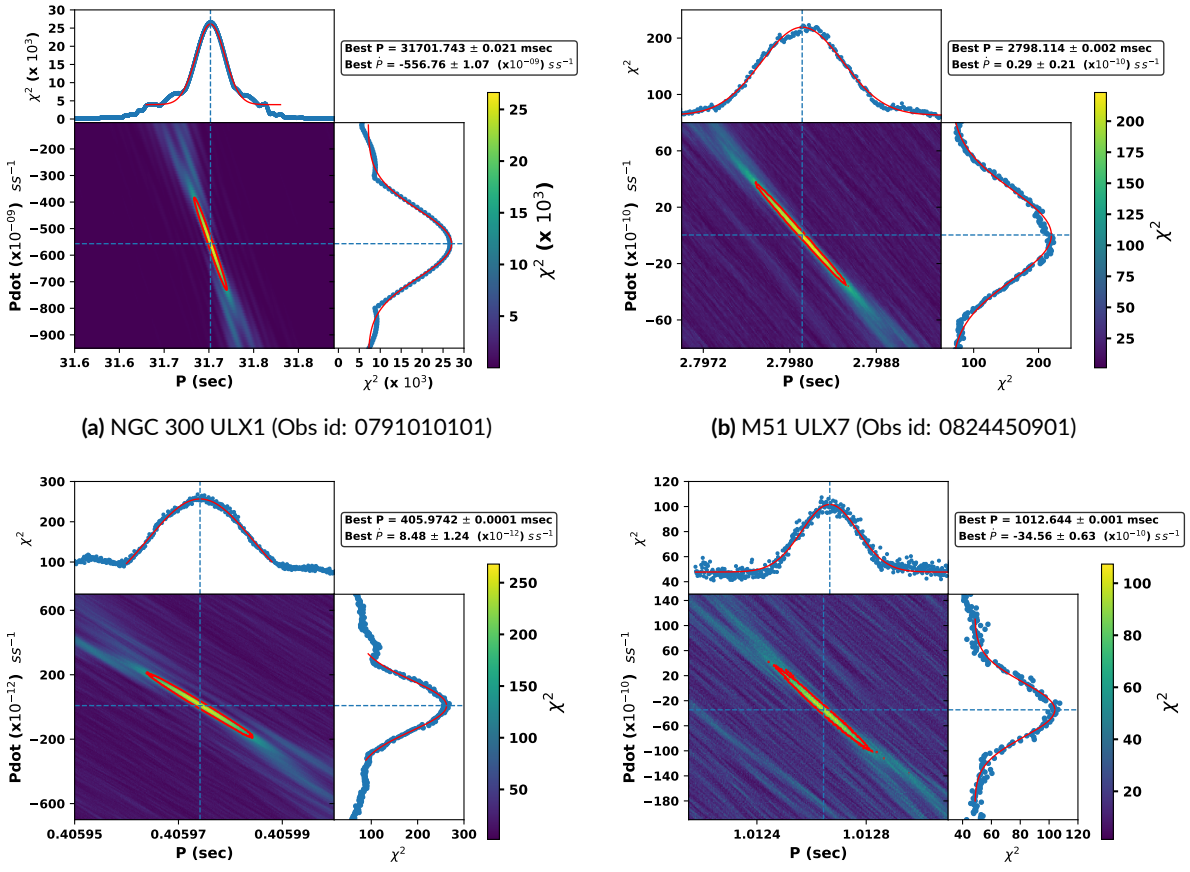
Source Name	ObsID	MJD	Src Rgn	GTE (ks)
NGC 300 ULX1	0791010101	57739.40	30″	96.29
	0791010301	57741.39	30″	44.78
M51 ULX7	0212480801	53552.29	20″	20.86
	0677980701[a]	55719.22	20″	9.60
	0824450901	58251.92	20″	64.73
	0830191501	58282.10	20″	51.59
	0830191601	58284.09	20″	51.66
	0852030101	58675.49	20″	58.78
NGC 5907 ULX1	0145190201	52690.67	30″	10.14
	0729561301	56847.95	30″	37.57
	0804090401	57939.02	30″	31.30
	0824320201	58646.82	30″	42.85
	0824320301	58653.21	30″	40.64
	0824320601	59053.74	30″	26.45
	0884220201	59265.10	30″	19.87
	0891801501	59453.39	30″	49.44
	0953011001[a]	60521.89	30″	51.52
NGC 7793 P13	0693760401	56621.21	30″	41.1
	0748390901	57002.00	30″	41.97
	0781800101	57528.58	30″	15.61
	0804670301	57893.66	30″	39.89
	0804670401	57904.90	30″	24.99
	0804670601	57924.11	30″	21.05
	0804670701	58083.00	30″	41.81
	0823410301	58449.79	30″	19.35
	0823410401	58479.60	30″	18.78
	0840990101	58619.99	30″	10.24
	0853981001	58809.36	30″	30.43
	0922840101[a]	60100.91	30″	39.79
	0922840201[a]	60284.30	30″	46.75
NGC 1313 X2	0803990401[a]	57998.75	30″	52.43
NGC 1313 X2	0803990601[a]	58096.46	30″	109.38

[a] For these observations, the full light curve (including soft-proton flares) was used to increase photon statistics and the listed exposure reflects the used light curve, not the filtered GTE.

6.3 Data Reduction

In this work, we used only *XMM-Newton* EPIC-pn data for the analysis. Data reduction was carried out with the *XMM-Newton* Science Analysis System (SAS) version 20.0.0 following the standard SAS threads. Raw event files were generated using `epproc`, and background flaring intervals were removed where necessary. The cleaned event files were then barycenter-corrected with SAS task `barycen`. Source events were extracted from circular regions centred on the coordinates listed in Table 6.2, while background events were taken from nearby circular regions of 1.5 times the source-region radius. Source and background light curves were extracted for good single and double events (PATTERN ≤ 4) using `evselect`, and final background-subtracted light curves were produced with `epiclccorr`. In some observations, we retained the full light curve without removing the charged-particle (soft proton) flaring intervals in order to increase photon statistics. These flares do not modulate at the source spin period and therefore do not affect pulsation searches, although the luminosity was derived from spectra extracted using the cleaned event files.

6.4 Analysis and Preliminary Results



(a) NGC 300 ULX1 (Obs id: 0791010101)

(b) M51 ULX7 (Obs id: 0824450901)

(c) NGC 7793 P13 (Obs id: 0922840201)

(d) NGC 5907 ULX1 (Obs id: 0884220201)

Figure 6.1: Sample P–$\dot{P}$ diagrams for each ULXP, with the corresponding source name and observation ID indicated in the respective panel.

6.4.1 Reconstruction of Pulse Profiles

To determine the best-fit spin period ULX pulsars, we used the XRONOS task `efsearch`, exploring a grid of trial period and period-derivative values (P, $\dot{P}$). For each pair, `efsearch` computes the corresponding χ^2 statistic, and the combination that yields the maximum χ^2 is taken as the optimal solution. To visualise this search (see Fig. 6.1), we generated a two-dimensional P–$\dot{P}$ diagram in which the colour scale represents the computed χ^2 values. In addition to the 2D map, we also plot one-dimensional slices: (i) $\chi^2(P)$, obtained by maximising over $\dot{P}$, and (ii) $\chi^2(\dot{P})$, obtained by maximising over P. In both cases, the peak of the χ^2 curve provides the initial best-fit estimates of P and $\dot{P}$, and together these panels offer a clear and robust determination of the optimal spin evolution parameters. After locating the peaks in the one-dimensional $\chi^2(P)$ and $\chi^2(\dot{P})$ curves, we refined these parameter estimates by fitting a Gaussian model to the smoothed profiles. To ensure that the fit is local and robust, we perform an adaptive re-fit: the initial Gaussian provides a centre and width, which are then used to define a neighbourhood (typically a few times the fitted width) around the peak, and the Gaussian is re-fitted within this restricted interval. The residuals from this local fit are used to estimate an effective per-point scatter/error associated with that point, allowing a final weighted Gaussian fit to be performed. The covariance matrix from this fit gives the statistical uncertainties on the Gaussian parameters, and the square root of the diagonal element corresponding to the centre yields the 1σ uncertainty in the estimated value of P (or $\dot{P}$). It is important to note that these uncertainties are purely statistical, reflecting how well the local χ^2 peak is approximated by a Gaussian. The overall reliability of the folded pulse profile, however, still depends on the exposure time and the photon statistics of the underlying light curves. The final best-fit values and their associated uncertainties are summarised in Table 6.3. Using these optimal $(P, \dot{P})$ values, we generated the folded pulse profiles with the XRONOS task `efold`.

For the ULXP NGC 300 ULX1, the spin period is approximately 31 s, and the corresponding folded pulse profile is shown in Fig. 6.2. As this is one of the brightest ULXPs, we examined the pulse fraction* in several energy bands and found that it increases toward higher energies. This behaviour is consistent with that observed in Galactic accreting X-ray pulsars.

For M51 ULX7, detecting pulsations requires correcting the photon arrival times for orbital motion, as orbital Doppler shifts can smear out the pulsation signal. We used the orbital parameters reported by Castillo et al. (2020): $a_x \sin i = 28.3$ lt$-$s and an orbital period of $P_{\rm orb} = 1.9969$ days for the orbital correction to the photon arrival times. The ascending node time was initially taken as $T_{\rm asc} = 58283.0115$ (MJD) for Observation ID 0830191501, and for the remaining observations it was computed consistently using the same ephemeris i.e, without any orbital evolution. For all observations listed in Table 6.3, pulsations were detected using the corresponding values of P and $\dot{P}$. However, for Observation ID 0830191501, we could not constrain $\dot{P}$; therefore, we determined the best period and generated the folded profile assuming $\dot{P} = 0$.

For NGC 5907 ULX1, we successfully measured P and $\dot{P}$ for most observations, as summarised in Table 6.3. For Observation ID 0145190201, orbital corrections were necessary and applied using $a_x \sin i = 2.5$ lt$-$s, $P_{\rm orb} = 5.3$ days, and $T_{\rm asc} = 52689.55$ (MJD), following Israel et al. (2017b), and Belfiore et al. (2024). For Observation ID 0804090401, the one-dimensional $\chi^2(P)$ and $\chi^2(\dot{P})$ curves were noticeably asymmetric about the peak, preventing a robust Gaussian fit. In this case, we adopted the values of P and $\dot{P}$ that correspond to the maximum χ^2, without assigning formal uncertainties. For Observation ID 0824320601, pulsations were not detected; however, a folded profile was generated using the values of P and $\dot{P}$ reported by Fürst et al. (2023).

For NGC 7793 P13, both the spin period and the period derivative were reliably measured for all

*Pulse fraction is defined as $\mathrm{PF} = (I_{\rm max} - I_{\rm min})/(I_{\rm max} + I_{\rm min})$, computed from the normalized folded pulse profile.

observations, and the derived values are listed in Table 6.3. For NGC 1313 X-2, pulsations could not be detected using our analysis method, and hence reliable estimates of the spin period P and period derivative $\dot{P}$ could not be obtained from the available data. Therefore, we adopted the P and $\dot{P}$ values reported in the literature by Sathyaprakash et al. (2019) and folded the light curves using those parameters.

6.4.2 Luminosity-Dependent Evolution of Pulse Profiles

After determining the spin period P and period derivative $\dot{P}$, we generated folded pulse profiles in three energy bands: the full (0.3–$10\,\mathrm{keV}$), soft (0.3–$2.0\,\mathrm{keV}$), and hard (2.0–$10.0\,\mathrm{keV}$) bands. To investigate the evolution of the relative phase between the soft and hard X-ray pulse profiles as a function of luminosity, the folded profiles, for each source, were arranged in order of increasing luminosity in figures 6.3 – 6.7. For NGC 300 ULX1, only two observations are available, and both correspond to very similar luminosity levels. As a result, no significant difference is observed in the relative phase between the soft and hard X-ray pulse profiles for these two observations (see Fig. 6.3). For M51 ULX7, folded pulse profiles were generated for six observations spanning a wider luminosity range. One observation (ObsID 0677980701) has a relatively short exposure and limited photon statistics, making it difficult to reliably identify any phase offset between the soft and hard profiles. The folded pulse profiles for all six observations are shown in Fig. 6.4, arranged in order of increasing luminosity. Similarly, the luminosity-dependent evolution of the pulse profiles for NGC 5907 ULX1 and NGC 7793 P13 is shown in Figs. 6.5 and 6.6, respectively. For one observation of NGC 5907 ULX1 (ObsID 0824320601) and for NGC 1313 X-2, a significant P–$\dot{P}$ detection could not be obtained. In these cases, we adopted the values of P and $\dot{P}$ reported in previous studies and generated the folded pulse profiles using those parameters. These folded profiles are shown in Fig. 6.7 for completeness; however, these three observations were not included in the subsequent luminosity-dependent, phase-difference, or pulse-fraction analyses.

To quantify the phase difference between the soft and hard X-ray pulse profiles, each profile was fitted with a simple sinusoidal function of unit period, allowing the constant offset, amplitude, and phase to vary freely. The phase parameter ϕ was defined over the range $0 \leq \phi < 1$ and represents a horizontal shift of the sinusoid within one pulse cycle, with phase zero ($\phi = 0$) taken as the reference point of the folded profile; under this convention, a value of $\phi = 0.25$ corresponds to the pulse minimum occurring at phase zero. The phase difference was computed as $\Delta\phi = \phi_{\mathrm{hard}} - \phi_{\mathrm{soft}}$ and wrapped into the interval $[-0.5,\ 0.5]$ to account for the cyclic nature of the pulse phase, where positive (negative) values indicate that the hard-band pulse profile lags (leads) the soft-band pulse profile. To visualise any systematic trends, we plotted the phase difference as a function of luminosity for the sources M51 ULX7, NGC 5907 ULX1, and NGC 7793 P13. In addition to the phase difference, we also plotted the pulse fraction measured in the full energy band (0.3–$10\,\mathrm{keV}$) as a function of luminosity for all three sources. These results are shown in Fig. 6.8. It is important to note that the present analysis is based on fitting a simple sinusoidal model to the folded pulse profiles, which is employed solely to quantify the relative phase shifts between different energy bands. This approach provides a convenient and uniform measure of phase offsets, but it does not capture the full complexity of the pulse morphology. In reality, the pulse profiles often exhibit asymmetric shapes, multiple peaks, and energy-dependent substructures that cannot be adequately described by a single sinusoidal component. Therefore, the fitted sinusoid should be regarded as an approximate, phenomenological representation used for comparative purposes, rather than a physically complete description of the underlying emission geometry or beaming pattern.

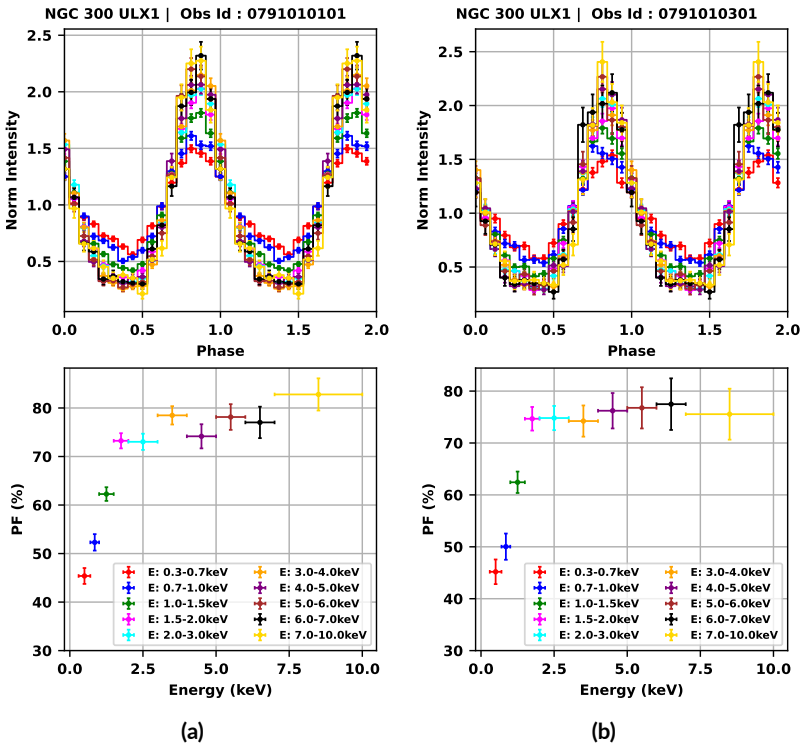


Figure 6.2: Pulse fraction as a function of energy for the two observations of NGC 300 ULX1 shown in panels (a) and (b). In each panel, the top plot shows the folded pulse profiles in different energy bands (indicated by different colours), and the bottom plot shows the corresponding pulse fraction as a function of energy.

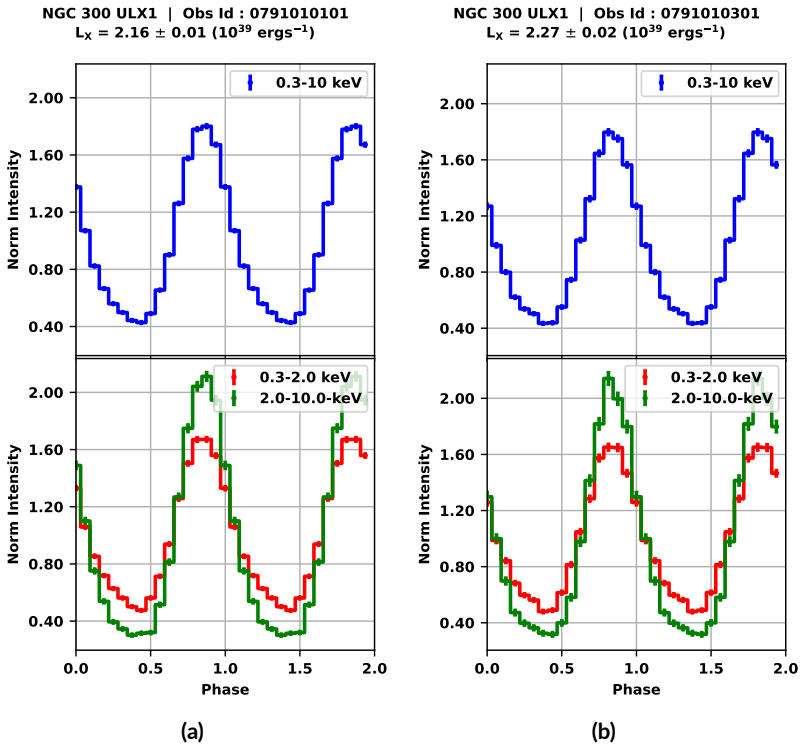


Figure 6.3: Panels (a) and (b) show the folded pulse profiles of NGC 300 ULX1 for the observations listed at the top of each panel. Each panel contains two plots: the top plot shows the folded pulse profile in the $0.3–10$ keV energy range (in blue), and the bottom plot shows the profiles in the soft ($0.3–2.0$ keV) and hard ($2.0–10.0$ keV) bands, plotted in red and green, respectively.

Table 6.3: Measured spin period P, period derivative $\dot{P}$, pulse fraction (PF), and X-ray luminosity L_X for the ULX pulsars, derived from the *XMM-Newton* observations analysed in this work.

Source Name	ObsID	P (ms)	$\dot{P}$ (ss^{-1})	PF [c] (%)	L_X [d] (10^{39} ergs s^{-1})
NGC 300 ULX1	0791010101	31701.743 ± 0.021	-556.76 ± 1.07 ($\times 10^{-09}$)	61.61 ± 0.64	2.16 ± 0.01
	0791010301	31605.605 ± 0.059	-559.89 ± 1.91 ($\times 10^{-09}$)	61.08 ± 0.94	2.27 ± 0.02
M51 ULX7	0212480801	3297.513 ± 0.002	14.27 ± 0.44 ($\times 10^{-12}$)	20.19 ± 5.51	7.06 ± 0.23
	0677980701[a]	2997.041 ± 0.004	46.94 ± 2.73 ($\times 10^{-12}$)	34.16 ± 8.58	5.07 ± 0.45
	0824450901	2798.114 ± 0.002	0.29 ± 0.21 ($\times 10^{-10}$)	22.01 ± 2.88	6.25 ± 0.11
	0830191501	2797.746 ± 0.005	-	10.70 ± 2.93	8.27 ± 0.14
	0830191601	2797.722 ± 0.005	-78.69 ± 7.17 ($\times 10^{-11}$)	17.26 ± 2.98	8.08 ± 0.14
	0852030101	2787.055 ± 0.004	-17.65 ± 0.39 ($\times 10^{-10}$)	16.58 ± 2.86	7.79 ± 0.13
NGC 5907 ULX1	0145190201	1428.622 ± 0.015	-134.24 ± 2.85 ($\times 10^{-10}$)	21.50 ± 5.11	89.03 ± 2.88
	0729561301	1137.832 ± 0.001	-497.70 ± 1.87 ($\times 10^{-11}$)	15.62 ± 2.53	100.97 ± 1.51
	0804090401	946.178	-46.00 ($\times 10^{-11}$)	28.10 ± 6.59	15.52 ± 0.63
	0824320201	1019.313 ± 0.001	-255.52± 0.44 ($\times 10^{-11}$)	20.82 ± 2.90	68.02 ± 1.18
	0824320301	1018.145 ± 0.001	-178.98± 2.77 ($\times 10^{-11}$)	13.46 ± 3.29	59.18 ± 1.12
	0824320601[b]	1032.94	-2.3 ($\times 10^{-09}$)	7.69 ± 3.83	66.92 ± 1.50
	0884220201	1012.644 ± 0.001	-34.56± 0.63 ($\times 10^{-10}$)	25.41 ± 4.33	62.90 ± 1.66
	0891801501	987.580 ± 0.001	-94.56± 1.36 ($\times 10^{-11}$)	20.96 ± 4.99	21.82 ± 0.63
	0953011001[a]	1044.508 ± 0.003	-183.56± 27.73 ($\times 10^{-12}$)	15.50 ± 4.49	42.33 ± 1.16
NGC 7793 P13	0693760401	419.7078 ± 0.0002	101.16 ± 3.07 ($\times 10^{-12}$)	20.38 ± 2.67	2.32 ± 0.04
	0748390901	418.3915 ± 0.0002	-19.69 ± 1.71 ($\times 10^{-12}$)	18.86 ± 1.96	5.76 ± 0.07
	0781800101	416.9387 ± 0.0005	22.92 ± 1.46 ($\times 10^{-11}$)	17.44 ± 2.33	11.07 ± 0.15
	0804670301	415.8762 ± 0.0001	-188.42 ± 1.72 ($\times 10^{-12}$)	11.08 ± 2.22	4.94 ± 0.06
	0804670401	415.7514 ± 0.0013	-323.99 ± 15.18 ($\times 10^{-12}$)	9.62 ± 1.89	9.53 ± 0.11
	0804670601	415.6528 ± 0.0002	305.83 ± 9.39 ($\times 10^{-12}$)	6.97 ± 1.91	11.04 ± 0.12
	0804670701	415.2242 ± 0.0002	-112.73 ± 2.01 ($\times 10^{-12}$)	13.77 ± 1.64	7.50 ± 0.07
	0823410301	413.6219 ± 0.0003	0.69 ± 3.76 ($\times 10^{-12}$)	31.81 ± 2.24	7.40 ± 0.10
	0823410401	413.5921 ± 0.0002	-246.94 ± 3.03 ($\times 10^{-12}$)	37.79 ± 2.95	4.27 ± 0.08
	0840990101	413.1508 ± 0.0022	3.87 ± 2.28 ($\times 10^{-11}$)	41.41 ± 4.71	3.00 ± 0.09
	0853981001	412.5938 ± 0.0001	-198.64 ± 2.18 ($\times 10^{-12}$)	43.94 ± 3.82	1.66 ± 0.04
	0922840101[a]	406.9150 ± 0.0001	-132.22 ± 1.06 ($\times 10^{-12}$)	29.68 ± 2.21	4.98 ± 0.11
	0922840201[a]	405.9742 ± 0.0001	8.48 ± 1.24 ($\times 10^{-12}$)	13.70 ± 1.39	9.96 ± 0.23
NGC 1313 X2	0803990401[a, b]	1457.639	1.38 ($\times 10^{-08}$)	5.01 ± 2.06	5.86 ± 0.16
NGC 1313 X2	0803990601[a, b]	1461.210	3.20 ($\times 10^{-08}$)	4.47 ± 1.80	3.98 ± 0.12

[a] For these observations, the full light curve (including soft-proton flares) was used to increase photon statistics.

[b] For these observations, the values of P and $\dot{P}$ were adopted from previous studies (Sathyaprakash et al. 2019, Fürst et al. 2023).

[c] Pulse fraction is calculated from the folded profile in the 0.3–10 keV energy range.

[d] Unabsorbed luminosity is calculated in the 0.3–10 keV energy range using spectra extracted from the cleaned event files.

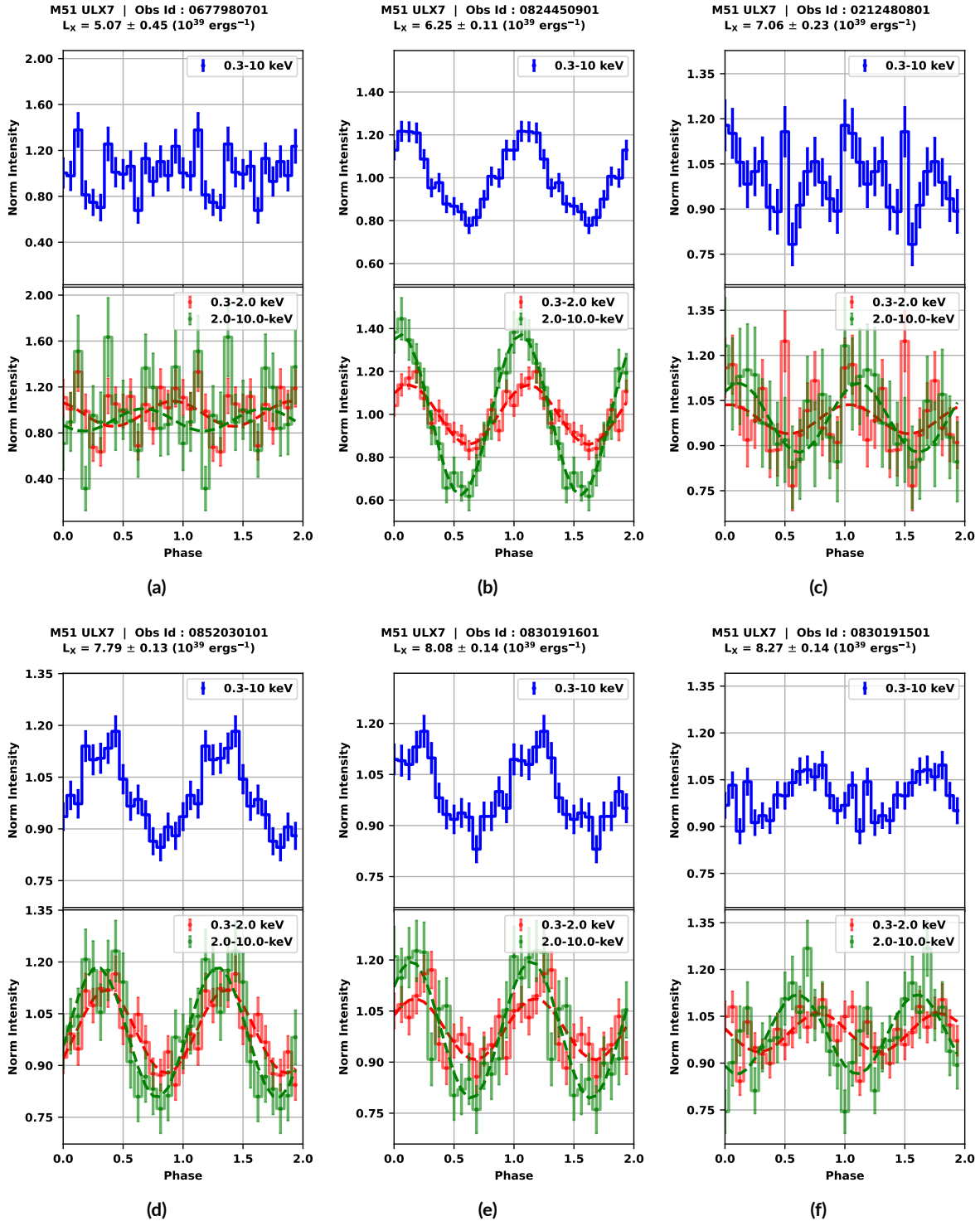


Figure 6.4: Folded pulse profiles of M51 ULX7 in the $0.3–10.0\,\mathrm{keV}$ (blue), soft ($0.3–2.0\,\mathrm{keV}$; red), and hard ($2.0–10.0\,\mathrm{keV}$; green) bands. Panels (a)–(f) are arranged in order of increasing luminosity to highlight phase differences between the soft and hard profiles. The dashed curves represent the best-fitting sinusoidal model to the folded pulse profiles.

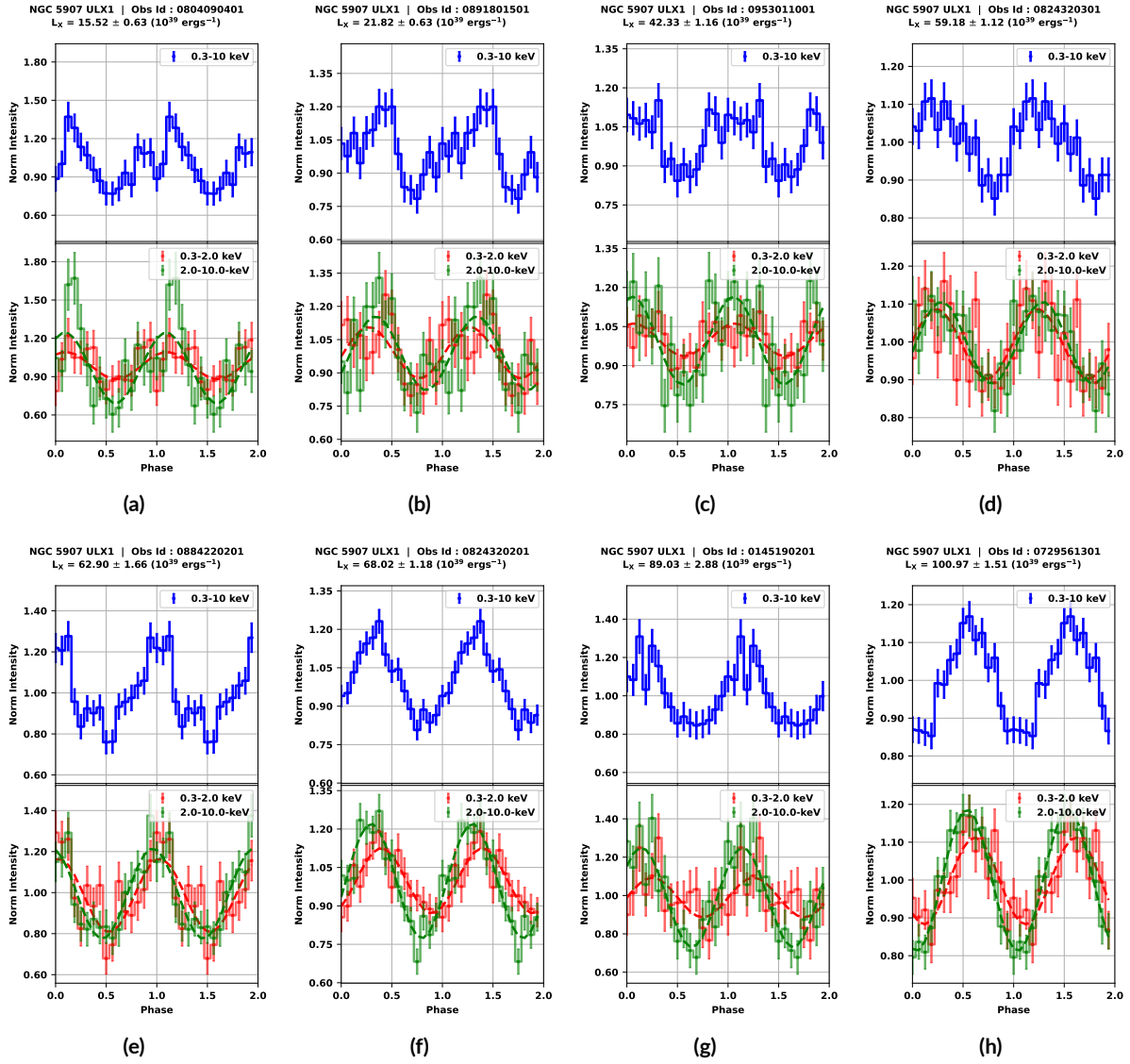


Figure 6.5: Folded pulse profiles of NGC 5907 ULX1 in the 0.3–10.0 keV (blue), soft (0.3–2.0 keV; red), and hard (2.0–10.0 keV; green) bands. Panels (a)–(h) are arranged in order of increasing luminosity to highlight phase differences between the soft and hard profiles. The dashed curves represent the best-fitting sinusoidal model to the folded pulse profiles.

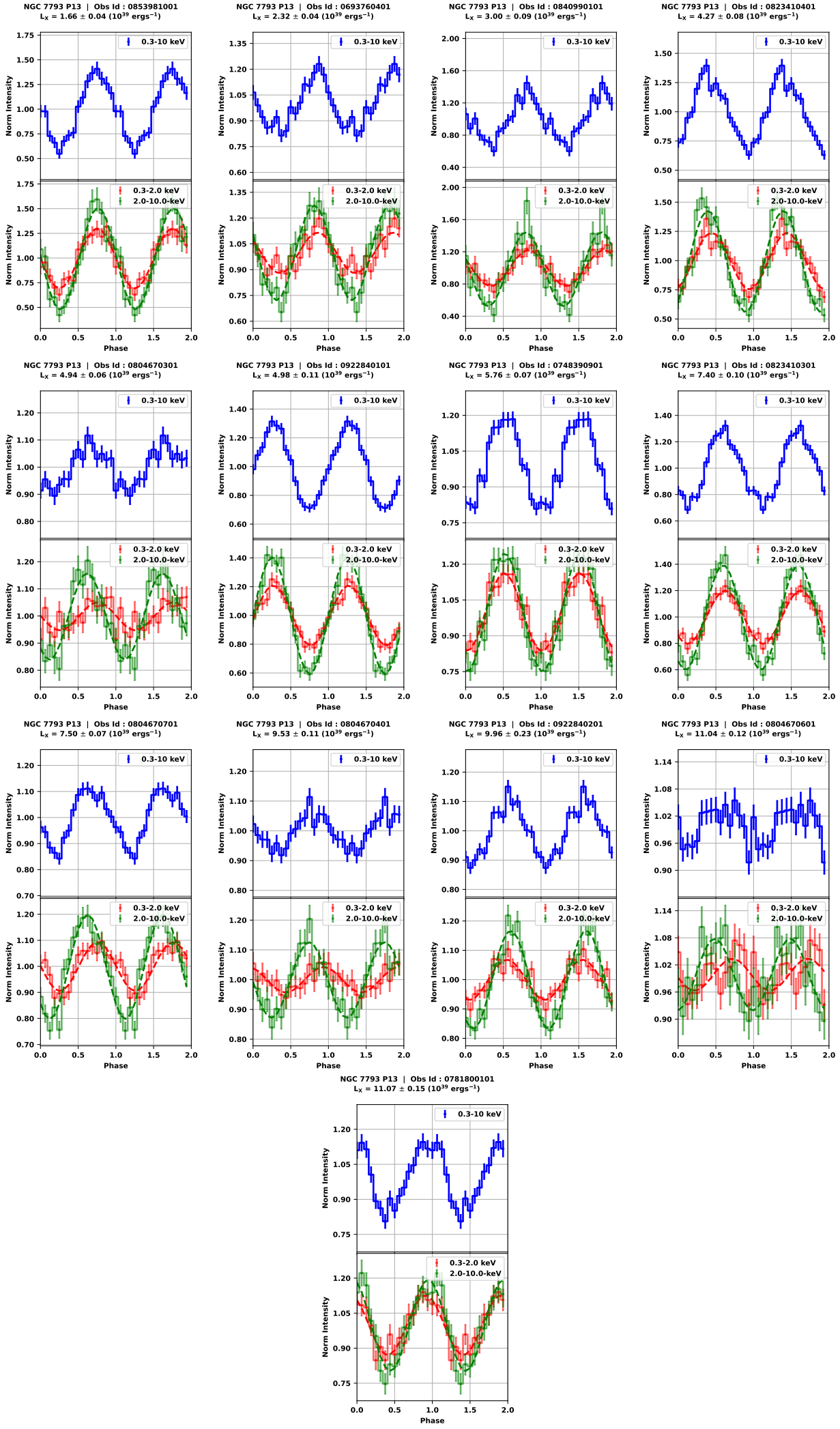


Figure 6.6: Folded pulse profiles of NGC 7793 P13, along with the best fitted sinusoidal modeled profile in dashed line, arranged in order of increasing luminosity (from top-left to bottom-center) to highlight soft–hard phase differences.

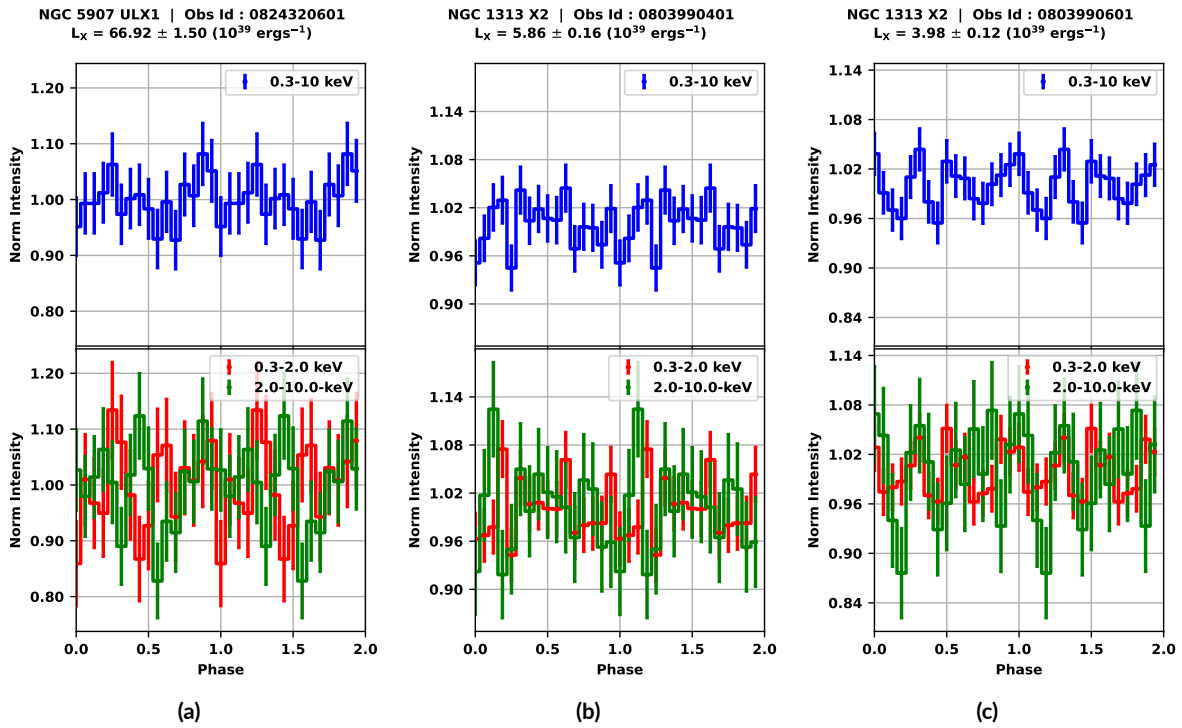


Figure 6.7: Folded pulse profiles of NGC 5907 ULX1 and NGC 1313 X2 in the $0.3–10.0$ keV (blue), soft ($0.3–2.0$ keV; red), and hard ($2.0–10.0$ keV; green) bands. No significant pulsed emission is observed.

6.5 Discussion

Timing studies of Galactic accreting X-ray binaries have shown that pulse-profile shape, pulse fraction, and energy-dependent phase behaviour provide powerful diagnostics of the accretion geometry and emission regions near the neutron star. In particular, the decrease of pulse fraction toward lower energies and the smoother pulse profiles in the soft X-ray band are commonly understood as consequences of soft X-ray emission being dominated by reprocessed radiation from the inner accretion disk or surrounding optically thick material, which tends to smear out the intrinsic pulsations (Paul et al. 2002, Hickox et al. 2004, Lutovinov & Tsygankov 2009a). In addition, long-term super-orbital variability observed in several luminous X-ray binaries has been associated with a precessing, warped accretion disk, whose changing orientation alters the visibility of the central source and leads to systematic variations in the relative phase between soft and hard X-ray pulse profiles (Hickox & Vrtilek 2005, Brumback et al. 2020). Motivated by these established results, in this work we analysed the pulse profiles of ULX pulsars to investigate whether similar energy-dependent pulse fraction trends and soft–hard phase behaviours are present under super-Eddington accretion conditions.

In this work, we utilised all available *XMM-Newton* observations of the known extragalactic ULX pulsars. For most observations listed in Table 6.3, we independently re-determined the spin period P and period derivative $\dot{P}$ using a systematic P–$\dot{P}$ search. For one observation of NGC 5907 ULX1 (ObsID 0824320601) and for NGC 1313 X-2, reliable P–$\dot{P}$ measurements could not be obtained; in these cases, values from literature were adopted and the corresponding folded pulse profiles are shown for completeness, but were excluded from the luminosity-dependent, phase-difference, and pulse-fraction analyses.

NGC 300 ULX1 is the brightest ULXP in our sample, providing high-quality photon statistics that

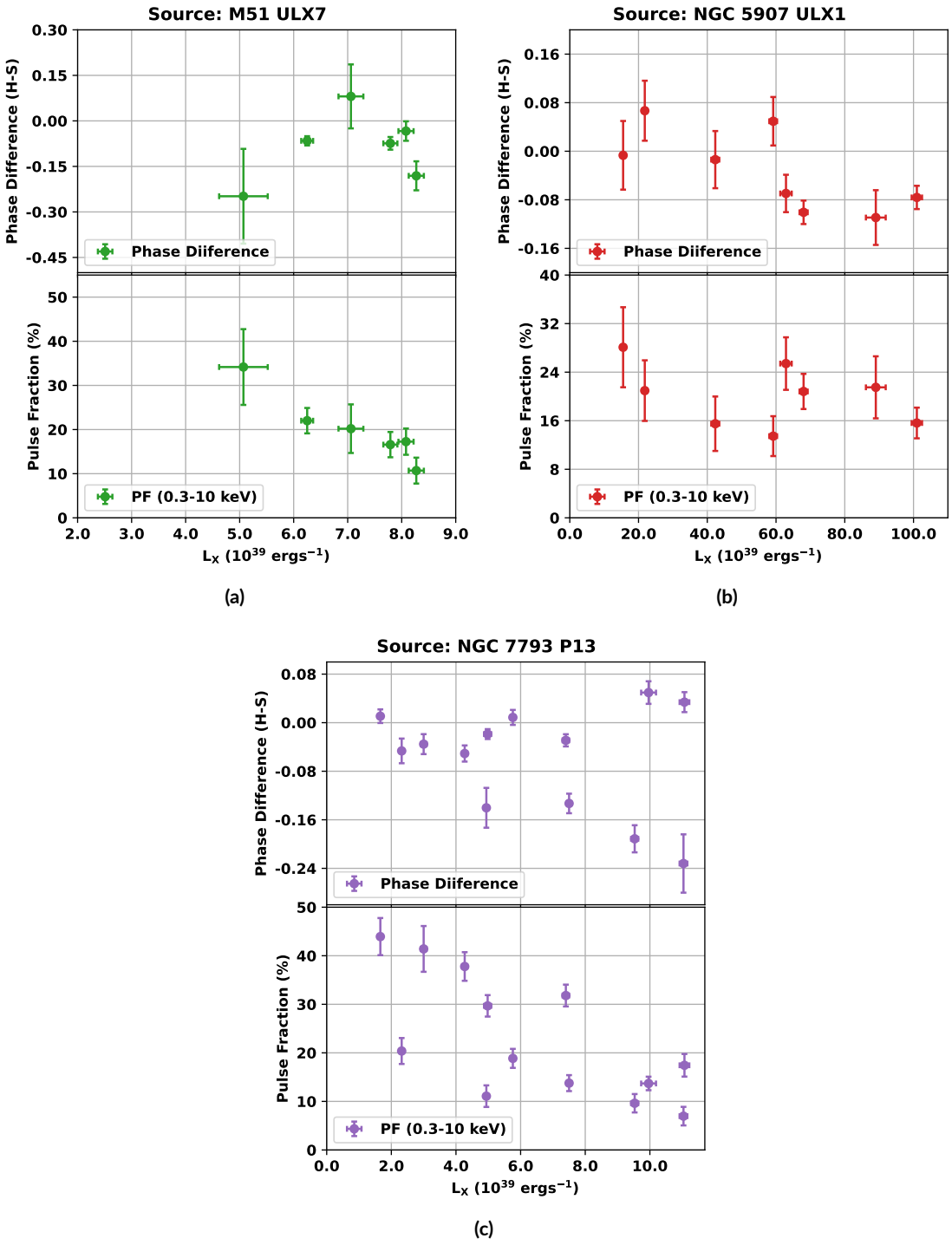


Figure 6.8: Phase difference between the hard and soft pulse profiles (top panels) and pulse fraction (bottom panels) plotted as a function of luminosity for M51 ULX7, NGC 5907 ULX1, and NGC 7793 P13 in panels (a), (b), and (c), respectively.

enable a detailed investigation of its pulse-profile properties across multiple energy bands. For this source, we examined the energy dependence of the pulse profile and pulse fraction. We find that the pulse fraction increases with energy, a behaviour that closely resembles that observed in Galactic accreting X-ray pulsars. This trend supports the interpretation that the soft X-ray emission is dominated by reprocessed radiation originating in the inner accretion disk or surrounding optically thick material. Such reprocessed emission is expected to be less strongly modulated at the neutron-star spin period, thereby diluting the pulsed signal and reducing the pulse fraction at lower energies. In contrast, the hard X-ray emission arises more directly from the accretion column and retains a stronger pulsation signature, leading to a higher pulse fraction at higher energies.

Although our primary aim was to investigate the evolution of pulse profiles with super-orbital phase, the available observational coverage is insufficient to perform a systematic comparison as a function of super-orbital phase. Instead, we examine the dependence of the pulse fraction and the phase difference between the soft and hard X-ray pulse profiles on luminosity. It is worth noting that energy-dependent pulse-profile phase differences as a function of luminosity have been studied extensively in several Be X-ray binaries, primarily in the context of transient outbursts, changing accretion regimes, and disk–neutron-star interactions (Paul & Naik 2011). In contrast, the present work focuses on persistent ULX pulsars, for which well-defined super-orbital ephemerides are often unavailable or poorly constrained due to limited observational coverage. Consequently, instead of examining phase-dependent evolution over a super-orbital cycle, we investigate the evolution of the phase difference between the soft and hard X-ray pulse profiles as a function of luminosity, with the aim of exploring whether luminosity-driven changes in the accretion flow can produce signatures consistent with geometric effects, such as a warped or precessing accretion disk, analogous to scenarios proposed for other luminous, persistent accreting X-ray pulsars.

Owing to the relatively good sampling of observations, we are able to carry out a luminosity-dependent analysis for three ULX pulsars: M51 ULX7, NGC 5907 ULX1, and NGC 7793 P13. For all three sources, we find that the overall pulse fraction decreases with increasing luminosity. A similar luminosity-dependent decrease in pulse fraction has been reported for several Galactic accreting X-ray pulsars (Tsygankov et al. 2007, Lutovinov & Tsygankov 2009a), suggesting that this behaviour may be a general feature of accretion onto magnetised neutron stars. At higher luminosities, particularly in the super-Eddington regime relevant for ULX pulsars, the structure of the accretion column is expected to change significantly. As the mass accretion rate increases, the radiative shock is predicted to move to larger heights above the neutron-star surface, leading to an extended accretion column and enhanced scattering of X-ray photons (Basko & Sunyaev 1976, Mushtukov et al. 2015b). In addition, a larger fraction of the observed emission may originate from optically thick material surrounding the neutron star, such as the inner accretion disk, accretion curtain, or radiatively driven outflows (Mushtukov et al. 2017). Emission from these regions is only weakly modulated at the spin period and can therefore dilute the intrinsically pulsed emission produced close to the magnetic poles, resulting in a reduced observed pulse fraction (Mushtukov et al. 2015a, 2017). In Galactic X-ray pulsars, the decrease of pulse fraction with luminosity is often interpreted as a consequence of both the increasing height of the accretion column and a transition in the beam pattern, from pencil-beam–dominated emission at lower luminosities to fan-beam–dominated emission at higher luminosities, together with increased multiple scattering within the column (Basko & Sunyaev 1976, Tsygankov et al. 2007, Lutovinov & Tsygankov 2009b). The qualitative similarity between the trends observed in ULX pulsars and Galactic systems suggests that related physical mechanisms may be operating in both cases, although under substantially more extreme accretion conditions in ULXPs.

In contrast to the pulse fraction, we do not find a clear or systematic dependence of the phase dif-

ference between the soft and hard X-ray pulse profiles on luminosity across the ULX pulsars analysed in this work. Although the measured phase offsets vary over the sampled luminosity range, they do not follow a coherent or monotonic trend when considered as a population. A closer, source-by-source inspection, however, reveals some qualitative differences in behaviour. For M51 ULX7, the phase difference exhibits a modest increase with luminosity at lower luminosities, followed by a decrease at higher luminosities, indicating a non-monotonic evolution. In the case of NGC 5907 ULX1, the phase difference shows an overall decreasing tendency with luminosity beyond a threshold of $\gtrsim 60 \times 10^{39}\,\mathrm{erg\,s^{-1}}$, although with noticeable scatter. For NGC 7793 P13, the phase difference remains approximately constant up to intermediate luminosities ($\sim 6 \times 10^{39}\,\mathrm{erg\,s^{-1}}$), with increased scatter observed at the highest luminosities probed.

Despite these source-specific variations, the absence of a consistent or common luminosity-dependent trend prevents us from drawing firm conclusions about systematic changes in the accretion geometry, such as the presence or evolution of a warped or precessing accretion disk. Given the current data quality and limited sampling, it is not possible to determine whether the observed variations reflect intrinsic source behaviour or are dominated by statistical uncertainties. More extensive long-term observations, covering a broader luminosity range and providing improved photon statistics, will be required to robustly characterise the evolution of phase differences and to place meaningful constraints on possible changes in the accretion flow of ULX pulsars.

7

POLIX : **I**ndian **X**-ray **Pol**arimeter

Acknowledgment

The work presented in this chapter is the outcome of a collective effort, and I am deeply grateful to be part of the POLIX team. The development, calibration, and testing of the instrument were made possible through the dedication, expertise, and hard work of **Prof. Biswajit Paul**, **Prof. Vikram Rana**, **Rishin P. V.**, **Krishna Murthy S.**, **Gopala Krishna M. R.**, **Harikrishna Sahu**, **Md. Irshad**, **Mamatha T. S.**, **Sandhya**, **Pooja Verma**, **Hemanth M.**, **Ketan Rikame**, **Sujay Mate**, **Kinjal Roy**, **Ashwin Devaraj**, **Rahul Sharma**, **Nandini Srianand**, **Anirban Dutta**, **Puttaswamy M.A.**, **Ajith Balu**, and many others, who contributed at various stages of the mission.

I humbly acknowledge that the work presented here is only a small contribution to the much larger effort carried out collectively by the entire POLIX team. I am grateful to the team for their continuous support and for giving me the opportunity to learn, contribute, and grow as part of this journey.

7.1 Introduction

The physical processes occurring in the vicinity of compact objects, such as neutron stars and black holes, have traditionally been explored through spectroscopic and timing analyses. These methods provide insights into emission mechanisms, accretion flows, magnetic field strengths, and variability patterns. However, spectral and timing studies alone cannot fully constrain the geometry of the emission region or the physical orientation of the radiation field. X-ray *polarimetry* adds a crucial third dimension to high-energy astrophysics by measuring the orientation and degree of polarization imprinted on photons as they escape from extreme environments. Polarization carries information about anisotropies, magnetic field topology, scattering geometry, and general relativistic effects, allowing us to probe the immediate surroundings of compact objects far more deeply than with intensity and spectral measurements alone (Novick 1975, Rybicki & Lightman 1979, Bellazzini & Muleri 2010).

X-ray polarization is measured by analyzing the angular distribution or track structure of secondary particles (scattered photons or ejected photo-electrons) produced when the incident X-ray photons interact with matter in the detector. The dominant interaction mechanism depends strongly on the photon energy, leading to different classes of X-ray polarimeters. At energies below $\sim$ 8 keV, the **photoelectric effect** overwhelmingly governs the interaction. When a photon is absorbed by an inner shell electron, the ejected photoelectron emerges preferentially along the direction of the electric field vector of the incoming photon. Imaging the ionisation track of the photoelectron therefore provides direct access to the polarization vector. This concept underlies modern photoelectric polarimeters such as the Gas Pixel Detector (GPD), where fine-pixel gas detectors are used to reconstruct the initial photoelectron emission direction (Costa et al. 2001, Bellazzini et al. 2006). These detectors require gas mixtures that balance sufficient stopping power with long electron drift paths to preserve the track morphology. The modulation factor is reduced by effects such as Auger electrons and electron diffusion, but the method remains highly effective in the soft X-ray band (2–8 keV).

In the intermediate energy band of 8–50 keV, the dominant interaction mechanism is **Thomson scattering**. In this regime, elastic scattering of photons by free or weakly bound electrons produces a strong azimuthal modulation, with photons preferentially scattered perpendicular to the polarization direction (Rybicki & Lightman 1979). Thomson polarimeters employ low-Z passive scattering elements to minimize photoelectric absorption, along with surrounding detectors to record the distribution of scattered photons. The azimuthal distribution of the scattered photons directly encodes the polarization degree in its modulation amplitude and the polarization angle in its phase (Novick 1975, Meszaros et al. 1988). This technique is particularly suited for bright X-ray sources, as the scattering probability is low and large photon statistics are required. However, Thomson scattering polarimeters can achieve high modulation factors and operate in the 8-30keV range where photoelectric and Compton techniques are less efficient.

At energies above $\sim$50 keV, **Compton scattering** becomes the dominant interaction mechanism. Here, the scattered photon loses energy upon interacting with an electron, and the azimuthal angle of the scattering event is modulated according to the incident polarization. The Klein–Nishina cross-section predicts that photons scatter preferentially perpendicular to the electric field vector (Rybicki & Lightman 1979, Krawczynski et al. 2011). Compton polarimeters therefore rely on detecting *double events*: a primary Compton scatter followed by the absorption of the scattered photon in a second detector element. By reconstructing the geometry of these two interactions, particularly the azimuthal scattering angle, it becomes possible to infer the polarization degree and angle. This technique requires detectors with fine spatial segmentation and good energy resolution.

The earliest efforts in X-ray polarimetry were carried out at soft X-ray energies using Bragg-reflection

payloads flown on sounding rockets, which achieved the first detection of X-ray polarization from the Crab Nebula (e.g. Novick et al. 1972). This was followed by the *satellite*-borne OSO–8 mission, which measured the Crab's polarization at 2.6 and 5.2 keV, confirming the synchrotron origin of its X-ray emission (Weisskopf et al. 1978). Despite this success, technological limitations prevented major progress for nearly four decades. The revival of the field began with the development of finely pixelated gas detectors capable of imaging photoelectron tracks, leading to the launch of the Imaging X-ray Polarimetry Explorer (IXPE) (Weisskopf et al. 2016, 2022). IXPE has since provided the most detailed soft X-ray polarization measurements to date, advancing our understanding of pulsar wind nebulae, X-ray binaries, supernova remnants, and AGN in the energy band 2–8 keV.

In the hard X-ray band, Compton-based polarization measurements have been demonstrated using both dedicated and non-dedicated instruments. The POLAR experiment aboard China's Tiangong-2 laboratory successfully implemented large-area Compton polarimetry in the 50–500 keV range and measured the polarization of multiple Gamma-Ray Bursts (Kole et al. 2017, Produit et al. 2018, Zhang et al. 2019). In addition, instruments primarily designed for imaging and spectroscopy, such as INTEGRAL/IBIS and AstroSat/CZTI, have shown that pixelated solid-state detectors can record Compton double events and extract polarization information for bright sources, including the Crab pulsar and several GRBs (Forot et al. 2008, Chattopadhyay et al. 2014, Vadawale et al. 2015). These results highlight the potential for future dedicated Compton polarimetry missions capable of probing high-energy emission mechanisms in magnetars, GRBs, and accreting black holes.

A major effort towards polarisation measurement in the intermediate energy band (8–30 keV) is the Indian X-ray polarimetry mission *XPoSat* (Paul 2022). Its primary instrument, *POLIX*, is a dedicated Thomson scattering polarimeter designed to measure the azimuthal distribution of scattered photons by rotating the instrument about the viewing axis. POLIX bridges the energy gap between photoelectric polarimeters (such as IXPE) and Compton polarimeters (such as CZTI), enabling measurements in a crucial but previously underexplored energy range. Together with the XSPECT instrument, which provides simultaneous spectroscopy and timing, XPoSat will allow comprehensive multi-parameter investigations of bright X-ray sources (Vatedka et al. 2025). This chapter outlines the fundamental principles, detection techniques, and standard formalism of X-ray polarimetry, with a particular focus on the POLIX instrument and the aspects of its development to which I have actively contributed.

7.2 Standard formalism for polarization measurement

X-ray polarimetry exploits the fact that polarized photons interact anisotropically with matter, producing characteristic angular distributions in the detected secondary particles, such as scattered photons or photoelectrons. When such photons are recorded as a function of azimuthal angle ϕ, the response of a polarimeter generally follows a $\cos^2$ modulation. Because this modulation is periodic over 180° rather than 360°, the polarization angle is defined only modulo 180°; equivalently, linear polarization is uniquely constrained to the range 0°–180°. The observed count rate may be written as

$$C(\phi) = A + B\cos^2(\phi - \phi_0), \tag{7.1}$$

where A represents the unpolarized component, B is the amplitude of the polarized component, and ϕ_0 is the polarization angle of the incident radiation. From this expression, the fractional modulation amplitude is defined as

$$a = \frac{C_{\max} - C_{\min}}{C_{\max} + C_{\min}} = \frac{B}{2A + B}. \tag{7.2}$$

A key performance metric for any polarimeter is the strength of modulation it produces when exposed to a fully (100%) polarized beam. This quantity, known as the modulation factor μ, is given by

$$\mu = \left(\frac{C_{\max} - C_{\min}}{C_{\max} + C_{\min}} \right)_{100\%\,\mathrm{pol}} = \left(\frac{B}{2A + B} \right)_{100\%\,\mathrm{pol}}. \tag{7.3}$$

In an ideal polarimeter $\mu = 1$, while a completely polarization-insensitive system has $\mu = 0$. For any instrument with $0 < \mu < 1$, the observed modulation amplitude for a source with intrinsic polarization degree p scales as $a = p\mu$. In the presence of source and background count rates r and b, respectively, the measured degree of polarization becomes

$$P = \frac{ar}{\mu r + b}. \tag{7.4}$$

Because photon arrivals follow Poisson statistics, even an unpolarized source can produce a non-zero measured modulation. The probability of measuring a modulation amplitude a and phase ϕ for a true amplitude $\hat{a}$ and phase $\hat{\phi}$ is described by (Weisskopf et al. 2010)

$$p(a, \phi | \hat{a}, \hat{\phi}) = \frac{a}{\pi \sigma^2} \exp\left[-\frac{a^2 + \hat{a}^2 - 2a\hat{a}\cos(\phi - \hat{\phi})}{\sigma^2} \right], \tag{7.5}$$

where $\sigma = \sqrt{2/N}$ for a total of N detected photons. Integrating over ϕ yields the probability distribution for the measured amplitude a, which takes the form of a Rice distribution:

$$p(a|\hat{a}) = \frac{a}{\sigma_a^2} \exp\left[-\frac{a^2 + \hat{a}^2}{2\sigma_a^2} \right] I_0\left(\frac{a\hat{a}}{\sigma_a^2} \right), \tag{7.6}$$

where I_0 is the modified Bessel function of the first kind and

$$\sigma_a = \sqrt{\frac{2(C_S + C_B)}{C_S}}, \tag{7.7}$$

with C_S and C_B being the source and background photon counts.

For an unpolarized source ($\hat{a} = 0$), this reduces to the Rayleigh distribution,

$$p(a|\hat{a} = 0) = \frac{a}{\sigma_a^2} \exp\left(-\frac{a^2}{2\sigma_a^2} \right), \tag{7.8}$$

illustrating that a non-zero modulation can arise purely from statistical fluctuations. The probability that a measured amplitude exceeds some threshold MDA for an unpolarized source is therefore

$$\int_{\mathrm{MDA}}^{\infty} p(a|\hat{a} = 0)\, da. \tag{7.9}$$

At the 99% confidence level, the corresponding minimum detectable amplitude becomes

$$\mathrm{MDA}_{99} = 3.03\,\sigma_a = 4.29\sqrt{\frac{C_S + C_B}{C_S}}. \tag{7.10}$$

Dividing this by the modulation factor yields the instrument-independent Minimum Detectable Polar-

ization (MDP),

$$\mathrm{MDP}_{99} = \frac{\mathrm{MDA}_{99}}{\mu} = \frac{4.29}{\mu}\sqrt{\frac{C_S + C_B}{C_S}}. \tag{7.11}$$

If the source has a flux S (counts s^{-1} cm^{-2}), the detector has effective area A_{eff}, efficiency ε, and the observation duration is T, substituting $C_S = \varepsilon S T A_{\mathrm{eff}}$ gives

$$\mathrm{MDP}_{99} = \frac{4.29}{\mu\sqrt{\varepsilon S T A_{\mathrm{eff}}}}. \tag{7.12}$$

Thus, the MDP represents the smallest polarization degree that can be reliably detected at a given confidence level and serves as the fundamental performance metric for any X-ray polarimeter.

Since the modulation curve encodes both the polarization degree (in its amplitude) and the polarization angle (in its phase), accurately constructing and fitting this curve is essential. In this context, the phase refers to the azimuthal angle at which the modulation peaks, i.e., the horizontal shift of the $\cos^2$ curve. For scattering polarimeters (Thomson/Compton) such as POLIX, this peak is offset by 90° relative to the polarization vector, whereas for photoelectric polarimeters, the peak directly corresponds to the polarization direction. The parameters A, B, and ϕ_0 are typically obtained by fitting the azimuthal distribution with the $\cos^2$ model above, though alternative methods based on event-by-event Stokes parameters are also widely used (Kislat et al. 2015). This formalism forms the basis for extracting polarization degree, polarization angle, sensitivity, and confidence levels for instruments such as the Thomson-scattering polarimeter POLIX onboard the XPoSat mission.

7.3 POLIX

POLIX is the primary scientific payload onboard the XPoSat mission, launched on 01 January 2024 by ISRO. The instrument is a Thomson–scattering X-ray polarimeter designed to measure the polarization of incident photons in the 8–30 keV energy range. Its working principle relies on the fact that linearly polarized photons scatter preferentially in the direction perpendicular to their electric-field vector. When such photons are incident along the viewing (z-) axis of POLIX, the scattered photons are redistributed anisotropically in the azimuthal (x–y) plane, producing a characteristic $\cos^2$ modulation in intensity. By recording this angular distribution of the scattered photons, POLIX derives both the polarization degree and polarization angle of the source. In essence, POLIX measures the azimuthal modulation of photons produced after Thomson scattering using four large-area gas proportional counters arranged around a central Beryllium scatterer.

7.3.1 Design

The POLIX instrument consists of four major components: (1) a top-mounted collimator, (2) a Beryllium scattering element, (3) four gas-filled proportional counters, and (4) the associated readout electronics. At the very top of the instrument is a flat-topped Aluminium collimator, which restricts the field of view to $3^\circ \times 3^\circ$ and ensures that only photons from the intended source enter the system. Its flat-topped angular response is essential for achieving uniform illumination of the scatterer while minimizing off-axis contamination. Directly below the collimator, fixed at the geometric center of the base plate, lies the Beryllium scattering disk with a diameter of 332 mm and a thickness of 40 mm. Beryllium, being a low-Z material, minimizes photoelectric absorption and allows Thomson scattering to dominate in the POLIX energy band. Only a small fraction ($< 3\%$) of the incident photons scatter in the disk, necessitating large-area detectors to intercept the scattered photons efficiently. Surrounding the Beryllium scatterer

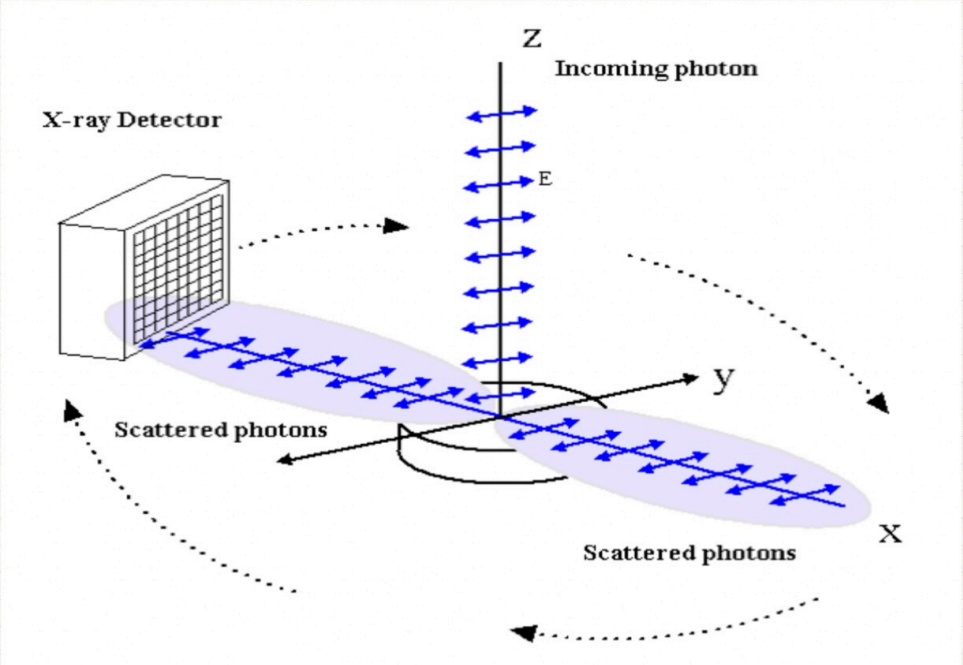


Figure 7.1: Thomson scattering of linearly polarized X-rays. Polarized photons incident along the z-axis scatter anisotropically in the x–y plane, producing a $\cos^2\theta$ modulation of intensity with azimuth (Fig. credit: POLIX Team).

on all four sides are the four identical proportional counters (D1–D4), arranged vertically like the four walls of a square enclosure. Each detector covers a specific azimuthal sector, and together they sample the entire 360° around the scattering element. As the spacecraft spins at 0.2 rpm, the orientation of each detector with respect to the incident polarization vector changes gradually, enabling POLIX to measure the azimuthal distribution $C(\phi)$ of the scattered photons and construct the characteristic modulation curve. The principal characteristics of POLIX are summarised in Table 7.1.

Table 7.1: Technical specifications of POLIX.

Parameter	Value / Description
Type	Thomson polarimeter
Energy range	8–30 keV
Field of View	$3^\circ \times 3^\circ$
Scattering element	Beryllium (332mm $\times$ 40mm)
Scattering efficiency	$< 3\%$
Photon collection area	640 cm^2
Detector type	Proportional Gas counters
Detector gas	90% Xenon + 9% Argon + 1% Methane
Gas pressure	800 Torr
Satellite spin rate	0.2 rpm

7.3.2 Proportional Gas Counter and Detection Principle

Each of the four POLIX detectors is a gas-filled proportional counter, and all four are identical in construction and operation. A single proportional counter consists of four major mechanical elements: (1) the Aluminium detector housing, (2) the wireframe containing the high-voltage anode and grounded

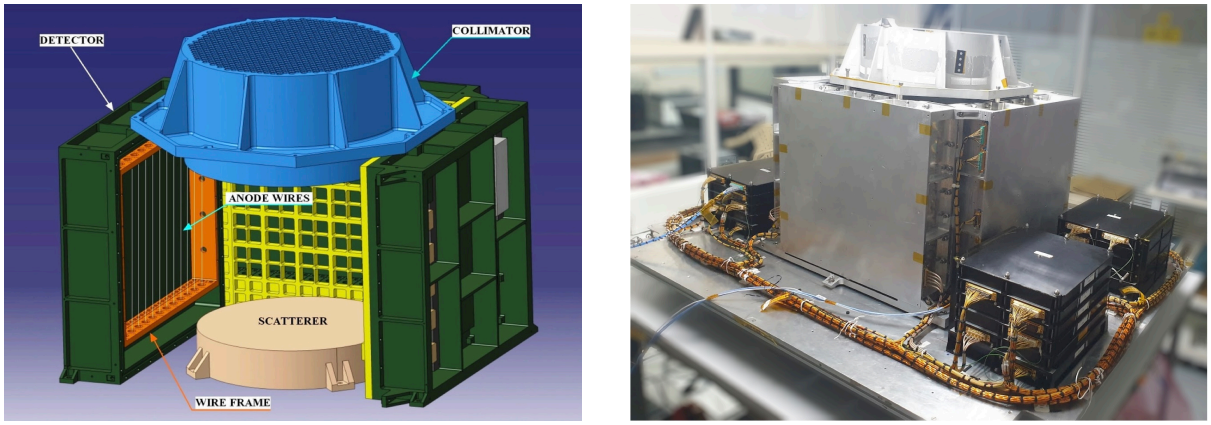


Figure 7.2: (a) Artistic illustration of the POLIX instrument with one detector removed to show the central Beryllium scatterer and internal structure. (b) Laboratory photograph of the fully assembled POLIX instrument, showing two of the four proportional counters and three attached back-end electronics modules (Fig. credit: POLIX Team).

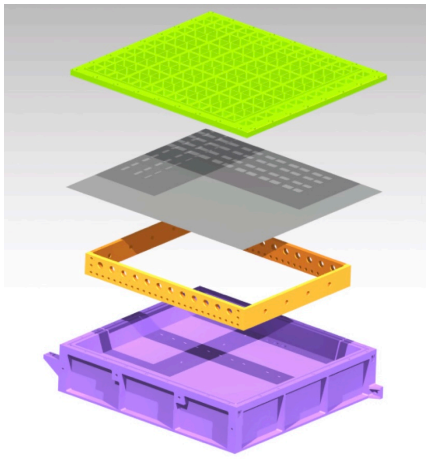
cathode wires, (3) the Mylar® window, and (4) the window-support plate. An exploded view of this assembly is shown in Fig. 7.3. The Mylar window, vapour deposited with a thin Aluminium layer, seals the detector gas while allowing X-ray photons to enter. It defines the low-energy threshold of the detector and is mechanically reinforced to withstand the internal gas pressure of 800 Torr. A wireframe is mounted inside the detector housing and contains twelve thin high-voltage anode wires. These twelve anode wires are connected in series in an alternating pattern to form two readout channels (Ch0 and Ch1), each channel consisting of six anode wires. The anode wires are surrounded on three sides (all sides except the window side) by grounded cathode wires, forming twelve well-defined anode cells within the detector volume. When a scattered photon enters the detector through the Mylar window, it undergoes photoelectric absorption in the high-Z Xenon-based gas mixture (90% Xe, 9% Ar, 1% CH_4). The absorbed photon ejects a photoelectron, initiating primary ionization. The liberated electrons drift toward the high-voltage anode wire and, in the strong electric field near the wire, undergo avalanche multiplication, producing a large number of secondary electrons. The total charge Q collected by the anode is proportional to the photon energy and splits between the two ends of the serial anode chain. The fraction of charge arriving at each end depends on the location of the photon interaction along the wire, owing to the uniform resistivity of the nichrome anode wire. As shown in figure-7.3, the charge collected at one end is proportional to the distance travelled by the charge through the resistive wire. Charge-sensitive preamplifiers (CSPAs) at the two ends of each channel measure the charges q_1 and q_2, producing voltage peaks proportional to these charge fractions. After digitization, the pulse heights PAN1 and PAN2 are obtained. Their sum,

$$\mathrm{PAN12} = \mathrm{PAN1} + \mathrm{PAN2},$$

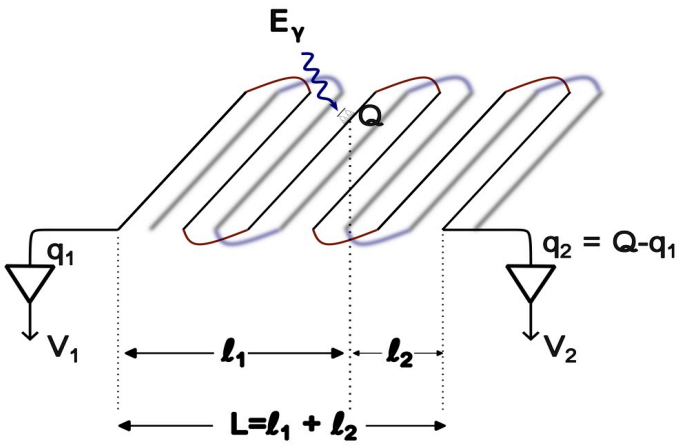
provides the photon energy, while the ratio

$$r = \frac{\mathrm{PAN2}}{\mathrm{PAN1} + \mathrm{PAN2}},$$

determines the anode wire in which the photon was detected. This charge-division method enables position sensitivity, allowing the azimuthal angle of each detected photon to be inferred. As the spacecraft spins about its pitch axis, each anode wire effectively behaves as an individual polarimeter, with its response exhibiting a characteristic phase shift determined by the POLIX geometric configuration.



(a) Components of Proportional Gas Counter



(b) Charge Divison Principle

Figure 7.3: (a) Exploded view of the POLIX proportional counter showing its main mechanical components: the detector housing (purple), the wireframe assembly (orange), the Mylar® window (grey), and the window support plate (green). (b) Illustration of the charge-division principle. The charge collected at the anode ends produces voltage pulses whose amplitudes are proportional to the distance travelled along the resistive wire. The ratio of the pulse amplitude at one end to the total pulse amplitude provides the position of photon interaction within the detector (Fig. credit: POLIX Team).

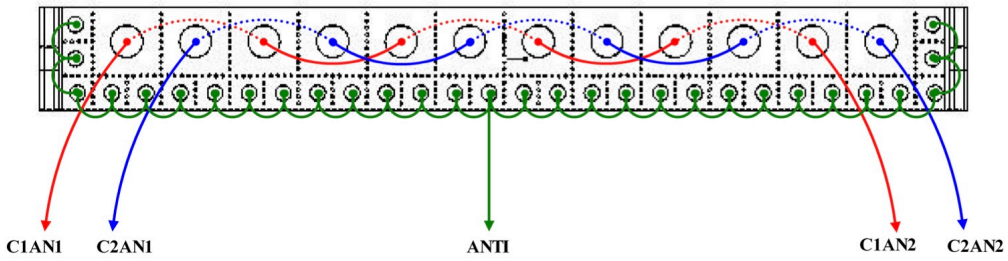


Figure 7.4: Side view of the wireframe. The red and blue segments represent detector channels 1 and 2, respectively, each formed by six main anode wires connected in series. The green segments correspond to the anti-anode wires connected to same HV source, which serve as an active veto layer for rejecting charged-particle background (Fig. credit: POLIX Team).

By combining the modulations from all 48 anode wires, and correcting each for its respective phase shift, the full azimuthal distribution of the scattered photons, $C(\phi)$, is reconstructed.

Surrounding the main anode cells on all sides, except the Mylar window, are 30 anti-anode cells, which serve as an active anti-coincidence shield for rejecting charged particle background. The anti-anode cells operate on the same detection principle as the photon-sensing anodes, but they do not require position sensitivity. All 30 anti-anode wires are connected to the same high voltage source and function as a single detector channel dedicated to background identification. Unlike X-ray photons, charged particles entering the detector gas volume typically produce long ionization tracks, depositing charge in both a main anode cell and an adjacent anti-anode cell simultaneously. This simultaneous triggering provides a reliable signature of charged particle events. Such events are rejected in real time through an on-board Field Programmable Gate Array (FPGA), which implements the anti-coincidence logic. Unlike the resistive nichrome anode wires used for charge division position sensing, the anti-anode wires are not designed to provide positional information. Their sole function is to act as an efficient veto layer, improving the purity of the detected X-ray events essential for precise polarization

measurements of a source.

7.3.3 Gas mixture and gain Stability for Propotional Gas Counter

The proportional counters of POLIX are filled with an optimized gas mixture comprising 90% Xenon, 9% Argon, and 1% Methane at a pressure of 800 Torr. This composition ensures efficient photoelectric absorption of X-rays in the 8–30 keV energy band while maintaining excellent gain stability and minimal long-term degradation during the mission lifetime.

Photon interaction in the gas mixture

The dominant interaction mechanism of X-rays within the detector gas is *photoelectric absorption*. In this process, a photon of energy E_γ interacts with a bound electron in an absorber atom, ionizing it and ejecting a photoelectron of kinetic energy

$$E_{\mathrm{PE}} = E_\gamma - E_b \tag{7.13}$$

where E_b is the binding energy of the electron shell. The scattering cross section (hence probability) of photoelectric absorption approximately follows (Knoll 2000)

$$\tau \propto \frac{Z^4}{E_\gamma^{3.5}} \tag{7.14}$$

indicating that absorption is favored for lower photon energies and higher atomic numbers. For this reason, Xenon (Z = 54) is used as the primary absorbing gas in POLIX, as its high atomic number provides superior efficiency in the target energy range. Depending on photon energy, the interaction primarily occurs in the K-shell or, for lower energies, in the L- and M-shells. The emitted photoelectron travels through the gas, producing numerous secondary ionizations and forming multiple electron–ion pairs. Not all of the photoelectron's energy contributes to ionization, some is lost through excitation and elastic scattering. Experimental measurements show that, on average, one electron–ion pair is produced for every 25–35 eV of deposited energy, a quantity known as the *W-value*. Thus, a photon of energy E_γ produces roughly E_γ/W primary ion pairs. Amplifying and detecting these charges is the fundamental principle of proportional counter operation, as their number is directly proportional to the incident photon energy.

Electron drift and avalanche multiplication

An electric field applied within the detector volume drifts the free electrons toward the anode wires. Because electrons are about 1000 times more mobile than ions, they reach the anodes within microseconds. In a sufficiently strong electric field ($\sim 10^6$ V/m), these electrons gain enough kinetic energy between collisions to ionize additional gas atoms, resulting in an avalanche of secondary electrons a process known as *Townsend avalanche multiplication*. This provides an intrinsic amplification of the initial signal. To allow the electrons to gain adequate energy before each collision, the mean free path must be sufficiently long. This is achieved by mixing a small proportion of low-Z gas (Argon) with Xenon. The added Argon ensures a balance between efficient absorption (from Xenon) and appropriate ionization dynamics.

Quenching and gain stability

After multiplication, the less mobile positive ions drift slowly toward the cathode and neutralize upon electron capture, which may lead to the emission of ultraviolet photons. These photons can trigger secondary avalanches, creating spurious pulses and dead time. To prevent this, organic polyatomic *quenching gases* are added to absorb recombination photons and de-excite ions collisionally. In POLIX,

1% Methane (CH_4) is used as a quench gas. Methane molecules efficiently suppress secondary ionizations by dissipating excess energy through molecular dissociation, thereby stabilizing the gas gain. This optimized gas mixture and design configuration provide high quantum efficiency, excellent proportionality, and long-term stability of the gain, ensuring reliable operation of the POLIX proportional counters throughout the mission.

Electric field geometry and gas gain

To preserve proportionality between the photon energy and the collected charge, the counters are designed such that the avalanche multiplication occurs uniformly near the anode wires. The electric field around a thin anode wire in cylindrical geometry decreases with distance r as (Knoll 2000)

$$E(r) = \frac{V}{r \ln(b/a)}, \tag{7.15}$$

where V is the applied voltage, a is the radius of the anode wire, and b is the radius of the surrounding cathode. This configuration ensures that the field strength reaches $\sim 10^6$ V/m only in the immediate vicinity of the anode wire (within a few wire radii). By employing thin anode wires ($b/a \sim 10^{-3}$), such high fields can be achieved with moderate operating voltages ($\sim 10^3$ V), eliminating the need for excessive High voltage.

The degree of amplification is quantified by the *gas multiplication factor*, or *gas gain* (M), which depends on the physical and operating parameters of the counter namely, the applied voltage V, gas pressure p, anode radius a, cathode radius b, the threshold field for multiplication $(E/p)_{\rm th}$, and the mean potential difference ΔV between ionizations. Assuming negligible space charge effects, the gain can be expressed as (Knoll 2000)

$$M = \exp\left[\frac{V}{\ln(b/a)} \frac{\ln 2}{\Delta V} \left(\ln \frac{V}{pa \ln(b/a)} - \ln K\right)\right], \tag{7.16}$$

where K is a proportionality constant related to the gas composition and ionization threshold.

Another factor that significantly affects the gas gain in proportional counters is the presence of trace amounts of water vapour within the detector volume. During laboratory tests, the detector may be intermittently exposed to the atmosphere, allowing small quantities of moisture to diffuse through the Mylar® window into the gas chamber. Although the Mylar window effectively retains the detector gas mixture, it is slightly permeable to water molecules. Once inside, these polar molecules act as efficient electron scavengers, capturing drifting electrons before they reach the high field region near the anode wire. This electron attachment process reduces the number of electrons available for avalanche multiplication, thereby lowering the effective gas gain. In addition, water vapour can quench the secondary electrons generated during multiplication through inelastic collisions or the formation of transient negative ions, further suppressing charge amplification. Consequently, even a small ingress of moisture can lead to a measurable drop in detector gain (Knoll 2000). However, if the detector is placed under vacuum for an extended period, the absorbed water molecules gradually diffuse out through the Mylar window, allowing the gas mixture to recover its original properties and restoring the initial gain (see figure 7.6).

7.4 Contributions to POLIX development activities

To evaluate the performance and operational readiness of the POLIX proportional counters, we analyse the spectral response and the charge ratio distributions (as defined in the previous section) for all four detectors after complete assembly and gas filling. The spectral response provides information on the

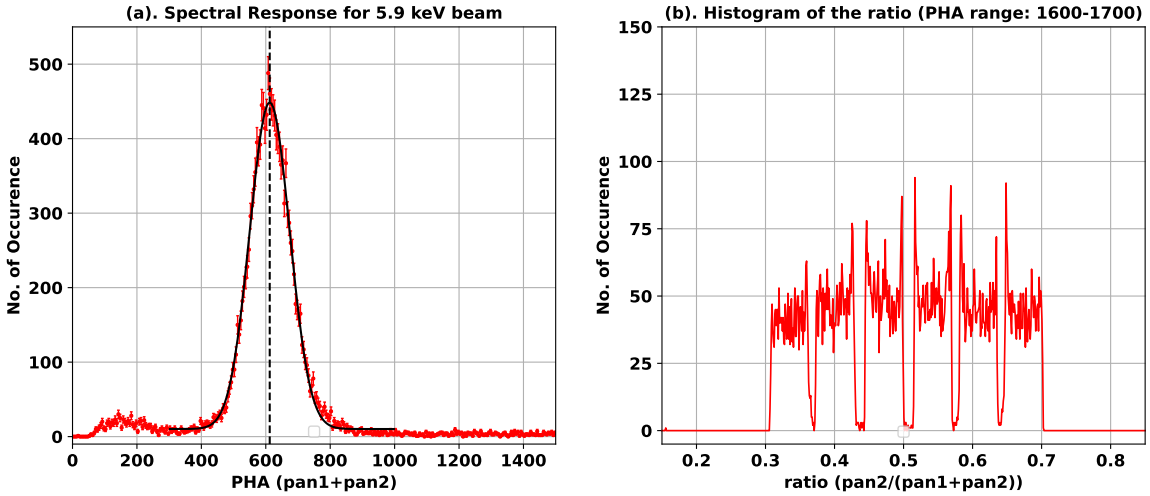


Figure 7.5: (a) Spectral response of the detector to the 5.9 keV line obtained from laboratory measurements. (b) Ratio distribution of the same data for the selected PHA range. Each pillar corresponds to one of the six anode wires, and the ratio distribution varies with the selected energy range.

energy resolution and gas gain uniformity, while the charge ratio histograms are used to verify the accuracy of position reconstruction across the anode wires. For these tests, two well-characterised radioactive calibration sources are used: ^{55}Fe, which emits monoenergetic X-rays at 5.9 keV, and ^{109}Cd, which produces prominent lines at 22.1 keV. These sources cover the lower and mid-energy parts of the POLIX operating range (8–30 keV), allowing both the position and energy calibration of each detector to be verified.

7.4.1 Gas Filling and Leak Test During Detector Assembly

Each proportional counter was filled with the prescribed gas mixture of 90% Xenon, 9% Argon, and 1% Methane at a pressure of 800 Torr and was carefully sealed. To ensure long-term no leakage of gas, the detectors were subjected to long-term gas gain monitoring following assembly. The gas gain was tracked using the 5.9 keV line from the ^{55}Fe source. A stable gas gain over time indicates that the pressure and gas composition remain unchanged, confirming proper sealing. In contrast, any significant variation in gain, particularly a gradual increase, can signal a possible slow leak, leading to reduced pressure and, consequently, a higher gain (as gas density decreases). For each detector, spectra were recorded at regular intervals, and the gain was computed from the centroid of the 5.9 keV peak. The long-term gas gain monitoring plots, shown in Figure 7.7, demonstrate the stability of the detectors over extended durations, confirming the integrity of the gas seals and the effectiveness of the leak testing procedures carried out during assembly. A similar procedure is repeated for the detectors FM03 and FM04.

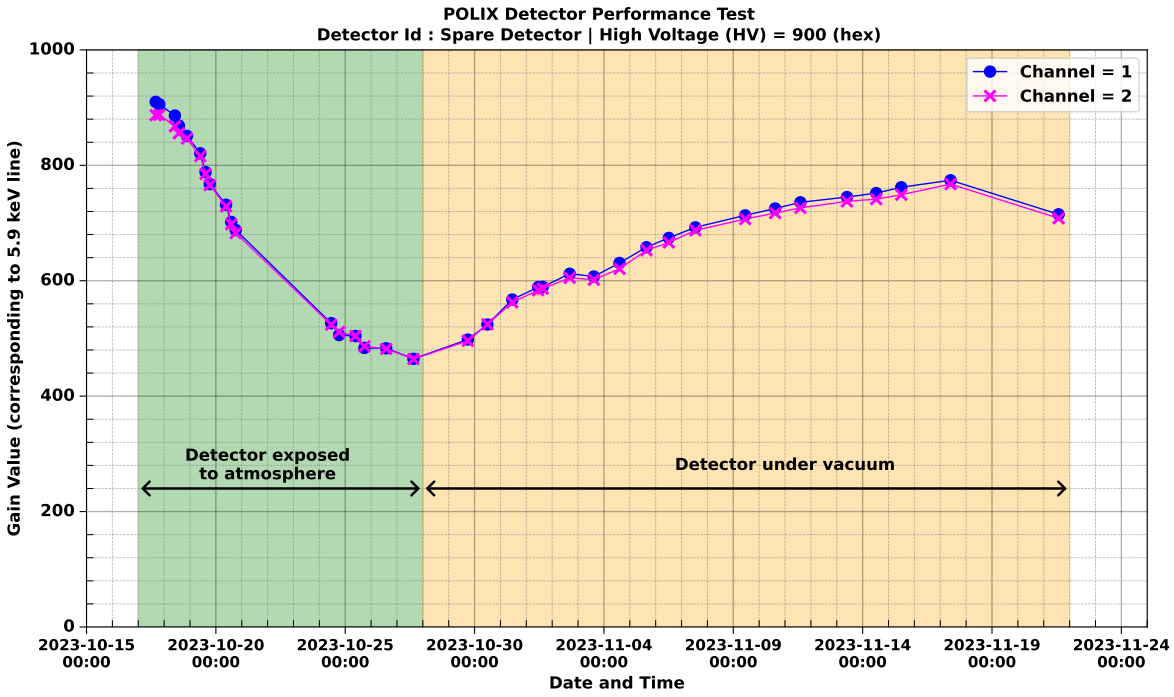
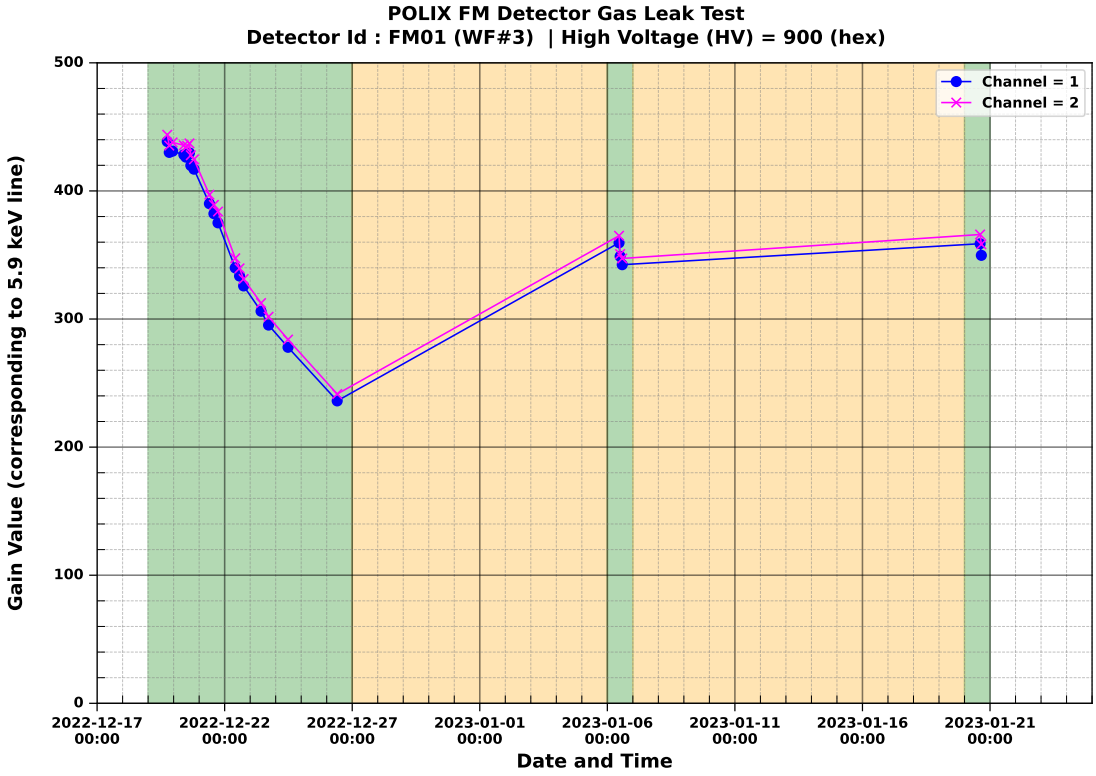
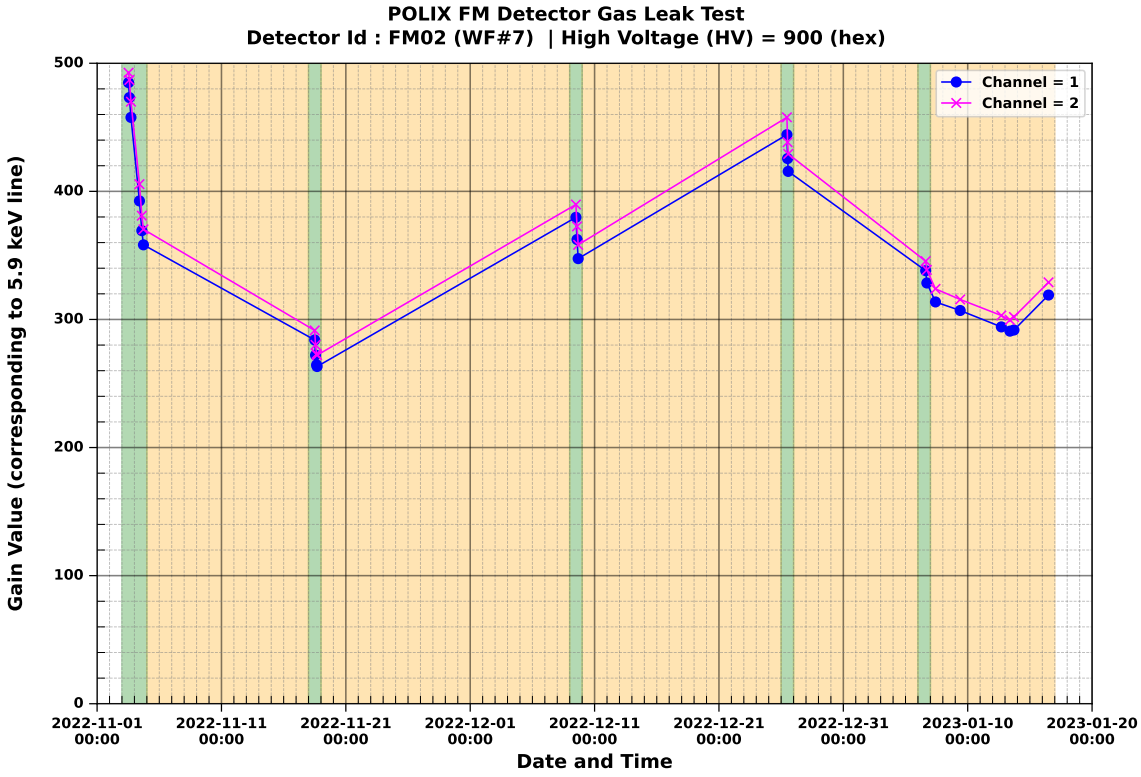


Figure 7.6: Gain monitoring using the ^{55}Fe source to assess detector performance and confirm no gas leakage. The initial gain drop arises from water vapor diffusion through the Mylar® window, while vacuum storage restores the gain as the moisture outgasses. The final small decrease is due to a temporary rise in ambient temperature on that day.



(a)



(b)

Figure 7.7: Long-term gain evolution measured using the 5.9 keV line for Detectors FM01 and FM02 following assembly. The green region denotes intervals during which the detector was exposed to ambient atmospheric conditions, whereas the orange region indicates periods when the detector was maintained under vacuum.

7.4.2 Position and Energy Calibration

Accurate determination of the photon interaction position and energy in each detector channel is essential for reconstructing the azimuthal modulation curve. Since the gas gain and energy resolution degrade rapidly when the detectors are exposed to ambient atmospheric conditions (see Fig. 7.6), the position and energy calibration measurements were carried out within a few hours of removing the detectors from the vacuum chamber to ensure optimal detector performance during calibration. To calibrate both position and energy, the two radioactive sources ^{55}Fe (5.9 keV) and ^{109}Cd (22.1 keV) were used in a systematic manner.

Experimental Setup

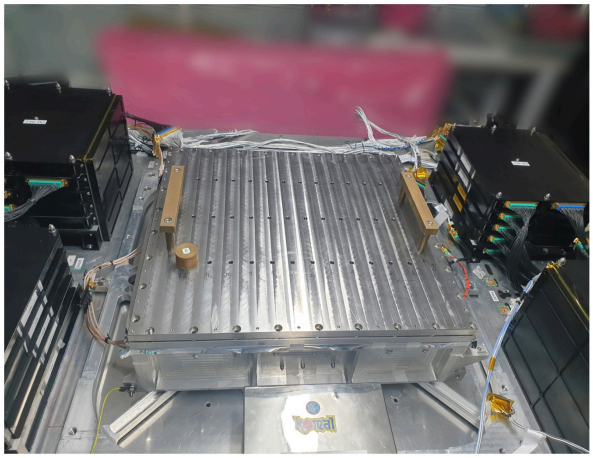
The calibration measurements are performed by sequentially placing the source at 36 well-defined positions across the detector face, corresponding to three positions on each of the twelve anode wires, as illustrated in Fig. 7.8. This ensures uniform illumination and enables mapping of the positional response along each anode channel.

Analysis

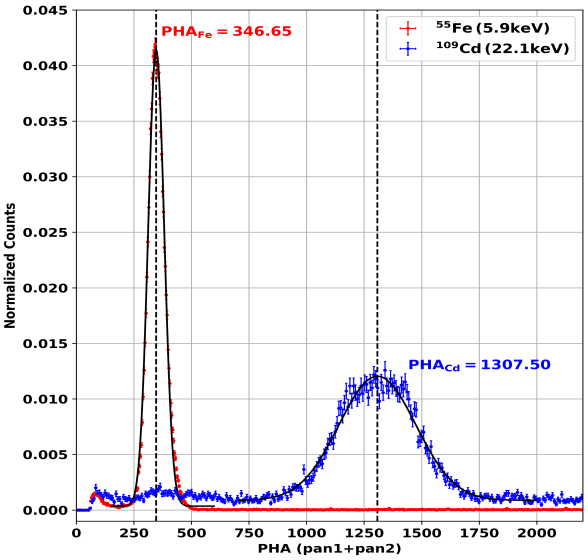
For each source position, spectra are accumulated and analyzed to determine the centroid of the photopeak corresponding to the incident photon energy. The gain-corrected pulse height (PAN1+PAN2) provides the energy calibration, while the ratio parameter $r = \mathrm{PAN2}/(\mathrm{PAN1} + \mathrm{PAN2})$ is used to determine the position along the anode, as discussed in the earlier section on charge division. The relationship between r and the physical position (distance from the one end of the wire) is then fitted with a linear function (limited to three positions on each anode wire) to derive the position calibration curve. Combining the data from all positions yields the complete position energy calibration matrix for each anode wire, ensuring precise localisation and energy measurement during in-flight operation.

Summary

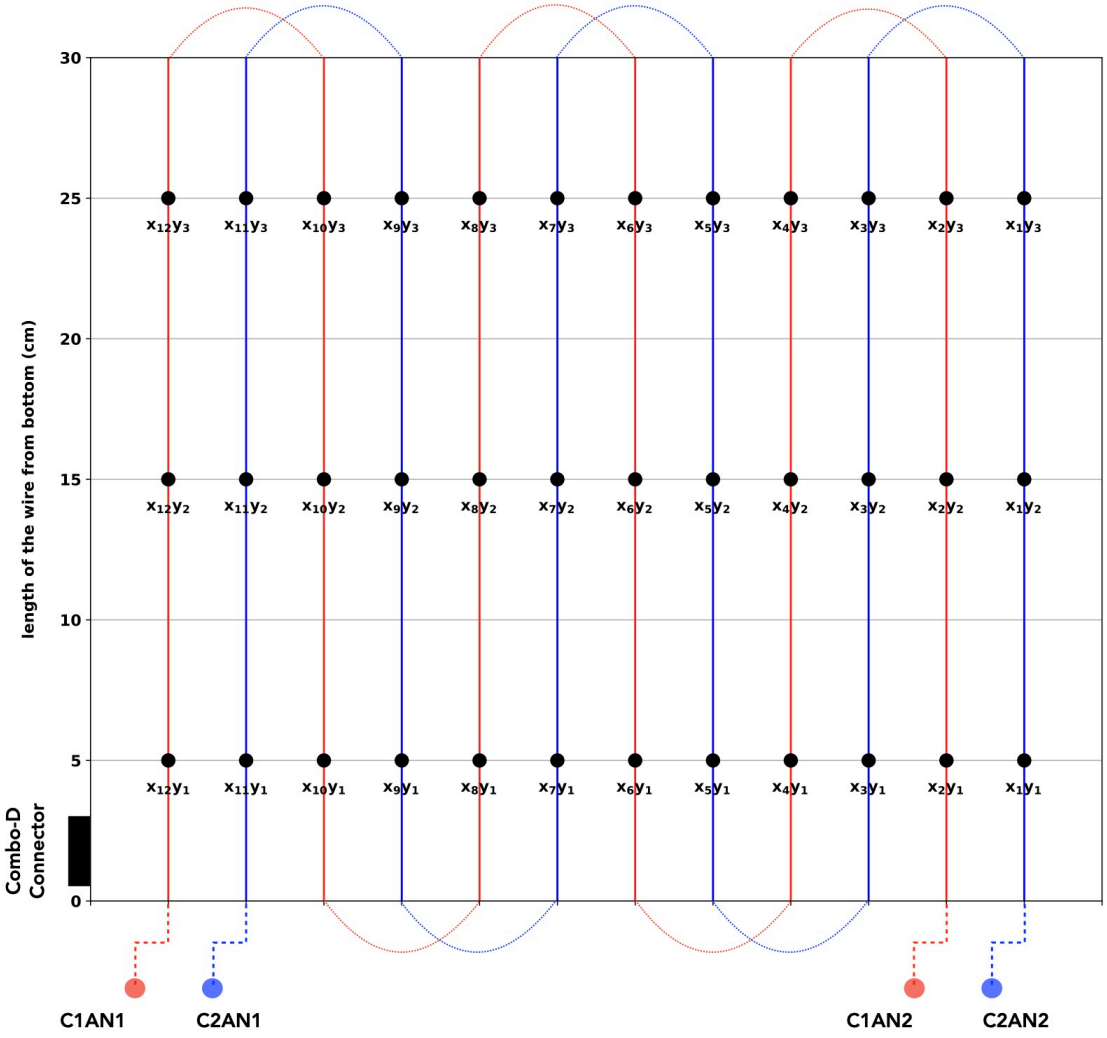
Calibration of all four POLIX detectors has allowed accurate characterization of their gain behavior and position sensitivity. Detectors 1, 2, and 3 exhibit uniform/similar gain across all 12 anode wires within each detector, indicating stable construction and consistent high-voltage response. Although the gain is uniform/similar wire-to-wire inside a detector, the overall mean gain differs slightly between detectors.Detector 4, however, shows two distinct gain groups: seven of its wires (three in Channel 1 and four in Channel 2) have a slightly larger diameter, resulting in systematically higher gain as expected from the dependence in Eq. 7.16. The ratio distributions provide reliable localization of photon interactions along each detector channel. As expected, the wire boundaries in ratio space become sharper at higher energies, leading to improved position sensitivity. An exception occurs in Detector 2, Channel 1, where the ends labelled C1AN1 and C1AN2 were interchanged during assembly, reversing the ratio definition. This is correctly handled in the calibration database and processing pipeline (see Fig. 7.13). Overall, the calibration establishes accurate position–energy mapping across the 36 reference points in each detector. The results, summarized in Figs. 7.9–7.15, confirm that the detectors achieve the required performance for constructing high-quality azimuthal modulation curves essential for polarization measurements.



(a)

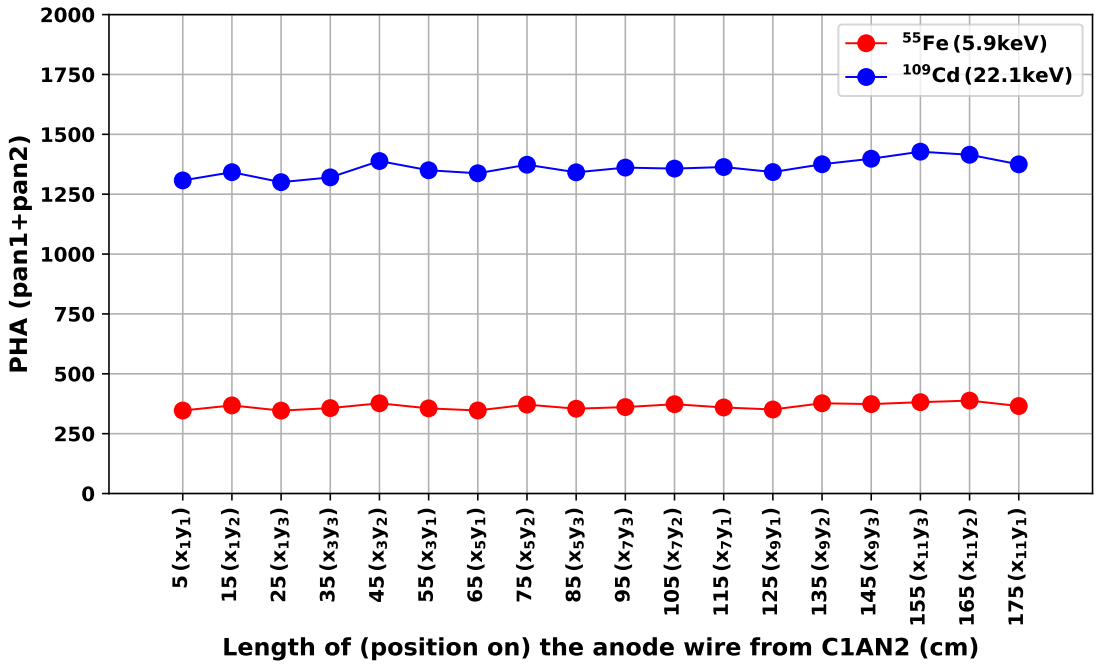


(b)

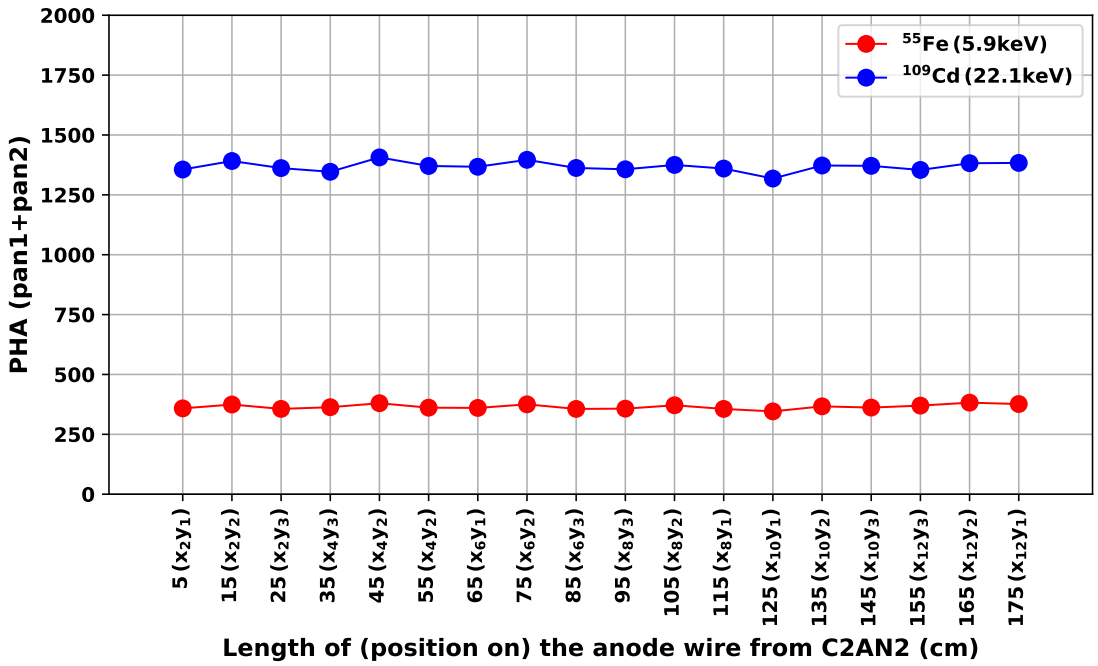


(c)

Figure 7.8: (a) Experimental setup used for detector position calibration. The sources are placed sequentially at each calibration hole, and the corresponding ratio and PHA values are recorded. (b) A sample spectral response obtained from both sources when placed at calibration position x_1y_1. (c) Artistic schematic showing the 36 calibration positions distributed across the detector surface (Fig. credit: POLIX Team).

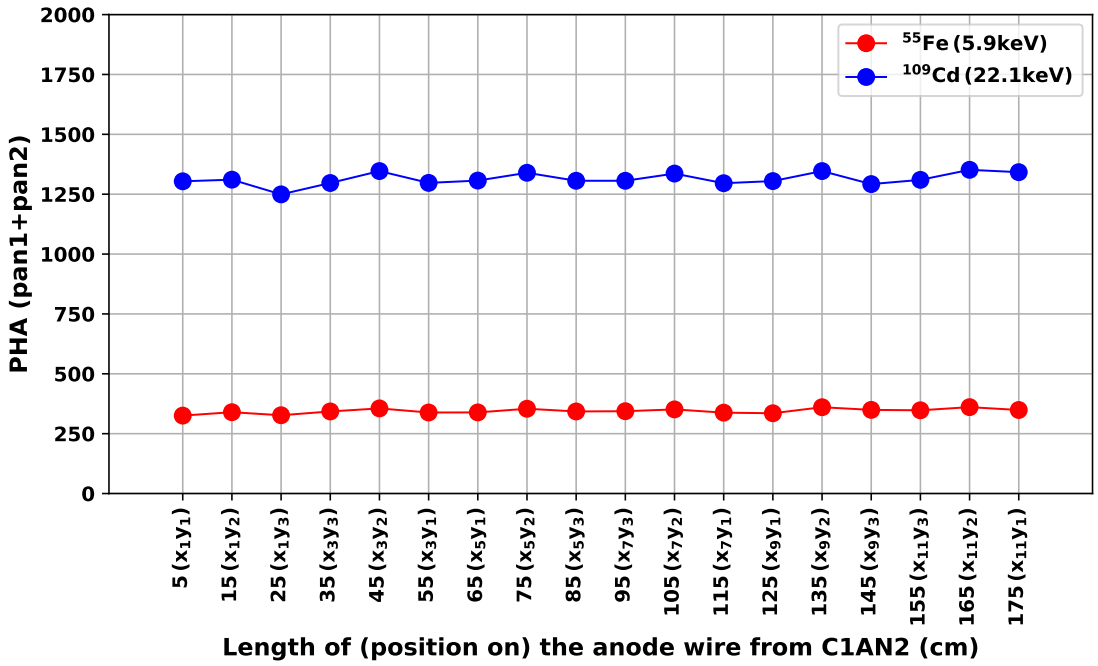


(a)

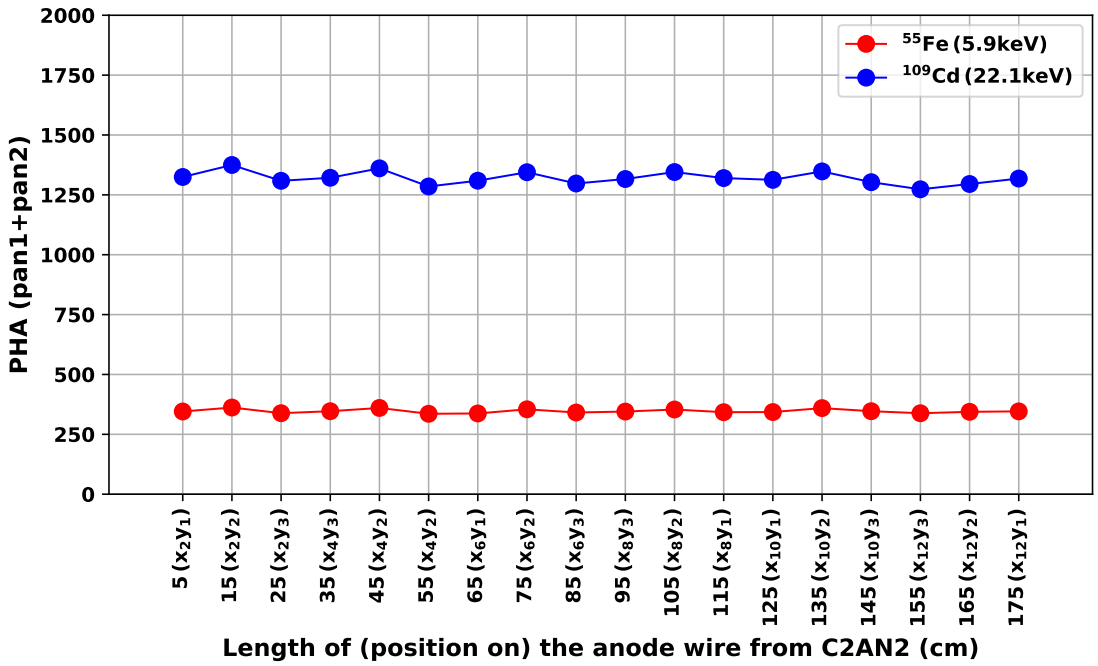


(b)

Figure 7.9: Panels (a) and (b) show the gain variation for Detector ID: FM01, corresponding to the ^{55}Fe (red) and ^{109}Cd (blue) sources across all 18 calibration positions in Channels 1 and 2, respectively, covering a total of 36 detector positions.

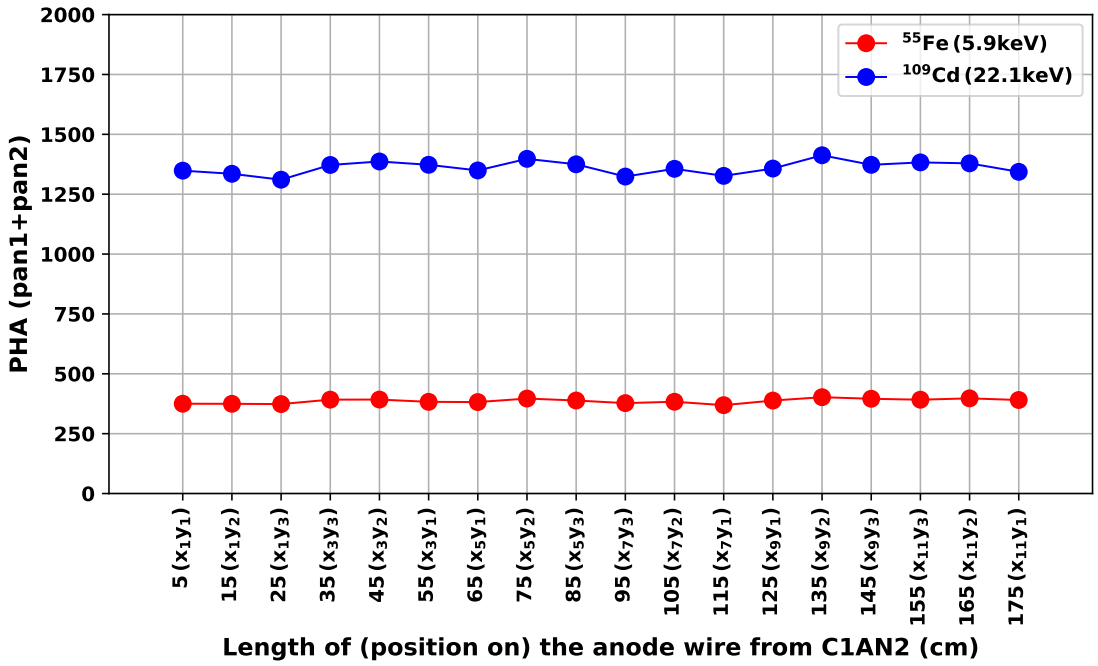


(a)

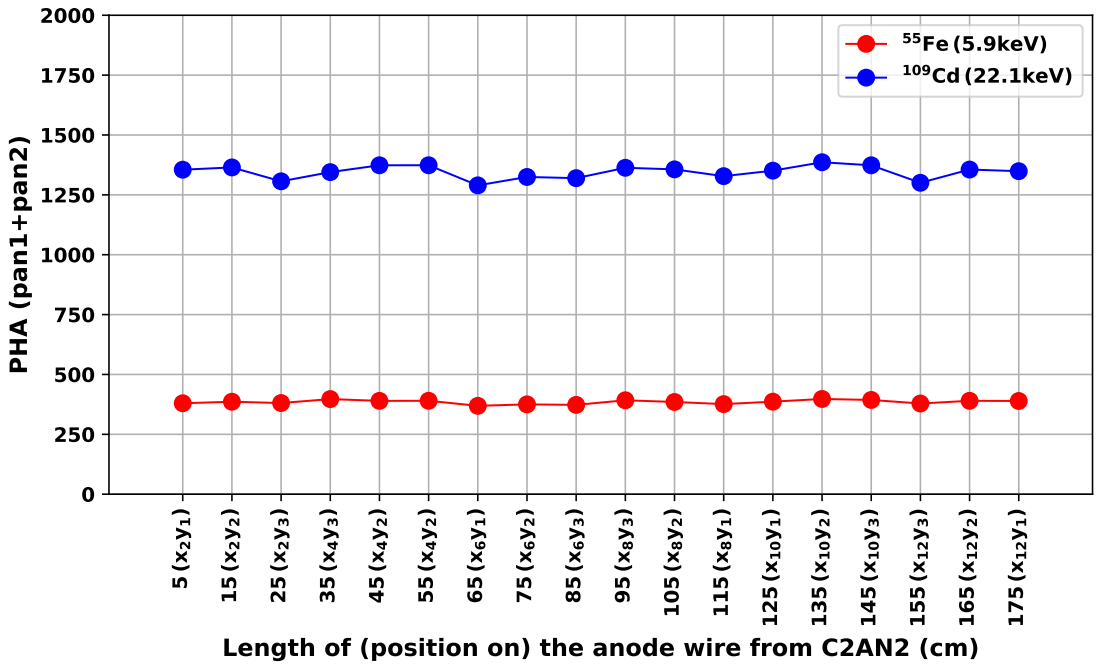


(b)

Figure 7.10: Panels (a) and (b) show the gain variation for Detector ID: FM02, corresponding to the ^{55}Fe (red) and ^{109}Cd (blue) sources across all 18 calibration positions in Channels 1 and 2, respectively, covering a total of 36 detector positions.

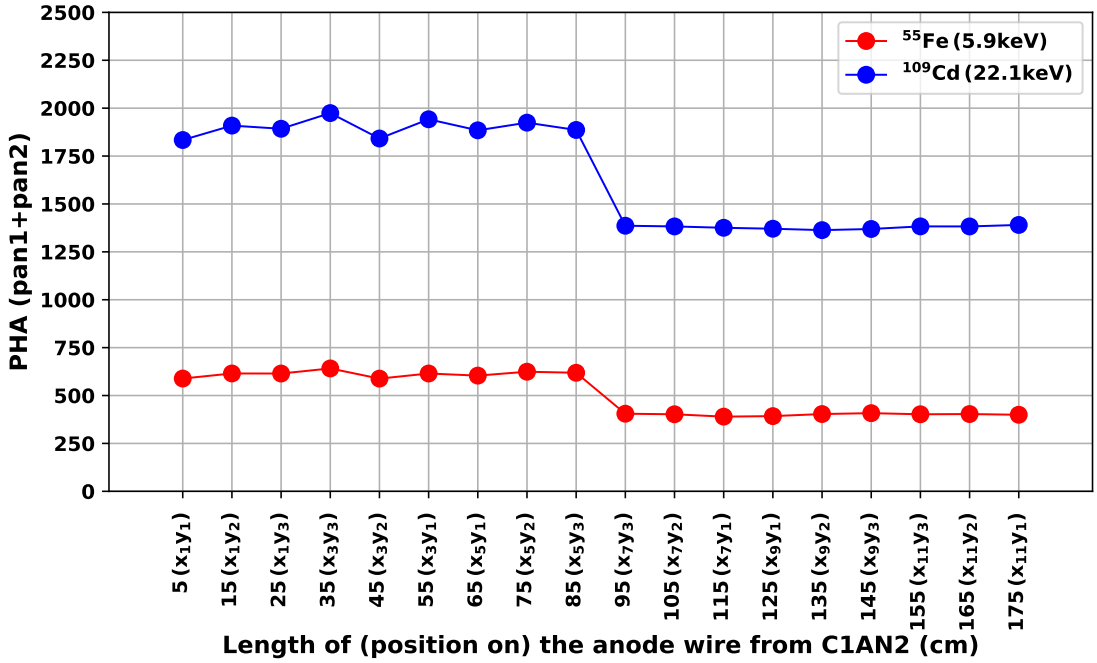


(a)

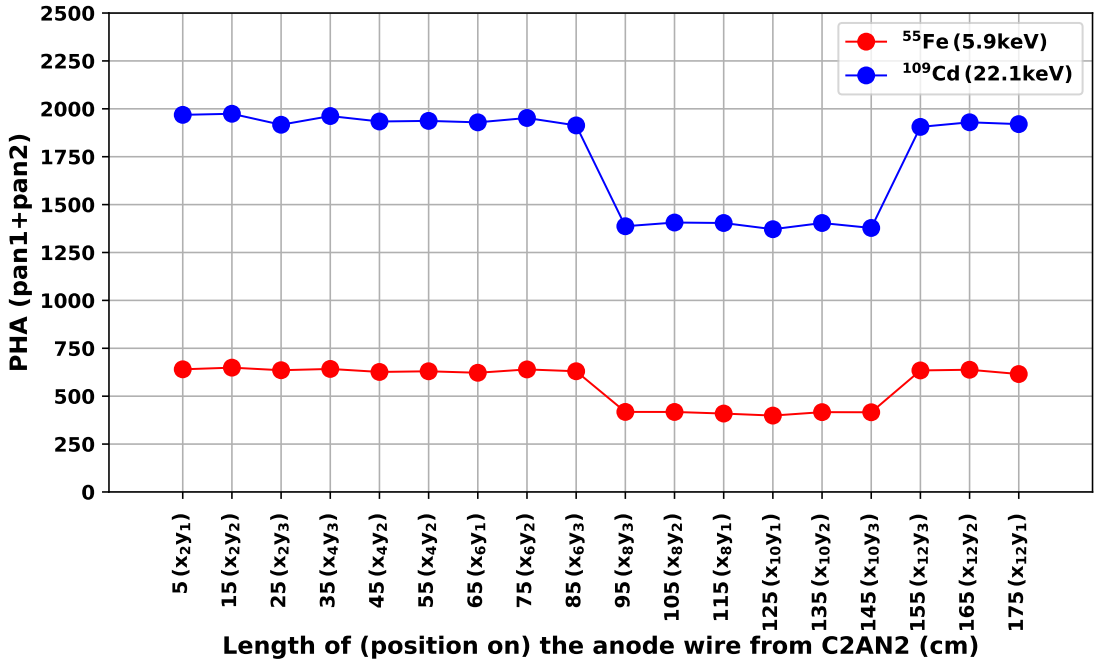


(b)

Figure 7.11: Panels (a) and (b) show the gain variation for Detector ID: FM03, corresponding to the ^{55}Fe (red) and ^{109}Cd (blue) sources across all 18 calibration positions in Channels 1 and 2, respectively, covering a total of 36 detector positions.



(a)



(b)

Figure 7.12: Panels (a) and (b) show the gain variation for Detector ID: FM04, corresponding to the ^{55}Fe (red) and ^{109}Cd (blue) sources across all 18 calibration positions in Channels 1 and 2, respectively, covering a total of 36 detector positions. In Detector FM04, seven anode wires (3 in CH1 and 4 in CH2) have a larger diameter, which leads to a higher gain relative to the other wires.

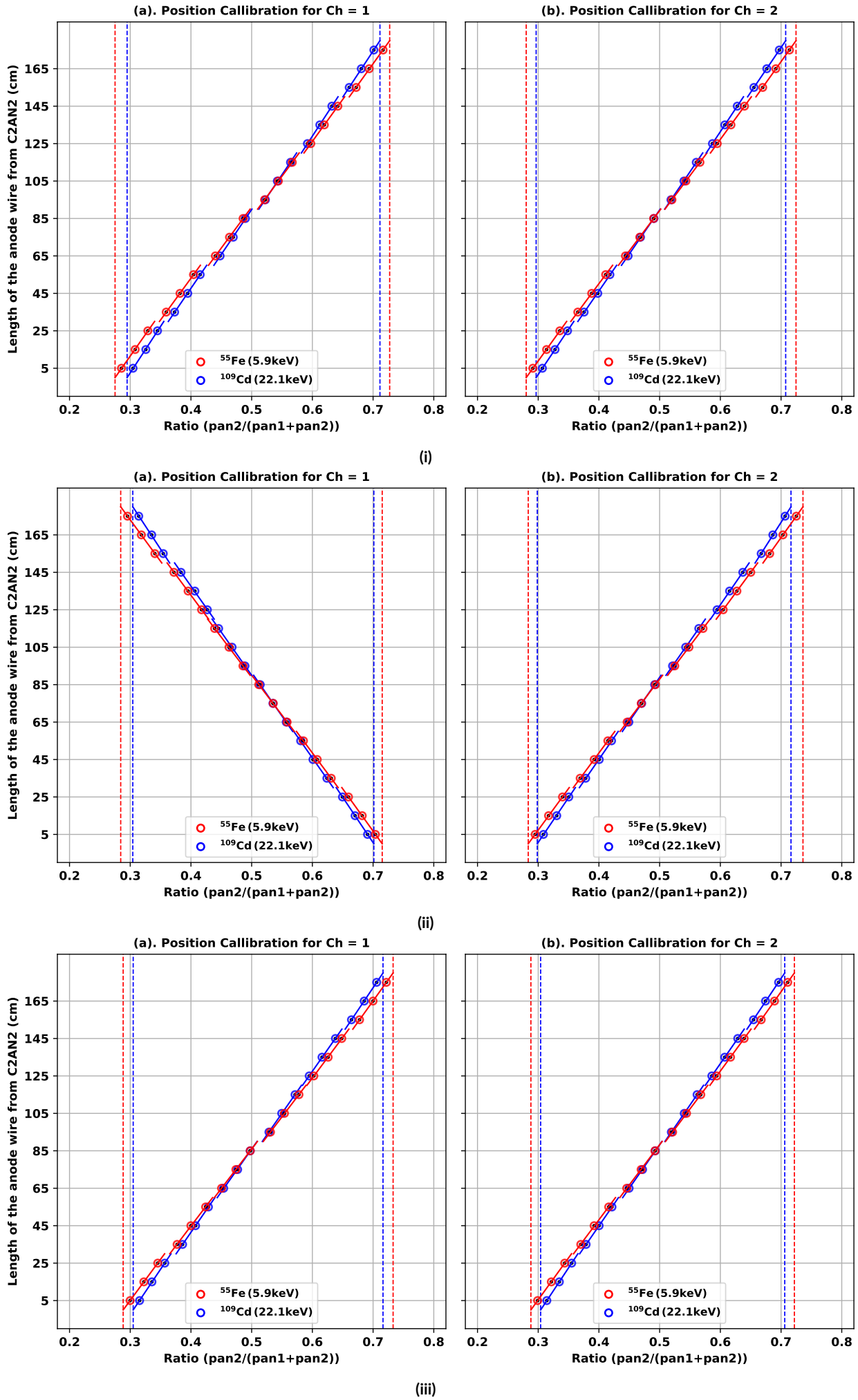


Figure 7.13: Panels (i), (ii), and (iii) show the position versus ratio distributions for both channels of detectors FM01, FM02, and FM03, respectively. As expected, the ratio spread across all six anode wires is narrower at higher energies. For Detector 2, Channel 1, the ratio trend appears reversed due to the interchange of the C1AN1 and C1AN2 ends during assembly.

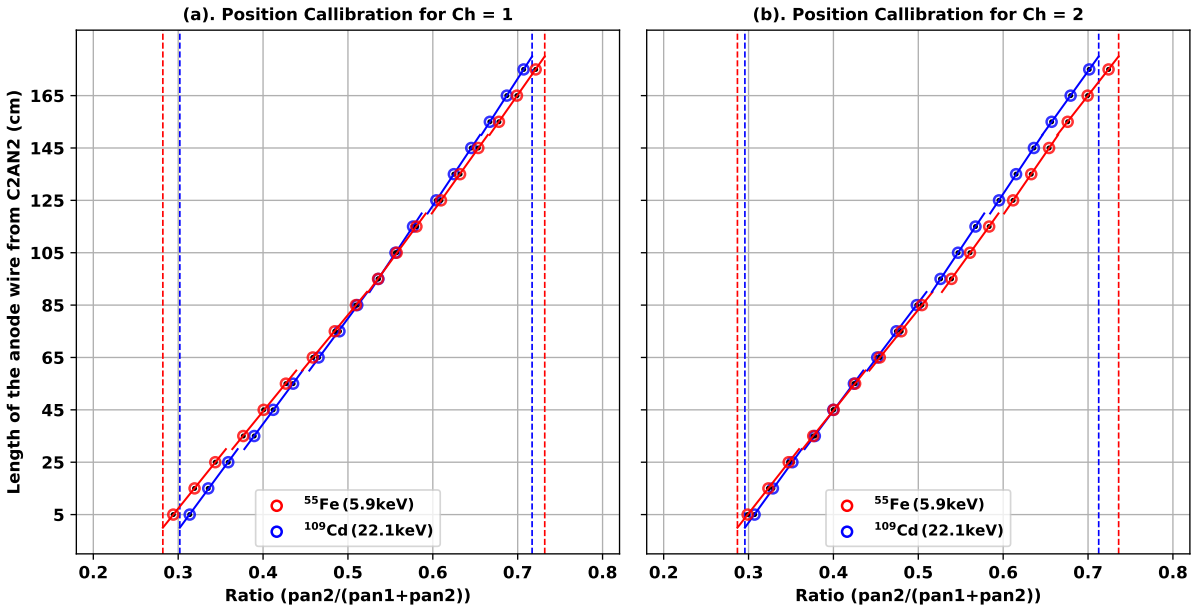


Figure 7.14: Position versus ratio distributions for both channels of detectors FM04. As expected, the ratio spread across all six anode wires is narrower at higher energies.

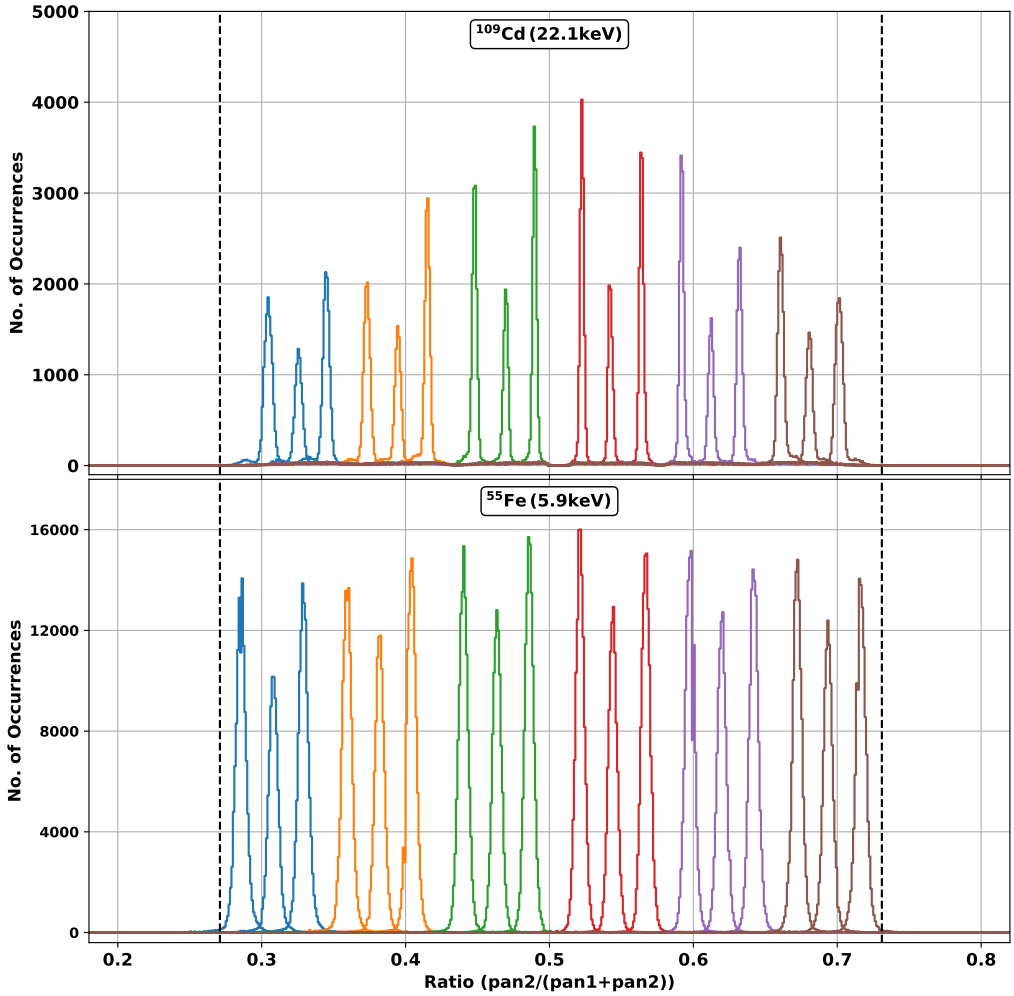


Figure 7.15: Ratio value distribution for all 18 calibration positions of Detector FM01, Channel 1. Each peak corresponds to 18 positions of channel 1, and peaks with the same color represent different positions along the same anode wire. The top panel shows results for the ^{109}Cd source, while the bottom panel corresponds to the ^{55}Fe source. As expected, the ratio spread is narrower for the higher-energy photons.

7.4.3 Gain monitoring during the mission

POLIX is a self-calibrating instrument because its in-flight spectrum consistently exhibits a stable background peak feature. By tracking the centroid of this peak over time, gain variations can be monitored, providing an indirect diagnostic of gas leakage and overall detector health.

To carry out this monitoring, the energy spectra are first extracted from all 48 anode wires in four detectors, 1, 2, 3 and 4 using the ratio-based position reconstruction described earlier. For each wire, the spectrum is fitted with a Gaussian function to model the background peak, together with a low-order polynomial to represent the underlying continuum. The Gaussian centroid is then taken as the gain indicator for that wire (see Fig. 7.16). For long-term trending, these gain values are averaged at the detector level. For Detectors 1, 2 and 3, the average is computed over all 12 wires and plotted as a single curve. Detector 4, however, contains seven wires with significantly higher intrinsic gain due to their larger anode diameter (see Fig. 7.12). To preserve meaningful interpretation, Detector 4 is therefore represented by two curves: one for the high-gain wires and another for the remaining low-gain wires, rather than a single combined average (see Fig. 7.16).

During in-orbit operation, the performance of the POLIX detectors has been continuously tracked. Detectors 1 and 2 have remained stable, showing consistent gain with no loss of functionality. Detector 4 exhibits a slow gas leak, resulting in a gradual increase in gain over time. To maintain the gain of Detector 4 at a level comparable to the other detectors, its high-voltage (HV) has been periodically reduced. Additionally, on 25 May 2024, an increase in wire resistance was observed at one end of Channel 2 of Detector 4, leading to the loss of position sensitivity for that channel. Detector 3 encountered a separate issue: on 14 November 2024, its anti-coincidence layer ceased functioning, causing a substantial increase in background and rendering its data unsuitable for scientific analysis. As a result, only 30 of the original 48 anode wires remain operational (12 each from Detectors 1 and 2, and 6 from Detector 4), corresponding to approximately two and a half effective detectors.

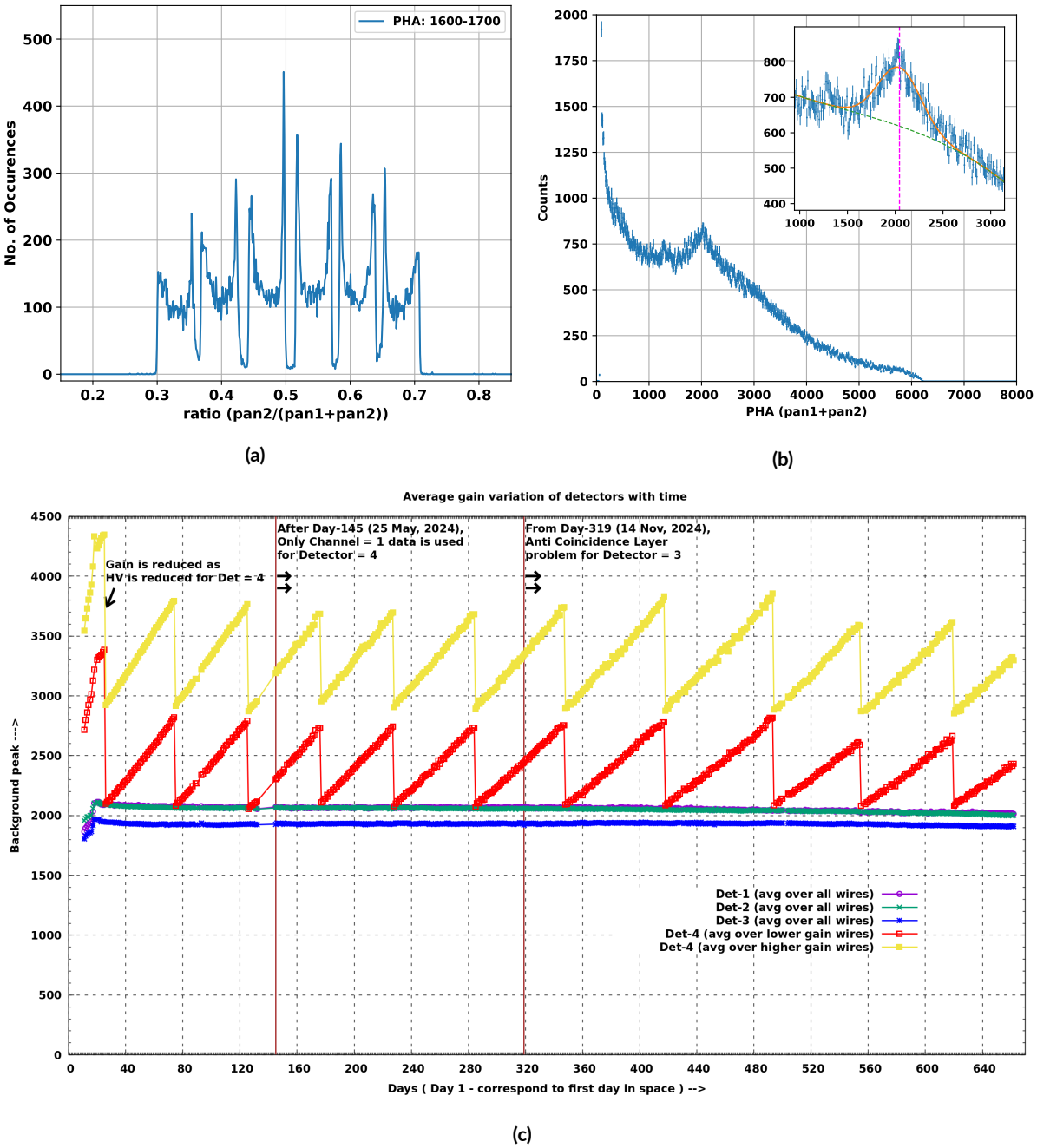


Figure 7.16: (a) Ratio distribution for Detector 1, Channel 1, obtained from POLIX observations on 10-07-2024. (b) Energy spectrum for Wire 1 from the same dataset, showing a prominent background peak that is monitored daily. (c) Gain monitoring plots for the flight data over time up to 23-10-2025.

7.5 Summary

The primary goal of POLIX is to measure X-ray polarization in the 8–30keV band using Thomson scattering. This chapter outlined the key steps involved in developing, calibrating, and validating the instrument:

- Introduced the working principles of proportional counters, the Thomson scattering geometry, and the overall POLIX design consisting of the collimator, Beryllium scatterer, and four detector units.
- Demonstrated gas integrity through long-term gain monitoring with the ^{55}Fe source; short-term gain drops due to moisture ingress were identified and shown to be fully recoverable under vacuum.
- Performed detailed position and energy calibration using ^{55}Fe and ^{109}Cd, establishing reliable ratio–position mapping and gain characterization. Detectors 1–3 showed uniform gain, while Detector 4 displayed two gain groups due to larger-diameter wires. The reversed ratio definition in Detector 2, Channel 1, was incorporated into the calibration pipeline.
- Verified in-orbit performance using the intrinsic background peak, showing that POLIX behaves as a self-calibrating instrument. Despite issues such as a slow leak in Detector 4 and failure of the anti-coincidence layer in Detector 3, 30 out of 48 anode wires remain operational and capable of delivering scientifically meaningful polarization measurements.

Overall, POLIX satisfies the essential requirements for constructing high-quality azimuthal modulation curves, and scientific data analysis is currently in progress.

8

Summary and Future Prospect

8.1 Summary

Ultra-luminous X-ray sources (ULXs) are extragalactic, off-nuclear X-ray sources with luminosities exceeding the Eddington limit for accretion onto stellar-mass compact objects. Their extreme luminosities, reaching several to over a hundred times the Eddington luminosity, initially motivated interpretations invoking intermediate-mass black holes accreting at sub-Eddington rates. However, subsequent observations and theoretical developments have favoured an alternative picture in which ULXs are powered by stellar-mass compact objects accreting at super-Eddington rates. A major breakthrough came with the discovery of coherent X-ray pulsations from several ULXs, unambiguously establishing neutron stars as the accretors in a subset of these sources and further supporting the super-Eddington accretion scenario onto stellar-mass compact objects. X-ray spectral studies reveal features such as high-energy curvature, soft excess emission, and ionized absorption or emission lines tracing powerful winds, while timing analyses, ranging from variability studies to pulsation detection, provide key constraints on the accretion geometry and emission mechanisms in these sources.

In this thesis, I presented our efforts to better understand the accretion processes and the environments of ULXs. The work started with a comparative study of the broadband spectra of ultra-luminous X-ray pulsars (ULXPs) and Galactic accretion-powered X-ray pulsars, including sources in the Magellanic Clouds, followed by an investigation of possible signatures of X-ray reprocessing in ULXs through iron line searches, hardness-ratio studies during the eclipse transitions, and eclipse to out-of-eclipse(OOE) flux ratio measurements in the eclipsing ULXs. Additionally, we investigated variability and pulse-profile properties in selected ULXs and ULXPs. Finally, I briefly presented my learning experience and contributions to the development and calibration of the POLIX, an X-ray polarimeter instrument.

8.1.1 Expressing ULXP spectra with local X-ray pulsar models

To investigate the accretion geometry in ultra-luminous X-ray pulsars (ULXPs), we analysed their broadband X-ray spectra using models commonly applied to Galactic accreting X-ray pulsars. We carried out a systematic spectral study of five ULXPs using simultaneous or quasi-simultaneous *XMM-Newton* and NuSTAR observations covering the 0.3–20 keV energy range, adopting the model **TBABS*(BBODYRAD + HIGHECUT*POW + GAUS)**.

- The broadband spectra of all ULXPs are well described by pulsar-like continua over the 0.3–20 keV energy range, with photon indices $\Gamma \sim 1$–1.5 and high-energy cutoffs at ~ 3–6 keV, closely resembling those of Galactic X-ray pulsars.

- A soft excess is consistently detected, characterized by a blackbody temperature of ~ 0.2–0.3 keV, comparable to that observed in local accreting pulsars.

- The inferred blackbody luminosity (~ 0.2–$3.1 \times 10^{39}\,\mathrm{erg\,s^{-1}}$) alone exceeds the Eddington luminosity, suggesting the presence of strong radiation-pressure-driven outflows. However, the physical origin of such intrinsically high soft X-ray luminosity remains unclear.

- The measured absorption column densities are relatively low compared to typical high-mass X-ray binaries (HMXBs), and no significant iron Kα emission lines are detected.

Overall, while the spectral shapes of ULXPs closely resemble those of Galactic X-ray pulsars, the combination of low absorption column density and the absence of iron Kα emission line indicates a markedly different accretion environment. These key differences motivated a focused investigation of X-ray reprocessing in ULXs.

8.1.2 Reprocessing of X-rays in ULXs

The results from the ULXP spectral study raise an important question. Several ULXPs are known to host high-mass companion stars, as indicated by their dynamical mass functions, long eclipse durations, and orbital properties. In such systems, especially at super-Eddington accretion rates, one would generally expect dense circumstellar material, strong absorption, and prominent X-ray reprocessing signatures, similar to those observed in Galactic high-mass X-ray binaries (HMXBs). However, the relatively low absorption column densities and the absence of iron Kα emission lines inferred from the spectral analysis suggest otherwise. Motivated by this apparent discrepancy, we investigated X-ray reprocessing in ULXs using three independent observational diagnostics: (i) searches for Fe Kα emission lines, (ii) evolution of the hardness ratio during eclipse ingress and egress, and (iii) measurements of the flux ratio between eclipse and out-of-eclipse (OOE) phases.

- By analysing the combined spectra of all available *XMM-Newton* observations of six bright ULXs and five ULXPs, we derived the most stringent upper limits to date on Fe Kα emission, with equivalent widths constrained to ~ 12–20 eV.

- No significant evolution of the hardness ratio is observed during eclipse ingress or egress of ULXs, unlike in Galactic eclipsing X-ray binaries, where enhanced absorption as the neutron star approaches the companion star produces spectral hardening, manifested as an increase in the hardness ratio during eclipse transitions.

- The eclipse to out-of-eclipse flux ratio is generally higher in ULXs than in the Galactic eclipsing HMXBs.

The higher eclipse flux to out-of-eclipse flux ratios observed in ULXs, compared to known Galactic HMXBs, suggest the presence of strong scattering. Considering this, the absence of detectable iron emission lines and the lack of increased hardness during the eclipse transitions may be indicative of either lower metallicity winds from the ULX companion stars or a very high level of ionisation of the metallic components of the stellar wind, which would suppress X-ray absorption and fluorescence line production.

8.1.3 Flaring behaviour in NGC 4559 X7 and NGC 7456 ULX1

Flaring type variability is observed in a number of ULXs, offering an important probe of their accretion geometry and emission processes. In this work, we examined a sample of variable ULXs and found that their spectral variability broadly falls into two distinct categories: a harder-when-brighter trend

and a softer-when-brighter trend. To investigate these behaviors in more detail, we performed state-resolved spectral analyses of two representative sources, NGC 4559 X7 and NGC 7456 ULX1, which exhibit contrasting variability patterns.

- NGC 4559 X7 shows a harder-when-brighter behaviour, with variability dominated by the hard X-ray component. The soft thermal component remains nearly constant across flux states, while the power-law index hardens with increasing luminosity.
- NGC 7456 ULX1 displays a softer-when-brighter trend, with variability primarily confined to the soft X-ray band. The disk temperature increases and the apparent disk radius decreases slightly with increasing luminosity, whereas the hard component shows little variation.

These contrasting behaviours are broadly consistent with super-Eddington accretion scenarios in which different emission regions dominate the observed variability, such as a central hard X-ray emitting region and an optically thick disk–wind component. However, the interpretations presented here are based on simplified spectral models and a limited number of flux states. These results highlight the need for systematic, population-level studies of variable ULXs to investigate whether spectral variability follows a continuum of behaviors, with sources such as NGC 4559 X7 and NGC 7456 ULX1 possibly representing the two extreme ends of this distribution.

8.1.4 Energy dependence and luminosity dependence of pulse profiles in ULXPs

Energy-dependent pulse profiles are commonly observed in Galactic accreting pulsars and provide important clues about beaming geometry and the origin of different spectral components. In several systems, particularly those exhibiting superorbital periods, changes in pulse profiles and phase offsets between soft and hard X-ray emission have been interpreted as signatures of a precessing accretion disk, whose visibility changes with the superorbital phase. Motivated by these considerations, we examined the energy and luminosity dependence of pulse profiles in ultra-luminous X-ray pulsars (ULXPs).

In this work, we reconstructed folded pulse profiles using all available *XMM-Newton* observations of known ULXPs. Among these sources, NGC 300 ULX1 provides sufficient statistical quality to allow a comparison of pulse profiles across multiple energy bands, while M51 ULX7, NGC 5907 ULX1, and NGC 7793 P13 have a sufficient number of observations to investigate the evolution of pulse profiles with luminosity.

- For NGC 300 ULX1, the pulse fraction increases with increasing energy, consistent with the interpretation that the soft X-ray emission is dominated by reprocessed radiation, which may originate in an optically thick disk or wind and tends to smear out pulsations.
- For M51 ULX7, NGC 5907 ULX1, and NGC 7793 P13, the overall pulse fraction shows a weak or decreasing trend with increasing luminosity.
- No systematic phase shift between the soft and hard X-ray pulse profiles is observed across the available luminosity range within the limitations of a simple sinusoidal modeling approach.

Overall, these results suggest that while reprocessing affects the observed pulse fraction in ULXPs, the relative geometry of the soft and hard X-ray emitting regions remains largely stable over the sampled luminosity range. More extensive observations are needed to determine whether subtle phase variations appear over a wider range of luminosity or superorbital phases.

8.1.5 POLIX: Indian X-ray Polarimeter

POLIX is designed to measure X-ray polarization in the 8–30 keV energy band, thereby extending polarization studies to higher energies beyond those covered by IXPE, the NASA X-ray polarimetry mission operating in the 2–8 keV range. In this chapter, I describe my involvement in the development and calibration stages of POLIX, carried out as part of the collective effort of the POLIX team.

- Long-term gas gain monitoring using a ^{55}Fe (5.9 keV) source was carried out to establish absence of gas leakage of the proportional counters. Temporary gain drops due to moisture ingress were identified and shown to be fully recoverable under vacuum, indicating no permanent gas leakage in ground-based tests.

- Detailed position and energy calibrations were performed using ^{55}Fe (5.9 keV) and ^{109}Cd (22.1 keV) sources, enabling reliable characterization of the detector response and incorporation of detector-specific effects into the calibration pipeline.

- In-orbit performance was verified using the intrinsic background peak observed in the spectra, demonstrating that POLIX functions effectively as a self-calibrating instrument. Although a slow gas leak was detected in Detector 4 during flight, the associated increase in gas gain was controlled by periodically lowering the high-voltage (HV) setting. Despite partial degradation in some detector elements, a majority of the anode wires remain operational and capable of delivering scientifically useful polarization measurements.

Overall, POLIX satisfies the essential performance requirements for X-ray polarization studies in the 8–30 keV energy range, and scientific analysis of the in-orbit data is currently in progress.

8.2 Ongoing/Future Research Direction

For the flaring ULXs, expanding the study to a larger sample would help establish whether the observed harder-when-brighter and softer-when-brighter behaviours are common across the ULX population, and whether these trends form a continuum of spectral variability, with sources such as NGC 4559 X7 and NGC 7456 ULX1 potentially representing two extreme ends of this distribution. In the case of ULX pulsars, pulse-profile comparisons were quantified using simple sinusoidal modeling, providing a first-order description of phase differences between soft and hard X-ray profiles. With additional observations covering a broader luminosity range, this analysis can be extended using more detailed profile modeling to better constrain the underlying emission geometry.

Beyond these immediate goals, several follow-up investigations naturally arise from this thesis work. In particular, a population-based study of quasi-periodic oscillations (QPOs) in ULXs can be pursued. During the analysis of NGC 4559 X7, we noticed a pulsation-like signal at a period of $\sim$0.27s, predominantly during brighter flux states. This feature requires further detailed timing and spectral analysis to establish its statistical significance and physical origin, and to assess whether it is indeed a pulsating source, or if the could arise from instrumental or systematic effects.

In addition, the scientific analysis of POLIX data is currently ongoing. POLIX has observed some of the brightest Galactic X-ray binaries, including the Crab, Sco X-1, and Cyg X-1. The analysis of these datasets will enable detailed polarization studies, providing new constraints on emission geometry and radiation mechanisms in strongly magnetized and accreting systems.

In the longer term, I aim to build on the data analysis and instrumentation expertise acquired during my PhD to continue exploring accretion processes in compact objects, particularly ULXs and X-ray

binaries. Future work will focus on combining spectral, timing, and polarimetric diagnostics to better understand the accretion geometry, radiative processes, and circumstellar environments of XRBs. In addition, I intend to continue learning and developing new instrumentation techniques to contribute to future high-energy astrophysics missions.

References

Abramowicz, M., Jaroszynski, M., & Sikora, M. 1978, Relativistic, accreting disks., Astronomy & Astrophysics, 63, 221

Abramowicz, M. A., Czerny, B., Lasota, J. P., & Szuszkiewicz, E. 1988, Slim Accretion Disks, The Astrophysical Journal, 332, 646, doi: 10.1086/166683

Aftab, N., & Paul, B. 2024, X-ray reprocessing: Through the eclipse spectra of low mass X-ray binaries with XMM-Newton, Nature Astronomy, 106, 102109, doi: 10.1016/j.newast.2023.102109

Aftab, N., Paul, B., & Kretschmar, P. 2019, X-Ray Reprocessing: Through the Eclipse Spectra of High-mass X-Ray Binaries with XMM-Newton, The Astrophysical Journal Supplement Series, 243, 29, doi: 10.3847/1538-4365/ab2a77

Antonucci, R. 1993, Unified models for active galactic nuclei and quasars., Annual Review of Astronomy and Astrophysics, 31, 473, doi: 10.1146/annurev.aa.31.090193.002353

Arnaud, K. A. 1996, in Astronomical Society of the Pacific Conference Series, Vol. 101, Astronomical Data Analysis Software and Systems V, ed. G. H. Jacoby & J. Barnes, 17

Atapin, K., Fabrika, S., & Caballero-García, M. D. 2019, Ultraluminous X-ray sources with flat-topped noise and QPO, Monthly Notices of the Royal Astronomical Society, 486, 2766, doi: 10.1093/mnras/stz1027

Bachetti, M., Harrison, F. A., Walton, D. J., et al. 2014, An ultraluminous X-ray source powered by an accreting neutron star, Nature, 514, 202, doi: 10.1038/nature13791

Bachetti, M., Heida, M., Maccarone, T., et al. 2022, Orbital Decay in M82 X-2, The Astrophysical Journal, 937, 125, doi: 10.3847/1538-4357/ac8d67

Balu, A., Roy, K., Manikantan, H., Tamang, A., & Paul, B. 2024, Studying the X-ray absorption characteristics of Centaurus X-3 using nearly 14 years of MAXI/GSC data, Astronomy & Astrophysics, 692, A47, doi: 10.1051/0004-6361/202451922

Barnard, R. 2010, In-depth studies of the NGC 253 ULXs with XMM–Newton: remarkable variability in ULX1, and evidence for extended coronae, Monthly Notices of the Royal Astronomical Society, 404, 42, doi: 10.1111/j.1365-2966.2010.16291.x

Barra, F., Pinto, C., Middleton, M., et al. 2024, Examining the nature of the ultraluminous X-ray source Holmberg II X-1, Astronomy & Astrophysics, 682, A94, doi: 10.1051/0004-6361/202348471

Basko, M. M., & Sunyaev, R. A. 1976, The limiting luminosity of accreting neutron stars with magnetic fields., Monthly Notices of the Royal Astronomical Society, 175, 395, doi: 10.1093/mnras/175.2.395

Begelman, M. C. 2002, Super-Eddington Fluxes from Thin Accretion Disks?, The Astrophysical Journal, 568, L97, doi: 10.1086/340457

Belfiore, A., Salvaterra, R., Sidoli, L., et al. 2024, The Orbit of NGC 5907 ULX-1, The Astrophysical Journal, 965, 78, doi: 10.3847/1538-4357/ad320a

Bellazzini, R., & Muleri, F. 2010, X-ray polarimetry: A new window on the high energy sky, Nuclear Instruments and Methods in Physics Research A, 623, 766, doi: 10.1016/j.nima.2010.04.006

Bellazzini, R., Angelini, F., Baldini, L., et al. 2006, Gas pixel detectors for X-ray polarimetry applications, Nuclear Instruments and Methods in Physics Research A, 560, 425, doi: 10.1016/j.nima.2006.01.046

Beri, & Paul. 2017, Post-flare formation of the accretion stream and a dip in pulse profiles of LMC X-4, Nature Astronomy, 56, 94, doi: 10.1016/j.newast.2017.05.001

Beri, A., Paul, B., & Dewangan, G. C. 2015, Pulse-phase dependence of emission lines in the X-ray pulsar 4U 1626-67, Monthly Notices of the Royal Astronomical Society, 451, 508, doi: 10.1093/mnras/stv922

Beri, A., Naik, S., Singh, K. P., et al. 2021, AstroSat observations of the first Galactic ULX pulsar Swift J0243.6+6124, Monthly Notices of the Royal Astronomical Society, 500, 565, doi: 10.1093/mnras/staa3254

Bondi, H. 1952, On spherically symmetrical accretion, Monthly Notices of the Royal Astronomical Society, 112, 195, doi: 10.1093/mnras/112.2.195

Bozzo, E., Romano, P., Ducci, L., Bernardini, F., & Falanga, M. 2015, Supergiant fast X-ray transients as an underluminous class of supergiant X-ray binaries, Advances in Space Research, 55, 1255, doi: 10.1016/j.asr.2014.11.012

Brightman, M., Harrison, F. A., Fürst, F., et al. 2018, Magnetic field strength of a neutron-star-powered ultraluminous X-ray source, Nature Astronomy, 2, 312, doi: 10.1038/s41550-018-0391-6

Brightman, M., Bachetti, M., Earnshaw, H., et al. 2022, Evolution of the Spin, Spectrum and Superorbital Period of the Ultraluminous X-Ray Pulsar M51 ULX7, The Astrophysical Journal, 925, 18, doi: 10.3847/1538-4357/ac3829

Brumback, M. C., Hickox, R. C., Fürst, F. S., et al. 2020, Modeling the Precession of the Warped Inner Accretion Disk in the Pulsars LMC X-4 and SMC X-1 with NuSTAR and XMM-Newton, The Astrophysical Journal, 888, 125, doi: 10.3847/1538-4357/ab5b04

Bykov, S. D., Gilfanov, M. R., Tsygankov, S. S., & Filippova, E. V. 2022, ULX pulsar Swift J0243.6+6124 observations with NuSTAR: dominance of reflected emission in the super-Eddington state, Monthly Notices of the Royal Astronomical Society, 516, 1601, doi: 10.1093/mnras/stac2239

Caballero-García, M. D. 2011, Weakly broadened iron line in the X-ray spectrum of the ultraluminous X-ray source M82 X-1, Monthly Notices of the Royal Astronomical Society, 418, 1973, doi: 10.1111/j.1365-2966.2011.19615.x

Cackett, E. M., Miller, J. M., Ballantyne, D. R., et al. 2010, Relativistic Lines and Reflection from the Inner Accretion Disks Around Neutron Stars, The Astrophysical Journal, 720, 205, doi: 10.1088/0004-637X/720/1/205

Campbell, C. G. 2012, Angular momentum transport through magnetic accretion curtains inside disrupted discs, Monthly Notices of the Royal Astronomical Society, 420, 1034, doi: 10.1111/j.1365-2966.2011.20003.x

Carpano, S., Haberl, F., Maitra, C., & Vasilopoulos, G. 2018, Discovery of pulsations from NGC 300 ULX1 and its fast period evolution, Monthly Notices of the Royal Astronomical Society, 476, L45, doi: 10.1093/mnrasl/sly030

Castillo, G. A. R., Israel, G. L., Belfiore, A., et al. 2020, Discovery of a 2.8 s Pulsar in a 2 Day Orbit High-mass X-Ray Binary Powering the Ultraluminous X-Ray Source ULX-7 in M51, The Astrophysical Journal, 895, 60, doi: 10.3847/1538-4357/ab8a44

Castor, J. I., Abbott, D. C., & Klein, R. I. 1975, Radiation-driven winds in Of stars., The Astrophysical Journal, 195, 157, doi: 10.1086/153315

Chakraborty, P., Ferland, G., Fabian, A., et al. 2024, Physics of 1 keV line in X-ray binaries. https://arxiv.org/abs/2407.02360

Chandra, A. D., Roy, J., Agrawal, P. C., & Choudhury, M. 2020, Study of recent outburst in the Be/X-ray binary RX J0209.6-7427 with AstroSat: a new ultraluminous X-ray pulsar in the Magellanic Bridge?, Monthly Notices of the Royal Astronomical Society, 495, 2664, doi: 10.1093/mnras/staa1041

Charles, P. A., & Coe, M. J. 2006, in Compact stellar X-ray sources, ed. W. H. G. Lewin & M. van der Klis, Vol. 39, 215–265

Chattopadhyay, T., Vadawale, S. V., Rao, A. R., Sreekumar, S., & Bhattacharya, D. 2014, Prospects of hard X-ray polarimetry with Astrosat-CZTI, Experimental Astronomy, 37, 555, doi: 10.1007/s10686-014-9386-1

Chen, X., Wang, W., & Tong, H. 2021, Studying magnetic fields of ultraluminous X-ray pulsars using different accretion torques, Journal of High Energy Astrophysics, 31, 1, doi: https://doi.org/10.1016/j.jheap.2021.04.002

Colbert, E. J. M., & Mushotzky, R. F. 1999, The Nature of Accreting Black Holes in Nearby Galaxy Nuclei, The Astrophysical Journal, 519, 89, doi: 10.1086/307356

Costa, E., Soffitta, P., Bellazzini, R., et al. 2001, An efficient photoelectric X-ray polarimeter for the study of black holes and neutron stars, Nature, 411, 662, doi: 10.1038/35079508

Culhane, J. L., & Sanford, P. W. 1981, X-ray astronomy / J. Leonard Culhane and Peter W. Sanford (New York: Scribner)

dal Fiume, D., Orlandini, M., Cusumano, G., et al. 1998, The broad-band (0.1-200 keV) spectrum of HER X-1 observed with BeppoSAX, Astronomy & Astrophysics, 329, L41, doi: 10.48550/arXiv.astro-ph/9711295

Davidson, K., & Ostriker, J. P. 1973, Neutron-Star Accretion in a Stellar Wind: Model for a Pulsed X-Ray Source, The Astrophysical Journal, 179, 585, doi: 10.1086/151897

Done, C., Gierliński, M., & Kubota, A. 2007, Modelling the behaviour of accretion flows in X-ray binaries. Everything you always wanted to know about accretion but were afraid to ask, The Astronomy and Astrophysics Review, 15, 1, doi: 10.1007/s00159-007-0006-1

Doroshenko, R., Santangelo, A., Doroshenko, V., & Piraino, S. 2017, BeppoSAX observations of XTE J1946+274, Astronomy & Astrophysics, 600, A52, doi: 10.1051/0004-6361/201630137

Dotan, C., & Shaviv, N. J. 2011, Super-Eddington slim accretion discs with winds, Monthly Notices of the Royal Astronomical Society, 413, 1623, doi: 10.1111/j.1365-2966.2011.18235.x

Earnshaw, H. P., Grefenstette, B. W., Brightman, M., et al. 2019, A Broadband Look at the Old and New ULXs of NGC 6946, The Astrophysical Journal, 881, 38, doi: 10.3847/1538-4357/ab20cd

Eddington, A. S. 1920, The Internal Constitution of the Stars, Nature, 106, 14, doi: 10.1038/106014a0

Eggleton, P. P. 1983, Aproximations to the radii of Roche lobes., The Astrophysical Journal, 268, 368, doi: 10.1086/160960

Fabbiano, G. 1989, X-rays from normal galaxies., Annual Review of Astronomy and Astrophysics, 27, 87, doi: 10.1146/annurev.aa.27.090189.000511

Fabian, A. C., & Ross, R. R. 2010, X-ray Reflection, Space Science Reviews, 157, 167, doi: 10.1007/s11214-010-9699-y

Fabrika, S. N., Atapin, K. E., Vinokurov, A. S., & Sholukhova, O. N. 2021, Ultraluminous X-Ray Sources, Astrophysical Bulletin, 76, 6, doi: 10.1134/S1990341321010077

Forot, M., Laurent, P., Grenier, I. A., Gouiffès, C., & Lebrun, F. 2008, Polarization of the Crab Pulsar and Nebula as Observed by the INTEGRAL/IBIS Telescope, The Astrophysical Journal Letters, 688, L29, doi: 10.1086/593974

Frank, J., King, A., & Raine, D. J. 2002, Accretion Power in Astrophysics: Third Edition

Friend, D. B., & Abbott, D. C. 1986, The Theory of Radiatively Driven Stellar Winds. III. Wind Models with Finite Disk Correction and Rotation, The Astrophysical Journal, 311, 701, doi: 10.1086/164809

Fruscione, A., McDowell, J. C., Allen, G. E., et al. 2006, in Observatory Operations: Strategies, Processes, and Systems, ed. D. R. Silva & R. E. Doxsey, Vol. 6270, International Society for Optics and Photonics (SPIE), 62701V, doi: 10.1117/12.671760

Fürst, F., Walton, D. J., Stern, D., et al. 2017, Spectral Changes in the Hyperluminous Pulsar in NGC 5907 as a Function of Super-orbital Phase, The Astrophysical Journal, 834, 77, doi: 10.3847/1538-4357/834/1/77

Fürst, F., Walton, D. J., Harrison, F. A., et al. 2016, Discovery of Coherent Pulsations from the Ultraluminous X-Ray Source NGC 7793 P13, The Astrophysical Journal Letters, 831, L14, doi: 10.3847/2041-8205/831/2/L14

Fürst, F., Walton, D. J., Israel, G. L., et al. 2023, Probing the nature of the low state in the extreme ultraluminous X-ray pulsar NGC 5907 ULX1, Astronomy & Astrophysics, 672, A140, doi: 10.1051/0004-6361/202245048

Garmire, G. P., Bautz, M. W., Ford, P. G., Nousek, J. A., & Jr., G. R. R. 2003, in X-Ray and Gamma-Ray Telescopes and Instruments for Astronomy, ed. J. E. Truemper & H. D. Tananbaum, Vol. 4851, International Society for Optics and Photonics (SPIE), 28 – 44, doi: 10.1117/12.461599

Ghosh, P., & Lamb, F. K. 1979, Accretion by rotating magnetic neutron stars. III. Accretion torques and period changes in pulsating X-ray sources., The Astrophysical Journal, 234, 296, doi: 10.1086/157498

Ghosh, T., Rana, V., & Bachetti, M. 2022, Hard X-Ray Flares and Spectral Variability in NGC 4395 ULX1, The Astrophysical Journal, 938, 76, doi: 10.3847/1538-4357/ac8f8f

Giacconi, R., Gursky, H., Paolini, F. R., & Rossi, B. B. 1962, Evidence for x Rays From Sources Outside the Solar System, Phys. Rev. Lett., 9, 439, doi: 10.1103/PhysRevLett.9.439

Giacconi, R., Murray, S., Gursky, H., et al. 1972, The Uhuru catalog of X-ray sources., The Astrophysical Journal, 178, 281, doi: 10.1086/151790

Giacconi, R., Branduardi, G., Briel, U., et al. 1979, The Einstein (HEAO 2) X-ray Observatory., The Astrophysical Journal, 230, 540, doi: 10.1086/157110

Gieren, W., Pietrzyński, G., Soszyński, I., et al. 2005, The Araucaria Project: Near-Infrared Photometry of Cepheid Variables in the Sculptor Galaxy NGC 300*, The Astrophysical Journal, 628, 695, doi: 10.1086/430903

Giménez-García, A., Torrejón, J. M., Eikmann, W., et al. 2015, An XMM-Newton view of FeKα in high-mass X-ray binaries, Astronomy & Astrophysics, 576, A108, doi: 10.1051/0004-6361/201425004

Harrison, F. A., Craig, W. W., Christensen, F. E., et al. 2013, The Nuclear Spectroscopic Telescope Array (NuSTAR) High-energy X-Ray Mission, The Astrophysical Journal, 770, 103, doi: 10.1088/0004-637X/770/2/103

Heemskerk, M. H. M., & van Paradijs, J. 1989, Analysis of the optical light curve of the massive X-ray binary LMC X-4., Astronomy & Astrophysics, 223, 154

Heil, L. M., Vaughan, S., & Roberts, T. P. 2009, A systematic study of variability in a sample of ultraluminous X-ray sources, Monthly Notices of the Royal Astronomical Society, 397, 1061, doi: 10.1111/j.1365-2966.2009.15068.x

Heyl, J., Doroshenko, V., González-Caniulef, D., et al. 2023, X-ray Polarization Reveals the Precessions of the Neutron Star in Hercules X-1, arXiv e-prints, arXiv:2311.03667, doi: 10.48550/arXiv.2311.03667

Hickox, R. C., Narayan, R., & Kallman, T. R. 2004, Origin of the Soft Excess in X-Ray Pulsars, The Astrophysical Journal, 614, 881, doi: 10.1086/423928

Hickox, R. C., & Vrtilek, S. D. 2005, Pulse-Phase Spectroscopy of SMC X-1 with Chandra and XMM-Newton: Reprocessing by a Precessing Disk?, The Astrophysical Journal, 633, 1064, doi: 10.1086/491596

Hirano, A., Kitamoto, S., Yamada, T. T., Mineshige, S., & Fukue, J. 1995, Accretion Disk Structure and Branch Behavior of Cygnus X-2, The Astrophysical Journal, 446, 350, doi: 10.1086/175793

Hoyle, F., & Lyttleton, R. A. 1939, The effect of interstellar matter on climatic variation, Proceedings of the Cambridge Philosophical Society, 35, 405, doi: 10.1017/S0305004100021150

Hu, C.-P., Ueda, Y., & Enoto, T. 2021, Possible Periodic Dips in the Pulsating Ultraluminous X-Ray Source M51 ULX-7, The Astrophysical Journal, 909, 5, doi: 10.3847/1538-4357/abd7a5

Hung, L.-W., Hickox, R. C., Boroson, B. S., & Vrtilek, S. D. 2010, Suzaku X-ray Spectra and Pulse Profile Variations During the Superorbital Cycle of LMC X-4, The Astrophysical Journal, 720, 1202, doi: 10.1088/0004-637X/720/2/1202

Illarionov, A. F., & Sunyaev, R. A. 1975, Why the Number of Galactic X-ray Stars Is so Small?, Astronomy & Astrophysics, 39, 185

Imbrogno, M., Motta, S. E., Amato, R., et al. 2024, Skipping a beat: Discovery of persistent quasi-periodic oscillations associated with pulsed fraction drop of the spin signal in M51 ULX-7, Astronomy & Astrophysics, 689, A284, doi: 10.1051/0004-6361/202450432

Ioannou, Z., Naylor, T., Smale, A. P., Charles, P. A., & Mukai, K. 2002, Understanding the LMXB X2127+119 in M 15. I. X-ray eclipses and dips, Astronomy & Astrophysics, 382, 130, doi: 10.1051/0004-6361:20011581

Israel, G. L., Papitto, A., Esposito, P., et al. 2017a, Discovery of a 0.42-s pulsar in the ultraluminous X-ray source NGC 7793 P13, Monthly Notices of the Royal Astronomical Society, 466, L48, doi: 10.1093/mnrasl/slw218

Israel, G. L., Belfiore, A., Stella, L., et al. 2017b, An accreting pulsar with extreme properties drives an ultraluminous x-ray source in NGC 5907, Science, 355, 817, doi: 10.1126/science.aai8635

Jaisawal, G. K., Wilson-Hodge, C. A., Fabian, A. C., et al. 2019, An Evolving Broad Iron Line from the First Galactic Ultraluminous X-Ray Pulsar Swift J0243.6+6124, The Astrophysical Journal, 885, 18, doi: 10.3847/1538-4357/ab4595

Jansen, F., Lumb, D., Altieri, B., et al. 2001, XMM-Newton observatory. I. The spacecraft and operations, Astronomy & Astrophysics, 365, L1, doi: 10.1051/0004-6361:20000036

Kaaret, P., Feng, H., & Roberts, T. P. 2017, Ultraluminous X-Ray Sources, Annual Review of Astronomy and Astrophysics, 55, 303, doi: 10.1146/annurev-astro-091916-055259

Kara, E., Pinto, C., Walton, D. J., et al. 2019, Discovery of a soft X-ray lag in the ultraluminous X-ray source NGC 1313 X-1, Monthly Notices of the Royal Astronomical Society, 491, 5172, doi: 10.1093/mnras/stz3318

Karachentsev, I. D., Karachentseva, V. E., Huchtmeier, W. K., & Makarov, D. I. 2004, A Catalog of Neighboring Galaxies, The Astronomical Journal, 127, 2031, doi: 10.1086/382905

Katz, J. I. 1973, Thirty-five-day Periodicity in Her X-1, Nature Physical Science, 246, 87, doi: 10.1038/physci246087a0

King, A., & Lasota, J.-P. 2016, ULXs: Neutron stars versus black holes, Monthly Notices of the Royal Astronomical Society, 458, L10, doi: 10.1093/mnrasl/slw011

King, A., & Lasota, J.-P. 2019, No magnetars in ULXs, Monthly Notices of the Royal Astronomical Society, 485, 3588, doi: 10.1093/mnras/stz720

King, A., Lasota, J.-P., & Kluźniak, W. 2017, Pulsing ULXs: tip of the iceberg?, Monthly Notices of the Royal Astronomical Society, 468, L59, doi: 10.1093/mnrasl/slx020

King, A., Lasota, J.-P., & Middleton, M. 2023, Ultraluminous X-ray sources, , 96, 101672, doi: 10.1016/j.newar.2022.101672

King, A. R. 2004, Ultraluminous X-ray sources and star formation, Monthly Notices of the Royal Astronomical Society, 347, L18, doi: 10.1111/j.1365-2966.2004.07403.x

Kislat, F., Clark, B., Beilicke, M., & Krawczynski, H. 2015, Analyzing the data from X-ray polarimeters with Stokes parameters, Astroparticle Physics, 68, 45, doi: 10.1016/j.astropartphys.2015.02.007

Kluźniak, W., & Rappaport, S. 2007, Magnetically Torqued Thin Accretion Disks, The Astrophysical Journal, 671, 1990, doi: 10.1086/522954

Knoll, G. F. 2000, Radiation detection and measurement

Kolb, U. 2010, Extreme Environment Astrophysics

Kole, M., Li, Z. H., Produit, N., et al. 2017, Instrument performance and simulation verification of the POLAR detector, Nuclear Instruments and Methods in Physics Research A, 872, 28, doi: 10.1016/j.nima.2017.07.070

Koliopanos, F., & Vasilopoulos, G. 2018, Accreting, highly magnetized neutron stars at the Eddington limit: a study of the 2016 outburst of SMC X-3, Astronomy & Astrophysics, 614, A23, doi: 10.1051/0004-6361/201731623

Kosec, P., Pinto, C., Fabian, A. C., & Walton, D. J. 2017, Searching for outflows in ultraluminous X-ray sources through high-resolution X-ray spectroscopy, Monthly Notices of the Royal Astronomical Society, 473, 5680, doi: 10.1093/mnras/stx2695

Kosec, P., Pinto, C., Walton, D. J., et al. 2018, Evidence for a variable Ultrafast Outflow in the newly discovered Ultraluminous Pulsar NGC 300 ULX-1, Monthly Notices of the Royal Astronomical Society, 479, 3978, doi: 10.1093/mnras/sty1626

Kosec, P., Pinto, C., Reynolds, C. S., et al. 2021, Ionized emission and absorption in a large sample of ultraluminous X-ray sources, Monthly Notices of the Royal Astronomical Society, 508, 3569, doi: 10.1093/mnras/stab2856

Kotze, M. M., & Charles, P. A. 2012, Characterizing X-ray binary long-term variability, Monthly Notices of the Royal Astronomical Society, 420, 1575, doi: 10.1111/j.1365-2966.2011.20146.x

Kozlowski, M., Jaroszynski, M., & Abramowicz, M. A. 1978, The analytic theory of fluid disks orbiting the Kerr black hole., Astronomy & Astrophysics, 63, 209

Krawczynski, H., Garson, A., Guo, Q., et al. 2011, Scientific prospects for hard X-ray polarimetry, Astroparticle Physics, 34, 550, doi: 10.1016/j.astropartphys.2010.12.001

Kubota, A., Ebisawa, K., Makishima, K., & Nakazawa, K. 2005, On the Temperature Profile of Radiatively Efficient Geometrically Thin Disks in Black Hole Binaries with the ASCA GIS, The Astrophysical Journal, 631, 1062, doi: 10.1086/432900

Kubota, A., & Makishima, K. 2004, The Three Spectral Regimes Found in the Stellar Black Hole XTE J1550-564 in Its High/Soft State, The Astrophysical Journal, 601, 428, doi: 10.1086/380433

Kubota, A., Tanaka, Y., Makishima, K., et al. 1998, Evidence for a Black Hole in the X-Ray Transient GRS 1009-45, Publications of the Astronomical Society of Japan, 50, 667, doi: 10.1093/pasj/50.6.667

Kumar, M., Sharma, R., Paul, B., & Rana, V. 2025, Spectral analysis of ultraluminous X-ray pulsars with models of X-ray pulsars, Monthly Notices of the Royal Astronomical Society, 536, 340, doi: 10.1093/mnras/stae2558

Lara-López, M. A., Zinchenko, I. A., Pilyugin, L. S., et al. 2021, Metal-THINGS: On the Metallicity and Ionization of ULX Sources in NGC 925, The Astrophysical Journal, 906, 42, doi: 10.3847/1538-4357/abc892

Leahy, D. A. 1987, Searches for pulsed emission - Improved determination of period and amplitude from epoch folding for sinusoidal signals, Astronomy & Astrophysics, 180, 275

Lobban, A. P., Porquet, D., Reeves, J. N., et al. 2018, A deep X-ray view of the bare AGN Ark 120. III. X-ray timing analysis and multiwavelength variability, Monthly Notices of the Royal Astronomical Society, 474, 3237, doi: 10.1093/mnras/stx2889

Lovelace, R. V. E., Romanova, M. M., & Bisnovatyi-Kogan, G. S. 1995, Spin-up/spin-down of magnetized stars with accretion discs and outflows, Monthly Notices of the Royal Astronomical Society, 275, 244, doi: 10.1093/mnras/275.2.244

Lutovinov, A. A., & Tsygankov, S. S. 2009a, Timing characteristics of the hard X-ray emission from bright X-ray pulsars based on INTEGRAL data, Astronomy Letters, 35, 433, doi: 10.1134/S1063773709070019

Lutovinov, A. A., & Tsygankov, S. S. 2009b, Timing characteristics of the hard X-ray emission from bright X-ray pulsars based on INTEGRAL data, Astronomy Letters, 35, 433, doi: 10.1134/S1063773709070019

Makishima, K., Maejima, Y., Mitsuda, K., et al. 1986, Simultaneous X-Ray and Optical Observations of GX 339-4 in an X-Ray High State, The Astrophysical Journal, 308, 635, doi: 10.1086/164534

Makishima, K., Kubota, A., Mizuno, T., et al. 2000, The Nature of Ultraluminous Compact X-Ray Sources in Nearby Spiral Galaxies, The Astrophysical Journal, 535, 632, doi: 10.1086/308868

Mapelli, M., Colpi, M., & Zampieri, L. 2009, Low metallicity and ultra-luminous X-ray sources in the Cartwheel galaxy, Monthly Notices of the Royal Astronomical Society: Letters, 395, L71, doi: 10.1111/j.1745-3933.2009.00645.x

Mapelli, M., Ripamonti, E., Zampieri, L., Colpi, M., & Bressan, A. 2010, Ultra-luminous X-ray sources and remnants of massive metal-poor stars, Monthly Notices of the Royal Astronomical Society, 408, 234, doi: 10.1111/j.1365-2966.2010.17048.x

McQuinn, K. B. W., Skillman, E. D., Dolphin, A. E., Berg, D., & Kennicutt, R. 2016, THE DISTANCE TO M104*, The Astronomical Journal, 152, 144, doi: 10.3847/0004-6256/152/5/144

Meng, F.-L., Pan, Y.-Y., & Li, Z.-S. 2022, Research on the Magnetic Field of NGC 7793 P13 and Other Confirmed Pulsating Ultraluminous X-Ray Sources, Research in Astronomy and Astrophysics, 22, 115018, doi: 10.1088/1674-4527/ac96b6

Meszaros, P., Novick, R., Szentgyorgyi, A., Chanan, G. A., & Weisskopf, M. C. 1988, Astrophysical Implications and Observational Prospects of X-Ray Polarimetry, The Astrophysical Journal, 324, 1056, doi: 10.1086/165962

Middleton, M. J., Brightman, M., Pintore, F., et al. 2019, On the magnetic field in M51 ULX-8, Monthly Notices of the Royal Astronomical Society, 486, 2, doi: 10.1093/mnras/stz436

Middleton, M. J., Heil, L., Pintore, F., Walton, D. J., & Roberts, T. P. 2015, A spectral-timing model for ULXs in the supercritical regime, Monthly Notices of the Royal Astronomical Society, 447, 3243, doi: 10.1093/mnras/stu2644

Middleton, M. J., Walton, D. J., Fabian, A., et al. 2015, Diagnosing the accretion flow in ultraluminous X-ray sources using soft X-ray atomic features, Monthly Notices of the Royal Astronomical Society, 454, 3134, doi: 10.1093/mnras/stv2214

Mineshige, S., Hirano, A., Kitamoto, S., Yamada, T. T., & Fukue, J. 1994, Time-dependent Disk Accretion in X-Ray Nova MUSCAE 1991, The Astrophysical Journal, 426, 308, doi: 10.1086/174065

Mitsuda, K., Inoue, H., Koyama, K., et al. 1984, Energy Spectra of Low-Mass Binary X-Ray Sources Observed from Tenma, Publications of the Astronomical Society of Japan, 36, 741, doi: 10.1093/pasj/36.4.741

Mondal, S., Różańska, A., Bagińska, P., Markowitz, A., & De Marco, B. 2021, Spectral state transitions in Circinus ULX5, Astronomy & Astrophysics, 651, A54, doi: 10.1051/0004-6361/202140459

Mondal, S., Różańska, A., De Marco, B., & Markowitz, A. 2021, Evidence for Fe Kα line and soft X-ray lag in NGC 7456 ultraluminous X-ray source-1, Monthly Notices of the Royal Astronomical Society: Letters, 505, L106, doi: 10.1093/mnrasl/slab061

Moon, D.-S., Eikenberry, S. S., & Wasserman, I. M. 2003, SMC X-1 as an Intermediate-Stage Flaring X-Ray Pulsar, The Astrophysical Journal Letters, 582, L91, doi: 10.1086/367782

Motch, C., Pakull, M. W., Soria, R., Grisé, F., & Pietrzyński, G. 2014, A mass of less than 15 solar masses for the black hole in an ultraluminous X-ray source, Nature, 514, 198, doi: 10.1038/nature13730

Motta, S. E., Marelli, M., Pintore, F., et al. 2020, The Slow Heartbeats of an Ultraluminous X-Ray Source in NGC 3621, The Astrophysical Journal, 898, 174, doi: 10.3847/1538-4357/ab9b81

Mushtukov, A. A., Ingram, A., Middleton, M., Nagirner, D. I., & van der Klis, M. 2019, Timing properties of ULX pulsars: optically thick envelopes and outflows, Monthly Notices of the Royal Astronomical Society, 484, 687, doi: 10.1093/mnras/sty3525

Mushtukov, A. A., Suleimanov, V. F., Tsygankov, S. S., & Ingram, A. 2017, Optically thick envelopes around ULXs powered by accreating neutron stars, Monthly Notices of the Royal Astronomical Society, 467, 1202, doi: 10.1093/mnras/stx141

Mushtukov, A. A., Suleimanov, V. F., Tsygankov, S. S., & Poutanen, J. 2015a, On the maximum accretion luminosity of magnetized neutron stars: connecting X-ray pulsars and ultraluminous X-ray sources, Monthly Notices of the Royal Astronomical Society, 454, 2539, doi: 10.1093/mnras/stv2087

Mushtukov, A. A., Suleimanov, V. F., Tsygankov, S. S., & Poutanen, J. 2015b, The critical accretion luminosity for magnetized neutron stars, Monthly Notices of the Royal Astronomical Society, 447, 1847, doi: 10.1093/mnras/stu2484

Nagase, F. 1989, Accretion-powered X-ray pulsars., Publications of the Astronomical Society of Japan, 41, 1

Naik, S., Das, M., Jain, C., & Paul, B. 2010, An X-ray bright nucleus in the low-surface-brightness galaxy UGC 6614, Monthly Notices of the Royal Astronomical Society, 404, 2056, doi: 10.1111/j.1365-2966.2010.16423.x

Naik, S., & Paul, B. 2003, Spectral variations of the X-ray binary pulsar LMC X-4 during its long period intensity variation and a comparison with Her X-1, A&A, 401, 265, doi: 10.1051/0004-6361:20030111

Naik, S., & Paul, B. 2004, Timing and Spectral Studies of LMC X-4 in High and Low States with BeppoSAX: Detection of Pulsations in the Soft Spectral Component, The Astrophysical Journal, 600, 351, doi: 10.1086/379803

Nandra, K., George, I. M., Mushotzky, R. F., Turner, T. J., & Yaqoob, T. 1997, ASCA Observations of Seyfert 1 Galaxies. I. Data Analysis, Imaging, and Timing, The Astrophysical Journal, 476, 70, doi: 10.1086/303600

Neilsen, J., Hickox, R. C., & Vrtilek, S. D. 2004, Phase Variation in the Pulse Profile of SMC X-1, The Astrophysical Journal Letters, 616, L135, doi: 10.1086/426890

Netzer, H. 2015, Revisiting the Unified Model of Active Galactic Nuclei, Annual Review of Astronomy and Astrophysics, 53, 365, doi: 10.1146/annurev-astro-082214-122302

Ng, C., Díaz Trigo, M., Cadolle Bel, M., & Migliari, S. 2010, A systematic analysis of the broad iron K line in neutron-star LMXBs with XMM-Newton, A&A, 522, A96, doi: 10.1051/0004-6361/200913575

Novick, R. 1975, Stellar and Solar X-Ray Polarimetry, Space Science Reviews, 18, 389, doi: 10.1007/BF00212912

Novick, R., Weisskopf, M. C., Berthelsdorf, R., Linke, R., & Wolff, R. S. 1972, Detection of X-Ray Polarization of the Crab Nebula, The Astrophysical Journal Letters, 174, L1, doi: 10.1086/180938

Ogilvie, G. I., & Dubus, G. 2001, Precessing warped accretion discs in X-ray binaries, Monthly Notices of the Royal Astronomical Society, 320, 485, doi: 10.1046/j.1365-8711.2001.04011.x

Paczyński, B., & Wiita, P. J. 1980, Thick Accretion Disks and Supercritical Luminosities, Astronomy & Astrophysics, 88, 23

Pakull, M. W., & Mirioni, L. 2002, Optical Counterparts of Ultraluminous X-Ray Sources. https://arxiv.org/abs/astro-ph/0202488

Paul, & Naik. 2011, Transient High Mass X-ray Binaries, Bulletin of the Astronomical Society of India, 39, 429, doi: 10.48550/arXiv.1110.4446

Paul, B. 2017, Neutron Stars in X-ray Binaries and their Environments, Journal of Astrophysics and Astronomy, 38, 39, doi: 10.1007/s12036-017-9475-4

Paul, B. 2022, in 44th COSPAR Scientific Assembly. Held 16-24 July, Vol. 44, 1853

Paul, B., & Kitamoto, S. 2002, Superorbital Period Variations in the X-ray Pulsar LMC X-4, Journal of Astrophysics and Astronomy, 23, 33, doi: 10.1007/BF02702462

Paul, B., Nagase, F., Endo, T., et al. 2002, Nature of the Soft Spectral Component in the X-Ray Pulsars SMC X-1 and LMC X-4, The Astrophysical Journal, 579, 411, doi: 10.1086/342701

Pinto, C., Middleton, M. J., & Fabian, A. C. 2016, Resolved atomic lines reveal outflows in two ultraluminous X-ray sources, Nature, 533, 64, doi: 10.1038/nature17417

Pinto, C., Alston, W., Soria, R., et al. 2017, From ultraluminous X-ray sources to ultraluminous supersoft sources: NGC 55 ULX, the missing link, Monthly Notices of the Royal Astronomical Society, 468, 2865, doi: 10.1093/mnras/stx641

Pinto, C., Soria, R., Walton, D. J., et al. 2021, XMM-Newton campaign on the ultraluminous X-ray source NGC 247 ULX-1: outflows, Monthly Notices of the Royal Astronomical Society, 505, 5058, doi: 10.1093/mnras/stab1648

Pintore, F., Zampieri, L., Stella, L., et al. 2017, Pulsator-like Spectra from Ultraluminous X-Ray Sources and the Search for More Ultraluminous Pulsars, The Astrophysical Journal, 836, 113, doi: 10.3847/1538-4357/836/1/113

Pintore, F., Zampieri, L., Wolter, A., & Belloni, T. 2014, Ultraluminous X-ray sources: a deeper insight into their spectral evolution, Monthly Notices of the Royal Astronomical Society, 439, 3461, doi: 10.1093/mnras/stu195

Pintore, F., Marelli, M., Salvaterra, R., et al. 2020, The Ultraluminous X-Ray Sources Population of the Galaxy NGC 7456, The Astrophysical Journal, 890, 166, doi: 10.3847/1538-4357/ab6ffd

Pintore, F., Motta, S., Pinto, C., et al. 2021, The rare X-ray flaring activity of the ultraluminous X-ray source NGC 4559 X7, Monthly Notices of the Royal Astronomical Society, 504, 551, doi: 10.1093/mnras/stab913

Pintore, F., Pinto, C., Rodriguez-Castillo, G., et al. 2025, A new pulsating neutron star in the ultraluminous X-ray source NGC 4559 X7?, Astronomy & Astrophysics, 695, A238, doi: 10.1051/0004-6361/202453240

Postnov, K., Shakura, N., Staubert, R., et al. 2013, Variable neutron star free precession in Hercules X-1 from evolution of RXTE X-ray pulse profiles with phase of the 35-d cycle, Monthly Notices of the Royal Astronomical Society, 435, 1147, doi: 10.1093/mnras/stt1363

Pradhan, P., Bozzo, E., & Paul, B. 2018, Supergiant fast X-ray transients versus classical supergiant high mass X-ray binaries: Does the difference lie in the companion wind?, Astronomy & Astrophysics, 610, A50, doi: 10.1051/0004-6361/201731487

Pradhan, P., Maitra, C., & Paul, B. 2020, Is Superorbital Modulation in SMC X-1 Caused by Absorption in a Warped Precessing Accretion Disk?, The Astrophysical Journal, 895, 10, doi: 10.3847/1538-4357/ab8224

Pringle, J. E., & Rees, M. J. 1972, Accretion Disc Models for Compact X-Ray Sources, Astronomy & Astrophysics, 21, 1

Produit, N., Bao, T. W., Batsch, T., et al. 2018, Design and construction of the POLAR detector, Nuclear Instruments and Methods in Physics Research A, 877, 259, doi: 10.1016/j.nima.2017.09.053

Qiu, Y., & Feng, H. 2021, Linking Soft Excess in Ultraluminous X-Ray Sources with Optically Thick Wind Driven by Supercritical Accretion, The Astrophysical Journal, 906, 36, doi: 10.3847/1538-4357/abc959

Qiu, Y., Soria, R., Wang, S., et al. 2019, CG X-1: An Eclipsing Wolf–Rayet ULX in the Circinus Galaxy, The Astrophysical Journal, 877, 57, doi: 10.3847/1538-4357/ab16e7

Raman, G., Maitra, C., & Paul, B. 2018, Observation of variable pre-eclipse dips and disc windsin the eclipsing LMXB XTE J1710-281, Monthly Notices of the Royal Astronomical Society, 477, 5358, doi: 10.1093/mnras/sty918

Reig, P. 2011, Be/X-ray binaries, , 332, 1, doi: 10.1007/s10509-010-0575-8

Rikame, K., Paul, B., Sharma, R., Jithesh, V., & Paul, K. T. 2024, Flares during eclipses of high-mass X-ray binary systems Vela X-1, 4U 1700-37, and LMC X-4, Monthly Notices of the Royal Astronomical Society, 529, 3360, doi: 10.1093/mnras/stae739

Robba, A., Pinto, C., Walton, D. J., et al. 2021, Broadband X-ray spectral variability of the pulsing ULX NGC 1313 X-2, Astronomy & Astrophysics, 652, A118, doi: 10.1051/0004-6361/202140884

Rosswog, S., & Bruggen, M. 2003, Introduction to High-Energy Astrophysics

Rybicki, G. B., & Lightman, A. P. 1979, Radiative processes in astrophysics

Sathyaprakash, R., Roberts, T. P., Walton, D. J., et al. 2019, The discovery of weak coherent pulsations in the ultraluminous X-ray source NGC 1313 X-2, Monthly Notices of the Royal Astronomical Society: Letters, 488, L35, doi: 10.1093/mnrasl/slz086

Sato, N., Hayakawa, S., Nagase, F., et al. 1986, X-ray probing of the circumstellar matter in the Vela X-1 system fromobservations over an eclipse phase., Publications of the Astronomical Society of Japan, 38, 731, doi: 10.1093/pasj/38.5.731

Shakura, N. I., & Sunyaev, R. A. 1973, Black holes in binary systems. Observational appearance., Astronomy & Astrophysics, 24, 337

Sharma, R., Jain, C., & Paul, B. 2023a, 4U 1626-67 returns to spin-down: timing features toe the line, Monthly Notices of the Royal Astronomical Society, 526, L35, doi: 10.1093/mnrasl/slad110

Sharma, R., Jain, C., Rikame, K., & Paul, B. 2023b, Broad-band mHz QPOs and spectral study of LMC X-4 with AstroSat, Monthly Notices of the Royal Astronomical Society, 519, 1764, doi: 10.1093/mnras/stac3572

Sidoli, L., Romano, P., Mangano, V., et al. 2008, Monitoring Supergiant Fast X-Ray Transients with Swift. I. Behavior Outside Outbursts, The Astrophysical Journal, 687, 1230, doi: 10.1086/590077

Soria, R., Cropper, M., Pakull, M., Mushotzky, R., & Wu, K. 2005, The star-forming environment of an ultraluminous X-ray source in NGC 4559: an optical study, Monthly Notices of the Royal Astronomical Society, 356, 12, doi: 10.1111/j.1365-2966.2004.08438.x

Srinivasan, G. 2024, Recycled pulsars - a historical perspective, , 369, 125, doi: 10.1007/s10509-024-04389-1

Stobbart, A.-M., Roberts, T. P., & Warwick, R. S. 2004, A dipping black hole X-ray binary candidate in NGC 55, Monthly Notices of the Royal Astronomical Society, 351, 1063, doi: 10.1111/j.1365-2966.2004.07848.x

Sutton, A. D., Roberts, T. P., & Middleton, M. J. 2013, The ultraluminous state revisited: fractional variability and spectral shape as diagnostics of super-Eddington accretion, Monthly Notices of the Royal Astronomical Society, 435, 1758, doi: 10.1093/mnras/stt1419

Tamang, A., Roy, K., Manikantan, H., Balu, A., & Paul, B. 2025, Unveiling the intensity-dependent wake structure of Vela X−1 using MAXI/GSC, Astronomy & Astrophysics, 698, A122, doi: 10.1051/0004-6361/202451923

Tauris, T. M., & van den Heuvel, E. P. J. 2006, in Compact stellar X-ray sources, ed. W. H. G. Lewin & M. van der Klis, Vol. 39, 623–665, doi: 10.48550/arXiv.astro-ph/0303456

Torrejón, J. M., Schulz, N. S., Nowak, M. A., & Kallman, T. R. 2010, A Chandra Survey of Fluorescence Fe Lines in X-ray Binaries at High Resolution, The Astrophysical Journal, 715, 947, doi: 10.1088/0004-637X/715/2/947

Truemper, J., Kahabka, P., Oegelman, H., Pietsch, W., & Voges, W. 1986, EXOSAT Observations of the 35 Day Cycle of Hercules X-1: Evidence for Neutron Star Precession, The Astrophysical Journal Letters, 300, L63, doi: 10.1086/184604

Tsygankov, S. S., Doroshenko, V., Lutovinov, A. A., Mushtukov, A. A., & Poutanen, J. 2017a, SMC X-3: the closest ultraluminous X-ray source powered by a neutron star with non-dipole magnetic field, Astronomy & Astrophysics, 605, A39, doi: 10.1051/0004-6361/201730553

Tsygankov, S. S., Doroshenko, V., Lutovinov, A. A., Mushtukov, A. A., & Poutanen, J. 2017b, SMC X-3: the closest ultraluminous X-ray source powered by a neutron star with non-dipole magnetic field, Astronomy & Astrophysics, 605, A39, doi: 10.1051/0004-6361/201730553

Tsygankov, S. S., Lutovinov, A. A., Churazov, E. M., & Sunyaev, R. A. 2007, 4U 0115+63 from RXTE and INTEGRAL data: Pulse profile and cyclotron line energy, Astronomy Letters, 33, 368, doi: 10.1134/S1063773707060023

Tsygankov, S. S., Lutovinov, A. A., Doroshenko, V., et al. 2016, Propeller effect in two brightest transient X-ray pulsars: 4U 0115+63 and V 0332+53, Astronomy & Astrophysics, 593, A16, doi: 10.1051/0004-6361/201628236

Tully, R. B., Courtois, H. M., & Sorce, J. G. 2016, COSMICFLOWS-3, The Astronomical Journal, 152, 50, doi: 10.3847/0004-6256/152/2/50

Urquhart, R., & Soria, R. 2016, Two Eclipsing Ultraluminous X-Ray Sources in M51, The Astrophysical Journal, 831, 56, doi: 10.3847/0004-637X/831/1/56

Urry, C. M., & Padovani, P. 1995, Unified Schemes for Radio-Loud Active Galactic Nuclei, Publications of the Astronomical Society of the Pacific, 107, 803, doi: 10.1086/133630

Vadawale, S. V., Chattopadhyay, T., Rao, A. R., et al. 2015, Hard X-ray polarimetry with Astrosat-CZTI, Astronomy & Astrophysics, 578, A73, doi: 10.1051/0004-6361/201525686

van der Klis, M. 1994, in American Institute of Physics Conference Series, Vol. 308, The Evolution of X-ray Binariese, ed. S. Holt & C. S. Day (AIP), 505, doi: 10.1063/1.45930

van der Klis, M. 1997, Rapid X-ray variability in galactic black hole candidates, Advances in Space Research, 19, 75, doi: 10.1016/S0273-1177(97)00040-9

van der Klis, M. 2006, in Compact stellar X-ray sources, ed. W. H. G. Lewin & M. van der Klis, Vol. 39, 39–112

Vasilopoulos, G., Ray, P. S., Gendreau, K. C., et al. 2020, The 2019 super-Eddington outburst of RX J0209.6-7427: detection of pulsations and constraints on the magnetic field strength, Monthly Notices of the Royal Astronomical Society, 494, 5350, doi: 10.1093/mnras/staa991

Vatedka, R., Tyagi, A., Vadodariya, K., et al. 2025, X-ray spectroscopy and timing experiment on XPoSat: instrument configuration and science prospects, Journal of Astronomical Telescopes, Instruments, and Systems, 11, 035001, doi: 10.1117/1.JATIS.11.3.035001

Verner, D. A., Ferland, G. J., Korista, K. T., & Yakovlev, D. G. 1996, Atomic Data for Astrophysics. II. New Analytic FITS for Photoionization Cross Sections of Atoms and Ions, The Astrophysical Journal, 465, 487, doi: 10.1086/177435

Walter, R., Lutovinov, A. A., Bozzo, E., & Tsygankov, S. S. 2015, High-mass X-ray binaries in the Milky Way. A closer look with INTEGRAL, The Astronomy and Astrophysics Review, 23, 2, doi: 10.1007/s00159-015-0082-6

Walton, D. J., Mackenzie, A. D. A., Gully, H., et al. 2021, A multimission catalogue of ultraluminous X-ray source candidates, Monthly Notices of the Royal Astronomical Society, 509, 1587, doi: 10.1093/mnras/stab3001

Walton, D. J., Miller, J. M., Reis, R. C., & Fabian, A. C. 2012, Searching for massive outflows in Holmberg IX X-1 and NGC 1313 X-1: the iron K band, Monthly Notices of the Royal Astronomical Society, 426, 473, doi: 10.1111/j.1365-2966.2012.21727.x

Walton, D. J., Reis, R. C., Cackett, E. M., Fabian, A. C., & Miller, J. M. 2012, The similarity of broad iron lines in X-ray binaries and active galactic nuclei, Monthly Notices of the Royal Astronomical Society, 422, 2510, doi: 10.1111/j.1365-2966.2012.20809.x

Walton, D. J., Fürst, F., Bachetti, M., et al. 2016, A 78 Day X-Ray Period Detected from NGC 5907 ULX1 by Swift, The Astrophysical Journal Letters, 827, L13, doi: 10.3847/2041-8205/827/1/L13

Walton, D. J., Fürst, F., Harrison, F. A., et al. 2017, The Broadband Spectral Variability of Holmberg IX X-1, The Astrophysical Journal, 839, 105, doi: 10.3847/1538-4357/aa683e

Walton, D. J., Fürst, F., Harrison, F. A., et al. 2018a, Super-Eddington accretion on to the neutron star NGC 7793 P13: Broad-band X-ray spectroscopy and ultraluminous X-ray sources, Monthly Notices of the Royal Astronomical Society, 473, 4360, doi: 10.1093/mnras/stx2650

Walton, D. J., Fürst, F., Heida, M., et al. 2018b, Evidence for Pulsar-like Emission Components in the Broadband ULX Sample, The Astrophysical Journal, 856, 128, doi: 10.3847/1538-4357/aab610

Walton, D. J., Pinto, C., Nowak, M., et al. 2020, The unusual broad-band X-ray spectral variability of NGC 1313 X-1 seen with XMM–Newton, Chandra, and NuSTAR, Monthly Notices of the Royal Astronomical Society, 494, 6012, doi: 10.1093/mnras/staa1129

Wang, S., Soria, R., Urquhart, R., & Liu, J. 2018, Discovery of two eclipsing X-ray binaries in M 51, Monthly Notices of the Royal Astronomical Society, 477, 3623, doi: 10.1093/mnras/sty872

Wang, Y.-M. 1995, On the Torque Exerted by a Magnetically Threaded Accretion Disk, The Astrophysical Journal, 449, L153, doi: 10.1086/309649

Watarai, K.-y., Fukue, J., Takeuchi, M., & Mineshige, S. 2000, Galactic Black-Hole Candidates Shining at the Eddington Luminosity, Publications of the Astronomical Society of Japan, 52, 133, doi: 10.1093/pasj/52.1.133

Weisskopf, M. C., Brinkman, B., Canizares, C., et al. 2002, An Overview of the Performance and Scientific Results from the Chandra X-Ray Observatory, Publications of the Astronomical Society of the Pacific, 114, 1, doi: 10.1086/338108

Weisskopf, M. C., Elsner, R. F., & O'Dell, S. L. 2010, in Society of Photo-Optical Instrumentation Engineers (SPIE) Conference Series, Vol. 7732, Space Telescopes and Instrumentation 2010: Ultraviolet to Gamma Ray, ed. M. Arnaud, S. S. Murray, & T. Takahashi, 77320E, doi: 10.1117/12.857357

Weisskopf, M. C., Silver, E. H., Kestenbaum, H. L., Long, K. S., & Novick, R. 1978, A precision measurement of the X-ray polarization of the Crab Nebula without pulsar contamination., The Astrophysical Journal Letters, 220, L117, doi: 10.1086/182648

Weisskopf, M. C., Ramsey, B., O'Dell, S. L., et al. 2016, The Imaging X-ray Polarimetry Explorer (IXPE), Results in Physics, 6, 1179, doi: 10.1016/j.rinp.2016.10.021

Weisskopf, M. C., Soffitta, P., Baldini, L., et al. 2022, The Imaging X-Ray Polarimetry Explorer (IXPE): Pre-Launch, Journal of Astronomical Telescopes, Instruments, and Systems, 8, 026002, doi: 10.1117/1.JATIS.8.2.026002

West, L. A., Lehmer, B. D., Wik, D., et al. 2018, On the Nature of the X-Ray Emission from the Ultraluminous X-Ray Source, M33 X-8: New Constraints from NuSTAR and XMM-Newton, The Astrophysical Journal, 869, 111, doi: 10.3847/1538-4357/aaec6b

White, N. E., Swank, J. H., & Holt, S. S. 1983, Accretion powered X-ray pulsars., The Astrophysical Journal, 270, 711, doi: 10.1086/161162

Wilms, J., Allen, A., & McCray, R. 2000, On the Absorption of X-Rays in the Interstellar Medium, The Astrophysical Journal, 542, 914, doi: 10.1086/317016

Wilson-Hodge, C. A., Malacaria, C., Jenke, P. A., et al. 2018, NICER and Fermi GBM Observations of the First Galactic Ultraluminous X-Ray Pulsar Swift J0243.6+6124, The Astrophysical Journal, 863, 9, doi: 10.3847/1538-4357/aace60

Wojdowski, P., Clark, G. W., Levine, A. M., Woo, J. W., & Zhang, S. N. 1998, Quasi-periodic Occultation by a Precessing Accretion Disk and Other Variabilities of SMC X-1, The Astrophysical Journal, 502, 253, doi: 10.1086/305893

XMM-Newton Science Operations Centre. 2025, Users Guide to the XMM-Newton Science Analysis System, issue 19.0 edn., ESA: XMM-Newton SOC

Zampieri, L., Mucciarelli, P., Falomo, R., et al. 2004, The Ultraluminous X-Ray Source NGC 1313 X-2 (MS 0317.7–6647) and Its Environment, The Astrophysical Journal, 603, 523, doi: 10.1086/381541

Zhang, S.-N., Kole, M., Bao, T.-W., et al. 2019, Detailed polarization measurements of the prompt emission of five gamma-ray bursts, Nature Astronomy, 3, 258, doi: 10.1038/s41550-018-0664-0